UNIVERSITY OF CALIFORNIA SAN DIEGO

Application of continuum mechanics for a variety of curvature generation phenomena in cell biophysics

A dissertation submitted in partial satisfaction of the
requirements for the degree
Doctor of Philosophy

in

Engineering Sciences (Mechanical Engineering)

by

Haleh Alimohamadi

Committee in charge:

Professor Padmini Rangamani, Chair
Professor Juan Carlos del Álamo
Professor Velia Fowler
Professor James Friend
Professor Andrew McCulloch
Professor David Saintillan

2021

The dissertation of Haleh Alimohamadi is approved, and it is acceptable in quality and form for publication on microfilm and electronically:

University of California San Diego

2021

DEDICATION

To my Husband, Mohsen, my Parents, Atekeh and Mohammad, Teachers, and Friends who supported me and kept me learning.

EPIGRAPH

A person who never made a mistake never tried anything new.

—Albert Einstein

TABLE OF CONTENTS

LIST OF FIGURES

LIST OF TABLES

ACKNOWLEDGEMENTS

First, I would like to acknowledge Prof. Padmini Rangamani for her support as the chair of my committee. She has consistently inspired me with her ambition, passion and management skills. She has also taught me to be a collaborative researcher and a passable communicator. My success would definitely not have been possible, had it not been such an exceptional advisor who provided an incredible research-oriented environment and all the resources that the students need to succeed.

I would like to thank my PhD committee members including Prof. Velia Fowler, Prof. Andrew McCulloch, Prof. David Saintillan, Prof. James Friend, Prof. Juan Carlos del Álamo, and Prof. Juan C. Lasheras for their invaluable advice. They have always been approachable and supportive of my ideas.

I would like also to thank the many collaborators who have contributed to my thesis. I list each of these contributions below.

For chapter 2, I would like to acknowledge my co-author Prof. Padmini Rangamani, and Dr. Morgan Chabanon, Miriam Bell, and Allen Leung for his suggestions on improving the manuscript. I would also like to acknowledge grant funding: the Visible Molecular Cell Consortium (VMCC) and the Center for Trans-scale Structural Biology and Biophysics (CTSBB) at UC San Diego. Figures used in this chapter adapted content from Servier Medical Art powerpoint image bank. Chapter 2 contains Material from "Modeling Membrane Curvature Generation due to Membrane–Protein Interactions" by Haleh Alimohamadi and Padmini Rangamani, which appears in Biomolecules, October 2018 [5]. The dissertation author was the primary investigator and author of this paper.

For chapter 3, I would like to acknowledge my co-authors Dr. Ritvik Vasan, Dr. Julian Hassinger, Feng Yuan, Brandon Bakka, Andrea Trementozzi, Kasey Day, Prof. Nicolas Fawzi, Prof. Jeanne Stachowiak, and Prof. Padmini Rangamani. I would also like to thank Prof. David

Drubin for initial discussions and Dr. Morgan Chabanon for his suggestions on improving the manuscript. I would also like to acknowledge grant funding: the Visible Molecular Cell Consortium (VMCC) and the Center for Trans-scale Structural Biology and Biophysics (CTSBB) at UC San Diego. Chapter 3 contains Material from "The role of traction in membrane curvature generation" by Haleh Alimohamadi, Ritvik Vasan, Julian Hassinger, Jeanne Stachowiak, and Padmini Rangamani, which appears in Molecular Biology of the Cell, August 2018 [6] and "Membrane bending by protein phase separation" by Feng Yuan, Haleh Alimohamadi, Brandon Bakka, Andrea Trementozzi, Kasey Day, Nicolas Fawzi, Padmini Rangamani, and Jeanne Stachowiak, which appears in Proceedings of the National Academy of Sciences, March 2021 [7]. The dissertation author was the primary investigator and author of this paper.

For chapter 4, I would like to acknowledge my co-authors Prof. Ben Ovryn and Prof. Padmini Rangamani. I would also like to thank Dr. Morgan Chabanon and Miriam Bell for their feedback on the study. Chapter 4 contains Material from "Modeling membrane nanotube morphology: the role of heterogeneity in composition and material properties" by Haleh Alimohamadi, Ben Ovrn, and Padmini Rangamani, which appears in Scientific reports, February 2020 [8]. The dissertation author was the primary investigator and author of this paper.

For chapter 5, I would like to acknowledge my co-authors Dr. Alyson Smith, Dr. Roberta Nowak, Prof. Velia Fowler, and Prof. Padmini Rangamani. I would also like to thank Dr. Christopher T. Lee and Miriam Bell for their feedback on the study. Chapter 5 contains Material from "Non-uniform distribution of myosin-mediated forces governs red blood cell membrane curvature through tension modulation" by Haleh Alimohamadi, Alyson Smith, Roberta Nowak, Velia Fowler, and Padmini Rangamani, which appears in PLoS computational biology, May 2020 [9]. The dissertation author was the primary investigator and author of this paper.

For chapter 6, I would like to acknowledge my co-authors Miriam Bell, Prof. Shelley Halpain, and Prof. Padmini Rangamani. Chapter 6 contains Material from "Mechanical principles

governing the shapes of dendritic spines" by Haleh Alimohamadi, Miriam Bell, Shelley Halpain, and Padmini Rangamani, which is posted in bioRxiv, September 2020 [10]. The dissertation author was the primary investigator and author of this paper.

I would like to acknowledge current and former members of my lab including Morgan, Miriam, Chris, Allen, Justin, Andrea, Kiersten, Ritvik, Arijit, Mickey, Jennifer, Mrunal, Cuncheng, Can, Donya, Poorya, Lucas, Mayte, Ben, Sage, and Marco. I would also like to thank my friends for supporting me during my PhD studies particularly my best friends Parisa and Zamzam!

Finally, I want to thank my family, Atekeh, Mohammad, and Ali who have always been incredibly supportive of my career. My husband, Mohsen, has been extremely supportive of me throughout this entire process and has made countless sacrifices to help me get to this point. I could overcome all the difficulties thanks to my family's understanding, patience, and love.

VITA

2012	B. S. in Mechanical Engineering, University of Tehran, Tehran, Iran
Winter 2019	Teaching Assistant, University of California San Diego
Spring 2019	Teaching Assistant, University of California San Diego
Winter 2021	Teaching Assistant, University of California San Diego
2021	Ph. D. in Engineering Sciences (Mechanical Engineering), University of California San Diego

PUBLICATIONS

Alimohamadi, H.*, Vasan, R.*, Hassinger, J.E., Stachowiak, J.C. and Rangamani, P., (2018). The role of traction in membrane curvature generation. *Molecular Biology of the Cell*, 29(16), pp.2024-2035. doi: 10.1091/mbc.E18-02-0087.

Alimohamadi, H. and Rangamani, P., (2018). Modeling membrane curvature generation due to membrane-protein interactions. *Biomolecules*, 8(4), pp. 120-145. doi: 10.3390/biom8040120.

Alimohamadi, H., Ovryn, B., and Rangamani, P., (2020). Modeling membrane nanotube morphology: the role of heterogeneity in composition and material properties. *Scientific Reports*, 10(1), pp.1-15. doi: 10.1038/s41598-020-59221-x.

Alimohamadi, H., Smith, A.S., Nowak, R. B., Fowler, V. M., and Rangamani, P., (2020). Non-uniform distribution of myosin-mediated forces governs red blood cell membrane curvature through tension modulation. *PLOS Computational Biology*, 16(5), pp.e1007890. doi: 10.1371/journal.pcbi.1007890.

Yuan, F., Alimohamadi, H., Bakka, B., Trementozzi, A.N., Day, K.J., Fawzi, N.L., Rangamani, P., and Stachowiak, J.C., (2021). Membrane bending by protein phase separation. *Proceedings of the National Academy of Sciences*, 118(11). doi: 110.1073/pnas.2017435118.

Alimohamadi, H., Bell, M., Halpain, S., and Rangamani, P., (2020). Mechanical principles governing the shapes of dendritic spines. *bioRxiv*. doi: 10.1101/2020.09.09.290650.

ABSTRACT OF THE DISSERTATION

Application of continuum mechanics for a variety of curvature generation phenomena in cell biophysics

by

Haleh Alimohamadi

Doctor of Philosophy in Engineering Sciences (Mechanical Engineering)

University of California San Diego, 2021

Professor Padmini Rangamani, Chair

To dynamically reshape the membrane, cells rely on a variety of intracellular mechanisms, ranging from forces exerted by the cytoskeleton to the spontaneous curvature induced by membrane–protein interactions. In this thesis, we present mathematical models in a continuum framework to understand the physics underlying membrane deformation by two different modes of curvature-generating mechanisms (1) protein-induced spontaneous curvature and (2) forces due to membrane-cytoskeleton interactions. In the first part of the thesis, we model the effects of curvature-generating proteins by extending the classical Helfrich-Canham bending energy and demonstrate how the local shape of the membrane can be used to infer the traction acting locally on the membrane. Particularly, we first propose a technique to extract effective line tension at the protein interface using the morphology and the composition of the membrane. We then analyze

the beading morphology of membrane nanotubes due to heterogeneity in the membrane properties and protein distribution. We find that there exists a discontinuity in the energy that impedes two beads from fusing. Finally, we show the application of our continuum framework for studying curvature generation due to protein phase separation on membranes.

In the second part of the thesis, we model the forces due to membrane-cytoskeleton interactions by adding an extra degree of freedom to the energy equation to account for heterogeneous forces representing the effects of actin polymerization and activity of molecular motors such as myosin on the plasma membrane. Using this framework, we show that a non-uniform force distribution coupled with membrane tension characterized the biconcave shape of Red Blood Cells (RBCs). We also explore the application of our mathematical framework to identify the possible force regimes that give rise to the classic shapes of dendritic spines which are bulbous protrusions along the dendrites of neurons and are sites of excitatory postsynaptic activity. We identify different mechanical pathways that are likely associated with different dendritic spine shapes, and find that some mechanisms may be energetically more favorable than others. We believe our models identify mechanisms of cell shape adaption by two modes of curvature generation, enabling future work to establish the contribution of cell membrane mechanics in many human diseases and designing better systems for drug and gene delivery.

Chapter 1

Cell shape regulation: A nano-scale curvature generating problem

1.1 Introduction

This thesis is a collection of problems in cell shape regulation organized by the mode of curvature generating mechanisms. The ability of cellular membranes to bend and adapt their configurations is critical for a variety of cellular functions including membrane trafficking processes [11, 12], fission [13, 14], fusion [15, 16], and differentiation [17]. Defects or disruptions in these processes can lead to drawbacks in development and disease [18, 19]. For example, changes in the level of cytosolic phospholipase A_2 (cPLA$_2\alpha$) enzyme affect the formation of transport vesicles from the Golgi to the plasma membrane [20]. This malfunction can cause diseases such as asthma [21], arthritis [22], cerebral ischemia [23], heart disease [24], and cancers [25].

The degree of membrane deformability depends on lipid packing, which can affect

membrane tension and the flow and diffusion of lipids in the plane of the membrane [26–28]. In order to dynamically reshape the membrane, cells rely on a variety of molecular mechanisms, ranging from forces exerted by the cytoskeleton [29–31] to the spontaneous curvature induced by the membrane-protein interactions [26, 32–34]. Each mechanism generates unique surface stresses on the membrane and these surface stresses can be mapped onto the shape to understand the mechanical aspects of the membrane deformation [6, 35–37].

1.1.1 Membrane curvature generation by proteins

The interplay between cellular membranes and membrane proteins is one of the major sources of curvature production in cells. Membrane-protein interactions result not only from proteins that are integral to the membrane, but also from proteins that can bind to the membrane surface locally in response to signaling events such as scaffolding molecules or GTPases [32, 33, 38–41].

Many different mechanisms have been proposed for how proteins can generate curvature of the membrane. For the purposes of theoretical modeling and capturing the key physical principles, the broadly accepted mechanisms can be grouped into two main categories; (i) the hydrophobic insertion mechanism, and (ii) coat proteins with hydrophilic domains [33, 42, 43]. In the hydrophobic insertion mechanism, partially embedded amphipathic helices of the protein domains change the relative area of the two membrane leaflets. This area mismatch produces stresses, which result in membrane bending [44, 45]. In contrast, when proteins are thought to coat the membrane, there is no insertion into the lipid bilayer and proteins simply oligomerize along the membrane surface [46, 47]. In this case, it has been suggested that the steric pressure generated due to protein crowding and scaffolding drive the membrane deformation [48, 49]. In the following, we outline the different type of proteins and their importance in cellular processes by adjusting the membrane curvature.

Conical and Inverted Conical-Shaped Proteins

The shape of transmembrane proteins can be approximated as conical or inverted conical shapes [50–52]. These proteins are thought to insert into the membrane, distort the packing of the lipids, and thus impose local negative or positive curvature to the underlying membrane [53]. The attached conical or inverted conical-shaped proteins induce membrane bending due to insertion causing a wedge effect (Fig. 1.1B), which can possibly be amplified by oligomerization (Fig. 1.1C), protein crowding (Fig. 1.1E), or hydrophobic mismatch [54]. Two classical examples of conical transmembrane proteins are potassium ion channels (1K4D) and Nicotinic acetylcholine receptors, which can generate long-range membrane deformations [55].

BIN-Amphiphysin-Rvs (BAR) Domain Proteins

BAR domain proteins are banana-shaped proteins that can both sense and influence membrane curvature [56,57]. BAR domain proteins are made of three coiled core helices attached to multiple positively charged residues [32,58]. BAR proteins are known to induce membrane curvature by two mechanisms–scaffolding (imposing their intrinsic shapes on the membrane substrate, Fig. 1.1D) [32] and insertion of amphipathic wedges at the interface of the lipid bilayer (Fig. 1.1B), locally creating a wedge effect [59]. In terms of functionality, BAR domain proteins are involved in numerous cellular processes including endocytosis, exocytosis, apoptosis, and cell-cell fusion [58].

Coat Proteins

In order to regulate some cellular trafficking phenomena, multiple proteins need to bind to the membrane and form a coat complex such as clathrin, coat protein complex I (COPI), and COPII [60]. These protein assemblies can act as a scaffold (Fig. 1.1D) to impose their spherical curvature on the underlying membrane [32]. However, other components of the coat

can contribute to the membrane bending through helix insertion into the bilayer (Fig. 1.1B) or protein crowding (Fig. 1.1E) [32]. Clathrin-mediated endocytosis (CME) and ESCRT protein assemblies at the neck of endocytic buds are all examples of membrane remodeling due to the activity of the coat proteins [61–63].

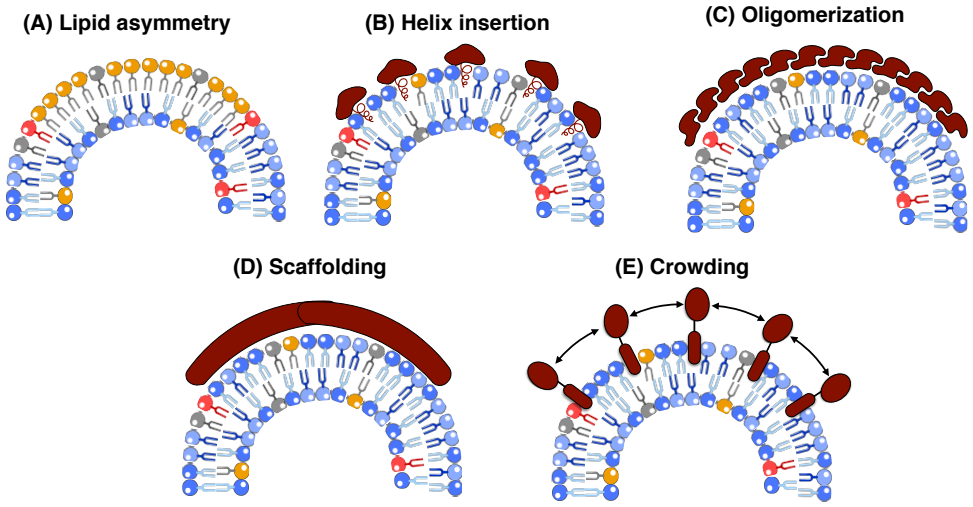

Figure 1.1: Different mechanisms of proteins curvature generation. (A) Different lipid composition between the two membrane leaflets induces curvature. (B) Helix insertion in one of the membrane leaflet bends the membrane. (C) Oligomerization of several monomers can scaffold and generate curvature. (D) Scaffolding proteins impose their curvatures on the underlying membrane. (E) Steric pressure due to the lateral collisions between the membrane-bound proteins can bend the membrane.

1.1.2 Membrane curvature generation by cytoskeleton

Maintenance or modification of cell shape is a concerted action of the actomyosin network at the whole cell level that allows for a stable actin network in polarized cells or a rapidly remodeling actin network for cell spreading and motility [64, 65]. Thus, networks of actin filaments (F-actin) and the F-actin-activated motor protein non-muscle myosin II (NMII) specify cell shape by exerting forces on the plasma membrane to control membrane tension and curvature [66–69]. These actomyosin networks determine cell shapes and interactions during tissue morphogenesis in

development [67, 70–74] and their dysregulation has been implicated in cancer, [75, 76], hearing disorders [77], and podocyte filtration in the kidney [77], among other physical issues. Local, nanoscale changes in actomyosin organization can lead to micron-scale changes in membrane curvature and cell shape to support normal cell function [78].

Actomyosin forces in Red Blood Cells (RBCs)

The spectrin-F-actin network was first discovered in mammalian RBCs. Studies of human and mouse congenital hemolytic anemias have shown the critical role of the RBC membrane skeleton in maintaining RBC biconcave shape and remarkable RBC mechanical deformability and stability, during their transits through the circulation [79–81]. A recent study by Smith et al. [82] highlighted a critical role for NMIIA interactions with F-actin in the membrane skeleton in controlling RBC membrane tension and curvature. This brings a new player onto the scene—NMIIA-generated forces that maintain RBC biconcave disk shape and deformability. Ultimately, RBCs can be used as a simple model system to explore the general role of NMII-generated forces in regulating plasma membrane curvature since RBCs are the only cell type where F-actin is exclusively in the membrane skeleton [81]. The ubiquity of the membrane skeleton at the plasma membranes of all metazoan cells, where F-actin is also present in a transcellular cytoskeleton, further emphasizes the utility of the RBC paradigm.

Actin-mediated forces in spines

In addition to playing a key role in RBC morphology, membrane-actin interactions are thought to play an important role in governing the geometries of dendritic spines. Dendritic spines are foci of synaptic communication in neurons and have characteristic shapes associated with aging, disease, and synaptic activity. It is well known that dendritic spines are rich in actin and have a complex cytoskeletal organization that aids in their dynamic plasticity and adaptability.

There are distinct subpopulations of F-actin in the dendritic spines including branched filaments in the spine head [83–85], long filaments in the spine neck [86–89], and periodic F-actin structures along the neck region of dendritic spines [90]. Actin dynamics in spines are tightly regulated by dozens of various actin binding proteins, some of which must also interact directly or indirectly with the spine plasma membrane [91–93]. Several proteins that crosslink or stabilize actin filaments, such as cortactin [94], spectrin [95], or drebrin [96] are known to regulate spine shape and separately, myosin motors can affect spine shape either directly by creating contractile forces, or indirectly by regulating the transport of cargo into and out of the spine [97, 98].

1.2 Biophysical modeling of cell membrane mechanics

There are various methods to visualize membrane curvatures in situ or in reconstituted systems such as X-ray crystallography [99, 100], fluorescence microscopy [101, 102], and electron microscopy (EM) [103, 104]. The use of these techniques provides an opportunity for scientists to decipher vast amounts of information about the molecular machinery underlying membrane shape transformations at high resolution. However, taking high resolution images is expensive and biological systems are very dynamic, making it challenging to experimentally quantify the role of a specific component, e.g., membrane-protein interactions, in biological phenomena [105–107]. The use of theoretical and computational approaches has become popular as complementary techniques to explore the mechanochemical aspects of membrane curvature generating mechanisms [108–113]. This provides not only great insight into the physical principles underlying each mechanism of curvature generation but also generates experimentally testable predictions for future investigations.

In this thesis, we focus on developing theoretical frameworks that can tightly integrate experiments with mathematical approaches to understand the physics underlying cell shape

regulation by two different curvature-generating mechanisms. Chapter 2, we summarized the commonly used continuum models for describing the constitutive relationships of the plasma membranes in contact with proteins. In Chapters 3, 4 and Appendix A, B, we focused on using continuum membrane mechanics models to study the role of protein-induced surface stress in driving endocytic buds, generating protein-lined tubules due to liquid-liquid phase separation of proteins, and governing the beading morphology of membrane nanotubes. In Chapter 5 and Appendix C, we proposed a new molecular mechanism – a non-uniform force distribution coupled with membrane tension– that could be responsible for maintaining the unique biconcave shape of RBCs. In Chapter 6 and Appendix D, we focused on the development of a minimal biophysical model of actin-mediated forces, curvature-inducing actin/protein rings, and membrane dynamics that can regulate the shape and size of dendritic spines. We finish with concluding remarks and possible future directions in Chapter 7.

Chapter 2

Membrane curvature generation by proteins

2.1 Composition of biological membranes

Biological membranes (BMs) form the outer boundary of living cells and compartments inside the cell. The main component of all biological membranes is a lipid bilayer, with a thickness of about 5–10 nm (see Figure 2.1) [114–116]. Proteins are the second major component of cell membranes in which the weight ratio of the lipids to membrane proteins can vary from 20 to 70%, depending on the cell type [115, 117, 118]. Proteins in cell membranes are classified into two categories: integral and peripheral proteins [119, 120] (see Figure 2.1). The third major component of BMs is carbohydrate molecules, which are found on the extracellular sides of cell membranes. [121, 122]. We briefly survey the two different classes of membrane proteins (integral and peripheral proteins), their functions, and their structures in cell membranes in what follows.

2.1.1 Integral proteins

Integral proteins are embedded permanently in the membrane by hydrophobic and electrostatic interactions [123]. Therefore, removing integral proteins from lipid bilayer is only possible by the use of detergents or nonpolar solvents that break down the strong membrane-protein interactions. The most common type of integral proteins are transmembrane proteins, which span across the lipid bilayer such that one end contacts the cell interior and the other end touches the exterior. Many of the integral membrane proteins function as ion channels or transporters. Also, cell surface receptors, linkers, and enzymatic proteins are all classes of integral membrane proteins [124].

2.1.2 Peripheral proteins

Peripheral proteins more or less temporarily bind to the surface of the membrane with weak interactions [123, 125]. This means that unlike integral proteins, peripheral proteins can be separated from the lipid bilayer by either altering the pH or the salt concentration of the cell culture medium [115]. The primary role of peripheral proteins is to provide a point of attachment for other components to the cell membrane. For instance, both membrane cytoskeleton and components of the extracellular matrix are linked to the cell membrane through peripheral proteins. This helps the cell maintain its shape while the membrane remains flexible to bend as needed for various cellular functions [126]. Besides the structural supports, peripheral proteins are involved in many other functions including cell-cell communication, energy transduction, and molecule transfer across the membrane [126].

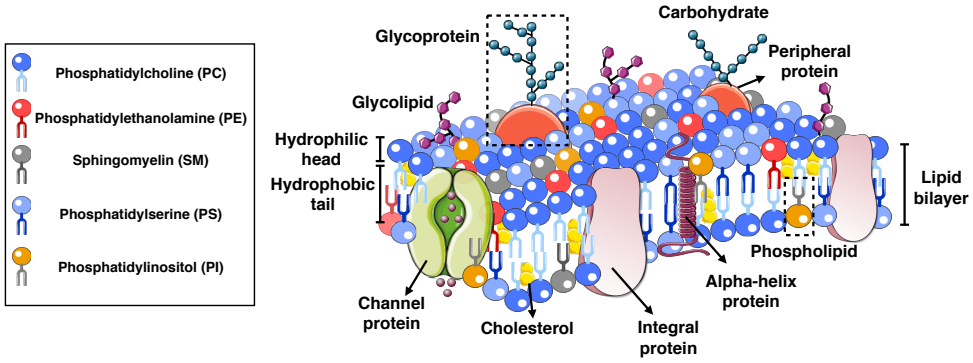

Figure 2.1: Schematic depiction of a cellular membrane highlighting its composition. There are two layers of amphipathic lipid molecules that self-assemble to form the bilayer. In each layer, the hydrophilic head groups form the outer surface and the hydrophobic tails face toward each other in the interior region. The distribution and organization of lipids and different proteins can vary from cell to cell. The cell membrane is composed of many different molecules including peripheral proteins, integral proteins, and carbohydrate molecules.

2.2 Theoretical models of biological membranes

2.2.1 Mechanical viewpoint

Theoretical approaches are complementary techniques that have been developed in the last few decades to understand how cells regulate their function through geometry, mechanics, and signaling [107, 127–129]. In general, theoretical approaches can be classified into discrete and continuum models. In discrete models, the equations of the atoms' motion in interaction with each other are solved by Molecular Dynamics (MD) or Coarse-Grained (CG) simulation techniques [130, 131]. Tracing all atoms in a system makes this model suitable for exploring the nature of biological processes at the molecular level that are typically very difficult to detect experimentally such as the biochemistry underlying the lipid-lipid or lipid-protein interactions. However, the high computational cost of MD or CG simulations limit the applications of discrete models to phenomena at nanoscopic length and time scales [127, 132].

On the other hand, the continuum approach treats the membrane as a continuous surface with average properties [127]. Indeed, the small length scale of the membrane constituents ($\sim$3–6

nm) compared to the length scales of the biological phenomena ($\sim$100 nm-μm), allows us to define the complex membrane as a single continuum surface [127]. The most popular and widely used model in continuum framework is the Helfrich model, which was proposed in 1973 [133]. In this model, the membrane is considered as a thin elastic shell that can bend such that at all times the lipids remain aligned and normal to the membrane surface. In addition, this model presumes that the curvature of the membrane is much larger than the thickness of the bilayer [133]. Under these assumptions, Helfrich proposed an energy function for the system that depends only on the mean and Gaussian curvatures of the membrane as [133]

$$W_{\text{Bending}} = \int_{\omega} \Big(2\kappa H^2 + \kappa_G K \Big) dA, \tag{2.1}$$

where W is total strain energy of the membrane due to bending, H is the membrane mean curvature, K is the membrane Gaussian curvature, and κ and κ_G are membrane properties which are called the bending and Gaussian modulii respectively. The integration in Equation (2.1) is over the entire membrane surface area ω and dA is a differential area element. We describe the geometrical concepts of curvature of manifolds in Box A.

2.2.2 Simulation techniques

From a mechanical perspective, cell membrane deformation can be characterized by balance laws for mass and momentum. Simplifying these mass and momentum conservation equations in a continuum framework results in a set of partial differential equations (PDEs) [134]. To solve the PDEs, we first need to define the constitutive relationship for the membrane deformation, for example, the Helfrich bending energy (Equation (2.1)). Other forms of suggested constitutive equations including the effects of proteins are presented in Section 2.3.

Besides the need for a constitutive equation, the derived PDEs from cell mechanics

are usually higher order and highly nonlinear differential equations. Therefore, in most cases, analytical solutions are not possible and the equations are often solved numerically. Over the last few decades, various computational approaches have been developed to solve the set of governing PDEs including the boundary value problem for axisymmetric coordinates [36,135–137], different finite element methods [138–140], Monte Carlo methods [141–143], finite difference methods [144, 145], and the phase field representation of the surface [146–148]. Each of these methods have their own advantages and disadvantages and depending on the complexity of the problem, one or more of them can be implemented.

A major challenge in modeling membrane-protein interactions is identifying a constitutive relationship that captures the different levels of complexities associated with membrane-protein interactions. In what follows, we discuss some of the popular models used for such purposes along with their applications. We then discuss where new constitutive relationships are needed and how these can be experimentally parameterized.

2.3 Continuum elastic energy models of membrane-protein interactions

2.3.1 Spontaneous curvature model

In the spontaneous curvature (SC) model, it has been suggested that the interaction between proteins and surrounding lipids changes the local membrane properties, particularly the preferred or spontaneous curvature of the membrane [33, 149–151]. In this case, the induced spontaneous curvature is a parameter that reflects a possible asymmetry between the two leaflets of the bilayer. This can be the result of any membrane bending mechanisms such as phase separation of membrane proteins into distinct domains, amphipathic helix or conically-shaped

transmembrane protein insertion, protein scaffolding, or protein crowding (Figure 2.2A). In reality, a combination of all these mechanisms can occur simultaneously; as a result the local value of spontaneous curvature can then be interpreted as a single measure of the curvature-generating capability of the membrane-protein interaction [32, 33]. In a continuum framework, the most common model for induced spontaneous curvature is the modified version of Helfrich energy (Equation (2.1)), given by [136, 150, 152].

$$W_{\mathrm{SC}} = \int_{\omega} \Big(2\kappa (H - C)^2 + \kappa_G K \Big) dA, \tag{2.2}$$

where C is the spontaneous curvature and its effective strength depends on the membrane composition, temperature, the membrane thickness, the protein density, and the membrane area coverage by proteins [133, 153].

Modeling the net effect of membrane-protein interaction as an induced spontaneous curvature (Equation (2.2)) has provided great insight into various aspects of membrane deformation, from caveolae and endosomal sorting complexes to cylindrical shapes of membrane ER [154–156]. By using the SC model, recent studies have shown for example how a line tension at a lipid phase boundary could drive scission in yeast endocytosis [36, 157, 158], or how a snap-through transition from open U-shaped buds to closed Ω-shaped buds in CME is regulated by the membrane tension [135, 136]. Furthermore, the experimentally observed change in the membrane tension (spontaneous tension) in response to protein adsorption [159–161], can be explained in the context of the SC model [153]. The SC model has also been used to elucidate the role of varying membrane tension due to protein-induced spontaneous curvature [153]. While the SC model has been very effective in capturing large-scale deformations of the membrane, it does not take into account the protein density or the curvature induced by individual moieties.

2.3.2 Bilayer couple model

In order to go beyond an idealized single manifold description of a membrane, the bilayer couple model (BC) was proposed by Sheetz and Singer in 1974 [162]. The basic assumptions in this model are that each lipid molecule has a fixed area and there is no lipid exchange between the two leaflets of the bilayer. Thus, any asymmetrical protein insertions into the inner and outer surfaces of the membrane can cause an area mismatch between the two leaflets. This mismatch creates in-plane compression in one leaflet and extension in the other leaflet, resulting in the membrane deformation to release the induced stress (Figure 2.2B) [33, 163]. For a thin lipid bilayer with thickness (d), the area difference between the leaflets (ΔA) can be expressed in terms of the mean curvature (H) as

$$\Delta A = 2d \int_{\omega} H dA. \tag{2.3}$$

Here, instead of having a spontaneous curvature term in energy, a "hard" constraint on the area difference between the leaflets (Equation (2.3)) regulates the membrane curvature. This difference in the mechanism of curvature generation of SC and BC models distinguishes their predictions for the same membrane deformation [163]. For example, in the case of membrane budding transition due to thermal expansion, the SC model predicts that the membrane budding is discontinuous, while the BC model predicts intermediate pear-shaped structures of the vesicle and that the transition of shapes is continuous [163].

2.3.3 Area difference elasticity model

In 1980, the area difference elasticity (ADE) model was developed by Svetina et al. [164, 165] to combine both SC and BC models including the missing macroscopic details of membrane bending phenomena. To better explain the physics underlying this model, we consider a flat membrane that bends downward due to different protein concentrations on two sides of the

membrane (Figure 2.2C). This bending, based on the single sheet descriptions of the membrane in the SC model, gives rise to the spontaneous curvature term in the energy equation (Equation (2.2)). However, if we treat each leaflet as an independent elastic plate—as was suggested in the BC model—we can then see that besides the curvature, the area of each monolayer will also change. For example, in Figure 2.2C, the outer monolayer is stretched and the inner one is compressed. The energy associated with the membrane bending and this relative change in the monolayers areas is given by [163, 166, 167]

$$W_{\mathrm{ADE}} = \underbrace{\int_{\omega} \Big(2\kappa(H-C)^2 + \kappa_G K \Big) dA}_{\text{Bending energy}} + \underbrace{\frac{\kappa_r}{2Ad^2}(\Delta A - \Delta A_0)^2}_{\text{Elastic stretching energy}}, \tag{2.4}$$

where κ_r is called the nonlocal membrane bending modulus and A is the total surface area of the neutral plane. ΔA_0 and ΔA are the relaxed initial and bent area differences between the membrane leaflets respectively ($\Delta A_0 = A_{0,\mathrm{out}} - A_{0,\mathrm{in}}$ and $\Delta A = A_{\mathrm{out}} - A_{\mathrm{in}}$, in which A_{out} is the area of the outer layer and A_{in} is the area of the inner layer). In Equation (2.4), κ and κ_r are both in order of $K_a d^2$, where K_a is the area stretching modulus of the bilayer [163, 167, 168]. This means that in any membrane deformation, both terms, the bending and the elastic stretching energies, are comparable and must be considered simultaneously. Using the ADE model, researchers for the first time could numerically simulate the shape transformations of the human red blood cell from stomatocyte to discocyte and to echinocyte [168–171]. Also, by using the ADE model, the experimentally observed vesicle shapes were mapped onto a theoretical phase diagram, enabling theoreticians to predict the range of parameters in which the vesicles may become unstable [163, 166]. These predictions have been very useful for detecting unstable shapes, which is challenging to do experimentally.

2.3.4 Deviatoric curvature model

In the SC model, the induced spontaneous curvature was assumed to be isotropic, meaning it has the same value in all directions (see Box A). However, not all proteins are rotationally symmetric and some can have intrinsically anisotropic curvatures such as banana-shaped BAR domain proteins (Figure 2.2D) [56, 172, 173]. These proteins can produce different curvatures in different directions, which is required for the formation of nonspherical structures such as membrane tubular protrusions [174, 175]. In order to take into account the anisotropic contribution of protein coats or inclusions in the continuum approach, Kralj-Iglic et al. proposed a deviatoric elasticity (DE) model [176]. In this model, each complex protein structure is simplified as a one-dimensional curve that lies on the membrane. The orientation and the position of the proteins in the plane of the membrane are important factors since an additional term is needed to adjust the actual local curvature of the membrane to the intrinsic curvatures of the proteins [176, 177]. The membrane free energy that was suggested by the DE model is given as [176, 178]

$$W_{\mathrm{DE}} = \int_{\omega} \underbrace{\left(2\kappa(H-C)^2 + \kappa_G K\right)}_{\text{Bending energy}} + \underbrace{2\kappa(D-D_0)^2}_{\text{Deviatoric mismatch}} \, dA, \tag{2.5}$$

where D is the membrane curvature deviator and D_0 is the spontaneous membrane curvature deviator. Since the DE model was proposed, there have been many modeling efforts to explain how the accumulation of BAR proteins in membrane necks stabilize membrane tubular protrusions without the support of the cytoskeleton [179–182]. Derivation of the Euler-Lagrange governing equations by a variational approach [183] provides a platform to systematically explore the impact of the induced stresses by anisotropic curvatures on the morphology of tubular structures [36].

2.3.5 Protein aggregation model

Aggregation of cytosolic proteins on the membrane surface or phase separation of bilayer proteins into specific domains have been observed in many biological processes [184–187]. This aggregation of proteins not only creates a concentration field on the membrane surface but also results in additional contributions to the membrane energy due to compositional heterogeneity and the entropic interactions of bulk proteins with the lipid bilayer (Figure 2.2E) [188–190]. While the exact form of the free energy is still a matter of debate and has not been verified experimentally, a simple model based on thermodynamic arguments is given as [188, 189, 191]

$$W_{\text{Aggregation}} = \int_{\omega} \underbrace{\left(2\kappa(H-C)^2 + \kappa_G K\right)}_{\text{Bending energy}} + \underbrace{\frac{T}{a^2}(\phi \ln \phi + (1-\phi)\ln(1-\phi))}_{\text{Entropic energy}} + \underbrace{\frac{J}{2a^2}\phi(1-\phi)}_{\substack{\text{Energy due to protein} \\ \text{aggregation}}} + \underbrace{\frac{J}{4}(\nabla\phi)^2\Big)}_{\substack{\text{Energy penalty due} \\ \text{to compositional} \\ \text{heterogeneity}}} dA, \tag{2.6}$$

where T is the environment temperature, a is the surface area occupied by one protein, ϕ is the relative density of the proteins, and J is the aggregation potential ($J > 0$ represents attractive interactions and $J < 0$ represents repulsive interactions). In Equation (2.6), the first term is the conventional Helfrich bending energy with induced spontaneous curvature [133]. The second term represents the entropic contribution due to the thermal motion of proteins in the membrane [188, 192]. The third term gives the aggregation energy, and the last term describes the energetic penalty for the spatial membrane composition gradient [188, 191, 192]. This model was used to conduct theoretical analyses of dynamic phase transitions of coupled membrane- proteins-cytoskeleton systems in membrane protrusions such as microvilli and filopodia [188, 193–195]. This model also reveals an interesting fact that in addition to the induced deviatoric spontaneous curvature of the BAR domain proteins, the associated energy with their aggregation at membrane

necks facilitates the stability of tubular structures [182, 196].

The aggregation energy in Equation (2.6) is a representative of the direct protein-protein interactions in protein assemblies. However, there are indirect membrane-mediated interactions of proteins which result from the local changes in the membrane curvature, membrane structure, or membrane fluctuations [172, 197–199]. For example, in the case of loose BAR domain assemblies, it is experimentally observed that the induced local membrane curvature due to protein binding generates a strong attractive interaction between two side-to-side crescent-shaped proteins without any direct protein-protein interactions [197, 200]. This attraction is a key factor for the aggregation and cooperative action of BAR domain proteins during the formation of membrane tubular structures. Furthermore, coarse-grained simulations of membrane remodeling have shown that curvature-inducing proteins or particles can aggregate and bend the membrane even in the absence of direct attractive/repulsive interactions [127, 201]. A major open question in the field is the relationship between protein density, size, and spontaneous curvature. Although current models use a linear proportionality [189, 202], this choice of functions is critical in determining the energy.

2.3.6 Protein crowding

The essence of the crowding mechanism is that the lateral collisions between the membrane-bound proteins on one side of the membrane generate a steric pressure that causes the membrane to bend away from the proteins (Figure 2.2F) [48, 203, 204]. As the density, the size, or the mobility of the bound proteins increases, the induced steric pressure becomes larger, which results in a more significant membrane bending [48, 49]. Modeling the free energy associated with protein crowding is more difficult because it profoundly depends on the specific composition of the underlying membrane as well as the lateral confinement of the membrane-bound proteins [205, 206]. However, in a recent paper, a simple 2D hard-sphere gas model based on the

Carnahan-Starling approximation has been proposed to describe the free energy of the crowding mechanism [48, 207]. To better visualize this, let us consider a membrane that is crowded with different protein concentration on each side as shown in Figure 2.2. If we model each protein as a hard-sphere gas particle that exerts a certain pressure on the membrane surface, the work that is done by this pressure to bend the membrane according to the standard thermodynamics is given by [208]

$$W_{\text{Crowding}} = \int p_{\text{in}} dA_{\text{in}} + \int p_{\text{out}} dA_{\text{out}}, \tag{2.7}$$

where p_{in} and p_{out} are the induced steric pressure by the crowding proteins on the inner and the outer side of the membrane respectively. This induced pressure (denoted by p here) for a 2D hard-sphere gas protein can be expressed as [206, 209, 210]

$$p = \frac{k_B T}{a} p_R(\phi), \tag{2.8}$$

where k_B is the Boltzmann constant and $p_R(\phi)$ is the reduced gas pressure depending on the relative density of the protein as [210]

$$p_R(\phi) = \phi(1 + 2\phi \frac{1 - \frac{7}{16}\phi}{(1-\phi)^2}). \tag{2.9}$$

Equation (2.9) is known as a 2D version of the Carnahan-Starling equation. Protein crowding is a recently discovered curvature generating mechanism that has challenged some conventional paradigms about the role of molecular machinery in a robust cell shape change [48, 49, 211–214]. Stachowiak et al. reported that confining a sufficiently high concentration of his-tagged green fluorescent proteins (GFP) to a local region can deform the membrane into buds or tubules in the absence of any protein insertion into the lipid bilayer [48, 212]. Later, Snead et al. showed that crowding among membrane-bound proteins can also drive membrane fission [211]. This paper predicts that the large disordered domains of BAR proteins induce crowding pressure

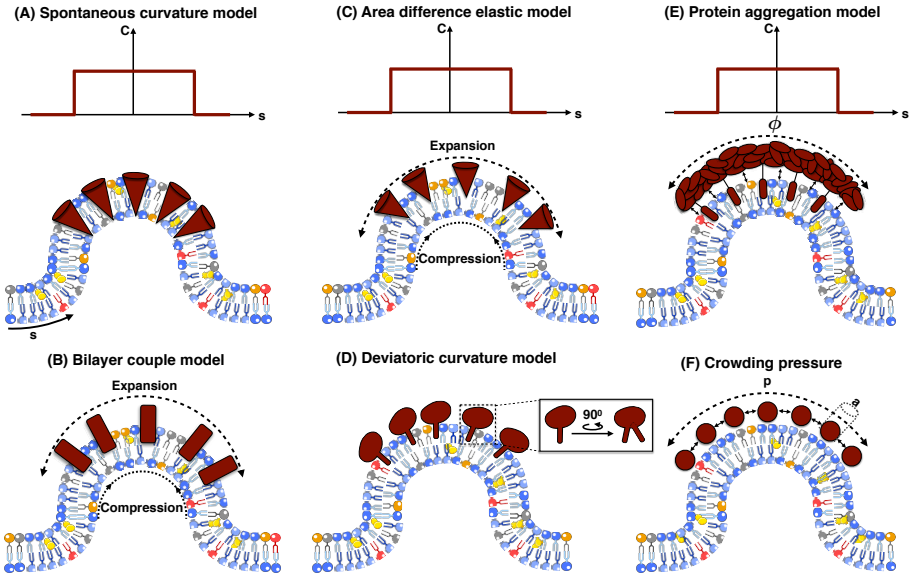

Figure 2.2: Cartoon models of the mechanisms of membrane curvature generation due to protein (shown in red) interactions in different continuum elastic models. (A) Local protein interactions with membrane produce a spontaneous curvature field. s is the arc length parameterization along the membrane and C is the induced spontaneous curvature. (B) The asymmetric insertion of conical proteins on one side of the membrane results in the expansion of the upper leaflet and compression of the lower leaflet. (C) Asymmetric insertion of proteins into the lipid bilayer induces both local spontaneous curvature and surface stresses due to membrane leaflets expansion/compression. (D) Rotationally non-symmetric proteins generate anisotropic curvature. (E) Aggregated proteins on the membrane surface create a spontaneous curvature field and also have entropic interactions with the membrane. Here ϕ represents the relative density of the accumulated proteins. (F) The induced pressure (p) by crowding proteins drives membrane bending. a is the surface area occupied by one protein.

that promotes membrane fission instead of stabilizing the membrane [215].

2.3.7 Hydrophobic mismatch

Transmembrane proteins embedded in the cell membrane have hydrophobic regions that are in contact with hydrophobic regions (lipid acyl chain) of the lipid bilayer. The difference between the thicknesses of hydrophobic regions of a transmembrane protein (d_p) and the lipid bilayer (d_l) is called the hydrophobic mismatch. Energetically, it is favorable that both hydrophobic regions have approximately a same thickness in order to prevent the exposure of the hydrophobic

surfaces to the hydrophilic environment. However, it is impossible to avoid a mismatch because there are various proteins with different lengths in a single membrane [216, 217] and a single protein can be surrounded by lipid bilayers with different thicknesses [218, 219].

Several theoretical approaches have been developed to incorporate the energy cost and the thermodynamic effects of membrane-protein interactions in term of hydrophobic mismatch [220–223]. The mattress model is one of the most well-known models that was proposed by Mouritsen and Bloom in 1984 [223]. In this model, both protein and lipid bilayer (called a mattress) are characterized by one dimensional springs with constant A_p and A_l respectively [223] (Figure 2.3). There are three sources of energy in this model. First, elastic energy ($W_{\text{Mattress-Elastic}}$) due to the vertical deformation of the two springs relative to their individual equilibrium lengths (d_p^0 and d_l^0) given by [223]

$$W_{\text{Mattress-Elastic}} = n_l A_l (d_l - d_l^0)^2 + n_p A_p (d_p - d_p^0)^2, \tag{2.10}$$

where n_l and n_p are the number of molecules in the lipid bilayer and protein domains respectively. The second source of energy is due to the indirect lipid-protein interactions induced by the hydrophobic mismatch ($W_{\text{Mattress-hydrophobic}}$). Based on the standard regular solution theory, this hydrophobic energy is given by [224]

$$W_{\text{Mattress-hydrophobic}} = \frac{n_l n_p}{n_l + n_p} B_{lp} |d_p - d_l|, \tag{2.11}$$

where B_{lp} represents the strength of the hydrophobic interactions. The last source of energy is due to the direct protein-lipid interactions which has been modeled by an attractive adhesive interaction ($W_{\text{Mattress-adhesive}}$) as [223]

$$W_{\text{Mattress-adhesive}} = \frac{n_l n_p}{n_l + n_p} C_{lp} min(d_p, d_l), \tag{2.12}$$

where $C_{lp} < 0$ shows the strength of the adhesive interactions between molecules. Therefore, the total energy associated with the mattress model is written as

$$W_{\text{Mattress}} = n_l A_l (d_l - d_l^0)^2 + n_p A_p (d_p - d_p^0)^2 + \frac{n_l n_p}{n_l + n_p} B_{lp} |d_p - d_l| + \frac{n_l n_p}{n_l + n_p} C_{lp} min(d_p, d_l). \tag{2.13}$$

There are different adaptation mechanisms that either the protein or the bilayer can utilize in order to avoid the energy cost of the hydrophobic mismatch [218, 225]. For example, for positive ($d_l < d_p$) or negative ($d_l > d_p$) mismatch, the lipid bilayer can be stretched or compressed respectively to adjust the length of hydrophobic regions [226, 227]. Another possibility is when the hydrophobic part of a transmembrane protein is too thick or too short as compared to the hydrophobic bilayer thickness. In this case, protein aggregation on the membrane or protein surface localization can efficiently minimize the exposed hydrophobic area [228, 229]. Also, for proteins that have helices that are too long compared to the thickness of the membrane, helix tilt is one possible mechanism to reduce the protein effective hydrophobic length [218, 230]. Effectively, the hydrophobic mismatch of integral membrane proteins is a clustering mechanism. However, this mechanism can generate membrane curvature depending on other membrane-protein interactions.

In addition to the models described above, there are additional considerations to the energy that have been suggested by numerous studies such as higher order bending terms [231–233], lipid volume constraints [234], the impact of protein shape on membrane deformation [235], and the electrostatic energy between a membrane and proteins [236–239].

2.4 Acknowledgements

I would like to acknowledge my co-author Prof. Padmini Rangamani, and Dr. Morgan Chabanon, Miriam Bell, and Allen Leung for his suggestions on improving the manuscript. I

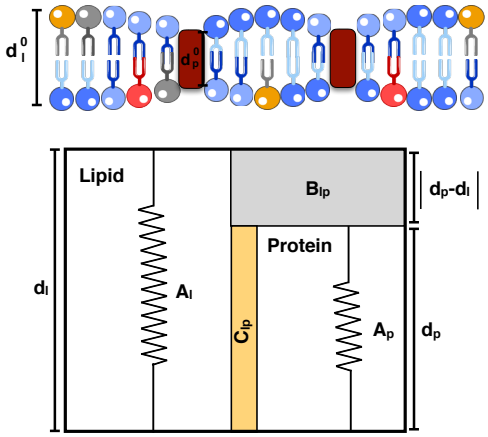

Figure 2.3: Mattress model representation of the hydrophobic mismatch phenomena [223]. Both protein and lipid bilayer are modeled as one-dimensional springs with constants A_p and A_l respectively. d_l^0 and d_p^0 are the initial lengths, and d_l and d_p are the final lengths of the lipid bilayer and the protein after deformation respectively. The gray area corresponds to the hydrophilic region with the strength of B_{lp}, and the yellow region indicates the adhesive region with adhesive interactions strength of C_{lp}.

would also like to acknowledge grant funding: the Visible Molecular Cell Consortium (VMCC) and the Center for Trans-scale Structural Biology and Biophysics (CTSBB) at UC San Diego. Figures used in this chapter adapted content from Servier Medical Art powerpoint image bank.

Chapter 3

Role of traction in membrane curvature generation

3.1 Introduction

Cell shape plays an important role in regulating a diverse set of biological functions including development, differentiation, motility, and signal transduction [26, 240, 241]. Additionally, the ability of cellular membranes to bend and curve is critical for a variety of cellular functions such as membrane trafficking processes, cytokinetic abscission, and filopodial extension [11, 242]. In order to carry out these functions, cells harness diverse mechanisms of curvature generation like compositional heterogeneity [243, 244], protein scaffolding [46, 203], insertion of amphipathic helices into the bilayer [44, 245], and forces exerted by the cytoskeleton [29, 30] (Fig. 3.1). Reconstituted and synthetic membrane systems also exhibit a wide range of shapes in response to different curvature-inducing mechanisms as seen from steric pressure due to protein crowding [48, 206, 246].

It is well-known that these various mechanisms of curvature generation induce surface stresses; expressions for these stresses have been derived using either variational methods [35,247] or by using auxiliary variables that enforce geometric constraints [37, 248]. These studies have established the physics underlying membrane stresses and clearly explained how these traction forces can be interpreted in linear deformations and in idealized geometries [37, 248]. However, many physiologically relevant membrane shapes display large curvatures [34, 249], non-linear deformations [250, 251], and heterogeneous membrane composition [49, 252]. How stresses are distributed along such shapes is not yet fully understood. In this article, we discuss how theory can help us evaluate membrane stresses based on the observed shape.

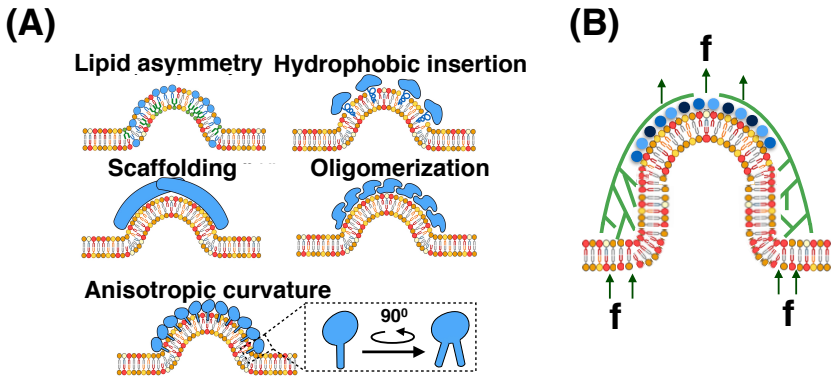

Figure 3.1: Curvature generation in biological membranes. Membrane curvature is controlled by different physical inputs including (A) protein-induced spontaneous curvature and (B) forces exerted by the cytoskeleton.

3.1.1 Shape as a reporter of force

Many biomechanics textbooks present the postulate that the relationship between the applied load and the resulting deformation can be obtained if a constitutive relationship between the stress and strain of a material is given [253–255]. Indeed, the idea that shape can be considered a reporter of the applied force is an idea as old as continuum mechanics [256]. A classical example illustrating how shape can be used as a reporter of force in biology can be understood by studying

the shape of a vesicle or a cell using micropipette aspiration [257, 258]. This method is used to calculate the tension f bilayer membranes in vesicles and cortical tension in cells through Laplace's law. Since the pressure applied by the micropipette is known, tension can be calculated using a force balance at the membrane.

Lee *et al.* suggested that membrane shape itself acts as a reporter of applied forces [259] and calculated the axial force required to form membrane tethers in optical tweezer experiments based on shape, given the material properties of the membranes (See Fig. 2 in [259]). They showed that the calculated value of force was in excellent agreement with their experimental measurements. Separately, Baumgart and colleagues showed that the Gaussian modulus has a strong effect on membrane budding in phase-separated vesicles and its magnitude can be obtained by analyzing the geometry of the vesicle [260].

An additional layer of complexity in how shape and forces are related arises through the heterogeneous composition of the lipid bilayer in cells. Most protein binding to cellular membranes are local processes [151, 261, 262]. Even in *in vitro* studies, several groups have shown that protein adsorption on lipid domains can alter the lateral pressure profile on the bilayer and induce tubulation [48, 263, 264]. Recently, theoretical studies have shown that adsorbed proteins give rise to spontaneous surface tension [263]. Therefore, there is a need to understand how applied forces and membrane heterogeneity can regulate the local stresses on the membrane. Going beyond the approximation of tension using Laplace's law, we sought to understand the local stresses in tubes and buds – two geometries that are critical to many cellular phenomena. Using the well-established Helfrich model [133, 265] for membrane bending as a framework, we illustrate how local forces can be understood from the shape of the membrane. We close with an extended discussion of how advances in image analysis and measurement of material properties can aid in our understanding of how traction can be calculated from the curvature of the membrane.

3.2 Local stresses in the membrane: governing equations

3.2.1 Surface stress tensor and traction calculation

A general force balance for a surface ω, bounded by a curve $\partial\omega$, is (Fig. 3.2)

$$\int_{\omega} p\mathbf{n}da + \int_{\partial\omega} \tilde{\mathbf{f}}dt + \mathbf{F} = 0, \tag{3.1}$$

where $t = r(s)\theta$ is the length along the curve of revolution perimeter (see Fig. 3.2), p is the pressure difference across the membrane, $\tilde{\mathbf{f}}$ is the traction along the curve of revolution t and $\mathbf{F}$ is any externally applied force on the membrane. Along any circumferential curve on the membrane at constant z, the traction is given by [137]

$$\tilde{\mathbf{f}} = \tilde{f}_{\nu}\nu + \tilde{f}_{n}\mathbf{n} + \tilde{f}_{\tau}\tau. \tag{3.2}$$

The values of f_{ν}, f_n and f_{τ} will depend on the particular form of strain energy we choose to depict the membrane properties (See Fig. 3.2 for definitions of the forces and the vectors). We choose the Helfrich Hamiltonian as the constitutive relationship in this case and use a modified version that includes spatially-varying spontaneous curvature $C(\theta^{\alpha})$, [135, 137, 150],

$$W = \kappa[H - C(\theta^{\alpha})]^2 + \kappa_G K. \tag{3.3}$$

where W is the energy per unit area, κ is the bending modulus, H is the local mean curvature, κ_G is the Gaussian modulus, K is the local Gaussian curvature and θ^{α} denotes the surface coordinates. This form of the energy density accommodates the local heterogeneity in the spontaneous curvature C. Note that W differs from the standard Helfrich energy by a factor of 2, which is accounted for by using the value of κ to be twice that of the standard bending modulus typically encountered in the literature. A more in-depth investigation of the role of anisotropic

spontaneous curvature using a version of the Helfrich energy that includes deviatoric curvature can be found in the Appendix A (Eq. A.11, [180, 266]).

While Eqs. 3.1 & 3.3 are general expressions that are independent of coordinates, for illustrative purposes we will restrict further analysis to rotationally symmetric membrane deformations for ease of analysis (Fig. 3.2). Using principles of force balance one can derive the "shape" equation and the tangential balance equation for the Helfrich energy (see Appendix A for detailed derivations). The traction, which is the force per unit length, across any boundary of constant z is given by

$$\underbrace{\tilde{f}_n}_{\substack{\text{Normal}\\ \text{traction}}} = \underbrace{-\kappa(H' - C')}_{\substack{\text{curvature}\\ \text{gradient}}}, \tag{3.4a}$$

$$\underbrace{\tilde{f}_v}_{\substack{\text{Tangential}\\ \text{traction}}} = \underbrace{\kappa(H - C)(H - C - \psi')}_{\text{curvature}} + \underbrace{\lambda}_{\text{tension}} \tag{3.4b}$$

where ψ is the angle the membrane makes with the horizontal (see Fig. 3.2), λ is the local membrane tension, and $()'$ denotes a derivative with respect to arc-length s, e.g. $H' = \mathrm{d}H/\mathrm{d}s$.

From the above equations, we see that the normal traction, $\tilde{f}_n$, captures the effect of curvature gradients while the tangential traction, $\tilde{f}_v$, captures the effect of local membrane tension and curvature. A complete derivation of the stress balance and the governing equations of motion is presented in the Appendix A. Additional derivations of traction including spatially heterogenous bending and Gaussian moduli, asymptotic approximations for small radius as well as anisotropic spontaneous curvature are presented in the Appendix A.

3.2.2 Interpretation of traction

Traction, which has the units of force per unit length, was initially introduced by physicists as a result of Noether's theorem [37, 267, 268]. This theorem states that for any elastic surface

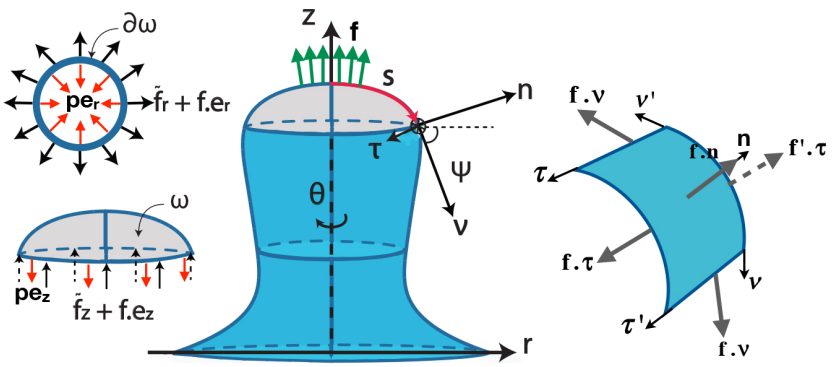

Figure 3.2: A schematic representing the axisymmetric coordinate system used for calculating curvature and traction. ω is the membrane surface area bounded by a curve ∂ω, **f** is an externally applied force per unit area on the membrane, **n** is the normal vector to the surface, ν is the tangent to the surface in the direction of increasing arc length, $\mathbf{e}_r$ and $\mathbf{e}_z$ are unit vectors in radial and axial directions, τ is a unit vector tangent to the boundary in the direction of the surface of revolution, ψ is an angle made by the tangent with respect to the horizontal, θ is the angle of revolution, s is the arc-length parameterization, p is transmembrane pressure difference, $\tilde{f}_r$ and $\tilde{f}_z$ are radial and axial tractions along the curve of revolution respectively. Inset shows that pressure opposes traction and external force in both the radial and axial directions.

that is in equilibrium, there exists a unique traction distribution such that its divergence is conserved [37]. Mechanically, the traction distribution gives us information about the response of the membrane to externally applied loading, including forces acting on the membrane or protein-mediated bending. Numerous studies have derived these equations mathematically and sought to explain them in a biophysical context. Capovilla and Guven [247, 267, 268] invoked the action-reaction law – if one were to cut the membrane along any curve, $\tilde{f}_n$ and $\tilde{f}_\nu$ are the forces per unit length of the curve in the normal and tangential directions respectively that the membrane on one side of the cut exerts on the other. Furthermore, the expressions for tractions (Eq. 3.4) reduce to their corresponding fluid analogues for negligible membrane rigidity and pressure difference. Thus, we can interpret the normal and tangential tractions as follows – the tangential traction distribution tracks the gradient in 'effective' surface tension (discussed below) while the normal traction distribution contains information regarding a force balance performed normal to the membrane at every point. Further physical interpretations of these quantities can be

obtained based on the particular biological phenomena, as illustrated below by examining two fundamental membrane deformations – tubes and buds.

3.2.3 Axial force and effective line tension

We obtain the formulae for traction in the axial and radial directions obtained by projecting the normal and tangential tractions onto these axes (Eqs. A.27) (full derivation in Appendix A). We can then calculate the magnitude of an applied axial force on the membrane by integrating the axial component of the traction (Eq. A.27b) along the circumference of the bounding curve $\partial\omega$, yielding

$$\tilde{F}_z = 2\pi r\Big[\underbrace{\kappa(H'-C')\cos\psi+\kappa(H-C)(H-C-\psi')\sin\psi}_{\text{Bending contribution}}+\underbrace{\lambda\sin\psi}_{\substack{\text{Tension}\\ \text{contribution}}}\Big], \tag{3.5}$$

where $\tilde{F}_z$ is the axial force generated in response to an external load.

An energy per unit length, ξ, associated with deformations in the radial direction can be found by integrating the radial traction along the curve $\partial\omega$, as

$$\xi = 2\pi r\Big[\underbrace{\kappa(H-C)(H-C-\psi')\cos\psi}_{\substack{\text{Curvature}\\ \text{contribution}}}+\underbrace{\lambda\cos\psi}_{\substack{\text{Tension}\\ \text{contribution}}}+\underbrace{\kappa(H'-C')\sin\psi}_{\substack{\text{Curvature gradient}\\ \text{contribution}}}\Big]. \tag{3.6}$$

ξ can be interpreted as an "effective" line tension [269]. While line tension denotes the force acting at the boundary of two interfaces – e.g. inward force for a liquid droplet on a hydrophobic substrate and an outward force on a hydrophilic substrate [158, 270], the "effective" line tension predicts a general resistive force acting at every point opposing any change in the membrane length, regardless of a phase boundary. This 'force' is not an actual radial force but represents the

change in energy with respect to the characteristic length scale [271]; going forward, we refer to it as an energy per unit length.

3.3 Illustrative examples of traction along the membrane

For spherical vesicles, where the mean curvature is constant and in the absence of spontaneous curvature curvature ($C = 0$) and homogeneous composition, the normal traction $\tilde{f}_n$ is zero because curvature gradients are zero (Eq. 3.4a), and the tangential traction, $\tilde{f}_\mathrm{v}$, reduces to the membrane tension (λ) (Eq. 3.4b). For surfaces with zero mean curvature (minimal surfaces such as catenoids [272]) and homogeneous composition, $\tilde{f}_n$ is zero and $\tilde{f}_\mathrm{v}$ is equal to λ, also consistent with the interpretation of membrane tension for these surfaces [272].

What happens when the mean curvature is not constant or if the membrane is not homogeneous in composition? Given a membrane shape and a constitutive relationship, Eqs. 3.4a and 3.4b tell us that we can calculate the local stresses along the membrane. One way of studying shapes is to use images from high resolution microscopy of membrane vesicles of known composition. However, these images can be noisy and obtaining the local curvature and curvature gradients requires fitting the curve with multiple splines or other functions [259]. Another way to generate membrane shapes is to use simulations. Since our goal is to illustrate the concept of local tractions, we use shapes generated from simulations to elucidate how the normal and tangential tractions are distributed along the membrane. The traction distributions are not the direct output of these simulations; instead they are calculated *a posteriori* using the output shapes from the simulations and the membrane properties, similarly to how one would calculate these distributions from experimentally observed membrane shapes.

3.3.1 Formation of buds due to spontaneous curvature is characterized by emergent line tension

Phase separation and lipid domains are classical mechanisms of bud formation and vesiculation [273]. Previously, we and others have shown that protein-induced heterogeneity on the membrane can be modeled using a spontaneous curvature field [150, 152]. We used this framework to investigate the nature of membrane tractions generated during budding due to a spontaneous curvature field. We conducted simulations for a constant area of the spontaneous curvature field $A = 10,000\,nm^2$ and varied the extent of spontaneous curvature, C, from 0 to $0.032\ nm^{-1}$ (Fig. 3.3A). We calculated the value of traction for three distinct shapes – a shallow invagination, a U-shaped bud, and a closed Ω- shaped bud (Fig. 3.3B-D).

The normal traction is negative along the applied spontaneous curvature field indicating a sharper change in mean curvature compared to the applied spontaneous curvature ($H' > C'$ in Eq. 3.4a). At the neck, where $\psi = \frac{\pi}{2}$, normal traction is maximum and acts purely inward, representing the tendency of the membrane to form small necks. The tangential traction shows a change in sign from positive to negative as the neck radius becomes smaller. This change in sign highlights the critical role of the gradient in tangential traction in the formation of narrow necks [135] (Figs. 3.3B-D). The dashed circles represent the equilibrium spherical vesicles calculated by Helfrich energy minimization ($R_{\text{vesicle}} = \frac{\kappa C}{\lambda_0 + \kappa C^2}$) [135]. The positive tangential traction in tent-like small deformations indicates that the membrane resists the bending deformation; however, in the U-shaped and closed buds, the negative tangential traction along the cap acts to pull the membrane inward and favors the adoption of a highly curved shape. The radial and axial tractions distribution along all three shapes are shown in Fig. A.1 which reveals that bud formation by spontaneous curvature is purely driven by radial traction while axial traction is zero everywhere.

Each equilibrium bud divides the membrane into two domains – (*i*) the membrane inside the bud with negative energy per unit length that bends to form a bud and (*ii*) the membrane

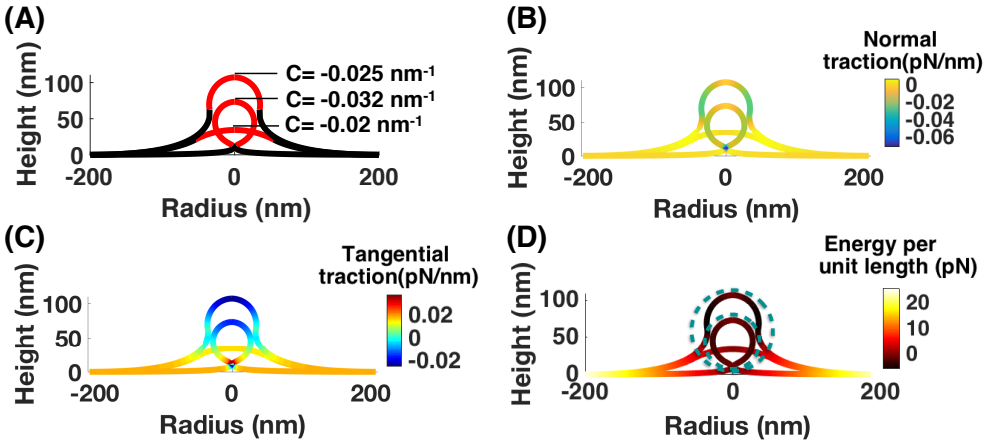

Figure 3.3: Analysis of budding due to protein-induced spontaneous curvature and calculation of line tension. Simulations were conducted with (A =10,053 nm^2) spontaneous curvature at the center of an initially flat patch increasing from $C = 0$ to $C = 0.032\,\mathrm{nm}^{-1}$, $\lambda_0 = 0.02\,\mathrm{pN/nm}$, $\kappa = 320\,\mathrm{pN\cdot nm}$, $p = 0\,\mathrm{pN/nm}^2$ [135]. (A) Membrane shapes for three different spontaneous curvature distributions with the value of C indicated in the red region and zero in the black region. (B) Normal traction along the membrane for the shapes shown in (A). (C) Tangential traction distribution along the shapes shown in (A); (D) Energy per unit length distribution for the three different shapes. The dashed line circles outline spheres with mean curvatures $H = 0.032\,\mathrm{nm}^{-1}$ (smaller circle) and $H = 0.025\,\mathrm{nm}^{-1}$ (larger circle).

outside the bud with positive energy per unit length that resists such a deformation. Previously, both modeling and experimental studies have shown that in heterogeneous membranes, line tension can be sufficient for scission of endocytic pits [158] or the formation of buds in vesicle experiments [243, 260]. In the case of an applied spontaneous curvature field, the expression of energy per unit length (Eq. A.30) can be interpreted as the actual line tension at the interface of the two phases. Through the process of bud formation, line tension undergoes a sign change from positive (acting outward) to negative (acting inward), effectively transitioning from a tension-dominated regime to a curvature-gradient dominated regime (Fig. 3.4). This transition from positive to negative line tension with increasing value of spontaneous curvature is also observed in other studies [274]. The value of the energy per unit length at the interface varies between -5 pN to 5 pN, which is of the order of the reported interfacial line tension between coexisting phases in lipid bilayers [158, 275].

There are two other factors that could affect the traction distribution along the bud – (i) a change in area of the membrane during budding and (ii) spatial heterogeneity in membrane moduli. To explore how the change of membrane area influences bud formation mediated by protein-induced spontaneous curvature, we conducted a simulation with a fixed available arc-length instead of area (Fig. A.2). Similar to the case of a homogenous membrane with fixed area, the energy per unit length at the interface changes sign from positive to negative in a range of -5 pN to 5 pN. However, protein segregation on the membrane can lead to heterogeneity in material properties such as bending moduli [276]. In order to investigate the effect of this spatial heterogeneity in the bending moduli along the membrane surface, we repeated the budding simulation from Fig. 3.3, assuming that the bending rigidity along the spontaneous curvature field is 7.5 times larger than the bending rigidity of the bare membrane (Fig. A.3) [276]. Because the membrane is stiffer and harder to bend, a wider neck is formed at C = -0.032 nm^{-1} compared to the case of a uniform membrane (Fig. A.3A) [135]. This membrane resistance to deformation is observed as a uniform positive normal traction everywhere along the membrane (Fig. A.3A).

To compare the behavior of the line tension at the edge of the spontaneous curvature field, we ran the budding simulation with the spatially heterogeneous bending moduli up to a larger value of spontaneous curvature (C = -0.035 nm^{-1}), in order to have the same range of neck radii as the uniform membrane (Fig. 3.3E). We can see that the trend of line tension variation versus the spontaneous curvature is almost the same in both cases (Fig. A.3E), changing sign from positive to negative followed by a critical point indicating the transition from a U to an Ω-shaped bud. However, the magnitude of line tension is different in the two cases. For small magnitudes of spontaneous curvature (tent shaped buds), the average difference in line tension is $\sim$ 1 pN. But for large magnitudes of spontaneous curvature (C $\geq$ -0.0275 nm^{-1}, Ω shaped buds), the average line tension for a rigid coat is $\sim$ 4 pN larger than the line tension in a homogeneous membrane. This larger value of line tension in a heterogeneous membrane has been reported in

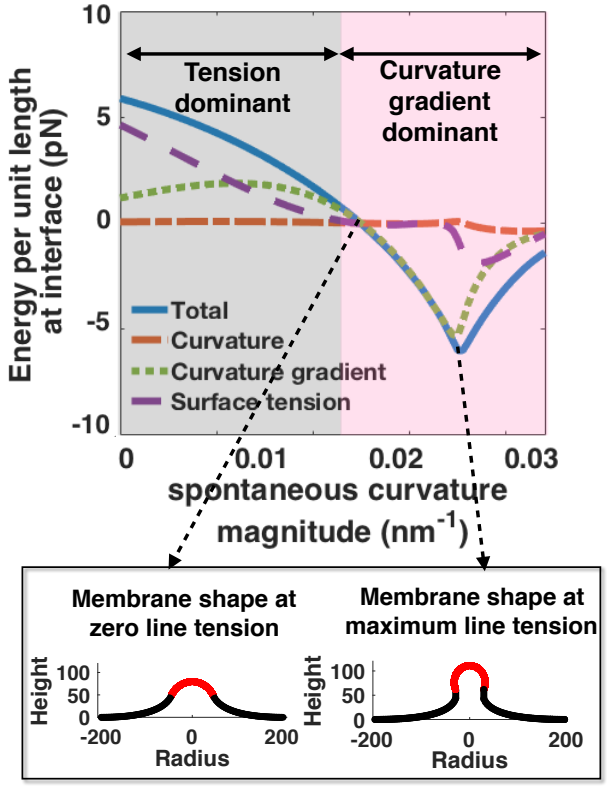

Figure 3.4: Change in energy per unit length and its components at the interface with increasing spontaneous curvature. Two regimes are observed: a surface tension-dominated regime for small values of spontaneous curvature and a curvature gradient-dominated regime for large vales of spontaneous curvature. The membrane configurations are shown for two spontaneous curvature $C = -0.02\,\mathrm{nm}^{-1}$, where energy per unit length at interface is zero and $C = -0.025\,\mathrm{nm}^{-1}$, where energy per unit length is maximum. The red domains show the region of spontaneous curvature for the corresponding shapes.

various experimental measurements [275, 277], and other theoretical studies [278, 279].

3.3.2 Traction distribution is a signature of distinct budding mechanisms

Conceptually, there are two primary means by which membrane buds can be maintained: an accumulation of protein or lipid-induced spontaneous curvature favoring a spherical geometry, or a constriction force that pinches the membrane into a budded shape. In Fig. 3.5, we illustrate the traction distribution in these two cases. The upper row represents spontaneous curvature-induced

budding, meant to resemble vesicle coat protein (such as the coatomer COPII) mediated budding from the endoplasmic reticulum [280] (Fig. 3.5A) and the lower row represents budding due to a local constriction force via a contractile ring in budding yeast [281] (Fig. 3.5E). Although the two simulated shapes are superficially similar, the traction distributions are quite different. The normal traction distribution for spontaneous curvature budding (Fig. 3.5C) is similar to the one seen in Fig. 3.3 where there is a large negative traction at the bud neck, indicating forces acting to minimize the neck radius. Conversely, for the constriction force budding, the normal traction is highly positive at the neck (Fig. 3.5G), indicating a resistance by the membrane to the applied force. The tangential tractions (Figs. 3.5D and H) are also quite different. For example, moving from the top to the bottom of the vesicle, the tangential traction in the case of the protein-induced spontaneous curvature budding is initially negative and then positive after the neck (Fig. 3.5D). However, for the constriction force mediated budding, the tangential traction is positive at first and then negative after the neck (Fig. 3.5D). This difference in the gradient of tangential traction at the membrane neck serves as a signature for spontaneous curvature mediated vs force mediated bud formation. Thus, the mechanism of curvature generation can be related to the computed traction profile, and some *a priori* knowledge can help uncover these differences (see Fig. 3.5).

Another mechanism of maintaining membrane buds (specific to endocytosis) is through actin-mediated forces where an actin network polymerizes in a ring at the base of the plasma membrane (PM) invagination and is connected to the coat, driving inward movement [136, 282]. We have previously considered these cytoskeletal effects in [135] and show here that the applied forces can be matched to axial forces calculated from traction (Figs. A.4 and A.5) for two orientations of the applied force.

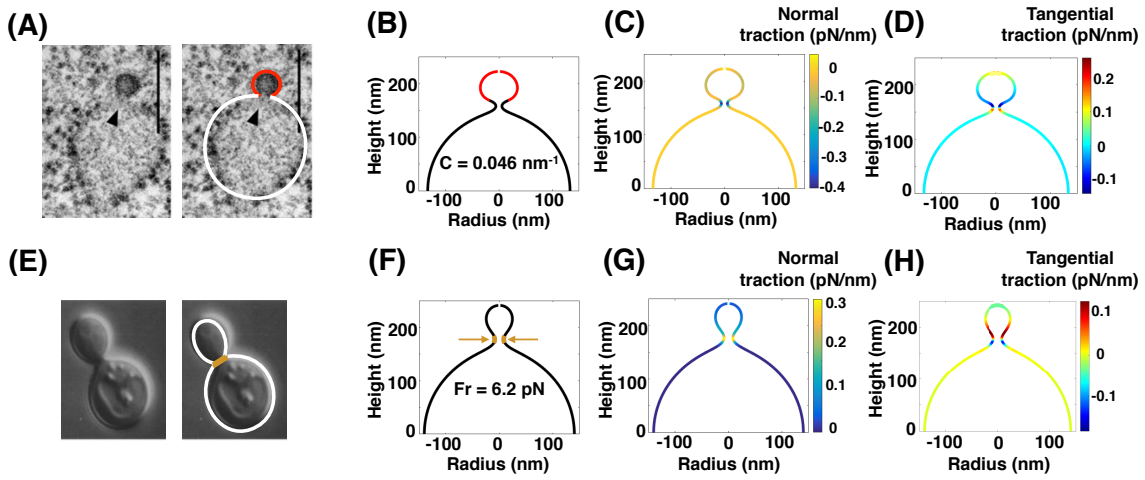

Figure 3.5: Comparison of normal and tangential tractions between two different mechanisms of membrane budding. (A) EM image of COPII budding from the endoplasmic reticulum (ER) in green algae [280]. Left, original EM image, Right, EM image with traced membrane shape. Red - COPII coat, white - bare membrane (B) Simulation of bud formation on a hemispherical cap using a constant spontaneous curvature (C= -0.046 nm^{-1}, red) (C) Normal traction distribution along the membrane shape in (B). A large negative normal traction can be seen at the neck of the formed vesicle. (D) Tangential traction distribution along the membrane shape in (B). There is a change in the sign of the tangential traction before and after the bud neck. (E) Brightfield microscopy image of a budding yeast [281]. Left, original EM image, Right, EM image with traced membrane shape. brown - contractile ring at the bud neck. (F) Simulation of bud formation on a hemispherical cap with a constant radial force ($F_r = 6.2$ pN, yellow) that locally constricts the hemisphere to form a bud. (G) Normal traction distribution along the membrane shape in (F). There is a positive normal traction at the vesicle neck in response to the applied force. (H) Tangential traction distribution along the membrane shape in (F).

3.3.3 Sensitivity analysis and sources of errors

In principle, calculating force from shape is at the heart of stress-strain relationships. However, there are some fundamental challenges associated with sources of errors in such a calculation. There are two main sources of errors – error in the measurement of material properties (membrane bending modulus and membrane tension), and error in the measurement of shape. We present some simple analysis of these sources of error in what follows.

Parametric sensitivity analysis of material properties

Ideally, one would like to define a sensitivity index similar to the parametric sensitivity conducted for systems of chemical reactions, where the sensitivity of a quantity F_i with respect to a parameter k_j is given by $S_{i,j} = \frac{\partial F_i}{\partial k_j}$ [283]. However, since we wish to simultaneously explore the effect of both the bending modulus and tension, we use a simple linear calculation of error. Uncertainties in either of these quantities will result in an uncertainty in the traction as well as the calculated axial force and energy per unit length (Eqs. 3.5 and 3.6) Here, we assume that the bending modulus and membrane tension can be written as $\kappa = \kappa_{\text{mean}} \pm \kappa_{\text{error}}$ and $\lambda = \lambda_{\text{mean}} \pm \lambda_{\text{error}}$ respectively. Then, by virtue of the relationships in Eqs. 3.5 and 3.6, we can estimate the error in the axial force and the energy per unit length as

$$F_{z,\text{error}} = \pm 2\pi r \left(\kappa_{\text{error}}(H' - C') \cos(\psi) + \kappa_{\text{error}}(H - C)(H - C - \psi') \sin(\psi) + \lambda_{\text{error}} \sin(\psi) \right), \tag{3.7a}$$

$$\xi_{\text{error}} = \pm 2\pi r \left(\kappa_{\text{error}}(H - C)(H - C - \psi') \cos(\psi) + \kappa_{\text{error}}(H' - C') \sin(\psi) + \lambda_{\text{error}} \cos(\psi) \right) \tag{3.7b}$$

These equations allow us to interrogate how errors in both membrane moduli and membrane tension affect the error in forces. We took our control to be the output of budding simulations described in Fig. 3.3. Then, we conducted the same simulations over a range of bending moduli and membrane tensions to reflect a range in error of these two quantities. From these simulations, we calculated the energy per unit length at the phase boundary using Eq. 3.6 for the budding simulations at the same value of spontaneous curvature. Fig. 3.6A show the result of this procedure that have been normalized to the output from the initial simulations (as indicated by X.) As expected, separately varying either bending modulus or membrane tension is translated into an error in the energy per unit length, though the magnitude of the final error does not match

that of the input error due to the coupling to shape (Eq. 3.6). Next, we investigate the nonlinear effect of varying bending modulus and membrane tension simultaneously on the computed errors. Interestingly, we see that in some cases the error in one parameter is compensated for by the error in the other, as highlighted by the dashed lines which indicate a band of less than 10% total error. This is due to the intrinsic scaling in budding [135] with respect to bending modulus and membrane tension. Overall, we observe that the final error is not simply a sum of the errors in the two material properties and compensatory behaviours can result (Eq. 3.7, Fig. 3.6A).

In the previous calculation, when the membrane modulus and tension were varied, both the characteristic length of the membrane and its shape were affected. We conducted another analysis, where the shape of the membrane was fixed to the control and an error was introduced in the values of bending modulus and membrane tension during the calculation of tractions (Fig. 3.6B).

Errors in quantification of shape metrics

One of the largest source of errors in calculating forces arises from imaging modalities for shape itself. Uncertainty in the shape of the membrane will depend on the method used to extract shapes from microscopy images. Additionally, the high curvatures at endocytic sites means that a higher imaging resolution is required. Live-cell light microscopy is limited in resolution (even in superresolution methods [284, 285]), and traditional electron microscopy following chemical fixation may not fully preserve the shape of the bilayer [103, 104]. To this end, cryo-electron tomography may provide the best preservation, but it suffers from anisotropic resolution as a result of the "missing wedge" effect [286]. As a result, error can be introduced into the fundamental position and geometric variables of the constitutive equations associated with the membrane deformation. Errors in the position and shape coordinates, coupled with non-axisymmetric geometries can result in non-linear error propagation in the calculations and

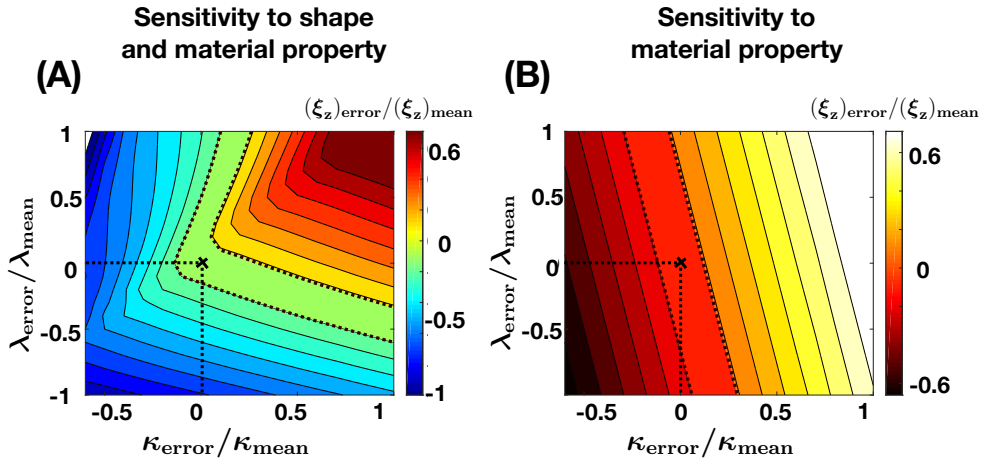

Figure 3.6: Parametric sensitivity analysis to material properties. Energy per unit length (Eq. 3.6) were calculated for a variation in the bending rigidity κ and membrane tension λ_0 . Dashed lines indicate 10 % error. $\lambda_{mean} = 0.02\,pN/nm$, $\kappa_{mean} = 320\,pN \cdot nm$, and $\xi_{mean} - 6.13pN$ (corresponding to a spontaneous curvature of 0.0276 nm^{-1} in Fig. 3.3). The sensitivity analysis was performed in two ways – *(i).* Sensitivity to shape and material property by running multiple simulations corresponding to the different parameter values (A) followed by an error calculation with respect to the mean value, *(ii).* Sensitivity to only material property by using a range of parameter values during calculation of energy per unit length (Eq. 3.6) for a single simulation (mean). (A) Sensitivity to shape and material property in a membrane bud. (B) Sensitivity to only material property in a membrane bud.

their effects are not yet understood.

3.4 Membrane bending by protein phase separation

Most of the proteins that bind to membranes using specific structural features, such as wedge-like amphipathic helices and crescent shaped scaffolds, are thought to be the primary drivers of membrane bending. However, many proteins involved in membrane remodeling contain intrinsically disordered regions, which have no stable structure. Recently, many of these disordered domains have been found to form weak multi-valent interactions leading to the condensation of protein liquid phases at membrane surfaces [287].

We used a continuum model of membrane and its interactions with liquid droplets to

understand how phase separation of proteins such as FUS LC at membrane surfaces can drive the assembly of protein-lined membrane tubules [7]. In fact, the set of shapes—pearls,undulations, and cylinders—can be classified as Delaunay surfaces [288], which have a constant, nonzero mean curvature (Fig. 3.7A). Unduloids are surfaces of revolution of an elliptic catenary [288,289]. With small changes in geometric parameters, a range of unduloid surfaces can be constructed [288] (Fig. 3.7A). More importantly, Delaunay surfaces, particularly unduloids and their variants, are known to minimize the Helfrich energy for membrane bending [289]. The radius and shape of the unduloids depends on a single dimensionless parameter $\alpha = \sqrt{\frac{\lambda}{2\kappa C_0^2} + \frac{1}{4}}$ in which λ is the membrane tension, κ is the bending modulus, and C_0 is the spontaneous curvature. When α = 0.75, the membrane resembles a cylinder and for $\alpha > 0.75$, the membrane resembles an unduloid (Fig. 3.7A).

Tubules with unduloid-like morphologies are known to arise when there is an area mismatch between the inner and outer leaflets of the lipid bilayer, such that the membrane has a finite spontaneous curvature [290]. For example, addition of lipids [291], polymers [292], and proteins to the surfaces of membrane vesicles have each been shown to produce such tubules. However, in these cases, the tubules protruded outward from the membrane surfaces, as would be expected when the area of the outer leaflet exceeds that of the inner leaflet. In contrast, we observe tubules that protrude inward from the membrane surface, suggesting that protein phase separation reduces the area of the outer leaflet relative to that of the inner leaflet (Fig. 3.7B).

We might expect such a reduction in area if attractive interactions between his-FUS LC peptides generates compressive forces at the membrane surface. How might these compressive forces arise? As an intrinsically disordered domain, FUS LC behaves more like a polymer than like a structured protein domain [293]. When polymers are tethered to surfaces, the density of polymer segments decreases substantially as the distance from the surface increases [294] (Fig. 3.7B). If the membrane were to remain flat, this reduced density of segments would result in

a reduction in interactions between the amino acids within FUS LC, as the distance from the membrane surface increased. These unsatisfied interactions create a driving force for membrane curvature. Specifically, if the membrane bends, such that proteinlined buds and tubules are formed, the density of protein segments will increase with increasing density from the membrane surface, such that some portion of the unsatisfied interactions can now be satisfied (i.e., x $>$ x' in Fig. 3.7B).

Another perspective on this potential mechanism comes from the work of Lipowsky [295] and Sung [296] who have examined the impact of adsorption of polymers on membrane surfaces. The assembly of FUS LC proteins at the membrane surface is analogous to adsorption of a polymer because the network of protein–protein interactions creates a macromolecular condensate that adheres to the membrane at multiple points. Using thermodynamic arguments in combination with the principles of membrane mechanics, these authors showed that when a polymer adsorbs strongly at multiple points to the membrane surface, the membrane will bend in order to maximize contact with the polymer.

To examine the set of membrane shapes created by this mechanism, we used the Helfrich model with spontaneous curvature to simulate a compressive stress being applied to one leaflet of a lipid bilayer [133]. The area difference between the two leaflets was modeled using a locally specified spontaneous curvature for simplicity in simulations (Fig. 3.7C). The spontaneous curvature effectively represents the stresses due to the area difference between the two leaflets [297]. The governing equations were solved in an axisymmetric parametrization for ease of computation to demonstrate the principles underlying the formation of undulating and pearled tubules.

We first simulated a domain of fixed area and homogeneous bending rigidity that included the protein-enriched phase and the surrounding protein-depleted phase. Our results showed that increasing the spontaneous curvature in the protein-rich phase resulted in the formation of

undulating tubules (Fig. 3.7D) similar to those observed in experiments [7]. Furthermore, the simulations predicted that the tubule diameter would increase linearly in proportion to the square root of the bending modulus (Fig. 3.7E). The bending energy corresponding to the formation of the undulating and pearled tubules is shown Fig. A.7. Notably, similar morphologies will arise anytime the membrane has a sufficient isotropic spontaneous curvature [291, 292].

It is likely that the protein-enriched phase has an increased bending rigidity compared to the protein-depleted phase, owing to the higher density of protein contacts. Therefore, we next asked if the ratio of bending rigidities in the attached protein layer and the underlying membrane layer could impact the shapes of the tubules. We defined the ratio of bending rigidities, $\kappa_{\text{ratio}} = \kappa_{\text{protein}}/\kappa_{\text{membrane}}$, and varied the ratio in the range of 1 to 20, in which $\kappa_{\text{ratio}} = 1$ denotes uniform bending rigidity. With increasing κ_{ratio}, we observed that the tubules took on a more clearly defined pearled morphology (Figs. 3.7F, 3.7G, and A.8) similar to those observed in experiments [7].

3.5 Discussion

In this thesis, we presented a framework for the calculation of axial and radial tractions for non-linear deformations of the membrane in the absence and in the presence of heterogeneities, solely based on the membrane geometry and material properties. From these calculations, we summarized that line tension can be calculated between two phases as an energy per unit length (Fig. 3.4). Importantly, using different examples of critical membrane shapes that occur in endocytosis and exocytosis, we have demonstrated that the local tractions are directly related to deviations from idealized geometries and can be generated by membrane heterogeneity. Moving forward, this procedure can be useful for the analysis of forces acting on membranes, both in reconstituted systems and in cells.

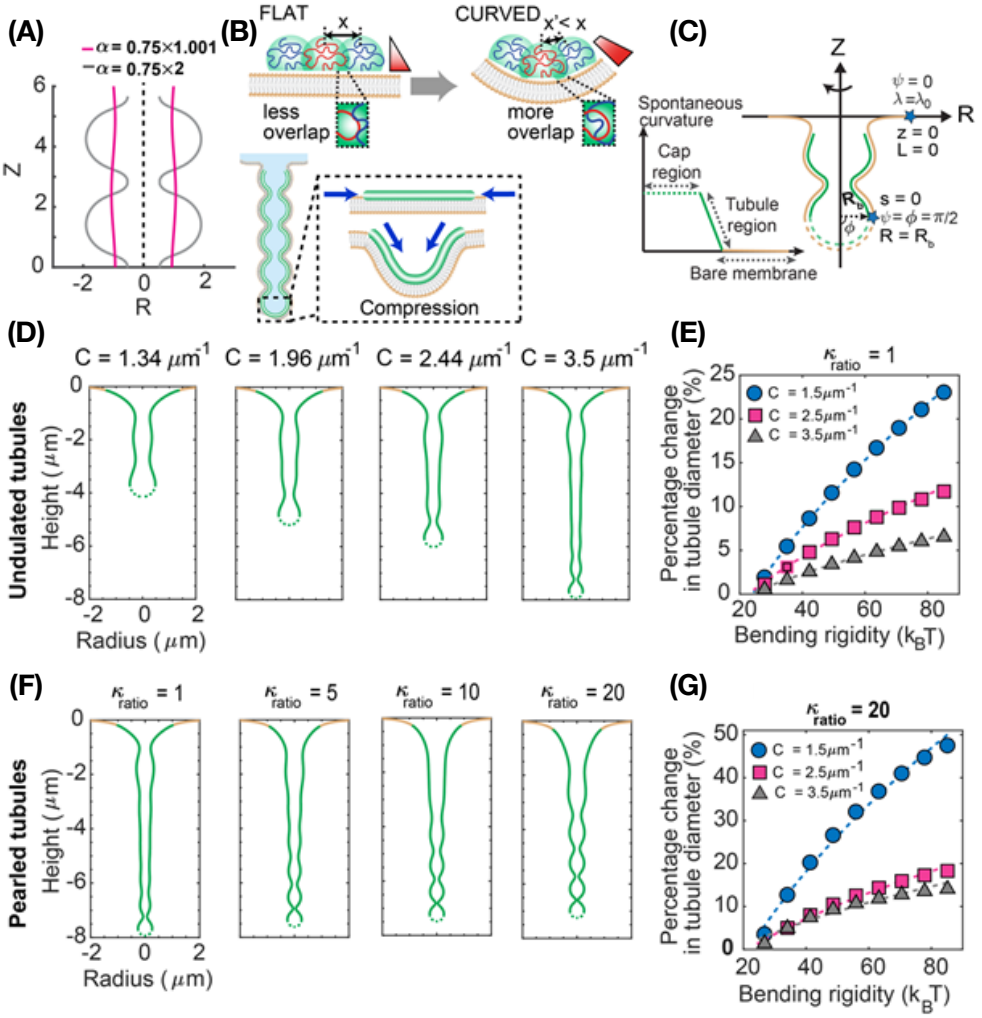

Figure 3.7: Mechanical model of undulating and pearled tubule formation. (A) Unduloid-like shapes solution for Helfrich energy minimization at different values of nondimensional parameter, α. For $\alpha \sim 0.75$, the membrane takes on a cylindrical shape (purple line); for $\alpha >$ 0.75, the unduloid becomes a sphere similar to a string of pearls (gray line). (B) Schematic depiction of membrane tubule formation due to the compressive stresses applied by liquid–liquid phase separation on the membrane. (C) Schematic of the axisymmetric simulations depicting the simulation domain and the boundary conditions. The yellow region represents the bare membrane, and the green region is the area coated by the proteins. The dashed lines indicate the cap of the tubule, assumed to have a constant curvature. The inset shows the spontaneous curvature distribution along the tubule region used to model the membrane shape. (D) Undulating tubules minimize the membrane bending energy as the spontaneous curvature increases for uniform bending rigidity of the membrane ($\kappa = 80 k_B T$). (E) Percentage of change in the tubule diameter as a function of the bending rigidity for three different values of spontaneous curvature. The dashed lines show a square root dependence on the bending modulus by fitting to the curve (F) Pearled tubules minimize the bending energy of the membrane for heterogeneous membrane rigidity ($\kappa_{\text{ratio}} = \kappa_{\text{protein}}/\kappa_{\text{membrane}}$), C_0 = 3.5 μm^{-1}. (G) Percentage of change in the tubule diameter as a function of the bending rigidity for three different values of spontaneous curvature for κ_{ratio} = 20. The dashed lines are the fitted curve.

Using the analysis presented here and having some knowledge of the shape and material properties will allow us to estimate the local stresses acting on the membrane. It is important to note that the tractions calculated here depend on the knowledge of the membrane strain energy and the material properties.

It has been demonstrated that PEGylation of lipids [298] and protein crowding can curve and even induce scission of artificial lipid bilayers. In addition to material properties, non-linear interactions between curvature-inducing proteins, membrane curvature, and protein aggregation play an important role in governing the molecular mechanisms by which proteins sense and induce curvature [299]. A theoretical treatment of the corresponding energy terms in given in [189]. Additional energy terms such as adhesion energy, entropic contributions from proteins, protein crowding, tilt, and cytoskeletal interactions will alter the expressions for tractions and introduce more material properties [30]. We also demonstrate that the knowledge of the underlying biophysical mechanism becomes important because the shape of the membrane, particularly in cells, is a many-to-one function (multiple processes can give rise to a similar shape). However, the fundamental principle that shape contains information about the underlying forces will apply regardless of the exact form of the energy used to perform the analysis.

There can be multiple sources of error in the quantification of forces – error in the measurement of material properties, errors in the measurement of the shape itself due to imaging, and finally error in the assumptions about stress-strain relationships themselves. While many of the measurements of material properties are conducted *in vitro*, recently, some studies have begun to measure the *in vivo* structure of lipids and their material properties [300]. Interestingly, recent works also suggest that there is no long range propagation of membrane tension in cells, seemingly reducing the uncertainty in calculating tension [161]. Additionally, efforts will need to focus on the development of image analysis methods to extract the shape of the membrane while reducing noise. There are already quite a few efforts in this direction, although these are

focused on tension-based mechanisms in epithelial sheets. Curvature-dependent effects are harder to discern from imaging data [301, 302].

There is also a need for the development of algorithms that do not *a priori* assume symmetry of the shape and can handle irregular geometries. Then, imaging data, which are abundant in the literature [211, 303, 304], can potentially be analyzed and used to populate a database/machine-learning framework. This can then be extended to analyze the shapes of complex structures in cells, which likely include contributions from multiple mechanisms. Finally, an assumption that we have made in this thesis is to neglect the surrounding fluid flow or inertial dynamics and assume that the membrane is at mechanical equilibrium at all times [232, 305, 306]. This assumption is commonly used in the modeling of membrane curvature to keep the mathematics tractable [150, 232]. While the Helfrich model has been used by us and others with great success, the role of these dynamics of deformations, thermal fluctuations [307, 308], and multiscale models will be needed to truly appreciate different spatial and temporal scales of forces. In fact, thermal fluctuations coupled with protein aggregation can lead to runaway instabilities and scission [240, 309] and must be considered in theoretical treatments.

As a small step in this direction, we have implemented a modified form of the Helfrich energy including deviatoric effects to consider the anisotropic nature of spontaneous curvature (Fig. A.6). While our current focus has been on explaining the mathematical and physical basis of local tractions and how these tractions can be used to understand important experimental systems and biological processes, to close the gap between modeling and experiments, future efforts will need to focus on relaxing the assumption of rotational symmetry and the ability to estimate local tractions in experimentally observed membrane shapes.

3.6 Acknowledgments

I would like to acknowledge my co-authors Dr. Ritvik Vasan, Dr. Julian Hassinger, Feng Yuan, Brandon Bakka, Andrea Trementozzi, Kasey Day, Prof. Nicolas Fawzi, Prof. Jeanne Stachowiak, and Prof. Padmini Rangamani. I would also like to thank Prof. David Drubin for initial discussions and Dr. Morgan Chabanon for his suggestions on improving the manuscript. I would also like to acknowledge grant funding: the Visible Molecular Cell Consortium (VMCC) and the Center for Trans-scale Structural Biology and Biophysics (CTSBB) at UC San Diego.

Chapter 4

Bead-like morphology of membrane nanotube

4.1 Introduction

Membrane nanotubes also known as tunneling nanotubes, have been identified as intercellular structures that can connect cells over long distances, i.e., tens of micrometers (see Fig.4.1A) [310, 311]. Membrane nanotubes have been observed in a wide variety of cell types [311–314] in addition to the artificial nanotubes that have been produced from lipid vesicles [311, 315]. Nanotubes are typically long and thin cylindrical protrusions with sub-micron diameter and lengths on the order of several hundred microns [310]. In contrast to other types of cellular projections, such as filopodia, which are attached to the substrate [316–318], nanotubes are suspended in the medium [314, 319–322]. Despite increasing observations in the literature highlighting the functional role of membrane nanotubes, the role of membrane mechanics in governing the morphology of these structures has largely remained unexplored.

Changes in the surrounding environment, rearrangement of membrane constituents, or mechanical stresses can result in dramatic shape transformations [310, 323–327]. For instance, in addition to the predominantly cylindrical geometry of many membrane nanotubes, the formation of pearl shapes along membrane nanotubes has been observed in various experiments [321, 328–330]. This morphological transition in nanotube structures resembles the well-known Rayleigh-Plateau fluid instability, where a change in the surface tension results in the break up of a cylindrical stream of fluid into multiple droplets [331–333]. Similarly, in the case of cylindrical membranes, various studies have shown a tension-driven Rayleigh-type instability, in which a perturbation in the membrane tension leads to the pearling instability [290, 334–338]. Indeed, the formation of beads along membrane nanotubes could result from any asymmetry in the lipid bilayer such as protein-induced spontaneous curvature arising from local phase separation of proteins, adsorption of nanoparticles and/or anchored polymers, or induced anisotropic curvatures by membrane inclusions [292, 324, 339, 340]. These interactions are accompanied by a change in the local tension of the membrane [153, 159–161].

A series of elegant modeling studies have proposed the idea that curved proteins and cytoskeletal proteins can induce protrusions along the membrane [299, 341–345]. Separately, experiments are have demonstrated that: (a) the composition of a membrane nanotube is not homogeneous [346]; (b) tension due to adhesion of rolling neutrophils can lead to tether formation [346]; and (c) spontaneous curvature along a nanotube can lead to the formation of bead-like structures [326, 329, 346–348]. It is not yet clear if such beaded structures are common to membrane nanotubes and if they have a physiological role in cells and tissues. Nonetheless, from a membrane mechanics standpoint, these structures are fascinating to study. Here, we examine how changes in the local membrane tension, originating from the heterogeneous distribution of the membrane components due to local phase separation, can cause the shape transformation from a cylindrical membrane to a beaded architecture. Therefore, we seek to answer the following

questions: how does the presence of a membrane protein domain affect the shape of a nanotube? What is the phase space that governs the energy landscape of membrane nanotubes? And finally, how do multiple beads interact with each other along the surface of a nanotube? To address these questions, we conducted simulations by implementing an augmented Helfrich model that includes protein density contributions [133, 202, 349] with local incompressibility constraints [135].

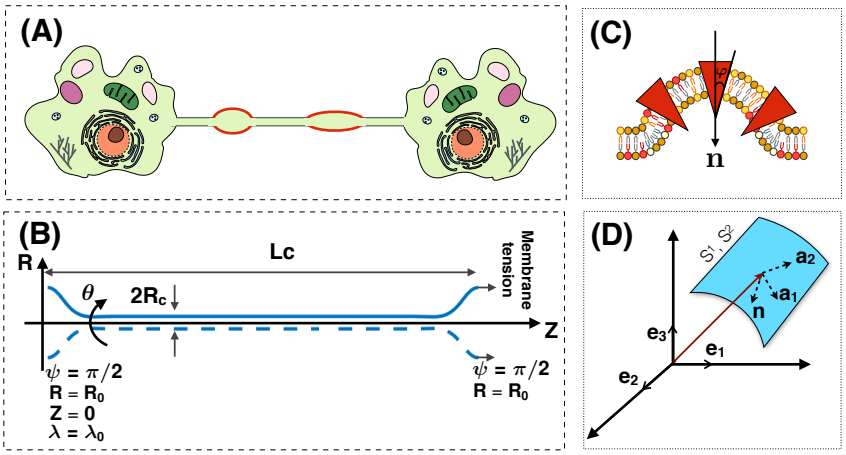

Figure 4.1: Formation of bead-like structures along the nanotubes can result from local heterogeneities in the membrane. (A) A cartoon showing an intercellular membrane nanotube with local bead-shaped deformations due to membrane-protein interactions (red domain). (B) Axisymmetric coordinates along the membrane nanotube and the boundary conditions used in simulations. L_c represents the length and R_c represents the radius of the nanotube. (C) A schematic depicting membrane-protein interactions that could lead to the formation of beads along a nanotube. Proteins (shown in red) can aggregate along the membrane to induce local curvature and heterogeneous tension . We assume these proteins are cone-shaped such that their meridian makes an angle φ ($\varphi < 0$) with the normal vector ($\mathbf{n}$) to the surface. (D) The coordinate system used to define a surface by the tangent basis $\mathbf{a_1}$, $\mathbf{a_2}$ and the normal vector $\mathbf{n}$. Note that the normal is pointing downwards in this case.

4.2 Methods

4.2.1 Assumptions

The plasma membrane is a complex structure; various molecules pack tightly together to form a semi-impermeable barrier for the cytoplasm, nucleus, and intercellular organelles [350]. Nevertheless, under certain assumptions as described below, it is appropriate to model this complex and heterogeneous surface using a simple mathematical framework.

- The length scale of the nanotube is assumed to be much larger ($\sim$ 20 times) than the thickness of the bilayer such that the membrane behaves as a thin elastic shell [133,150,351].

- We assume that the membrane nanotube is at mechanical equilibrium (i.e. no inertia) [305]. Because of the high stretching modulus of lipid bilayers [352], we also assume that the lipid bilayer is areally incompressible and we use a Lagrange multiplier to implement this constraint [35, 150].

- We consider the case that there is a local phase separation of proteins along the membrane surface (see Fig. 4.1A). We assume that the local phase separated membrane proteins are rotationally symmetric, induce a negative spontaneous curvature ($\varphi < 0$), and ignore the influence of anisotropic curvature inducing proteins such as BIN-Amphiphysin-Rvs (BAR) domain proteins [36, 299, 342].

- We assume that the total energy of the system includes the membrane bending energy and a contribution from local protein phase separation in a dilute regime (low protein density). Thus, the membrane energy is modeled using an augmented version of Helfrich energy for elastic manifolds including membrane-protein interaction contributions [189,193,353–356]. In mechanical equilibrium, the total energy of the membrane including the effects of the local phase separation of proteins is similar to a standard Cahn-Hilliard model [357] with

the gradient penalty for the spatial heterogeneity of the protein distribution. For simplicity, we prescribe the local distribution of proteins along the surface of the membrane nanotube using a hyperbolic tangent function [358–360].

- We do not consider the role of any other forces, e.g. actin [342], so that we can focus only on membrane nanotube deformation due to membrane-protein interactions [361–363].

- For simplicity in the numerical simulations, we assume that the membrane in the region of interest is rotationally symmetric and long enough so that boundary effects can be ignored (Fig. 4.1B) [292, 363].

4.2.2 Membrane mechanics

We model the membrane with two contributions to the strain energy – one from protein-protein interactions and the other from the membrane bending. The protein-protein interaction is written as a constitutive function of the protein density σ (number per unit area). While the exact form of this energy is yet to be experimentally verified, based on thermodynamic arguments, the dependence of the energy on the local protein density, the protein density gradient, and the thermal entropic contribution has been proposed as [5, 188, 189, 356, 364, 365]

$$W_{\text{Protein}} = \underbrace{-\alpha\sigma(\theta^{\xi})^2}_{\substack{\text{Protein} \\ \text{aggregation}}} + \underbrace{\beta(\nabla\sigma)^2}_{\substack{\text{Inhomogeneous} \\ \text{protein distribution}}} + \underbrace{k_B T\sigma(\log(\frac{\sigma}{\sigma_s}) - 1)}_{\substack{\text{Entropic contribution} \\ \text{due to thermal diffusion}}}, \tag{4.1}$$

where W is the energy per unit area, α indicates the strength of the attractive energy between two neighboring proteins, β is a positive constant that depends on the excluded area and the effective interaction area of the proteins [186, 357], ∇ is the gradient operator, k_B is the Boltzmann constant, and T is temperature [189, 364]. In Eq. 4.1, $\beta(\nabla\sigma)^2$ is a first order correction for a spatial inhomogeneity in the membrane composition that allows the interfacial energy to be

modeled with a sharp gradient in a continuous surface [357]. We should mention that in Eq. 4.1, we ignore the higher order terms in σ [356, 365] since we assume that the system is in the dilute regime and the protein density is low.

In Eq. 4.1, σ can depend explicitly on the surface coordinates θ^{ξ} to allow for local heterogeneity (Fig. 4.1D). Also, the proteins are assumed to be transmembrane, conical insertions such that the meridian of each protein is at an angle φ ($\varphi < 0$) with the normal vector to the membrane surface ($\mathbf{n}$) (Fig. 4.1C) [202]. In the dilute regime, the locally induced-spontaneous curvature due to membrane-protein interaction can be modeled as a linear function of the surface protein density as [202]

$$C(\sigma) = \mu\varphi\sigma(\theta^{\xi}), \tag{4.2}$$

where μ is a length scale that represents the lipid-protein specific entropic interactions. The energy associated with membrane bending due to the isotropic spontaneous curvature is given by the Helfrich Hamiltonian, modified to include the heterogeneous membrane properties as [133, 137]

$$W_{\text{Bending}} = \kappa(\theta^{\xi}) \left[H - C(\sigma(\theta^{\xi}))\right]^2 + \kappa_G(\theta^{\xi})K, \tag{4.3}$$

where H is the local mean curvature and K is the local Gaussian curvature. κ and κ_G are bending and Gaussian moduli respectively, which can vary along the surface coordinate θ^{ξ} [136, 137]. Hence, the total energy of the membrane including both bending and protein contributions is given by

$$W(H,K,\sigma;\theta^{\xi}) = \underbrace{\kappa(\theta^{\xi})\left[H - C(\sigma(\theta^{\xi}))\right]^2 + \kappa_G(\theta^{\xi})K}_{\text{Bending}} \quad \underbrace{-\alpha\sigma(\theta^{\xi})^2}_{\text{Protein aggregation}} \quad + \quad \underbrace{\beta(\nabla\sigma)^2}_{\substack{\text{Inhomogeneous}\\ \text{protein distribution}}}$$
$$+ \underbrace{k_B T\sigma(\log(\frac{\sigma}{\sigma_s}) - 1)}_{\substack{\text{Entropic contribution}\\ \text{due to thermal diffusion}}}. \tag{4.4}$$

We note that $\frac{k_B T}{\kappa}$ is small because the membrane bending modulus is in the range of 20-40 $k_B T$ [366, 367]. Additionally, in the dilute regime of low protein density $k_B T\sigma \ll 1$. Based on this analysis, we neglect the entropic term in the rest of our calculations.

A local balance of forces normal to the membrane, subject to the energy density given in Eq. (4.4) yields the so-called "shape equation" [33, 202, 349]

$$\underbrace{\Delta[\kappa(H - (\mu\varphi)\sigma)] - (\kappa_G)_{;\xi\eta}\tilde{b}^{\xi\eta} - 2\kappa H\left(H - (\mu\varphi)\sigma\right)^2 + 2\kappa\left(H - (\mu\varphi)\sigma\right)\left(2H^2 - K\right)}_{\text{Elastic effects}}$$
$$+ \quad \underbrace{2H(\alpha\sigma^2)}_{\text{Protein aggregation}} \quad - \quad \underbrace{2H\beta(\nabla\sigma)^2)}_{\substack{\text{Inhomogeneous}\\ \text{protein distribution}}} \quad = \underbrace{(p + 2\lambda H)}_{\substack{\text{Capillary}\\ \text{effect}}}, \tag{4.5}$$

where Δ is the surface Laplacian operator, p is the pressure difference across the membrane, λ is interpreted as the membrane tension [150], $()_{;}$ is the covariant derivative with the respect to the surface metric, and $b^{\tilde{\xi}\eta}$ is the co-factor of the curvature tensor. A local balance of forces tangent to the membrane, which enforces the incompressibility condition in a heterogeneous membrane, yields the spatial variation of membrane tension λ [6, 135, 202],

$$\underbrace{\nabla\lambda}_{\substack{\text{Gradient of}\\ \text{membrane tension}}} = \underbrace{2[\kappa\mu\varphi(H-(\mu\varphi)\sigma)+\alpha]\frac{\partial\sigma}{\partial\theta^{\xi}}-\beta(\nabla\sigma)\frac{\partial(\nabla\sigma)}{\partial\theta^{\xi}}}_{\text{Protein density variation}}-\underbrace{\frac{\partial\kappa}{\partial\theta^{\xi}}(H-(\mu\varphi)\sigma)^{2}}_{\substack{\text{Bending modulus-}\\ \text{induced variation}}}-\underbrace{\frac{\partial\kappa_{G}}{\partial\theta^{\xi}}K}_{\substack{\text{Gaussian modulus-}\\ \text{induced variation}}} . \tag{4.6}$$

4.2.3 Analytical solutions (limit cases)

In this section, we explore the analytical solution for Eq. 4.4, ignoring the boundary effects, the Gaussian curvature, and the entropic term. In this condition, for a nanotube with uniform bending rigidity and no protein density, the free energy density (Eq. 4.4) is given by $W_0 = \kappa H_0^2$, where H_0 is the mean curvature of the nanotube equal to $1/(2\mathrm{R_c})$ ($H_0 = 1/(2\mathrm{R_c})$). W_0 is the energy minimizer for this geometry; adding proteins locally or including heterogeneous bending rigidity increases the energy of the system ($W \geq W_0$). To find an analytical expression for the mean curvature of the nanotube at the center of the protein-enriched domain as a function of the protein density and the bending rigidity, we consider the limit case that $W = W_0$. This gives us an expression for the mean curvature at the center of protein-enriched domain as

$$H_{\text{analytical}} = \underbrace{\mu\varphi\sigma}_{\substack{\text{Spontaneous}\\ \text{curvature}}} + \sqrt{\underbrace{\frac{\frac{1}{(2R_c)^2}}{\kappa_{\text{ratio}}}}_{\substack{\text{Preexisting curvature}\\ \text{of the tube}}} + \underbrace{\frac{\frac{\alpha\sigma^2}{\kappa}}{\kappa_{\text{ratio}}}}_{\substack{\text{Aggregation}\\ \text{effects}}} - \underbrace{\frac{\frac{\beta(\nabla\sigma)^2}{\kappa}}{\kappa_{\text{ratio}}}}_{\substack{\text{Inhomogeneous}\\ \text{protein distribution}}}} , \tag{4.7}$$

Here, κ_{ratio} represents the ratio of the bending rigidity in the protein-enriched domain (κ_{protein}) compared to the bending rigidity of the bare lipid membrane ($\kappa_{\text{ratio}} = \kappa_{\text{protein}}/\kappa$).

For low protein density ($\sigma \ll 1$), the higher order terms in Eq. 4.7 can be ignored and the equation can be simplified using Taylor expansion around σ which gives

$$H_{\text{analytical}} = \underbrace{\mu\varphi\sigma}_{\substack{\text{Spontaneous}\\ \text{curvature}}} + \frac{1}{\sqrt{\kappa_{\text{ratio}}}}\Big(\underbrace{\frac{1}{(2R_{\text{c}})}}_{\substack{\text{Preexisting curvature}\\ \text{of the tube}}} + \frac{R_{\text{c}}}{\kappa}\big(\underbrace{\alpha\sigma^2}_{\substack{\text{Aggregation}\\ \text{effects}}} - \underbrace{\beta(\nabla\sigma)^2}_{\substack{\text{Inhomogeneous}\\ \text{protein distribution}}} \big)\Big). \tag{4.8}$$

The relationship in Eq. 4.7 can be used to predict how the local curvature of the nanotube at the center of the protein-enriched domain varies with protein density and κ_{ratio}. For a homogenous membrane ($\kappa_{\text{ratio}} = 1$), as σ increases, the negative spontaneous curvature becomes dominant and the mean curvature at the center of the protein-enriched domain decreases (Fig. 4.2A). For a constant protein density ($\sigma = 2.5 \times 10^{-5}$ nm^{-2}), as κ_{ratio} increases, the positive term under the square root becomes smaller and therefore the mean curvature decreases (Fig. 4.2B). A decrease in the mean curvature of the nanotube at the center of the protein-enriched domain corresponds to a larger radius in that point. This implies that protein aggregation with heterogeneous properties alters the morphology of the membrane nanotube where bead-shaped structures with larger radii than the nanotube radius ($r_b > R_c$, where r_b is the radius of the bead) forms along the protein-enriched domains.

In Fig. 4.2C, we plotted the derived analytical mean curvature at the center of the protein-enriched domain (Eq. 4.7) as a function of protein density and bending rigidity ratio. Interestingly, we observed that the sign of the analytical mean curvature at the center of the protein-enriched domain changes from positive (pink domain) to negative (blue domain) for large values of the bending rigidity ratio and protein density. However, we know that for a rotational symmetric nanotube, the mean curvature at the center of the protein-enriched domain cannot be negative. This suggests that for low protein density and bending rigidity ratio (pink domain in Fig. 4.2C), the energy of the system can be minimized with decreasing the local mean curvature along the protein-enriched domain. But, for large protein density and the bending rigidity ratio (blue

domain in Fig. 4.2C), the system needs to exploit another mechanism to lower the work done on the system.

We next relate the analytical curvature in the protein-enriched domain (Eq. 4.7) to the radius of the bead assuming that the bead shape can be approximated by a cylinder and therefore $H_{\text{analytical}} = 1/(2\mathrm{r}_{\text{b, analytical}})$. Thus, using Eq. 4.7, we have

$$2\mathrm{r}_{\text{b,analytical}} = \left[\mu\varphi\sigma + \sqrt{\frac{\frac{1}{(2\mathrm{R}_c)^2} + \frac{\alpha\sigma^2}{\kappa} - \frac{\beta(\nabla\sigma)^2}{\kappa}}{\kappa_{\text{ratio}}}}\right]^{-1}. \tag{4.9}$$

Similar to Eq. 4.7, we can simplify Eq. 4.9 for low protein density given by

$$\mathrm{r}_{\text{b,analytical}} = \sqrt{\kappa_{\text{ratio}}}R_{\text{c}}\left(1 - 2R_{\text{c}}\sqrt{\kappa_{\text{ratio}}}(\mu\varphi\sigma) - \frac{2R_{\text{c}}^2}{\kappa}(\alpha\sigma^2 - \beta(\nabla\sigma)^2)\right). \tag{4.10}$$

Because Eq. 4.10 is valid only for small membrane deformation, we use the mechanical model (Eqs. 4.5 and 4.6) to run simulations and obtain the shape and the size of the large beads.

4.2.4 Numerical implementation

In axisymmetric coordinates, the equations of motion (Eq. B.14 and Eq. B.15) simplify to a system of first-order differential equations (Eq. B.24) with six prescribed boundary conditions (Eq. B.25). In order to solve these coupled equations, we used the commercially available finite element solver COMSOL MULTIPHYSICS. In this thesis, we assume that the total length of the membrane nanotube is conserved and to focus on the net effect of membrane tension, we

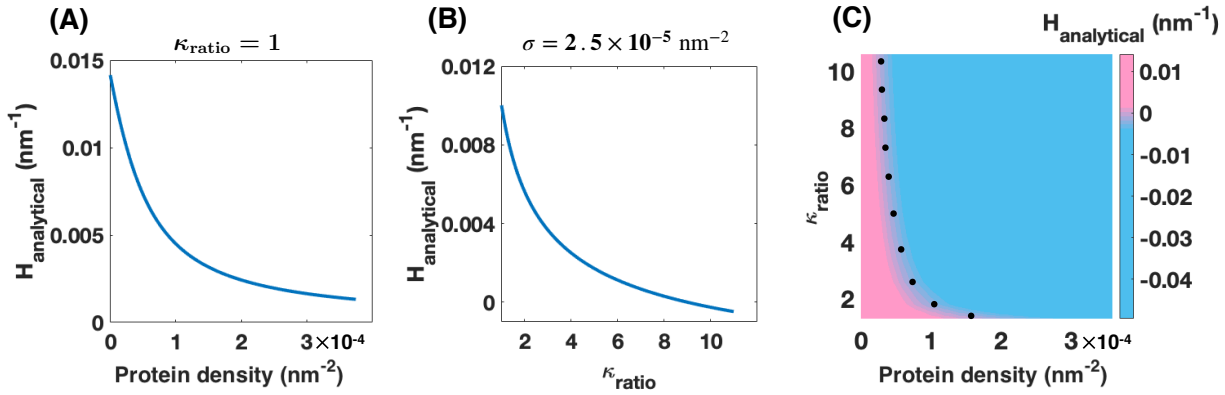

Figure 4.2: Analytical mean curvature along the protein-enriched (Eq. 4.7) domain as a function of the protein density (σ) and bending rigidity ratio (κ_{ratio}). (A) With increasing the protein density, the mean curvature along the protein aggregation domain decreases ($\kappa_{ratio} = 1$). (B) Decrease in the mean curvature of the protein-enriched domain as the bending rigidity ratio increases ($\sigma = 2.5 \times 10^{-5}$ nm^{-5}).(C) Heat map shows the analytical mean curvature along the protein-enriched domain (Eq. 4.8) as a function of the protein density and bending rigidity ratio. The sign of the analytical mean curvature changes from positive to negative along the dotted black line.

set the transmembrane pressure at zero ($p = 0$). The values of parameters used in the model are summarized in Table 4.1.

4.3 Results

4.3.1 Formation of beads along a nanotube due to protein-induced spontaneous curvature

For membrane nanotubes, it has been shown that the composition of the lipid bilayer is a critical factor in determining their shapes and radii [337, 363, 372, 373]. To explore how heterogeneity in the membrane properties due to a surface protein aggregation affects the shape of a nanotube, we conducted simulations on cylindrical nanotubes with the aspect ratio of radius $R_c = 35$ nm and length $L_c = 20$ μm, and set the boundary tension to $\lambda_0 = 0.064$ pN/nm. The effect of boundary tension on the initial nanotube radius and length is shown in Fig. B.1. To

Table 4.1: Parameters used in the model

Notation	Description	Value
λ_0	Edge membrane tension [205, 368]	0 – 0.064 pN/nm
κ	Bending rigidity of the bare lipid membrane [367]	320 pN $\cdot$ nm
κ_{protein}	Bending modulus of rigid protein domain [266, 369, 370]	320 – 9600 pN $\cdot$ nm
σ	Protein density [371]	0 – 3.75×10^{-4} nm^{-2}
α	Strength of protein-protein interactions [189, 193, 202]	128×10^5 pN $\cdot$ nm^3
μ	Constant length scale [202]	200 nm
φ	The cone-shaped protein angle [202]	-1
L_c	Nanotube length	20 μm
R_c	Nanotube radius	35 nm
k_BT	Boltzmann energy	4.114 pN $\cdot$ nm
p	Transmembrane pressure	0 pN $\cdot$ nm^{-2}

ensure a smooth continuous transition between the domains, we implemented the difference in the protein density using a hyperbolic tangent function (Eq. B.33), such that the covered domain by the protein-enriched domain at the center of the nanotube remains constant ($L_{\text{protein}} = 8\,\mu$m), and the number of proteins per area increases from $\sigma_0 = 0$ to $\sigma_0 = 1.25 \times 10^{-4}\,\text{nm}^{-2}$ (Fig. 4.3A).

As the number of proteins in the fixed domain (L_{protein}) is increased, the membrane bends outward such that it resembles a bead-shaped structure that forms along the nanotube (Fig. 4.3B). This bead formation can be understood by considering the energy of the membrane (Eq. 4.4). In the absence of any protein ($\sigma = 0$, therefore $C = 0$), the curvature of the nanotube is constant everywhere ($H_0 = 1/(2R_c) = 1/70\,\mu\text{m}^{-1}$). Increasing the density of the conical-shaped proteins induces a negative spontaneous curvature (see Fig. 4.1C) and therefore increases the bending energy (Eq. 4.4). As a result of this increase in energy, the membrane curvature locally decreases by bending outward in the domain of the protein aggregation to minimize the total energy (Fig. 4.3B). For example, with increasing the protein density from $\sigma_0 = 0$ to $\sigma_0 = 1.25 \times 10^{-4}$ nm^{-2}, a bead with a radius of ~ 350 nm forms (Fig. 4.3B).

To understand the relationship between increasing σ and the shape of the bead, we

compared the results from our simulations against the analytical approximation for the bead radius (Eq. 4.10) as a function of σ assuming a uniform bending rigidity all along the nanotube ($\kappa_{ratio} = 1$) (Fig. 4.3C). For small protein densities ($\sigma_0 < 5 \times 10^{-5}$ nm^{-2}) and small membrane deformation ($r_b < 200$ nm), we found a good match between the analytical approximation and numerical results (Fig. 4.3C). However, for larger protein densities, the membrane deformation along the protein-enriched domain is large and the bead no longer has a cylindrical shape anymore exposing the limits of the analytical expression.

We next investigated the effect of the extent of the protein aggregation in Eq. 4.1 on the bead morphology. We repeated the simulations in Fig. 4.3 for three different values of α (Fig. B.2). We found that varying α does not alter the shape or the radius of the bead significantly (Fig. B.2). This is because the protein aggregation term in the energy has a small contribution to membrane bending; the dominant effect comes from the coupling between the protein density and spontaneous curvature (Eqs. 4.2 and 4.3).

Another important factor that controls the lipid flow on the surface of nanotubes and lipid packing is membrane tension [186, 374]. Consistent with the previous studies [153, 159], we observed that a local decrease in the membrane tension of the beaded domain corresponding to membrane bending and the applied area incompressibility constraint (Fig. B.3). This variation in the membrane tension allows us to also represent the radius of the bead radius as a function of the local membrane tension, where we found a nonlinear relationship between the increase in the radius of the bead and the decrease in the local membrane tension (Fig. B.3).

4.3.2 Heterogeneity in membrane stiffness lead to the formation of bead-like structures along a nanotube

Motivated by our numerical observation that a protein-induced spontaneous curvature along the membrane can result in the bead-like structures, we next asked if a change in the

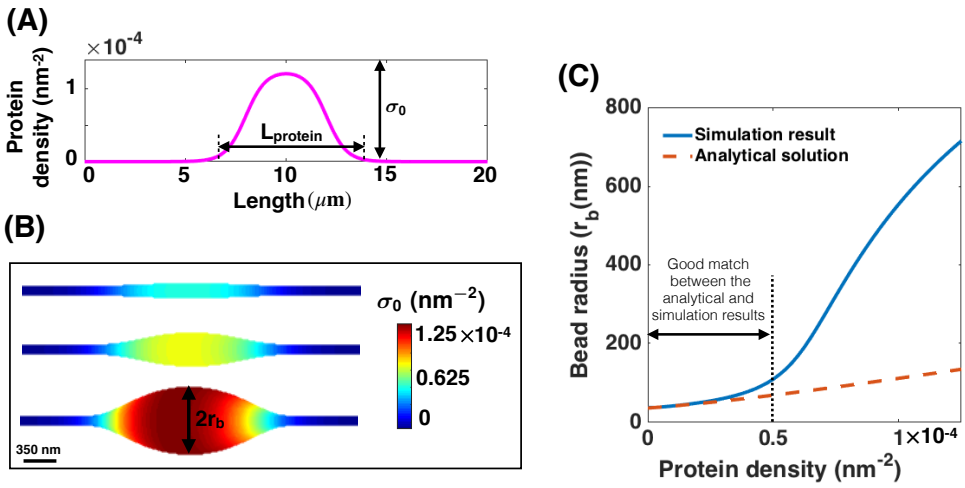

Figure 4.3: Protein-mediated bead formation along a membrane nanotube. (A) Protein density distribution on the membrane surface in which $L_{protein} = 8\,\mu$m shows the length of the protein-enriched domain and σ_0 represents the number of the proteins per unit area. (B) The formation of a large bead-shaped structure along the membrane nanotube as the density of proteins (σ_0) increases for $\lambda_0 = 0.064\,$pN/nm and uniform bending rigidity. The scale bar in panel (B) is 350 nm. (C) Bead radius (r_b) increases as a function of the protein density for both the analytical solution (Eq. 4.10) (dashed red line) and the simulation result (solid blue line).

membrane stiffness due to membrane-protein interaction could also induce a similar deformation along the nanotube. To answer this question, we repeated the simulation in Fig. 4.3 for $\sigma_0 = 1.25 \times 10^{-4}$ nm^{-2} assuming that the bending rigidity along the domain covered by the proteins is higher than the rest of the membrane, but $C = 0$ (e.g for cylindrical proteins where $\varphi = 0$) [369, 373] (Fig. 4.4A). This represents a case where the membrane-protein interaction induces a change in the membrane composition but does not induce an asymmetry between the leaflets.

As it is clear, by increasing κ_{ratio} from $\kappa_{ratio} = 1$ to $\kappa_{ratio} = 30$ [260, 369, 373], the membrane bending energy (Eq. 4.4) increases. To compensate for this increase in the bending energy, the membrane curvature decreases by bending outward significantly in the domain of the rigid segment and an ellipsoidal bead-shaped structure forms along the nanotube (Fig. 4.4B). For instance, we found that with increasing bending rigidity ratio from $\kappa_{ratio} = 1$ to $\kappa_{ratio} = 30$, a large bead with a radius of ~ 400 nm forms in the domain of the rigid protein (Fig. 4.4B).

Comparing radius of the bead obtained from numerical simulation (Fig. 4.4B) and the analytical expression (Eq. 4.10) as a function of the bending rigidity ratio for constant protein density ($\sigma_0 = 1.25 \times 10^{-4}$ nm^{-2}), we observed that for low values of the bending rigidity ratio ($\kappa_{\text{ratio}} < 5$), the membrane deformation is small ($r_b < 200$ nm) and therefore there is a good agreement between the analytical and simulation results (Fig. 4.4C). However, for large membrane deformations (when $\kappa_{\text{ratio}} > 5$), the analytical solution underestimates the radius of the bead because of our assumption in Eq. 4.9 that the bead has a cylindrical shape is no longer valid (Fig. 4.4C).

Additionally, we observed a local reduction in the membrane tension with increasing the bending rigidity of the protein domain and the formation of the bead along the nanotube (Fig. B.4). Interestingly, we found a similar trend in the reduction of the local membrane tension for both protein-induced spontaneous curvature and the protein rigidity mechanisms (Figs. B.3 and B.4). The membrane tension decreases from $\lambda = 0.064$ pN/nm to about zero with the formation of a bead with a radius of $r_b = 100$ nm. After that, for the larger beads, the local membrane tension is almost zero and remains constant (Figs. B.3 and B.4). For completeness, we also varied the Gaussian modulus along the domain of protein aggregation ($\Delta\kappa_G = (\kappa_{G,\text{protein}} - \kappa_{G,\text{lipid}})/\kappa_{G,\text{lipid}}$). Varying $-20 < \Delta\kappa_G < 20$ for $\sigma_0 = 1.25 \times 10^{-4}$ nm^{-2} and $\kappa_{\text{ratio}} = 1$, we found that the changes in the Gaussian modulus alone lead to small membrane deformations as compared with other effects (see Fig. B.5).

4.3.3 Energy landscape of bead-shaped structures along a nanotube

Our simulation results have demonstrated that two unrelated mechanisms, protein-induced curvature, and heterogeneity in the membrane rigidity, each independently lead to the formation of the bead-like structures along the membrane nanotube and that the radius of the bead increases nonlinearly with increasing strength of the heterogeneity. In order to explore how these two mechanisms might interact and modulate the shape of a nanotube, we conducted simulations

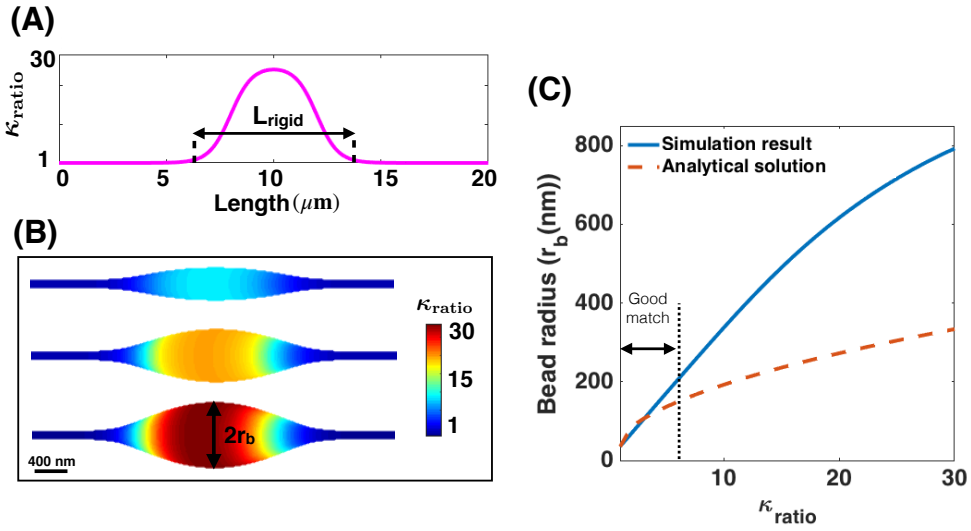

Figure 4.4: Heterogeneous membrane properties result in the formation of local bead-shaped structures. (A) Bending modulus variation along the length of the nanotube. κ_{ratio} is the bending rigidity ratio of the rigid protein domain compared to that of the bare lipid membrane ($\kappa_{ratio} = \kappa_{rigid}/\kappa_{lipid}$) and L_{rigid} represents the length of the rigid protein domain ($L_{rigid} = 8\ \mu$m). (B) Membrane deformation in the region of large bending rigidity resembles a local bead formation phenomenon; the tension at the boundary is set as $\lambda_0 = 0.064$ pN/nm and the protein density is fixed to be constant as $\sigma_0 = 1.25 \times 10^{-4}$ nm^{-2} and $C = 0$. The scale bar in panel (B) is 400 nm. (C) Increase in the radius of the bead as a function of κ_{ratio} for both the derived analytical solution in Eq. 4.10 (dashed red line) and the simulation result (solid blue line).

where the heterogeneous domain has effects from both the protein-induced spontaneous curvature and from increased bending rigidity. We repeated the simulations shown in Fig. 4.3 but this time assumed that the bending rigidity is heterogeneous ($\kappa_{ratio} = 11$).

Interestingly, we found that the competition between these two mechanisms leads to the formation of beads with different shapes. Based on the magnitude of the protein density, three different oblate spheroid shapes were obtained – *(i)* an ellipsoidal bead at $\sigma_0 = 2 \times 10^{-5}$ nm^{-2}, *(ii)* a flat cylindrical bead at $\sigma_0 = 1 \times 10^{-4}$ nm^{-2}, and *(iii)* a large unduloid-shaped bead at $\sigma_0 = 1.85 \times 10^{-4}$ nm^{-2} (Fig. 4.5A). These different bead shapes are classified according to the sign of H'' (the second derivative of the mean curvature), (*i*) in the ellipsoidal bead, H'' is positive everywhere along the bead, (*ii*) in the cylindrical bead, the change in the radius of the bead is very small compared to the radius of bead ($\frac{\Delta r_b}{r_b} < 0.01$, we set 0.01 as our threshold), and (*iii*) in

the unduloid-shaped bead, H'' changes sign along the bead (see Fig. B.6).

These results showed that the coupling between two modes of spatial heterogeneity along a membrane nanotube not only increases the radius of a bead (see Fig. B.7) but also broadens the energy landscape, enabling the formation of a variety of bead shapes. Furthermore, these shape transitions suggest that the energy landscape of the membrane, which is now modulated by heterogeneities in κ and σ plays an important role in the shape of the bead.

To further understand the relationship between the mean curvature and the bead shape transition, we plotted the mean curvature distribution that was obtained from our mechanical solution along the nanotube length for three different observed beads shapes in panel A (Fig. 4.5B). As expected for all shapes, the mean curvature decreases along the beaded domain to lower the energy of the system (Fig. 4.5B). For the large ellipsoidal bead in panel A, the mean curvature of the middle point of the bead is very small (Fig. 4.5B, dotted blue line). As the mean curvature becomes very small, the only possible behavior to further decrease the energy of the system is to use the third dimension, arclength ($H(\sigma, \kappa_{\text{ratio}}, s)$). Therefore, by increasing the protein density from $\sigma_0 = 2 \times 10^{-5}$ nm^{-2} to $\sigma_0 = 1 \times 10^{-4}$ nm^{-2} in Fig. 4.5A , the mean curvature decreases all along the bead which leads to the formation of the cylindrical bead (Fig. 4.5B, dotted red line). After the formation of the cylindrical bead, any further increase in the energy of the system causes a buckling instability where the large unduloid-shaped bead forms(Fig. 4.5B, dotted green line).

4.3.4 Competition between length scales determines the morphology of the bead-shaped structures along a nanotube

To identify the range of protein density and κ_{ratio} over which three different bead shapes in Fig. 4.5A can form, we performed simulations over a range of protein densities, ($\sigma_0 = 0 - 3.75 \times 10^{-4}$ nm^{-2}), as well as over a range of $\kappa_{\text{ratio}} = 2 - 11$, encompassing soft protein domains to very stiff clusters. This variation allowed us to construct a phase diagram to identify

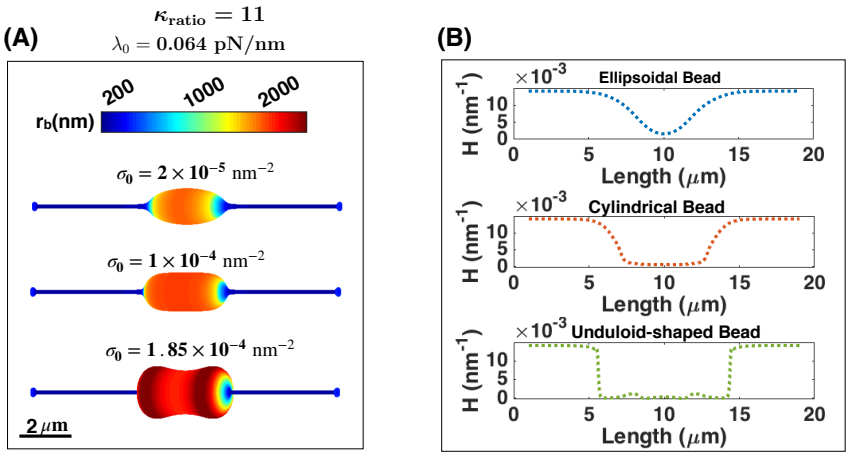

Figure 4.5: Three different possible shapes of a bead-like structure resulting from the presence of a rigid protein domain. (A) Formation of (*i*) an ellipsoidal bead (top) at low protein density, (*ii*) a cylindrical bead (middle) at average protein density, and (*iii*) an unduloid-shaped bead (bottom) at high protein density; $\kappa_{ratio} = 11$. The scale bar in panel A is 2 μm. (B) The mean curvature (H) distribution along the nanotube length for ellipsoidal (blue line), cylindrical (red), and unduloid-shape (green) beads in panel (A). See Fig. B.6 for details of the change in the second derivative of H.

the regions of different bead morphologies (Fig. 4.6A). The pink region represents the formation of ellipsoidal bead-shaped structures, the blue region denotes the cylindrical beads, and the green region indicates the unduloid-shaped beads configuration.

To determine the dominant length scale for each bead shape morphology in Fig. 4.6A, we compared the two "induced" length scales, one by the rigid domain ($l_k = 1/2\sqrt{\kappa_{protein}/\bar{\lambda}}$) and the other one associated with the protein aggregation ($l_\sigma = 1/\mu\varphi\sigma$) [135, 153, 343]. The background of the phase diagram in Fig. 4.6A shows that these two length scales act in tandem to regulate the bead size and shape. When $l_\sigma \gg l_k$ or $\log(\frac{l_\sigma}{l_k}) > 0$, ellipsoidal beads form along the protein-enriched domain (Fig. 4.6A, blue). When the two length scales become comparable ($\log(\frac{l_\sigma}{l_k}) \sim 0$), the formation of cylindrical beads are energetically favorable for the system (Fig. 4.6A, pink). Finally, at very large values of protein density, when the "induced" length scale by the rigid domain becomes dominant ($\log(\frac{l_\sigma}{l_k}) < 0$), the unduloid-shaped bead forms along the membrane nanotube (Fig. 4.6A, green).

Regardless of which mechanism dominates, the edge tension λ_0 implicitly governs the length scale of the membrane; therefore the natural question that arises is: how does this tension govern the shape and length scale transitions of the beads? We explore these questions by conducting two sets of simulations. For the first set of simulations, we varied the edge membrane tension (λ_0) and the protein density (σ_0) in a range ($\lambda_0 = 0.004 - 0.064$ pN/nm and $\sigma_0 = 0 - 3.75 \times 10^{-4}$ nm^{-2}) assuming that $\kappa_{\text{ratio}} = 2$ (Fig. 4.6B). We observed that high edge tension shifted the transition of ellipsoidal to cylindrical and unduloid-shaped beads to the large protein densities while the shape transition of the beads is still governed by the ratio of the two induced length scales l_σ and l_κ (Fig. 4.6B). For the second set of simulations, we fixed the protein density ($\sigma_0 = 6 \times 10^{-5}$ nm^{-2}) and varied the edge tension (λ_0) and the rigidity ratio (κ_{ratio}) between 0.004- 0.064 pN/nm and 2-11 respectively (Fig. 4.6C). As our results show, in this case, all three possible shapes of beads are only formed at high membrane tension and the ratio of the induced length scale govern the morphology of the bead (Fig. 4.6C). In general, we can see that by increasing the edge membrane tension either at a constant protein density or a fixed rigidity ratio, we decrease the value of the induced length scale by the rigid domain ($\sqrt{\kappa_{\text{protein}}/\lambda}$), and therefore we move from the cylindrical and unduloid-shaped beads to the ellipsoidal bead-shaped region of the phase space.

Another aspect of the heterogeneous membrane properties is the variation of the Gaussian modulus between the protein-enriched domain and the bare membrane [260]. Specifically, in the unduloid-shape bead that the Gaussian curvature along the bead changes the sign from positive to negative, the heterogeneity in the Gaussian modulus can play an important role. To explore how the variation in the Gaussian modulus can affect the morphology of the unduloid-shape bead, we repeated the simulation in Fig. 4.5A ($\sigma_0 = 1.85 \times 10^{-4}$ nm^{-2} and $\kappa_{\text{ratio}} = 11$) varying the relative Gaussian modulus of the protein-enriched domain between $-20 < \Delta\kappa_G < 20$ (Fig. B.8). As our results show, the variation in the Gaussian modulus has no observable effect on the

morphology of the bead and only changes the size of the bead; increasing the Gaussian modulus of the protein-enriched domain respect to the bare membrane decreases the radius of the bead, whereas decreasing it makes the bead larger (Fig. B.8).

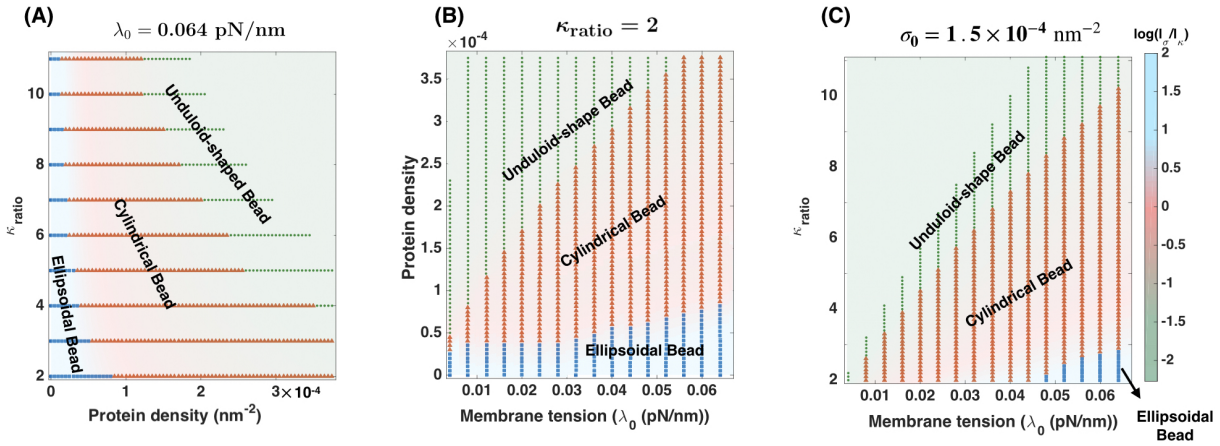

Figure 4.6: Bead morphology depends on the protein density (σ_0), the bending rigidity ratio of the protein-enriched domain compared to the lipid membrane (κ_{ratio}), and the edge membrane tension λ_0. (A) Phase diagram for bending rigidity ratio versus the number of proteins per unit area, $\lambda_0 = 0.064$ pN/nm. The background of the phase diagram shows the log of the ratio of the two induced length scales ($\frac{l_\sigma}{l_\kappa}$). The three different bead shapes can be distinguished by the dominant length scale: (*i*) ellipsoidal beads when $\log(\frac{l_\sigma}{l_\kappa}) > 0$ (blue domain), (*ii*) cylindrical beads when $\log(\frac{l_\sigma}{l_\kappa}) \sim 0$ (pink domain), and (*iii*) unduloid-shaped beads when $\log(\frac{l_\sigma}{l_\kappa}) < 0$ (green domain). (B) The protein density versus the edge membrane tension λ_0 phase diagram for $\kappa_{ratio} = 2$. The background of the phase diagram of the log of the $\frac{l_\sigma}{l_\kappa}$ for a range of the membrane tension and the protein density. (C) The bending rigidity ratio versus the edge membrane tension λ_0 phase diagram for $\sigma_0 = 1.5 \times 10^{-4}$ nm^{-2}. The background of the phase diagram of the log of the $\frac{l_\sigma}{l_\kappa}$ for a range of the membrane tension and the bending rigidity ratio. The colors in panels (B) and (C) represent the same bead shapes as panel (A).

4.3.5 Interaction between multiple beads along a nanotube

Often, multiple beads are observed along a membrane nanotube, suggesting that multiple domains of heterogeneity exist along the nanotube [324, 326, 328, 347, 348, 375, 376]. (Fig. 4.1A). These observations lead to the following question: how does the profile of these beaded strings depend on the different length scales associated with beaded nanotubes? Previous studies have

shown that membrane curvature and tension can control the interaction between two domains of membrane heterogeneities [172, 377, 378]. Here, in order to answer this question from the perspective of beading morphology of membrane nanotubes, we conducted simulations for the formation of two beads along the membrane by prescribing two domains of heterogeneity for three cases: (i) varying membrane rigidity alone in each domain in the absence of protein-induced spontaneous curvature, (ii) varying protein density for uniform rigidity, and (iii) varying protein density for domains with higher bending rigidity respect to the bare lipid membrane.

First, we found when there are two regions of proteins far from each other with an end-to-end distance given by $L_{separation} = 4\ \mu$m (Fig. 4.7A, top), two independent beads form (Fig. 4.7A bottom). The size and the shape of the beads are independent of the number of domains as long as the domains are far away from each other (Fig. B.9). Having established that the regions of heterogeneity are independent when they are far from each other, we next asked under what conditions might these beads interact with one another? In other words, what length scales govern the stability of multiple beads knowing that there is a certain relaxation length between the beads and the cylinder? To answer this question, we repeated the simulation of two beads (Fig. 4.4), and varying the rigidity ratio (κ_{ratio}) and end-to-end distance ($L_{separation}$) between 1-11 and $0-4\ \mu$m respectively (Fig. 4.7B). Based upon the results, we constructed a phase diagram separating the two possible morphologies; (*i*) two distinct beads represented by the color blue, and (*ii*) one single bead denoted by the color red (Fig. 4.7B).

We found that when the distance between two rigid domains is shorter than $2r_b$, there is a smooth transition from two beads connected by a string to a single bead (purple line in Fig. 4.7B). We observe that the smooth transition in the number of beads is accompanied by the shape transition from an unduloid-shaped bead to a large ellipsoidal bead (Fig. 4.7C). This suggests that at close distances ($L_{separation} < 2r_b$), the energy minimum (Eq. 4.4) of the nanotube with rigid protein domains is attained for a single large bead rather than for two beads connected by a

string. As expected, with increasing κ_{ratio}, the larger beads form along the nanotube (Fig. 4.4) and therefore the transition from two beads to one bead occurs even when the beads are far from each other (Fig. 4.7B). For example, for a very rigid protein domain ($\kappa_{ratio} = 11$), the transition to one bead happens when $L_{separation} < 0.8\ \mu$m (Fig. 4.7B). However, for the case that $\kappa_{ratio} = 4$, the single bead does not form until the centers of two beads almost overlap (Fig. 4.7B).

Interestingly, when we varied the separation distance between the beads for a range of protein densities (Fig.4.7A), we found a sharp transition from two beads to one bead accompanied by a snap-through instability (Fig. 4.7D, E, and F). Indeed, for small protein densities, when the separation between the two beads is shorter than $2r_b$ (purple line in Fig. 4.7E), the nanotube appears to have one large bead, while the transition from two beads to one bead is continuous indicating that there is no energy barrier or discontinuity to move from one state to another (Fig. 4.7D and black dotted line in Fig. 4.7E). However, as the protein density increases, larger beads form along the nanotube and we found the emergence of a snap-through instability for small separation distance (Fig. 4.7E) corresponding to bead shapes that show a distinct transition from two ellipsoids to a flower-shaped bead to a large ellipsoidal bead (green dashed line in Fig. 4.7E and Fig. 4.7F). This means that the landscape between two beads and one bead at high protein densities is governed by a large energy discontinuity, and therefore there is no stable solution for the membrane nanotube in the transition stage from two beads to one bead. The existence of this type of elastic energy discontinuity is also observed between two neighboring embedded nanoparticles in membranes [379–381].

Finally, when we repeated these calculations for a rigid protein domain such as $\kappa_{ratio} = 4$ (Fig. 4.7G, H, I), we found that the distance and protein density still govern the energy and stability landscape, but the transition point, where the snap-through instability occurs, is shifted towards the lower protein densities, with no change in bead shapes (Fig. 4.7G, H, I). This is because for rigid protein domains, larger beads form along the nanotube compared to the uniform

bending rigidity in Figs. 4.7D and G. Therefore, the snap-through transition from two beads to one bead for the rigid protein domain occurs in smaller values of the protein density (Fig. 4.7H).

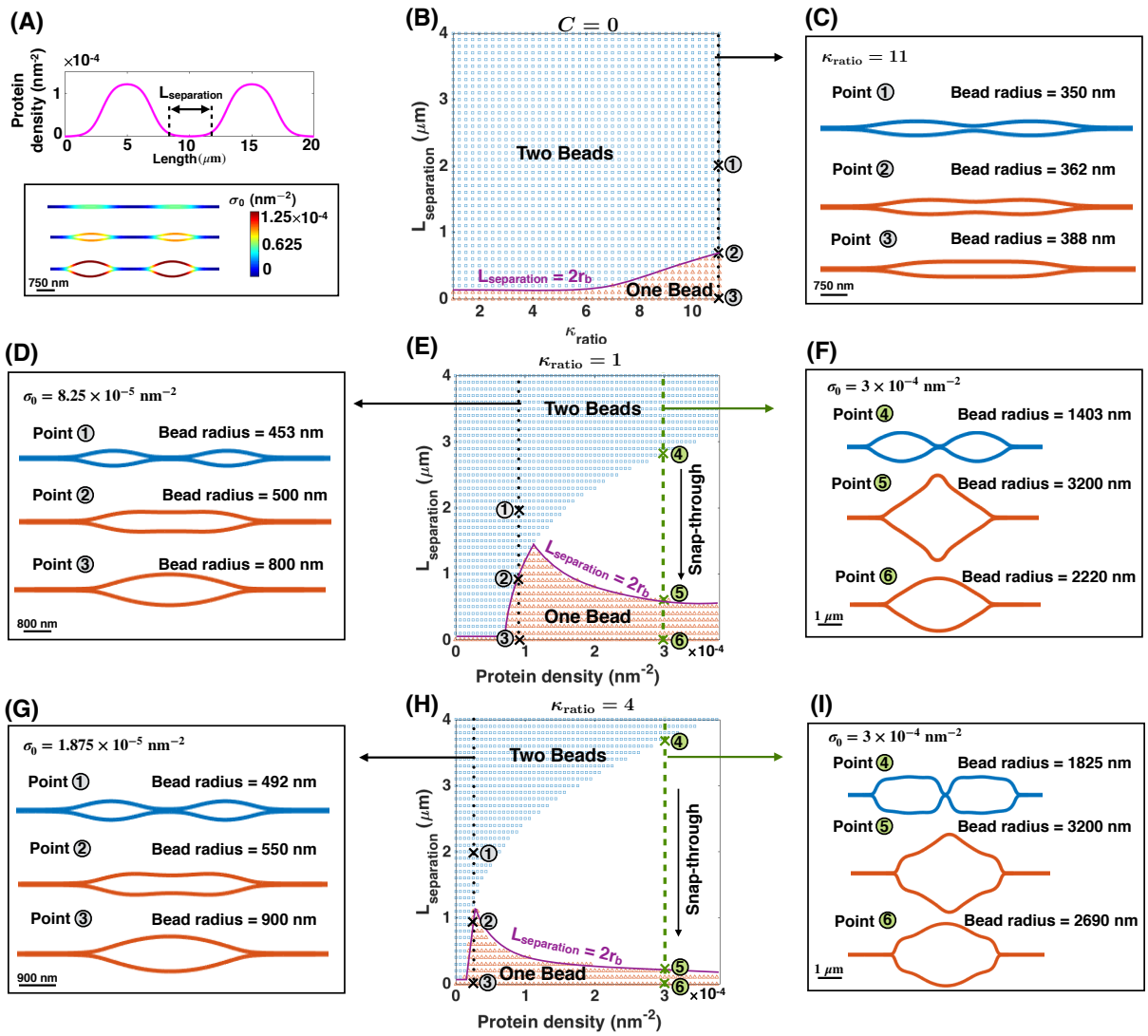

Figure 4.7: Multiple beads along a nanotube. (A, top) Protein density distribution with two domains of protein accumulation. (A, bottom) Two beads form corresponding to each protein-enriched domain, $\lambda_0 = 0.064$ pN/nm. (B) The distance between two beads versus the bending rigidity ratio phase diagram with $C = 0$ and $\sigma_0 = 1.25 \times 10^{-4}$ nm^{-2}. There are two possible shapes, (*i*) two separated beads denoted with the color blue, and (*ii*) one single bead marked by the color red. (C) Membrane profiles for the marked points along the dotted black line in panel (B). (D) Membrane profiles for the black dotted line in panel (E) show the smooth evolution of membrane shape from two beads to one bead. (E) Phase diagram for the distance between two beads versus the protein density. (F) Membrane profiles show the snap-through transition from two kissing beads to one large bead at $\sigma_0 = 3 \times 10^{-4}$ nm^{-2} corresponding to the marked points along the green dashed line in panel (E). (G) Membrane profiles for the black dotted line in panel (H) show the smooth evolution of membrane shape from two beads to one bead. (H) Phase diagram for the distance between two beads versus the protein density. (I) Membrane profiles show the snap-through transition from two kissing beads to one large bead for the green dashed line in panel (H).

4.4 Discussion

Tunneling nanotubes are membranous projections between cells [310, 311, 326]. Much of the biophysics associated with these dynamic structures are only beginning to be explored but it is becoming increasingly clear that the cellular membrane and membrane-protein interactions play a critical role in maintaining these cellular architectures [324, 328, 363, 372, 382]. In this thesis, we explored how the energy landscape and the role of heterogeneity in the membrane either due to protein aggregation or material properties alter the architecture of nanotubes. Our results can be summarized as follows – membrane heterogeneity due to either protein-induced spontaneous curvature (Fig. 4.3) or membrane rigidity (Fig. 4.4) can result in the formation of bead-like structures along a nanotube. Additionally, the interaction between these two modes of heterogeneity can lead to the formation of beads with distinct shapes while the transitions between these shapes from ellipsoidal to cylindrical to unduloid-shaped beads are consequences of energy minimization and competing length scales in the system (Figs. 4.5 and 4.6). Finally, we found that there is an energy discontinuity that impedes any fusion of two beads which suggests the formation of multiple stable beads along the nanotube due to membrane heterogeneity (Fig.4.7).

Interaction between membrane inclusions has been studied extensively [383–386]. The membrane inclusions may attract or repel each other depending on the local membrane deformation due to the induced spontaneous curvature or the hydrophobic mismatch of the membrane inclusion [384, 387]. For instance, Gil et al. showed that the interaction between two adjacent inclusions is attractive if both inclusions change the membrane thickness in the same manner [388]. Phillips et al. [198] and later Simunovic et al. [389] demonstrated that there is an attractive force between inclusions with opposite intrinsic curvature. Even in the case of the nano particles, it is suggested that the long-range Casimir-like forces in the fluctuating membrane can induce attractive forces between two neighboring particles [390]. Despite the rich literature on the interaction of the membrane inclusions, the shape of membrane nanotubes resulting from the interplay

between a spatially varying membrane rigidity and protein-induced spontaneous curvature has not been previously explored. Our findings should be a motivation for future studies to investigate the interaction between two regions of heterogeneity, particularly for estimating the effective force between two beads and how membrane tension, lipid flow, and other force generating mechanisms can regulate this force between two domains of heterogeneity.

Various recent studies have demonstrated that inducing a constant homogeneous membrane tension along a cylindrical membrane can also lead to a dramatic shape transformation into a modulated structure of a string of pearls [290, 334–338]. However, the tension of lipid membranes can change not only globally but also locally due to the absorption of proteins, nanoparticles, inclusions, or actomyosin interactions with the membrane [153, 159–161]. Here, we show that local variation of the membrane tension corresponding to the membrane heterogeneities in the beaded nanotubes (Figs. B.3 and B.4) may play a role in governing the morphology of the membrane nanotubes. In addition to the membrane nanotubes, the beaded morphologies have been observed on different membrane structures which make direct connect with the extracellular matrix [391, 392]. The membrane mechanics of these "beaded apotopodia" is still a matter of the debate [393]. However, we anticipate that an extension of our membrane mechanical model can be a powerful tool to understand the physics behind the formation of these unusual beaded structures.

Our simulations lead to the following predictions. Tension at the edge of the nanotube not only governs the nanotube radius but also its response to heterogeneity. Therefore, manipulating cell tension and evaluating how it affects the morphology of the nanotube will provide information on how the tensional homeostasis of cells affects the membrane nanotubes. Additionally, we found that there is an energy discontinuity that governs the landscape of the transition from two beads to one bead. This energy discontinuity, governed by a snap-through instability, suggests that the fusion of two beads depends on the membrane composition and its material properties

such that under high protein density or high rigidity conditions, there is a large crossover energy discontinuity for fusion. These predictions can be extended to multiple beads as well.

In the broader context of interactions between the bilayer membrane and curvature inducing moieties (proteins and cytoskeletal filaments), Shlomovitz and Gov showed that the coupling between membrane shapes and membrane-bound FtsZ filaments can induce high-density FtsZ rings along a cylindrical membrane [376]. With no entropic effects, these rings interact with each other, can coalesce and form larger rings depending on the membrane tension and separation distances. They predict that when the separation between two rings is larger than $2\pi R$ (R is the radius of the cylinder), membrane shape undulations around each ring act as an energy barrier to stabilize the separate rings and preventing coalescence [376]. These results suggest that the observed energy discontinuity in our model and Shlomovitz and Gov paper could have a similar origin since both responses appear due to the elastic behavior of the lipid membranes in interactions with local curvature inducing moieties.

Recent experiments on the fission of yeast have demonstrated that the formed rings along the tubular membranes by the actin-myosin contractile force interact and fuse when the natural width of the ring is much smaller than their separation distance [376, 394]. This is also consistent with our simulation results, as we found that the transition from two beads to one bead occurs when the distance between two beads is shorter than the diameter of the beads ($L_{separation} < 2r_b$) (Fig. 4.7). Ultimately, to explore the instability that we observed in the interaction of two beads, futures studies will be needed to focus on detailed non-linear stability analysis for large deformations including tension and shape coupling and without the restriction of small deformations and linearization [186, 376].

Although our model has provided several fundamental insights into the role of membrane composition in nanotube morphology, we have made simplifying assumptions that may need to be revisited as more experimental evidence is gathered regarding these structures. Additionally,

the dynamics of membrane-protein diffusion and what could be the underlying mechanisms that govern protein aggregation along the nanotube as suggested in our model are not yet fully explored. While there is evidence for the strong curvature-mediated feedback for the protein aggregation [189], it is possible that feedback between proteins in the lumen of the nanotube and biochemical signaling can lead to the formation of protein microdomains. For example, it is known that phase separation between two main components of the membrane – clusters of sphingolipids and cholesterol molecules – can result in the formation of lipid rafts [369, 395].

In addition, the role of the cytoskeleton (actin and microtubule filaments) and motor protein transport along the nanotube is known to be an important contributor [310, 311, 396], but a correlation with the beading morphology is yet to be established. Also, there are only a handful of direct experimental observations of membrane heterogeneities along nanotubes in cells [346]. And finally, the role of the active transport versus the flow of cytosolic components in governing the stability of these nanotubes is not captured by our model and remains an active focus of our research and modeling efforts.

4.5 Acknowledgements

I would like to acknowledge my co-authors Prof. Ben Ovryn and Prof. Padmini Rangamani. I would also like to thank Dr. Morgan Chabanon and Miriam Bell for their feedback on the study.

Chapter 5

Biconcave morphology of Red Blood Cells (RBCs)

5.1 Introduction

Human red blood cells (RBCs) have a biconcave disk shape, with a thin central dimple region surrounded by a thicker rim [397, 398] (Fig. 5.1). This shape enables efficient gas and ion exchange and increases RBC deformability and resilience in the circulation [79, 80, 399]. Deviations from biconcavity interfere with RBC function in diseases such as congenital hemolytic anemias [79, 80, 400], sickle cell disease [401], and malaria [402, 403]. Due to its lack of transcellular cytoskeleton or internal organelles, RBC shape depends exclusively on the plasma membrane, and has long served as a simple model for membrane structure and function [81]. The RBC membrane is supported by the membrane skeleton, a two-dimensional network of short F-actins interconnected by long, flexible spectrin molecules [81, 404, 405], which bind to transmembrane proteins to maintain membrane tension, curvature, and mechanical properties of

the RBC [79–81, 406, 407].

Historically, the biconcave disk shape of the RBC has been modeled as a thin elastic shell using the Helfrich-Canham energy model, treating the RBC as a lipid bilayer whose properties are spatially homogeneous along the entire RBC membrane [128, 133]. This model, a classic in the field of membrane mechanics, was able to explain the observed RBC shape as a family of solutions for a given area and volume [128, 133, 408]. The calculated shapes corresponding to the minimal Helfrich-Canham local bending energy are scale invariant for zero spontaneous curvature [408]. Subsequent extensions of this model include consideration of reduced volume [128, 133], spontaneous curvature [409], area differences between the two leaflets of the bilayer [162,410], and lateral distribution of membrane constituents [176,183,365,411–414]. A recent theoretical study predicted that the coupling between inhomogeneously distributed curved membrane protein inclusions and active cytoskeletal forces can govern the morphology of the membrane vesicles [189, 415]. Additional refinements have modeled the membrane as a two-component system composed of an incompressible lipid bilayer associated with an elastic spectrin-actin network uniformly distributed along the membrane [169, 410, 416–419].

To date, computational models to account for the biconcave disk shape of the RBC have not considered the contribution of actomyosin contractility even though RBCs contain NMII. NMIIA is the predominantly expressed isoform and has biochemical properties similar to NMIIs in other cell types [420–422]. Due to its low abundance, a potential role for NMIIA in RBC shape had been largely ignored by experimental biologists. However, we showed recently in Smith et al. [82] that RBC NMIIA forms bipolar filaments that bind to the membrane skeleton F-actin via their motor domains to control RBC membrane tension, biconcave disk shape and deformability [82] (Fig. 5.1A). Specifically, we showed that blebbistatin inhibition of NMIIA motor activity in RBCs leads to loss of the biconcavity and the formation of elongated shapes, indicating an important role for NMIIA-generated forces in maintaining RBC biconcave disk

shape and deformability [82]. Notably, the NMIIA filaments are sparsely distributed along the RBC membrane ($\sim$0.5 filaments per square micrometer), and thus would be expected to apply localized forces to the membrane [82]. However, it remains unclear how the magnitude and distribution of NMII-mediated localized forces could provide a mechanism to influence membrane curvature with respect to the morphology of RBCs.

In this thesis, motivated by our recent experimental observations [82], we investigated the role of local forces in modulating the shape of the RBC. We revisited the classical Helfrich-Canham model and modified it to account for localized forces representing the NMIIA-generated forces on the plasma membrane. By adding this extra degree of freedom to the classical Helfrich-Canham model, we sought to focus on how forces applied to the membrane, rather than spontaneous curvature or reduced volume, can result in the shapes that are comparable to the experimentally observed RBC shapes. To determine the set of force distributions that most closely reproduce experimentally observed RBC shapes, we varied the applied force heterogeneously along the membrane (Fig. 5.1B).

Model Development

The RBC membrane is a thin elastic material that can bend but resists stretching. This feature enables the RBC to deform and adjust its shape in response to applied stresses. Here, we outline the assumptions underlying the development of the model and the associated governing equations of our model.

5.1.1 Assumptions

- We consider that the radii of membrane curvatures are much larger than the thickness of the bilayer [409]. Therefore, we treat the lipid bilayer as a thin elastic shell and model the

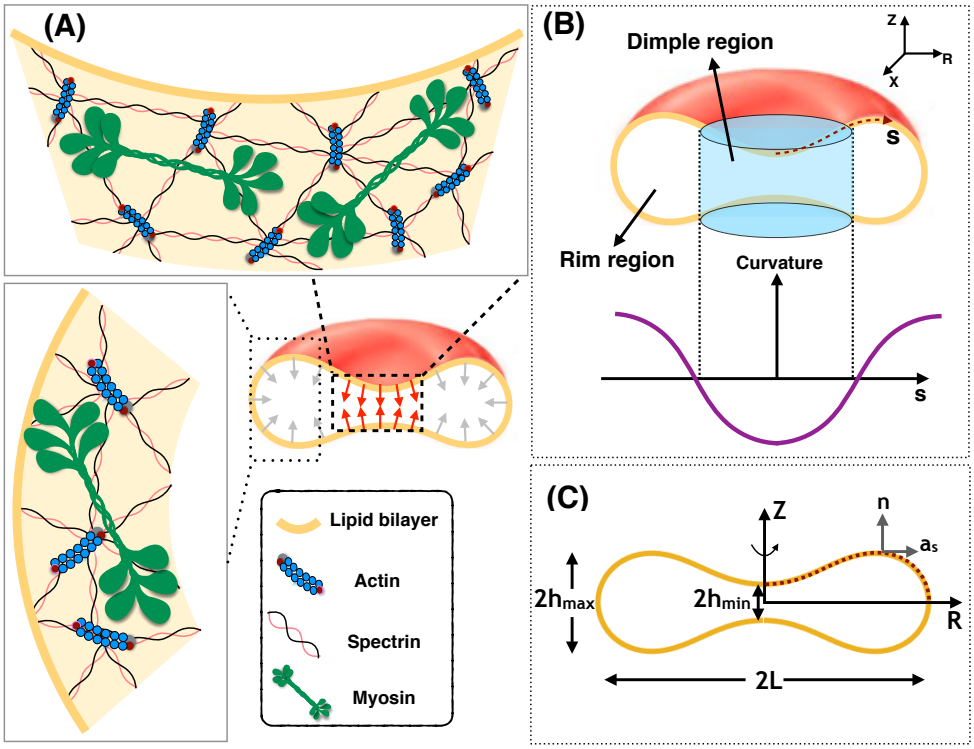

Figure 5.1: Interaction of the membrane and skeleton controls the shape of the RBC. (A) Schematic depiction of the biconcave disk shape of an RBC plasma membrane and the membrane skeleton underneath. The effect of NMIIA filaments (shown in green) is modeled by local forces applied to the plasma membrane (red and gray arrows). (B) Two distinct regions are identified in a biconcave RBC – the dimple and the rim regions. In the dimple region (blue cylinder), each RZ cross-section of the shape has a negative curvature along its arclength. In contrast, at the rim, the curvature of each RZ section is positive along the arclength. (C) The geometry of a simulated RBC in axisymmetric coordinates and the three characteristic length scales that represent the biconcave shape of the RBC. $2h_{min}$ is the minimum height at the dimple, $2h_{max}$ is the maximum height at the rim, and 2L denotes the cell's maximum diameter. The dotted red curve shows the computational domain for our mechanical model. $\mathbf{n}$ is the unit normal vector to the membrane surface and $\mathbf{a}_s$ is the unit tangent vector in the direction of arclength.

bending energy of the membrane using the Helfrich–Canham energy, which depends only on the local curvatures of the surface and compositional heterogeneities [128, 133].

- Due to the high stretching modulus of lipid bilayers, we assume that the membrane is locally incompressible [352]. We use a Lagrange multiplier to implement this constraint [150]. We refer the reader to [150] for a detailed interpretation of this Lagrange multiplier as

membrane tension.

- We assume that the RBC is at mechanical equilibrium at all times, allowing us to neglect inertia [35, 423, 424]. This assumption is consistent with the experimentally observed shapes for the resting RBCs in both vivo and vitro [425, 426].

- We assume that the total surface area of the RBC membrane is constant (135 μm^2) [427, 428].

- For simplicity in the numerical simulations, we assume that the RBC is rotationally symmetric and also has a reflection symmetry with respect to the Z = 0 plane (see Fig. 5.1C) [128,165,427,429]. This assumption reduces the computational cost of the simulation to simply calculating the shape of the curve shown by the red dotted line in Fig. 5.1C.

5.1.2 Membrane mechanics

In mechanical equilibrium, the shape of the membrane in response to an applied force can be obtained as a result of the minimization of the membrane bending energy and the work done by the applied forces by the cytoskeleton. In this case, the total energy is given by [136, 343]

$$\underbrace{E}_{\substack{\text{Total}\\ \text{energy}}} = \underbrace{E_b}_{\substack{\text{Bending}\\ \text{energy}}} - \underbrace{E_f}_{\substack{\text{Work done}\\ \text{by forces}}} , \tag{5.1}$$

where E is the total energy of the system, E_b is the bending energy and E_f is the work done by

the applied forces given by

$$E_b = \int_\omega (W(H,K;\theta^\alpha) + \lambda(\theta^\alpha))da - pV, \tag{5.2a}$$

$$E_f = \int_\omega \mathbf{F}(\theta^\alpha) \cdot (\mathbf{r} - \mathbf{r}_0)da, \tag{5.2b}$$

where ω is the total surface area of the membrane, W is the energy density per unit area, θ^α denotes the surface coordinate where $\alpha \in \{1,2\}$, H is the mean curvature, K is the Gaussian curvature, λ is the membrane tension (also see assumption 2), p is the pressure difference across the membrane, V is the enclosed volume, $\mathbf{F}$ is the force density per unit area representing the applied force density to the membrane surface by the NMIIA motor proteins, $\mathbf{r}$ is the position vector in the current configuration, and $\mathbf{r}_0$ is the position vector in the reference configuration. The bending energy of the membrane is modeled using the Helfrich-Canham energy, defined by [5, 128, 133, 150],

$$W(H,K;\theta^\alpha) = \kappa H(\theta^\alpha)^2 + \kappa_G K(\theta^\alpha), \tag{5.3}$$

κ and κ_G are constants representing the bending and Gaussian moduli respectively [430]. To minimize the bending energy (Eq. 5.1) and obtain the RBC shapes from simulations under the action of local forces, we used the variational approach which yields the so-called "shape equation" [152],

$$\underbrace{\kappa\Delta[H] + 2\kappa H(H^2 - K)}_{\text{Elastic effects}} = \underbrace{p + 2\lambda H}_{\text{Capillary effects}} + \underbrace{\mathbf{F}\cdot\mathbf{n}}_{\substack{\text{Force due} \\ \text{to NMIIA}}}, \tag{5.4}$$

where Δ is the is the surface Laplacian (also known as the Laplace-Beltrami operator). The incompressibility condition for the lipid membrane results in the spatial variation of membrane tension given by [8, 152]

$$\underbrace{\lambda'}_{\substack{\text{Membrane tension} \\ \text{variation}}} = - \underbrace{\mathbf{F} \cdot \mathbf{a}_s}_{\substack{\text{Force induced} \\ \text{to variation}}} , \tag{5.5}$$

where $(.)'$ is the derivative with respect to the arclength. The shape equation (Eq. 5.4) along with the incompressibility condition (Eq. 5.5) represents the relationship between the forces applied by NMIIA motor proteins and the resulting shape of RBCs. A complete derivation of the governing equations of the force balance, the notations used, and the non-dimensionalization procedure are presented in Appendix C.

5.1.3 Parameterization of RBC biconcave morphology and shape error estimation

The geometry of human RBCs has been studied extensively using a variety of different methods such as light microscopy [431, 432], interference holography [433, 434], resistive pulse spectroscopy [435], micropipette aspiration [436, 437], and light scattering [438, 439]. In Fig. 5.2A, we summarize the reported values for the RBC geometrical parameters from the literature [431, 433, 436, 439–441] in terms of the three characteristic lengths (h_{min}, h_{max} and L) (Fig. 5.1C), the volume (V), the surface area (A), and the sphericity index (SI).

Several parametric models have been proposed to describe the biconcave morphology of the RBC [433, 434, 442–446]. Funaki proposed a Cassini oval model with two coefficients to represent the RBC geometry [442]. Kuchel et al. [443] and later Yurkin [444] modified the

Cassini oval model to implicit equations with three and four coefficients, respectively. Borovoi et al. introduced a function in spherical coordinates to characterize the RBC morphology [445]. The most realistic model was proposed by Evans and Fung [433], where they first obtained images from 50 human RBC samples using light microscopy and then fitted a parametric equation to the RZ cross-sectional shape of the RBCs (Fig. 5.1C) using statistical analysis. The Evans and Fung proposed function is given by

$$Z(R) = \pm 0.5\sqrt{1-(\frac{2R}{L})^2}\Big(0.81+7.83(\frac{2R}{L})^2-4.39(\frac{2R}{L})^4\Big), \tag{5.6}$$

where R is the radius from the axis of rotation and is the height from the base plane. In Fig. 5.2B, we plotted the different proposed parametric models for the biconcave shape of an RBC. We observed that for the fixed height of the dimple (h_{min}), height of the rim (h_{max}), and the maximum diameter (L), all models generate similar shapes, but with slight differences. In this thesis, we used the Evans and Fung parametric equation in Eq. 5.6 as the reference data for the experimental shape of an RBC, because Eq. 5.6 was developed based on the direct experimental measurement and fit well with the observed RBC shapes [447, 448].

To quantify the deviation between simulated geometries obtained from our mechanical model and the parametric shape equation for the RBC (Eq. 5.6), we define three error metrics – ε_{hmin}, ε_{hmax} and ε_{L} as follows

$$\begin{aligned}
\varepsilon_{hmax} &= \frac{|h_{max,par}-h_{max,sim}|}{L_{par}} = \frac{|\Delta h_{max}}{L_{par}} \\
\varepsilon_{hmin} &= \frac{|h_{min,par}-h_{min,sim}|}{L_{par}} = \frac{|\Delta h_{min}}{L_{par}} \\
\varepsilon_{L} &= \frac{|L_{par}-L_{sim}|}{L_{par}} = \frac{|\Delta L}{L_{par}},
\end{aligned} \tag{5.7}$$

where $()_{\text{par}}$ is the experimentally measured length scale fitted to the parametric equations (Eq. 5.6) and $()_{\text{sim}}$ is the length scale obtained from the numerical simulation (Eqs. 5.4 and 5.5). The total error ($\varepsilon_{\text{total}}$) in the shape of the simulated RBCs is then calculated by the root mean square between every two mapped points in the parametric shape of an RBC and the simulated geometries (Fig. 5.2C) given by

$$\varepsilon_{\text{total}} = \frac{\sqrt{\frac{1}{N}\left(\sum_{i=1}^{i=N}(Z_{\text{i,sim}} - Z_{\text{i,par}})^{+}(R_{\text{i,sim}} - R_{\text{i,par}})^{2}\right)}}{\text{L}_{\text{par}}}, \tag{5.8}$$

where N is the total number of nodes across the RBC shapes, i is the index node, $Z_{\text{i,sim}}$ and $Z_{\text{i,par}}$ are the height of the simulated and the parametric (Eq. 5.6) RBC shape at index i, respectively. $R_{\text{i,sim}}$ is the radius of the simulated shape at index i , and $R_{\text{i,par}}$ is the radius of the RBC parametric shape (Eq. 5.6) at index i.

While Eq. 5.8 represents the error in the simulated shapes compared to the RBC parametric shape, it does not capture measurement errors as Eq. 5.6 was developed based on the average dimensions of experimentally observed RBCs. However, there are standard deviations in the measured dimensions as reported by Evans and Fung [433] and the resolution of imaging methods introduces additional uncertainties. Here, to account for these uncertainties, we assume that the given parametric equation by Evans and Fung [433] can be written as

$$Z(R) = Z_{\text{mean}}(R) + Z_{\text{error}}(R), \tag{5.9}$$

where $Z_{\text{mean}}(R)$ is the given function in Eq. 5.6 and we define $Z_{\text{error}}(R)$ as the fitting error of the Evans and Fung parametric equation to the actual shape of an RBC. Here, we assume that is approximately 10% of $Z_{\text{mean}}(R)$ to represent the variance of RBC dimensions.

5.1.4 Numerical simulation

Simplifying the shape equation (Eqs. 5.4 and 5.5) for a rotationally symmetric RBC gives us a set of first order differential equations (Eq. C.11). In order to obtain the RBC shapes from simulations and determine the role of NMIIA-generated forces in maintaining the biconcave morphology, we need to solve the coupled differential equations (Eq. C.11) for the defined boundary conditions (Eq. C.12). Here, we used the commercially available finite element solver COMSOL MULTIPHYSICS 5.3a to solve the governing differential equations (Eqs. C.11 and C.12). In all our simulations, the transmembrane pressure is set to zero (p =0).

(A)

Reference	2L (μm)	2h$_{min}$ (μm)	2h$_{max}$ (μm)	V (μm^3)	A (μm^2)	SI $(4.83(V)^{2/3}/A)$
Canham and Burton	8.07 ± 0.55			107 ± 18.8	138 ± 17.4	0.783
Evans and Fung	7.82 ± 0.62	0.81 ± 0.35	2.58 ± 0.27	94 ± 14	135 ± 17	0.742
Linderkamp et al.	7.9 ± 0.4	1.84 ± 0.13		90.5 ± 4.4	137 ± 6.7	
Tarasov et al.				87 ± 20	135 ± 28	
Ergul et al.	7.7			80.9		
Das et al.	9.52 ± 0.56					

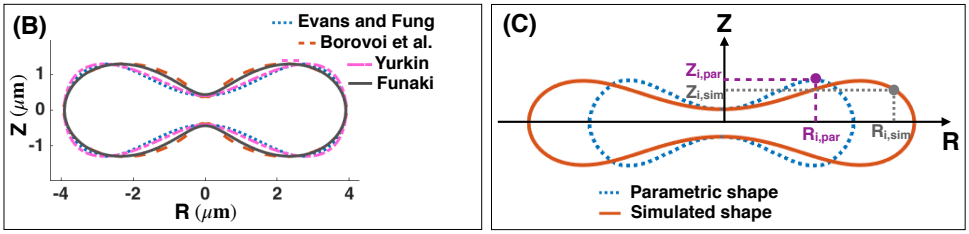

Figure 5.2: Dimensions of healthy human RBC from the literature [431, 433, 436, 439–441]. (B) Comparison between the proposed parametric models describing the biconcave morphology of an RBC. There is a close match between the four models for the fixed minimum height of the dimple, maximum height of the rim, and the maximum diameter (C) Discretization scheme of the parametric shape of an RBC (Eq. 5.6) (dotted blue line) and the simulated geometry obtained from our mechanical model (Eqs. 5.4 and 5.5) (solid red line). Each experimental and simulated shape is discretized into nodes where indicates the node index. These nodes are used to compute the total error in the simulated RBC geometry (Eq. 5.8).

5.2 Results

5.2.1 Uniform distribution of force density across the membrane surface is not sufficient to recover the biconcave shape of an RBC

Modeling studies of RBC shapes have been based on the assumption that the RBC membrane and skeleton are spatially homogeneous [79–81, 430]. Therefore, we first performed simulations with a uniform pulling force density ($F_{uniform}$) applied normally on the membrane surface (Figs. 5.3A, B). This uniform pulling force density can be interpreted as a pressure difference between the inside and outside of the RBC that specifies the change in the RBC volume compared to an equivalent sphere (the reduced volume) [408, 409, 449].

To perform our simulations, we assumed that the RBC membrane area is large enough that the lateral membrane tension is negligible ($\lambda = 0$) [161, 450, 451]. We also set the bending modulus to be in the range of physiologically reported values for the RBC membrane ($\kappa = 9 \times 10^{-19}$ J) [451]. For a given value of uniform pulling force, we were able to match two out of three characteristic length scales of the simulated shapes with the parametric shape of an experimentally observed RBC (Eq. 5.6) (see Fig. 5.3B). Furthermore, we observed that for all configurations in Fig. 5.3C, the calculated uniform force density from our mechanical model is in the order of the reported pressure difference for a biconcave RBC ($F_{uniform} \sim O(1)$ pN/μm^2 [440–443], which validates our numerical results (Fig. 5.3C, bottom row).

We observed that for the large value of the pulling force density ($F_{uniform}$ = 1.92 pN/μm^2, the maximum and the minimum heights of the simulated shape match well with the parametric shape, while the maximum diameter does not (Fig. 5.3C, left). For the intermediate pulling force density ($F_{uniform}$ = 1.83 pN/μm^2, the minimum height and the maximum diameter of the simulated shape are in good agreement with the parametric shape, but the maximum height is not (Fig. 5.3C center). Finally, for the small pulling force density ($F_{uniform}$ = 1.23 pN/μm^2,

the mismatch between the simulated geometry and the parametric shape of the RBC is in the minimum height of the dimple (Fig. 5.3C right). For each value of the applied pulling force density, we calculated the error for each of the characteristic lengths (L, h_{max} or h_{min}) (Eq. 5.7) and the total error (Eq. 5.8) (Fig. 5.3C). We found that both characteristic and the total shape errors have the lowest value (ε_{hmax} 10.23% and ε_{total} 8.2%) at the intermediate uniform force density and there is only a relatively small mismatch in the maximum height (Δh_{max}) (Fig. 5.3C center). Thus, we can predict that among the three main characteristic length scales of an RBC, the maximum height of the rim ($2h_{max}$) appears to be the least critical dimension in order to minimize the shape error of the simulated geometries. It should be mentioned that for each case here, we first calculated the mean errors based on the given parametric equation (Eq. 5.6) and then we computed the error bars using Eq. 5.9.

In addition to the biconcave shape of an RBC, the volume of the RBC is one of the critical parameters that is regulated by multiple transport systems [449]. We calculated the volume of each simulated geometry (V) using Eq. C.13b (Fig. 5.3C). We found that for all three values of the uniform force densities, the volume of the simulated shapes is far from the reported experimental data in Fig. 5.2A. For the large and the intermediate force densities ($F_{uniform}$ = 1.92 pN/μm^2 and $F_{uniform}$ = 1.83 pN/μm^2, the volumes of the simulated geometries (Fig. 5.3C) are much smaller than the reported values, which range from V= 80 μm^3 to V= 107 μm^3given in Fig. 5.2A. In contrast, for the small force density ($F_{uniform}$ = 1.23 pN/μm^2, the volume of the shape obtained from the simulation is significantly larger than the experimental values (Fig. 5.3C).

5.2.2 Local force density at the RBC dimple reduces the shape error

Given that the shape mismatch and volume difference of the simulated RBC (Fig. 5.3) are relatively large compared to the experimentally measured RBC dimensions, we next asked if we could change the distribution of the non-uniform pulling force density to reduce the shape

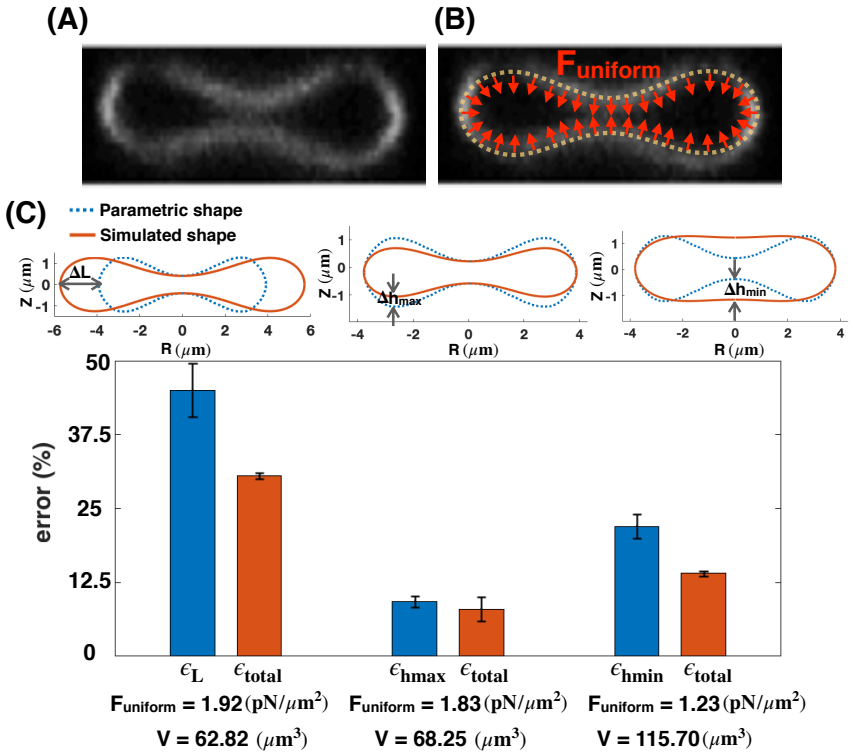

Figure 5.3: Mismatch between the parametric shape of an experimentally observed RBC (Eq. 5.6) and the shapes obtained from simulations (Eqs. C.11) with a uniform distribution of the pulling force density across the membrane surface. (A) RZ view of the center of an RBC from a confocal Z-stack of an RBC stained for the membrane marker glycophorin A. (B) Schematic of a biconcave RBC with a uniform distribution of the normal pulling force density (red arrows). Funiform represents the magnitude of the pulling force density. (C) Calculated error in the characteristic length scales (Eq. 5.7), and total shape error (Eq. 5.8) for different values of the force density. The total shape error (ε_{total}) calculated by Eq. 5.8 is minimum for $F_{uniform}$ = 1.83 pN/μm^2 when there is only a mismatch in the maximum height of the RBC morphology (center bar). For all three values of the applied uniform force densities, the calculated volume (V) is shown on the X-axis and is significantly different from the reported experimental data.

error and obtain a better agreement between the experimentally reported shapes for RBCs and our model. We conducted simulations of Eqs (C.11, C.12) but now assumed that the applied normal force per unit area is locally concentrated in the dimple region (F_{dimple}) and that there is no force along the surface of the rim (Figs. 5.4A, B). This heterogeneous force distribution along the membrane was implemented using a hyperbolic tangent function (Eq. C.24).

In Fig. 5.4C, we compare the RBC shapes obtained from the simulation with the ap-

plication of increased local pulling force density at the dimple. We found that the total error is a nonmonotonic function of F_{dimple}; as F_{dimple} increases, the total error in shape mismatch decreases and then increases again. Based on the shape of the simulated RBC, we can identify three different regimes (Fig. 5.4C). For low dimple force density ($F_{dimple} < 1.81$ pN/μm^2, the simulated geometry has a spherical shape ($h_{max} = h_{min}$) and therefore the shape error is large ($\varepsilon_{total} > 50\%$) (yellow area in Fig. 5.4C). With increasing the magnitude of dimple force density (1.81 pN/μm$^2 < F_{dimple} < 3.73$ pN/μm^2, the dimple forms biconcave shapes where $h_{max} > h_{min}$ the shape error decreases sharply (purple area in Fig. 4C). When higher levels of force are applied at the dimple ($F_{dimple} > 3.73$ pN/μm^2, the error increases because the distance between the two bilayers in the dimple becomes too narrow (kissing shapes where $h_{min} = 0$) (Fig. 5.4C). We also observed a similar nonmonotonic trend in the calculated errors for the characteristic lengths (Eq. 5.7) as a function of dimple force density (Fig. C.1).

Based on our results in Fig. 5.4C, the shape error has a minimum value of $\varepsilon_{total} \sim 5.6\%$ for the case where F_{dimple}= 3.73 pN/μm^2. This total error is less than that for all the simulated shapes determined in the case of a uniform force applied to the membrane (Fig. 5.3C). We found that the volume of the simulated RBC at F_{dimple}= 3.73 pN/μm^2 is about V = 76.78 μm^3 which is closer to the reported experimental value for the RBC volume by Evans and Fung [433]. From these results, we can conclude that there is a better agreement between the simulated shape and the parametric shape of an experimentally observed RBC when a localized force is applied at the RBC dimple compared to the case with a uniform force distribution (Fig. 5.3).

5.2.3 Non-uniform distribution of force density in the RBC dimple region versus the rim region minimizes the shape error

While localizing the force density at the dimple decreased the error and the volume mismatch in our simulated RBC shapes, NMIIA is known to be distributed throughout the

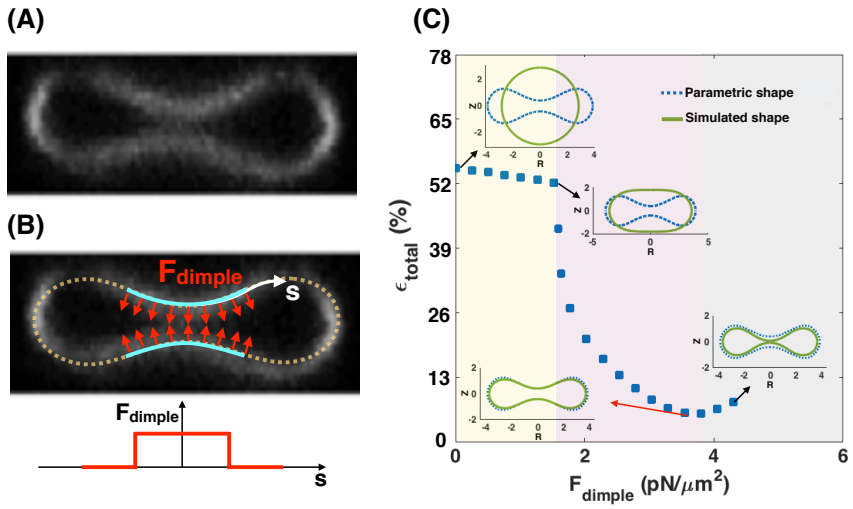

Figure 5.4: A local distribution of the pulling force density at the RBC dimple results in a better agreement between the parametric shape of an RBC (Eq. 5.6) and the shape obtained from the simulation. (A) RZ view of the center of an RBC from a confocal Z-stack of an RBC stained for the membrane marker glycophorin A. (B, upper) A schematic depicting a biconcave RBC with a local force at the dimple area (red arrows) and no force in the rim region. F_{dimple} represents the magnitude of the pulling force density in the dimple region. (B, lower) The applied force density at the dimple as a function of the arclength (Eq. C.24). (C) The simulated shape of the RBC with a local pulling force density in the dimple (solid green line) in comparison with the RBC parametric shape (dotted blue line). (C) The nonmonotonic behavior of the total error when increasing the dimple force density (F_{dimple}). Three different regimes can be identified based on the shape of the simulated RBC; (i) the spherical shapes where $h_{max} = h_{min}$ for the low F_{dimple} (yellow area), (ii) the biconcave shapes where the dimple forms ($h_{max} > h_{min}$) for the mid-range of F_{dimple} (purple area), and (iii) the kissing shapes where $h_{min} \to 0$ for large F_{dimple} (gray area). The shape error has the lowest value at F_{dimple}= 3.73 pN/μm^2 ($\varepsilon_{total} \sim 5.62\%$) when the minimum height of the dimple in the simulated geometry matches closely with the minimum height of the parametric shape. The volume of the simulated RBC at F_{dimple}= 3.73 pN/μm^2 is about 76.78 μm^3.

RBC [82]. Therefore, we next asked if the shape error can be minimized by including a normal force at the rim region in addition to the applied force at the dimple region (Fig. 5.5A). This analysis allowed us to predict the RBC shape not only in terms of absolute values of forces in the dimple and rim regions but also as a function of force per unit volume ratio in these two regions. In our model, based on the given force density per unit area in the dimple (F_{dimple}) and rim (F_{rim}) regions, we defined the ratio of forces per unit volume as

$$F_{ratio} = \frac{F_{dimple}}{F_{rim}} \times \frac{A_{dimple} V_{rim}}{A_{rim} V_{dimple}}, \tag{5.10}$$

where A_{dimple} and A_{rim} are the area of the membrane surface in the dimple and rim regions, and V_{dimple} and V_{rim} are the volume occupied by the dimple and rim regions, respectively. For a given RBC shape, the area and the volume of the dimple and rim regions can be calculated by Eq. C.13a and Eq. C.13b, respectively.

We begin our analysis with the case where the pulling force in the dimple area is larger than the pulling force in the rim area ($F_{rim} < F_{dimple}$). We implemented this distribution of force along the RBC membrane using a hyperbolic tangent function (Eq. C.24) and performed the simulations over a range of forces at the dimple and the rim regions (F_{dimple} = 3.5 - 14 pN/μm^{2}and F_{rim} = 0 - 3.5 pN/μm^2. The range of dimple force (F_{dimple}) was chosen based on our previous results (Fig. 5.4) to have a close comparison with the parametric shape and obtain biconcave shapes from simulations with hmax $>$ hmin and hmin > 0. The force along the rim (F_{rim}) was set between F_{rim} = 0 and F_{rim} = 3.5 pN/μm^{2}based on the imposed condition of $F_{ratio} < 1$ for all simulations.

The heat map in Fig. 5.5B represents the magnitude of the shape error for a given force density at the dimple and rim area. The simulations were stopped when the height at the RBC dimple approached zero, shown as white domains in the heat map (Fig. 5.5B). Based on these calculations, we found that the shape error has the lowest value ($\varepsilon_{total} \sim 4.1\%$) when v = 4.05 pN/$\mu$m^2 and F_{rim} = 0.28 pN/μm^2 (the point X on the heat map). For these specific force values, the parametric shape of the RBC (Eq. 5.6) and the shape obtained from the simulation at point X were very well-matched (Fig. 5.5B lower panel). Additionally, the volume of the simulated shape at point (X), is close (V = 85.62 μm^3 to the experimentally reported value by Evans and Fung [433].

To further understand the relationships between F_{rim} and F_{dimple} in governing the shape of the RBC, we plotted the shape error as a function of F_{dimple} for five different values of the force density at the rim section (Fig. 5.5C). We found that the shape error shows the same nonmonotonic dependence for different values of F_{rim}. By increasing the value of F_{dimple}, the shape error initially decreases by an order of magnitude and attains a relative minimum for each curve (Fig. 5.5C). Any further increase in the dimple force density results in a larger shape error (Fig. 5.5C), similar to Fig. 5.4B. As expected from Fig. 5.5B, the shape error has the lowest value on the red curve (F_{rim} = 0.28 pN/μm^2 when F_{dimple} = 4.05 pN/μm^2. Using Eq. 5.10, this set of dimple and rim forces in Fig. 5.5B is equivalent to F_{ratio} 14.27, which reflects the fact that to obtain the best match between the simulated RBC shape and the experimentally observed morphology, 14.27 times larger force per unit volume should be applied in the dimple region than the rim region.

Thus far, we have only considered the cases in which NMIIA motors were able to exert small pulling forces in the rim region. However, two other force configurations are possible; (i) NMIIA motors apply a larger force density in the rim region than the dimple area ($F_{rim} > F_{dimple}$) (Fig. C.2A), and (ii) NMIIA motors exert pushing forces in the rim region (Fig. C.3A). We found that a large pulling force in the rim region ($F_{rim} > F_{dimple}$) generates a shape resembling a peanut-shaped vesicle with a large shape error of $\varepsilon_{total} \gg 50\%$ (Fig. C.2). We also observed that applying a pushing force in the rim region (F_{rim}= 3.73 pN/μm^2 with no force in the dimple causes an error of $\varepsilon_{total} \sim 12.5\%$ (Fig. C.3B). Even adding a small pushing force in the rim region (F_{rim} = 0.53 pN/μm^2 with F_{dimple} = 3.73 pN/μm^2 increases the shape error to $\varepsilon_{total} \sim 9.7\%$ (Fig. C.3C). Our major prediction is that RBC biconcave shape depends on a heterogeneous distribution of NMIIA forces, which can be accomplished by more NMIIA motors density in the dimple compared to the rim.

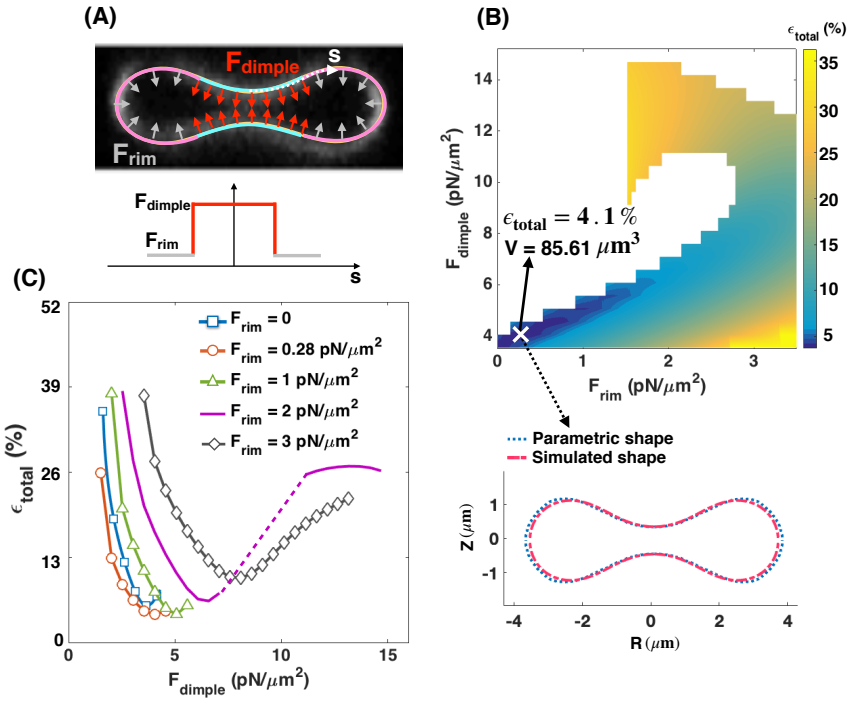

Figure 5.5: The applied force densities at the RBC dimple and rim regions regulate the shape error. (A, upper) Schematic of a biconcave RBC with a large force density (red arrows) at the dimple and a small force density (gray arrows) at the rim region. Schematic is overlaid on an RZ view of the center of an RBC from a confocal Z-stack of an RBC stained for the membrane marker glycophorin A. (A, lower) The applied force density along the membrane as a function of the arclength (Eq. C.24). (B) Heat map shows the calculated shape error (Eq. 5.8) for a range of the force densities at the dimple (F_{dimple}) and rim (F_{rim}) regions. We stopped the simulations when the height at the dimple tends to zero ($h_{min} \to 0$). The marked point X shows the case that has the lowest value of the error in the heat map at $F_{dimple} = 4.05$ pN/μm^2 and $F_{rim} = 0.28$ pN/μm^2 ($\varepsilon_{total} \sim 4.1\%$) with V = 85.61 μm^3. A comparison between the parametric shape of an RBC (dotted blue line) and the shape obtained from the simulation at point X (dashed red line) is shown in the lower panel. (C) The shape error as a function of force density at the dimple (F_{dimple}) for five different values of the applied force density at the rim region. The dotted purple line shows a discontinuous transition in the shape error with increasing the dimple force density for $F_{rim} = 2$ pN/μm^2. Similar to Fig. 5.4B, independent of the value of F_{rim}, the total error is a nonmonotonic function of the dimple force density (F_{dimple}).

5.2.4 RBC dimple region has a higher concentration of the NMIIA puncta as compared to the rim region

Our simulations suggest that NMIIA-mediated force densities are not uniformly distributed across the RBC membrane but instead are larger in the dimple region than the rim region (Fig. 5.5). Therefore, we hypothesized that the NMIIA distribution in RBCs is also non-uniform, with more NMIIA in the dimple region than the rim region. To test this hypothesis, we localized NMIIA motor domain puncta in three-dimensional reconstructions of AiryScan confocal Z-stacks [82, 452] (Fig. 5.6A). The puncta in these images are individual NMIIA bipolar filaments, based on our previous study showing that that RBCs contain $\sim$150 NMIIA puncta/cell [82], consistent with calculations of numbers of NMIIA bipolar filaments/cell using quantitative biochemical assays [420].

We divided each RBC into dimple and rim regions based on F-actin staining at the membrane (Fig. 5.6B) and quantified the number of NMIIA motor domain puncta in each region and the volumes of each region and the whole RBC using Volocity software. The dimple region accounted for about 7.4% of the total RBC volume (based on the F-actin staining, Fig 5.6C). This value agrees with calculations of dimple volume ($\sim$7.1% of total volume) from our simulated shapes, in which we classify the dimple and rim regions based on the sign of the local mean curvature (Fig. 5.1B). The number of NMIIA puncta varies between RBCs, with 125 ± 47 puncta in the whole RBC, 113 ± 42 puncta in the rim, and 12 ± 9 puncta in the dimple (all values are mean $\pm$ SD). The dimple region contains about 9.1% of the total NMIIA motor domain puncta (Fig. 5.6D). In the dimple and rim regions as well as the whole RBC, the number of NMIIA puncta tends to increase with increasing the region or cell volume (Fig. C.5).

The number of NMIIA puncta per unit volume (μm^3 in an RBC region is likely proportional to the number of NMIIA filaments that interact with membrane skeleton F-actin to exert force on the RBC membrane. The whole RBC and the rim region have similar NMIIA puncta

densities ($1.73 \pm 0.562\ \mu m^3$ and $1.70 \pm 0.556\ \mu m^3$ respectively), while the dimple region has a $\sim$25% higher density ($2.15 \pm 0.888\ \mu m^3$ (Fig. 5.6E). Thus, the dimple region has $\sim$1.29 times higher NMIIA puncta density compared to the rim region (Fig. 5.6F).

To determine whether differences in NMIIA densities relate to the extent of RBC biconcavity, we related NMIIA density to the minimum and maximum heights of XZ slices at the center of each RBC (Fig. C.5). In both whole RBCs (Fig. S5A) and the dimple region (Fig. C.5C), RBC biconcavity increased with increasing NMIIA density, while NMIIA density in the rim region was not related to biconcavity (Fig. C.5B). These results agree with the results of our simulations, which predict that the maximum height of the rim (h_{max}) is the least critical dimension to minimize the shape error (Fig. 5.3) and furthermore, that NMIIA exerts a larger force density at the RBC dimple (Fig. 5.5). Together, our simulations and experimental data suggest that this non-uniform force distribution is required to specify RBC biconcave disk shape.

5.2.5 Effective membrane tension regulates the required force densities ratio in the RBC dimple versus the rim region

We found that for the simulated RBC shapes, the shape error is minimized when the force per unit volume applied normally in the dimple region is about 14.27 times larger than the force per unit volume applied in the rim region (F_{ratio} = 14.27), in a tensionless membrane (Fig. 5.5). However, our experimental measurements reveal that in a healthy human RBC, the dimple region has only 25% higher density of NMIIA puncta than the rim region (Fig. 5.6). If we assume that the NMIIA density is proportional to the force generation capacity, then the induced force in the dimple region should be 1.25 times larger than the rim area. Therefore, we set out to reconcile this apparent discrepancy in the predicted F_{ratio} and measured the NMIIA density ratio. Literature suggests that the membrane tension in RBCs can vary from 10^{-1} pN/nm to 10^{-4} pN/nm [430,451,453]. Here, we interpret membrane tension to be the effective contribution of the

membrane in-plane stresses and the membrane-cytoskeleton interactions [374]. We hypothesized that this in-plane tension of the RBC could play a critical role in relating the RBC shape to the NMIIA-generated force ratio in dimple and rim regions.

To investigate how this variation in membrane tension can modulate F_{ratio} and the shape error, we repeated the simulations as in Fig. 5.5 for three different effective membrane tensions: (i) low membrane tension (tension = 10^{-4} pN/nm) (Fig. 5.7A), (ii) intermediate membrane tension (tension = 10^{-3} pN/nm) (Fig. 5.7B), and (iii) high membrane tension (tension = 10^{-2} pN/nm) (Fig. 5.7C). The marker (X) in each heat map shows the point with minimum shape error for that set of simulations. To visualize the geometry of the simulated RBC at each point marked with an 'X', we plot the shapes that were obtained from simulations (solid yellow line) versus the reference experimental data (dotted blue line) [433] and also calculated the volume of the simulated geometry using Eq. C.13b.

We observe that the shape error remains almost constant ($\varepsilon_{total} \sim 3.8\%$) with increasing the membrane tension from zero to low and intermediate values (Fig. 5.7A, B). However, varying the membrane tension alters the force ratio that gives the minimum shape error as well as the volume of the simulated geometry. For example, at low tension, the minimum shape error occurs at $F_{ratio} = 4.35$ where V = 79.62 μm^3 and at intermediate tension the shape error is minimum when $F_{ratio} = 1.27$ with V = 91.37 μm^3 (Fig. 5.7A, B), close to the volume experimentally reported by Evans and Fung [433]. In the case of high membrane tension, we found that the simulated shape deviates significantly from the biconcave disk and becomes closer to a pancake with a small volume (V = 36.58 μm^3 and the error goes up noticeably to about 12 percent ($\varepsilon_{total} \sim 12.5\%$) (Fig. 5.7C).

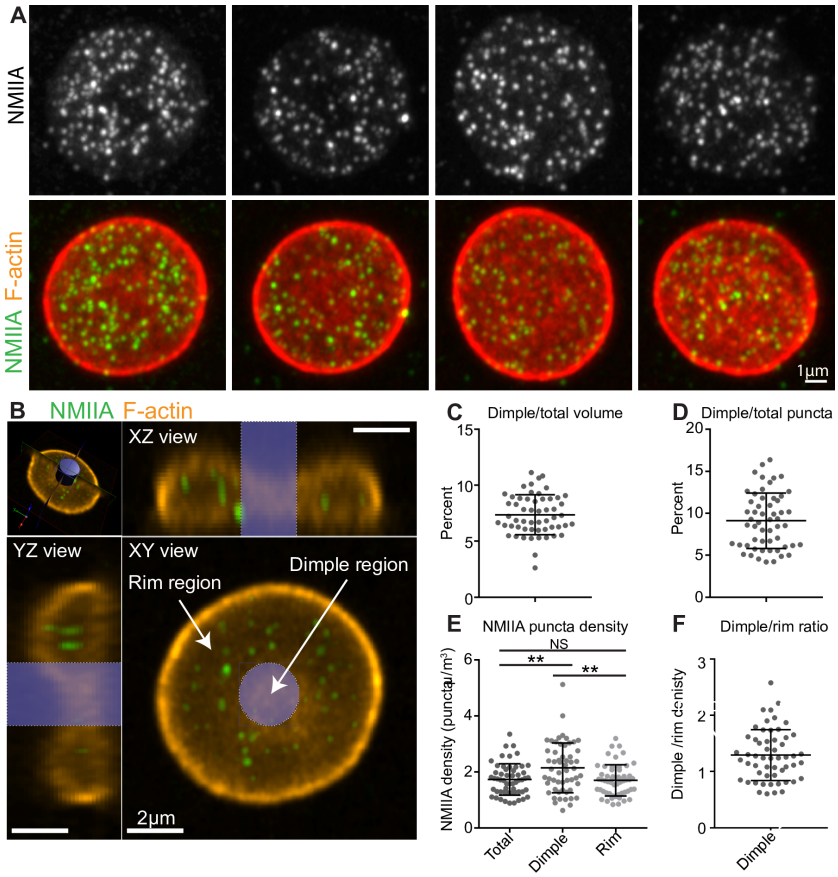

Figure 5.6: The RBC dimple has a higher average NMIIA puncta density than the RBC rim. (A) Maximum intensity projections of super-resolution Airyscan confocal Z stacks of individual human RBCs immunostained with an antibody to NMIIA motor domain (grey scale, top row), together with merged images (second row) of NMIIA (green) and rhodamine phalloidin for F-actin (red). (B) Schematic illustrating volume segmentation of RBCs and NMIIA puncta distribution. Optical section of a super-resolution Airyscan confocal Z-stack of human RBC immunostained with an antibody to the motor domain of NMIIA (green) and rhodamine-phalloidin for F-actin (orange). The top left image shows a perspective view of the optical section. Top right and bottom left images show YZ and XZ slices, respectively, of the RBC from planes perpendicular to this optical section. The bottom right image shows an XY view of the optical section. The blue cylinder represents the region identified as the dimple region. The rest of the RBC is identified as the rim region. Note, the myosin puncta near the RBC membrane are difficult to visualize in these merged images due to the bright F-actin staining. (C) The percent of total RBC volume occupied by the dimple region. Mean $\pm$ S.D. = 7.37 $\pm$ 1.79. (D) The percent of total NMIIA puncta in the dimple region. Mean $\pm$ S.D. = 9.11 $\pm$ 3.30. (E) The RBC dimple region has a $\sim$25% higher density of NMIIA puncta than whole RBCs (Total) ($p = 0.0051$) or the rim region ($p = 0.0023$) by Tukey's multiple comparisons test. Mean $\pm$ S.D.: Total = 1.73 $\pm$ 0.562; Dimple = 2.15 $\pm$ 0.888; Rim = 1.70 $\pm$ 0.556. (F) Ratio of dimple and rim region NMIIA puncta densities for each RBC. Mean $\pm$ S.D. = 1.29 $\pm$ 0.452. (B-E) n = 55 RBCs from 3 individual donors.

Additionally, we found that for low and intermediate tensions independent of the value of F_{rim}, the shape error has the same non-linear relationship with increasing F_{dimple} as previously observed for the tensionless membrane (Fig. 5.7D, E). At low tension, the minimum shape error occurs when F_{dimple} = 5.06 pN/μm^2 and F_{rim}= 1.4 pN/μm^2 (blue square line) (Fig. 5.7D). At intermediate tension, a combination of F_{dimple} = 12.66 pN/μm^{2}and F_{rim} = 9.95 pN/μm^2 gives the minimum shape error (green triangle line) (Fig. 5.7E). However, for high tension, because of the stiffness of the membrane, we observe not only a deviation from the biconcave shape but also a deviation from the nonmonotonic error - dimple force relationships (Fig. 5.7F).

Based on these results, we concluded that in addition to a non-uniform force distribution along the RBC membrane, a non-zero intermediate tension is required to obtain a close match between the shape and the volume of the simulated RBC and the experimental data. Furthermore, the intermediate value of tension (tension = 10^{-3} pN/nm) gives an excellent quantitative match for the predicted value of F_{ratio} (Fig. 5.7B) and the experimentally observed NMIIA density ratio (Fig. 5.6).

5.2.6 The angle of applied forces in the RBC dimple and rim regions controls the shape error

Until now, we have assumed the net effects of NMIIA motor proteins act as local forces applied normally to the membrane surface. However, there is evidence that these molecules also exert forces tangential to the membrane [454]. To examine how the orientation of the induced forces by NMIIA can affect the morphology of the RBC, we repeated the simulation in Fig. 5.7 for different membrane tension values assuming that the applied forces make an angle ϕ with the tangent vector as (Fig. 5.8A). Because the exact orientation of the applied forces by NMII molecules is currently unknown, we varied angle ϕ from $\phi = 90^0$ (normal to the membrane) to ϕ= 0 (tangential to the membrane) and for each case found the combination of the force densities

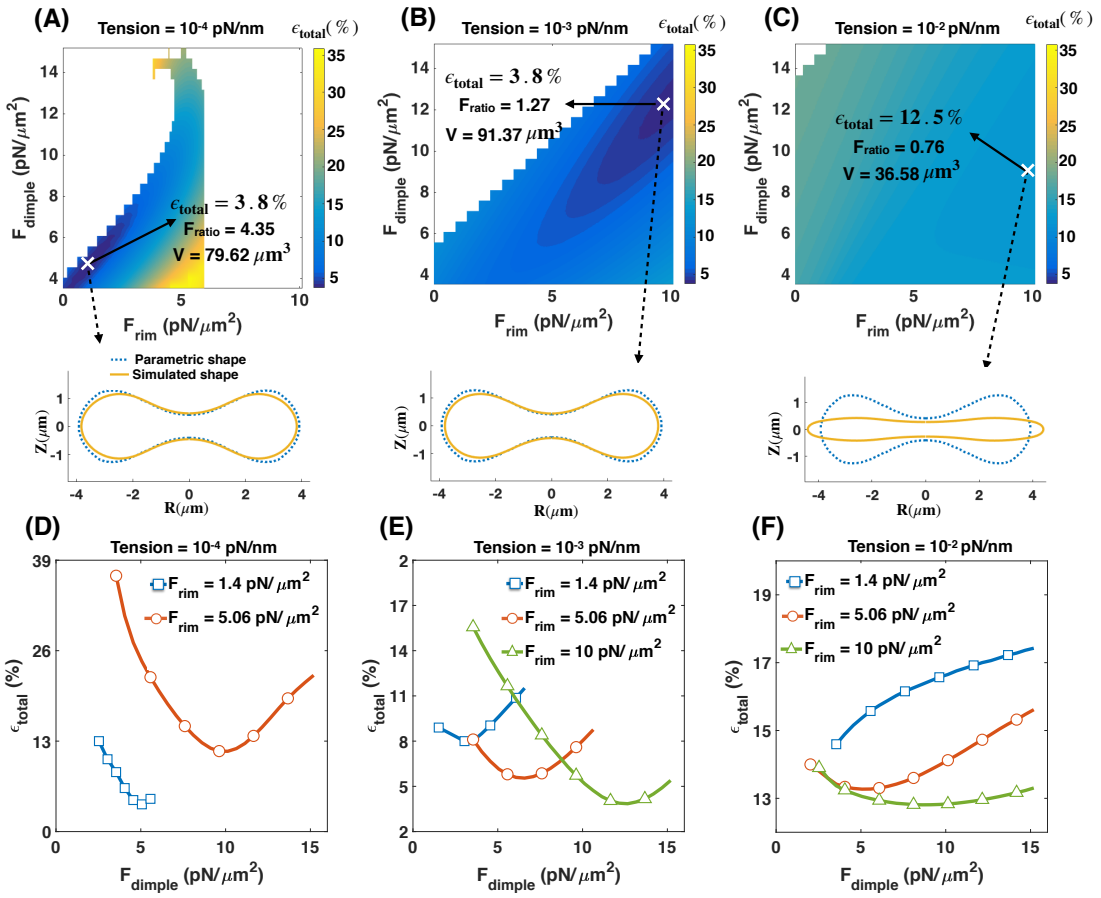

Figure 5.7: Effective membrane tension is a key parameter in regulating the RBC biconcave shape in addition to applied forces in the dimple and rim regions. (A-C) Heat maps show the total error in the shape of the simulated RBCs for (A) low tension (tension = 10^{-4} pN/nm), (B) intermediate tension (tension = 10^{-3} pN/nm), and (C) high tension (tension = 10^{-2} pN/nm). In each heat map, the point with the minimum error is marked with X. Also, for each marked point, the volume of the simulated RBC (V) is calculated using Eq. S13b, and the shape (solid yellow line) is shown in comparison with the reference parametric shape (dotted blue line). At intermediate tension, the shape error has the lowest value when F_{ratio} = 1.27 consistent with our experimental results in Fig. 5.6. (D-F) The calculated shape error (Eq. 5.8) as a function of the dimple force density (F_{dimple}) for different values of the force density at the rim region and the membrane tension.

that gives the minimum shape error (Figs. C.6-C.9).

In Figs 5.8B-D, we plotted the minimum shape error as a function of angle $\phi$for three different values of the membrane tension; (B) tensionless membrane, (C) low membrane tension (tension = 10^{-4} pN/nm), and (D) intermediate tension (tension = 10^{-3} pN/nm). We observed that

in all three cases, with varying the angle ϕ from normal to tangential orientation, the simulated shapes deviate from the biconcave disks to the pancake shapes with an almost three times larger shape error. Based on our results, we found that for tensionless membranes, the transition from the biconcave shapes with $\varepsilon_{\text{total}} < 5\%$ (pink area) to the pancake shapes where $\varepsilon_{\text{total}} \gg 5\%$ (gray area) occurs for angles smaller than 45^0 ($\phi < 45^0$) (Fig. 5.8B). This transition to pancake shapes shifted toward the smaller angles ($\phi < 30^0$) for low and intermediate membrane tension (Fig. 5.8C, 5.8D). Finally, in the case of high membrane tension, as expected from Fig. 5.7C, independent of the angle of force ϕ the simulated shapes have a pancake-shaped morphology with very large shape errors (see Fig. C.9). Thus our model predicts that membrane tension and the orientation of the applied forces can be collectively tuned to actively maintain the biconcave morphology of an RBC.

5.3 Discussion

The biconcave disk shape of mammalian RBCs provides a maximum surface-area-to-volume ratio, which enables efficient gas and ion exchange and increases RBC deformability and resiliency [455]. This shape has been studied extensively from a mechanical standpoint to identify stress-strain relationships in cell membranes. Most studies modeling RBC shapes have been based on the work of Canham and Helfrich [35, 429] and have reinforced the idea that mechanical force balance on the membrane by itself can provide insights into the unique shape of the RBC. The studies by Canham and Helfrich and other researchers suggested that the minimization of the membrane bending energy and the asymmetry between the inner and outer membrane leaflets generate the RBC biconcavity [128, 133]. For example, Markin showed how the induced nano-scale curvature field due to the lateral distribution of membrane components can prescribe the biconcave shape of RBCs [411]. Here, we focused on micron-scale differences

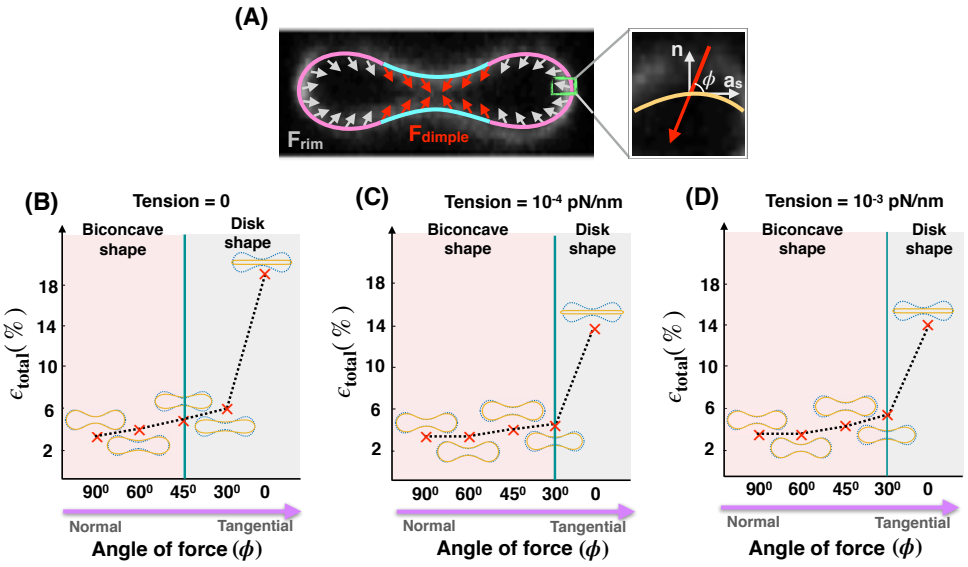

Figure 5.8: Effective membrane tension and the angle of applied forces in the RBC dimple and rim regions work together to maintain the biconcave shape of an RBC. (A) Schematic of a biconcave RBC with a non-uniform distribution of force density across the dimple and rim regions. In both regions, the forces per unit area are applied with angle ϕ with respect to the tangent vector (as). (B-D) The shape error and the RBC shapes obtained from simulation for different angles of the applied forces (ϕ for (B) tensionless membrane, (C) low tension (tension = 10^{-4} pN/nm), and (D) intermediate tension (tension = 10^{-3} pN/nm). For all values of the membrane tension, as the angle of forces deviates from normal ($\phi = 90^0$) to tangential orientation (ϕ= 0), the simulated shapes flatten and the shape error increases.

in lateral distribution of myosin-mediated forces as another degree of freedom and demonstrated how they are important for maintaining the RBC biconcave shape.

In this thesis, we revisited the classical Helfrich-Canham energy model for the RBC membrane to include non-uniform forces along the membrane due to NMIIA-actin interactions. Undoubtedly, adding an additional degree of freedom to the energy allows us to attain a better match between the simulated and the experimentally observed RBC shapes compared to previous studies. Further, based on our results, we predicted two conditions that need to be satisfied to produce the best fit with the experimental shapes of RBCs. First, the density of the NMIIA-generated force must be non-uniform along the RBC membrane to produce the best fit with the shapes measured experimentally. By conducting a parameter sweep of the force density

configurations, we found that the non-uniform force distribution must be such that F_{dimple} is larger than F_{rim} (Figs. 5.4, 5.5). Experimental measurements of NMIIA density in the dimple and rim regions of RBCs using immunofluorescence showed that indeed NMIIA density is higher in the dimple than in the rim (Fig. 5.6) by about 25%. Our combined computational and experimental results highlight that a micron-scale, non-uniform force distribution of NMIIA plays a fundamental role in maintaining the biconcave shape of RBCs. We emphasize that this non-uniform density of forces is at the length scale of microns rather than at the length scale of fluctuations of the RBC membrane [456].

Second, we predicted that the effective membrane tension and the orientation of the applied forces are important physical parameters in modulating the RBC morphology and the required NMIIA-mediated force density ratio in the RBC dimple versus the rim region (F_{ratio}) (Figs. 5.7, 5.8). As compared to tensionless or low-tension membranes, the intermediate tension values F_{ratio} for minimum shape error ($\sim$1.27) are a better match with the experimentally reported NMIIA density ratio at the dimple versus the rim. Furthermore, we found that the deviation of the applied forces from normal to tangential orientations results in pancake-shaped morphologies with very large shape errors compared to the actual biconcave shape of RBCs (Fig. 5.8). Additionally, we calculated the reduced volume (ν); the volume of the simulated RBC with respect to the volume of the sphere with no force (Eq. C.14). Based on our calculation, the reduced volume of biconcave RBC varies in a wide range between $\sim$0.62 and 0.83. A recent study by Mesarec et al. has also shown that in stable discocyte RBS shapes, the reduced volume varies in a wide range (between 0.58 and 0.8) if the membrane's in-plane ordering is taken into account [457].

Therefore, we predict that in mature, healthy biconcave RBCs, NMIIA motor domains exert force on the membrane with angle $\phi > 30^0$ under intermediate membrane tension ($\sim 10^{-2}$ pN/nm) and the reduced volume can vary in a broad range. Currently, the exact value of membrane tension and the angle of forces in an intact RBC are hard to measure because of the

contributions from both the membrane and the underlying skeleton [458, 459]. In the literature, a wide range of values are reported for the membrane tension from 10^{-1} pN/nm to 10^{-4} pN/nm [430, 451, 453]. This range can be attributed to dynamic lipid rearrangements [460], membrane-skeleton interactions [461], and based on our work here, rearrangement of force-generating NMIIA molecules [82]. The angle of applied forces by NMIIA at the RBC membrane is still a matter of debate because nanoscale 3D images of F-actin and NMIIA motors using cryoelectron tomograms would be required to explore the relative configurations of myosin motors, F-actin and the RBC membrane surface [459]. This will require the development of novel sample preparation approaches for RBCs and is a subject for future study. Our theoretical analyses, supported by experimental measurements, implicitly suggest that for a biconcave RBC, the effective membrane tension should be on the order of 10^{-2} pN/nm and the NMIIA motors should apply forces with angles $\phi > 30^0$ with respect to the membrane surface.

Our conclusions of non-uniform force density and tension regulation can be used to obtain insight into the effective activity of NMIIA motor domains at any given time. Assuming that a single NMIIA motor domain produces an average force of $\sim$ 2 pN [462, 463], the calculated force densities in Fig. 5.7B corresponds to 90 and 815 myosin motor domains in the dimple and rim regions, respectively. This means that the force generated by a total of $\sim$850 active NMIIA motor domains, distributed between the dimple and the rim as we predicted, is sufficient to sustain the biconcave disk shape of an RBC. Previous studies estimated that each mature human RBC contains $\sim$ 6,000 NMIIA molecules, $\sim$12,000 motor domains [420, 421] and at any given time, roughly 40-50% of these molecules are bound to the membrane skeleton [82]. Our calculations suggest that approximately 15% of these bound NMIIA molecules are active and exerting forces distributed unevenly along the membrane. It is also possible that the amount of force generated by a single NMIIA motor domain varies due to the stiffness of the membrane skeleton network, the processivity (the duration over which the motor stays attached to actin), and the cross-linking

activity of NMIIA myosin filaments [462, 463]. Therefore, further research will be required to determine the quantitative relationship between the copy number of NMIIA molecules and their activity, that together determine the overall magnitude of the force exerted on the RBC membrane.

The idea of the asymmetrical distribution of the membrane skeleton and its components in the dimple and rim areas of RBCs was initially introduced by Hoffman, although no direct evidence for this was obtained [464]. Recently, Svetina et al. modeled RBC volume regulation according to the permeability of the Piezo1 channel. Based on their simulation results, they found that Piezo1 channels are expected to be distributed non-uniformly in a biconcave RBC, tending to localize in the dimple region [465]. They speculated that the simulated localization of Piezo1 channels in the dimple region is controlled by the membrane curvature and induced surface tractions [6]. The RBC membrane curvature may also influence the localization of NMIIA motor proteins, as has been observed in other cell types [75]. Alternatively, a shear-induced Ca^{2+} influx through localized Piezo1 channels could locally activate NMIIA through activation of myosin light chain kinase and phosphorylation of the regulatory light chain [420–422], leading to enhanced NMIIA binding to F-actin and enhanced local contractility at the dimple, activating Piezo1 and Ca^{2+} influx in a feed-forward loop. We believe our findings here are a motivation for future studies to develop quantitative relationships between the myosin-mediated forces, Ca^{2+} influxes, and the membrane curvature of the cell surface.

We acknowledge that despite the conclusions from our studies, there are some limitations and simplifying assumptions that will need to be revisited for future studies. First, we limited our model to axisymmetric shapes, while RBCs often adopt non-axisymmetric shapes [466]. Future studies will involve simulations without any assumptions of symmetry. Experimental tests probing whether NMIIA activity is non-uniform along the RBC membrane will also give insight into NMIIA density distribution versus activity distribution along the membrane. Second, we assumed that the contributions from thermal fluctuations and the deformation of the membrane skeleton are

negligible compared to the bending energy [425, 467]. However, for a more general quantitative model, these effects should be considered [456]. Particularly, in the case of discocyte-echinocyte RBC shape transformation and in RBC membrane vesiculation, previous studies have shown the important role of membrane skeleton in driving these shape transformations [169, 419, 468–470]. Future efforts focusing on the shape transformations of RBCs from discocytes to echinocytes or stomatocytes will be important to connect RBC morphology to physiological function and molecular mechanisms. There is also an opportunity to extend the current models for non biconcave RBCs shape including experimental manipulation of the membrane tension or inhibition of the myosin activity in RBCs [458, 471]. These require the adaptation of newly emerging technologies for RBC biology and will provide new insight into the molecular mechanisms of RBC shape generation and maintenance.

5.4 Acknowledgements

I would like to acknowledge my co-authors Dr. Alyson Smith, Dr. Roberta Nowak, Prof. Velia Fowler, and Prof. Padmini Rangamani. I would also like to thank Dr. Christopher T. Lee and Miriam Bell for their feedback on the study.

Chapter 6

Mechanical principles governing the shapes of dendritic spines

6.1 Introduction

Dendritic spines are small, bulbous protrusions along the dendrites of neurons that occur at postsynaptic glutamatergic synapses [472–474]. They respond to a glutamate release by orchestrating a series of biochemical and biophysical events that span multiple spatial and temporal scales [475–477]. Spine morphology is tightly coupled to synaptic function, with larger spines tending to represent stronger synapses [478, 479] due to their greater surface expression of functional glutamate receptors. Synaptic activity regulates spine shape and volume. For example, several forms of physiological synaptic plasticity, such as long-term potentiation (LTP) and long-term depression (LTD) are associated with spine enlargement and spine shrinkage, respectively [480–482]. Although average spine volume is approximately 0.1 femtoliter, the shape and volume of dendritic spines are highly variable, depending both on the developmental

stage and a combination of genetic and environmental factors, including the prior history of activity [483–486]. Moreover, spine morphology is highly dynamic on the scale of seconds to minutes, due to a dynamic actin-based cytoskeleton [473, 487].

Despite their broad range of morphological features and highly dynamic nature, dendritic spines can be classified into four broad categories. Spines in the mature nervous system are typically classified as being stubby, thin, or mushroom-shaped [1, 488] (Fig. 6.1A). These categories of spines can be identified in electron micrographs as postsynaptic structures connected to presynaptic nerve terminals. Stubby spines are short and wide, and lack a discernible neck. Such spines appear early during synaptogenesis and may represent an emerging spine, but they also might result from spine shrinkage driven by physiological or pathological conditions (Fig. 6.1A) [475, 483, 489].

The adult mammalian brain is dominated by either thin or mushroom-shaped spines. Thin spines have a long thin neck that is connected to a small bulbous head (Fig. 6.1A) [483]. Within the head is the postsynaptic density (PSD), an area just beneath the synaptic plasma membrane containing a high concentration of glutamate receptors, scaffolding molecules, and other proteins essential for postsynaptic function. Thin spines have flexible structures that allow them to adapt their morphology based on different levels of synaptic activity [490, 491]. It has been proposed that thin spines are "learning spines," because they display a high capacity for expansion and strengthening via insertion of new AMPA-type glutamate receptors into the PSD, which is the key basis for synapse strengthening [490–494]. Compared to thin spines, mushroom-shaped spines have a shorter neck and a greatly expanded head (Fig. 6.1A) [483]. Mature mushroom-shaped spines are more likely to be stable for months to years [490, 491, 494–496], with slower turnover, and are associated with strong synapse functionality, as they contain on average higher concentrations of AMPA-type glutamate receptors. Such spines have therefore been called "memory spines", in the sense that their potentiated strength reflects a history of

high activity and thus "memory" storage, yet their capacity for further potentiation may be near saturation [492–494, 497–499]. Table 6.1 provides the reported dimensions for different shape categories of dendritic spines observed in hippocampal neurons [1–4, 500].

In addition to synapse-bearing spines, the fourth category of spine-like protrusions is dendritic filopodia. These are commonly observed during early development, and are thought to facilitate the pairing of presynaptic and postsynaptic glutamatergic sites during synaptogenesis by spatially scanning the neuropil volume for a partner axon [489, 501–503]. Thus, a fraction of these "protospines" become synapse-bearing spines if they come into contact with and are stabilized in partnership with presynaptic nerve terminals [501, 504]. Filopodia are long (>2 μm) and thin (< 0.3 μm diameter) protrusions that lack a bulbous head (Fig. 6.1A) [3].

Because the size and shape of functional subcellular domains are closely tied to the mechanics of actin-membrane interactions [1, 3, 500], a more complete understanding of dendritic spine dynamics, development, and function would benefit from biophysical models that address the underlying mechanical aspects. We have therefore begun to build a computational model of spines that incorporates both membrane forces and actin-based forces, and their interaction. This model is based on published experimental observations in dendritic spines, non-neuronal cells, and biochemical experiments. The goal of this model is to inform our understanding of the development of spines and the plasticity of their structure under different physiological scenarios.

Currently, there are hundreds of studies that address various aspects of the regulation of dendritic spine size and shape. In building our model, we have chosen to focus on several key observations, as follows.

1. **Actin enrichment in spines:** Dendritic spines are enriched in filamentous actin, which, along with scaffolding molecules, establish spine architecture [83, 505, 506]. Membrane-actin interactions associated with spine enlargement and shrinkage during plasticity can be modeled at the single filament level using the elastic Brownian ratchet and the net force

acting on the membrane due to actin remodeling can be represented as work done by actin to deform the membrane [507–509].

2. **Different subpopulations of actin:** There appear to be distinct subpopulations of F-actin in dendritic spines, and spine actin can be thought of as an independent network with interconnected nodes [510]. The spine head typically consists of short, cross-linked filaments; branched filaments have been observed in the spine head [83–85]. The spine neck was initially thought to contain long filaments [86–89], but current evidence has suggested the presence of short, branched filaments [84]. Additionally, recent high resolution imaging techniques have shown that there are likely periodic F-actin structures along the neck region of dendritic spines [90, 511]. These periodic F-actin structures are very stable and in contrast to long and branched filaments, resist depolymerization [90].

3. **Roles for actin binding proteins:** Actin dynamics in spines are tightly regulated by dozens of various actin binding proteins, some of which must also interact directly or indirectly with the spine plasma membrane [91–93]. First, the turnover of filaments themselves can drive forces against the membrane that regulate the expansion, maintenance, or shrinkage of spine compartments [512]. The key factors that govern this balance are (a) the rate of polymerization, which is regulated by actin nucleating factors such as formins and the Arp2/3 complex [83]; (b) the rate of depolymerization, which is regulated by actin severing factors such as cofilin and gelsolin [513]; (c) the number of free barbed ends, which is regulated via actin severing activity and the activity of barbed end capping proteins [97]; and (d) the concentration of available actin monomer, which is dependent upon the G-actin concentration and also the activities of profilin, which delivers ATP-bound G-actin to the above actin nucleators, and regulators such as N-WASP, which controls Arp2/3 activity [97, 514]. In addition, several proteins that crosslink or stabilize actin filaments, such as cortactin [94], spectrin [95], or drebrin [96] are known to regulate spine shape and

separately, myosin motors can affect spine shape either directly by creating contractile forces, or indirectly by regulating the transport of cargo into and out of the spine [97, 98]. Finally, an important role for calcium/calmodulin-dependent protein kinase in structural plasticity of spines has been demonstrated through its ability not only to transduce calcium signals, but also to regulate actin directly through the direct binding of F-actin via its β-subunit [515–517].

4. **Membrane mechanics:** All cells regulate their shape by coordinating the properties of the cytoskeleton with that of the plasma membrane. Proteins such as MARCKS that interact directly with both F-actin and the lipid bilayer can strongly influence spine shape [518]. Membrane curvature is especially important in spines and represents a specific mechanical force that is regulated by specific proteins, as well as lipid composition. Bin/Amphiphysin/Rvs (BAR)-domain containing proteins assemble on the membrane to produce anisotropic curvature and promote tubulation. Studies have demonstrated critical roles for specific BAR-domain proteins in dendritic spines. Recently, the role of membrane mechanics has been elucidated in the initiation of dendritic spines [519]. A series of studies showed that dendritic spines can be initiated by membrane bending due to protein patches containing BAR domains such as I-BAR and F-BAR proteins [520–523]. These proteins are known to polymerize on the membrane [56,174,175,303], induce anisotropic curvature [324,524,525], and promote tubulation [174, 176, 178, 181, 526].

The above findings suggest that membrane bending and actin-membrane interactions are major determinants of spine morphology. Recent studies have modeled the role of either membrane mechanics alone [509] or actin dynamics alone in spines [527], but the interaction between the two has not yet been addressed. Here, we present a general theoretical model that relates membrane bending and actin-mediated forces to spine morphology. Using this model, we investigate the mechanical landscape of the different shapes of spines and map the relationships

among actin-mediated force generation, membrane elasticity, and curvature induced by periodic ring structures and proteins such as BAR domains.

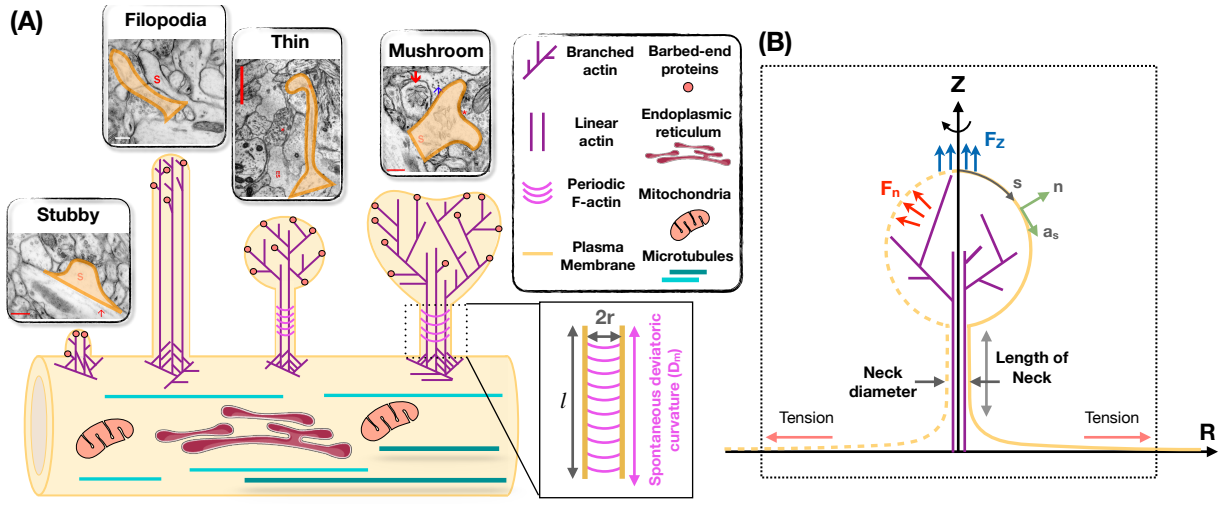

Figure 6.1: Modeling of forces relevant to spine shape. (A) Schematic depiction of different shape categories of dendritic spines (Reprinted with permission from SynapseWeb, Kristen M. Harris, PI, http://synapseweb.clm.utexas.edu/). The inset shows a schematic of a tubular neck with a radius r and a spontaneous deviatoric curvature D_m along the total neck length l. (B) The surface parametrization of the membrane geometry in axisymmetric coordinates. s is the arclength, **n** is the unit normal vector to the membrane surface, and $\mathbf{a}_s$ is the unit tangent vector in the direction of arclength. We assume that the actin filaments can apply axial (F_z) or normal (F_n) forces to the membrane surface. We assume that there is a large membrane reservoir with a fixed area, and we focused on the local region of the membrane under tension λ, as indicated by the dotted box.

Table 6.1: Dimensions of different spine shapes compiled from the literature [1–4].

	Stubby	Filopodia	Thin	Mushroom
Total length (L) (μm)	0.44 ± 0.15	2-20	0.98 ± 0.42	1.5 ± 0.25
Length of neck (l) (μm)	–	–	0.51 ± 0.34	0.43 ± 0.21
Neck diameter (2r) (μm)	0.32 ± 0.13	< 0.3	0.1 ± 0.03	0.2 ± 0.07
Total volume (μm^3)	0.03 ± 0.01	–	0.04 ± 0.02	0.29 ± 0.13
Volume of head (V) (μm^3)	–	–	0.03 ± 0.15	0.27 ± 0.13
Total surface area (μm^2)	0.45 ± 0.14	–	0.59 ± 0.29	2.7 ± 0.93
Area of head (μm^2)	–	–	0.4 ± 0.15	2.4 ± 0.92
Area of PSD (μm^2)	0.07 ± 0.02	–	0.05 ± 0.02	0.3 ± 0.1
Area of PSD/head	–	–	0.1 ± 0.06	0.18 ± 0.15

6.2 Model development

6.2.1 Assumptions

- We treat the lipid bilayer as a continuous thin elastic shell, assuming that the membrane thickness is negligible compared to the radii of membrane curvature [133, 409]. This allows us to model the bending energy of the membrane using the modified version of the Helfrich–Canham energy, including the effect of spatially varying deviatoric curvature to represent the induced anisotropic curvatures by periodic F-actin rings and other ring-shaped structures [5, 128, 133, 176, 178, 180].

- We assume that the membrane is locally inextensible, since the stretching energy of the lipid bilayer is an order of magnitude larger than the membrane bending energy [352]. We implemented this constraint using a Lagrange multiplier, which can be interpreted as the membrane tension [150, 528]. We note that this membrane tension, in this thesis, is better interpreted as the cortical tension including the effective contribution of the membrane in-plane stresses, induced tension by actin polymerization, and myosin-driven contractility against membrane [9, 195, 374, 529].

- We assume that the time scales of mechanical forces are much faster than other events (such as actin polymerization) in dendritic spines, allowing us to assume mechanical equilibrium and neglect inertia [150, 509]. This assumption is justified by the fact that the timescale of the equilibration of the mechanical forces is much smaller than the timescale of actin polymerization in dendritic spines [530].

- We assume that the force exerted by the actin cytoskeleton can be represented as work done on the membrane and do not include the molecular details of the actin network [9, 135, 136, 509, 531]. Additionally, we assume that the periodic ring shaped structures of

actin and related proteins such as βII spectrin and BAR-domain proteins can be represented using an anisotropic spontaneous curvature [176, 178, 180, 525].

- For ease of computation we assume that the geometry of a dendritic spine is rotationally symmetric (see Fig. 6.1B) [509]. This assumption allows us to parametrize the whole surface by a single parameter, arclength.

6.2.2 Mechanical force balance

In this section we present a concise derivation of the governing mathematical shape equations for the shape of dendritic spines at mechanical equilibrium. The complete derivation with details is given in [136, 150, 152]. The total free energy of the system (E) includes the elastic storage energy of the membrane (E_{elastic}), and the work done by the applied forces due to actin filaments (W_{force}) [5, 136, 183, 266] is given by

$$E = E_{\text{elastic}} - W_{\text{force}}, \tag{6.1}$$

where

$$E_{\text{elastic}} = \int_{\omega} (\sigma(H, D, K; \theta^{\alpha}) + \lambda(\theta^{\alpha}))da - pV, \quad \text{and} \tag{6.2a}$$

$$W_{\text{force}} = \int_{\omega} \mathbf{f}(\theta^{\alpha}) \cdot (\mathbf{r} - \mathbf{r}_0)da. \tag{6.2b}$$

Here, ω is the total membrane surface area, σ is the bending energy density per unit area, θ^{α} denotes the surface coordinate where $\alpha \in \{1, 2\}$, H is the mean curvature of the surface, D is the curvature deviator, K is the Gaussian curvature of the surface, λ is the tension field and represents

the Lagrange multiplier associated with the local area constraint, p is the transmembrane pressure and represents the Lagrange multiplier associated with the volume constraint, V is the enclosed volume, $\mathbf{f}$ is the applied force per unit area, $\mathbf{r}$ is the position vector in the current configuration, and $\mathbf{r}_0$ is the position vector in the reference frame. To model the energy density σ in Eq. 6.2a, we used the modified version of Helfrich energy including the effects of induced anisotropic curvature by periodic F-actin structures and BAR domain proteins [5, 36, 128, 133, 176, 178, 324], given as

$$\sigma(H, D, K; \theta^{\alpha}) = \kappa H^2 + \kappa(D - \mathrm{D_m}(\theta^{\alpha}))^2, \tag{6.3}$$

where κ is a constant representing the bending moduli and $\mathrm{D_m}$ is the spontaneous (intrinsic) deviatoric curvature which can be spatially heterogeneous along the membrane surface [176, 178, 324]. It should be mentioned that in Eq. 6.3, we assumed that periodic rings can only induce anisotropic curvature and we set the isotropic curvature (spontaneous curvature) to be zero throughout this chapter. Substituting Eqs. 6.2a, 6.2b, and 6.3 into Eq. 6.1 gives

$$E = \underbrace{\int_{\omega} \kappa H^2 da}_{\substack{\text{Bending energy} \\ \text{of the membrane}}} + \underbrace{\int_{\omega} \kappa(D - \mathrm{D_m})^2 da}_{\substack{\text{Bending energy due to} \\ \text{deviatoric curvature}}} + \underbrace{\int_{\omega} \lambda da}_{\substack{\text{Work done} \\ \text{by tension}}} - \underbrace{pV}_{\substack{\text{Work done} \\ \text{by pressure}}} - \underbrace{\int_{\omega} \mathbf{f}(\theta^{\alpha}) \cdot (\mathbf{r} - \mathbf{r}_0) da}_{\text{Work done by actin-mediated forces}} . \tag{6.4}$$

Minimization of the energy (Eq. 6.4) using the variational approach results in the governing shape equation (Eq. D.6) and the incompressibility condition (Eq. D.7) for a heterogeneous membrane.

6.2.3 Numerical implementation

In axisymmetric coordinates, the membrane shape equation (Eq. D.6) and the incompressibility condition (Eq. D.7) simplify to a coupled system of first order differential equations (Eq. D.19). In order to solve this system of equations along with the prescribed boundary conditions (Eq. D.21), we used 'bvp4c,' a boundary value problem solver in MATLAB. In all our simulations, we assume that the total area of the membrane is conserved and we also fixed the bending modulus to be $\kappa = 0.18$ pN·μm based on previous models for spines [532, 533]. We also set the transmembrane pressure to zero ($p = 0$) to focus only on the mechanism of membrane-actin interactions in governing the shapes of dendritic spines.

6.3 Results

Using the model described above, we conducted simulations for different mechanical parameters with the goal of identifying the range of forces, the associated heterogeneities, and the protein-induced and cytoskeleton-induced anisotropic curvatures that could result in shapes and sizes of spines corresponding to those observed experimentally (Table 6.1). Specifically, we sought to recreate the filopodial, stubby, thin, and mushroom-shaped spines as shown in Fig. 6.1. We must emphasize that all the shapes are equilibrium shapes, and our model does not provide insight into dynamic transitions from one shape to another. Our simulation results are described below. In these data, we emphasize the relationships among different mechanical parameters to obtain the desired shapes, and give specific values for mechanical parameters that result in sizes as listed in Table 6.1. These provide some realistic magnitudes for forces present at various locations within the compact spine volume.

6.3.1 Localized axial forces along the membrane are sufficient for the formation of stubby and filopodial shaped spines

We begin with an analysis of the force-shape relationship of stubby spines. We assumed that actin filaments exert axial forces in the nascent PSD area, which is a small fraction of the membrane surface area (Table 6.1). This heterogeneous force distribution along the membrane was implemented using a hyperbolic tangent function (Eq. D.22). We observed that the relationship between the magnitude of the forces and the length of the stubby spines depends on the value of tension. To map this relationship, we performed the simulation for (*i*) a fixed height (L = 0.44 μm) and a wide range of tensions (Fig. 6.2A) and (*ii*) a fixed tension (e.g., $\lambda = 10$ pN/μm) and different heights of the stubby spine (Fig. 6.2B). As shown in previous studies [272, 343], for a small membrane deformation, such as a stubby spine, the axial force is linearly proportional to both tension and the height of the stubby spine (Figs. 6.2A & B) [272, 343]. Thus, from a mechanical standpoint, the stubby spine shape is accessible for a wide range of forces and tensions in the physiological range. For example, based on our simulation, when tension is $\lambda = 10$ pN/μm, an axial force of F_z = 7.5 pN is required to form a stubby spine of the length of L = 0.44 μm (Table 6.1) (Fig. 6.2C).

Next, we investigated the role of forces in the formation of long spines that resembled filopodia. For the simplest case with no steric interaction between membrane and bundled actin, we found that the formation of a long filopodium follows well-established results for tube formation from a membrane reservoir [343]. Ignoring the spherical cap, a filopodium is a tubular membrane and its equilibrium radius (r) depends on the tension and bending rigidity of the membrane as $r = \sqrt{\kappa/(2\lambda)}$ (Fig. 6.2D) [343]. The axial force F_z required to maintain the tubule with radius r is given as $F_z = 2\pi\sqrt{2\kappa\lambda}$ (Fig. 6.2E & F) [343], which is independent of the length of the protrusion (Fig. D.3A). In addition to the actin-mediated filopodium formation from a large membrane reservoir (fixed membrane area) that we focused on here, Miermans et al. showed that

an increase in the surface area of a spine can drive a filopodium elongation from a stubby-shaped spine [509]. They suggested that exocytosis of endosomes at synapses provides this membrane addition to the system [509].

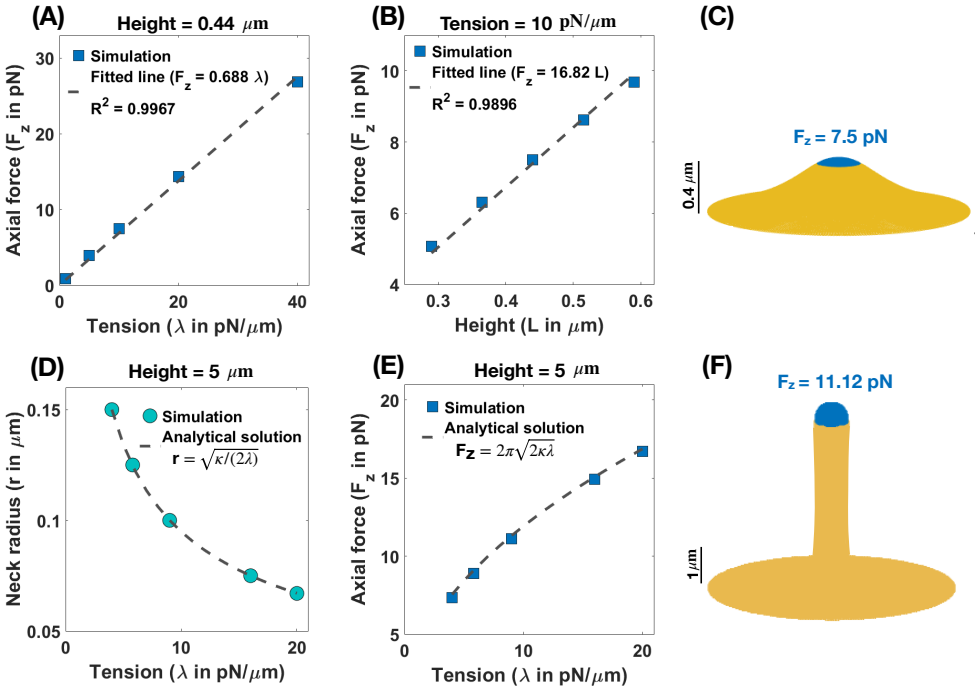

Figure 6.2: Formation of stubby and filopodia shaped spines with a localized axial force. (A) Linear relationship between the magnitude of axial force and tension in a small stubby-shaped membrane deformation [272, 343]. The dashed line is the fitted curve ($F_z = 0.688\lambda$) with R^2 = 0.9967. (B) Linear relationship between the magnitude of axial force and the height of the stubby spine for a fixed tension [272, 343]. The dashed line is the fitted curve (F_z = 16.82L) with R^2 = 0.9896. (C) A stubby-shaped spine with a total length L = 0.44 μm is formed with F_z = 7.5 pN applied along the blue area (λ =10 pN/μm). (D) Neck radius of a filopodium as a function of tension ($r = \sqrt{\kappa/(2\lambda)}$) [343]. (E) The magnitude of axial force needed to form a filopodium as a function of tension ($F_z = 2\pi\sqrt{2\kappa\lambda}$) [343]. (F) A filopodium-shaped protrusion with a total length L = 5 μm and neck radius r = 0.2 μm is formed with F_z = 11.2 pN applied along the spherical cap of the filopodium, which is shown in blue (λ = 9 pN/μm).

6.3.2 Normal forces along the membrane support the formation of thin shaped spines

We next investigated the nature of forces that could be associated with the formation of thin-shaped spines. Because thin-shaped spines have a bulbous head, axial forces such as those used in Fig. 6.2 are insufficient to generate the spherical shape of the head. Since spherical shapes can be obtained by a normal force acting locally on the head region, we repeated the simulation in Fig. 6.2 but now included a localized uniform normal force density along the area of the spine head ($A_{\text{force}} = A_{\text{spine head}}$). It is possible that such normal forces result from the dense actin meshwork in the spine heads [509, 534]. We estimated the forces required to generate a spherical head by assuming that a thin spine is ideally a sphere with radius R which is connected to a cylinder with radius r and height l (Fig. D.1B). If a uniform normal force density, $\mathrm{f_n}$, is applied all along the sphere, then, ignoring the interface between the sphere and the cylinder, the total energy of the system can be written as

$$E = E_{\text{sphere}} + E_{\text{cylinder}}, \tag{6.5}$$

where $E_{\text{sphere}} = (\kappa/R^2 + \lambda)4\pi R^2 - (4\pi/3)R^3\mathrm{f_n}$ and $E_{\text{cylinder}} = 2\pi\sqrt{2\lambda\kappa}l$ (see section D.2.5 in Appendix D). Minimizing the total energy of the system with respect to R by taking $\partial E/\partial R = 0$, we obtain the equilibrium normal force density as $\mathrm{f_n} = 2\lambda/R$. This resembles the Young-Laplace equation where normally pressure (normal force density) is a global parameter; in this case, $\mathrm{f_n}$ is a local normal force density. In our simulation, we prescribe the area of the applied force and thus we can rewrite the force density as

$$f_n = 4\lambda\sqrt{\frac{\pi}{A_{force}}}. \tag{6.6}$$

In order to generate thin-shaped spines, we first fixed the neck diameter based on the magnitude of tension ($r = \sqrt{\kappa/(2\lambda)}$) as shown in Fig. 6.2D. Similar to filopodia, in thin spines, the radius of the neck is related to the tension and the bending rigidity, given by $r = \sqrt{\kappa/(2\lambda)}$ [343] (Fig. 6.3A). This relationship suggests that in order to have a thin spine with a neck radius between 0.035 μm $< r <$ 0.065 μm (given range in Table 6.1), the tension can vary between 20 pN/μm $< \lambda <$ 80 pN/μm. Based on Eq. 6.6, the magnitude of the normal force density linearly depends on the tension, while it varies as the inverse of the square root of the area of applied force.

In Fig. 6.3B, we plotted the magnitude of the normal force density as a function of tension obtained from numerical solutions (red squares) versus the analytical expression given in Eq. 6.6 (dotted line) for fixed A_{force} = 0.44 μm^2. We found a good agreement between the analytical solution and the results obtained from simulation such that by changing tension between 20 pN/μm $< \lambda <$ 80 pN/μm, the magnitude of the normal force density required to form a thin-shaped spine varies in a large range between 200 pN/μm^2 $< f_n <$ 900 pN/μm^2 (Fig. 6.3B). To further validate our numerical results, we plotted the magnitude of the normal force density as a function of the area of the applied force (A_{force}) obtained from numerical solution (red squares) versus the analytical expression given in Eq. 6.6 (dotted line) for a fixed tension, λ = 36 pN/μm (Fig. 6.3C). We observed a good agreement between the analytical solution and the numerical results where by increasing the area of the applied force from $A_{force} = 0.25$ μm^2 to $A_{force} = 0.55$ μm^2, the magnitude of the normal applied force density needed to form a thin spine decreases from $f_n \sim 500$ pN/μm^2 to $f_n \sim 300$ pN/μm^2 (Fig. 6.3C).

As an example, to form a thin spine with an average neck diameter of r = 0.05 μm (see

Table 6.1), we set our tension to be λ =36 pN/μm (r = $\sqrt{\kappa/(2\lambda)}$). Based on our calculation for λ =36 pN/μm and A_{force} = 0.44 μm^2 (average area of the spine head in Table 6.1), a total normal force density of f_n = 382.23 pN/μm^2 (applied along the red area) is required to form a thin spine with a total length L = 0.98 μm, a neck radius r = 0.05 μm, and a head volume V = 0.033 μm^3 (Fig. 6.3D). Also, in Fig. D.3B, we show that the magnitude of the normal force density needed to form a thin spine is independent of the height of the spine.

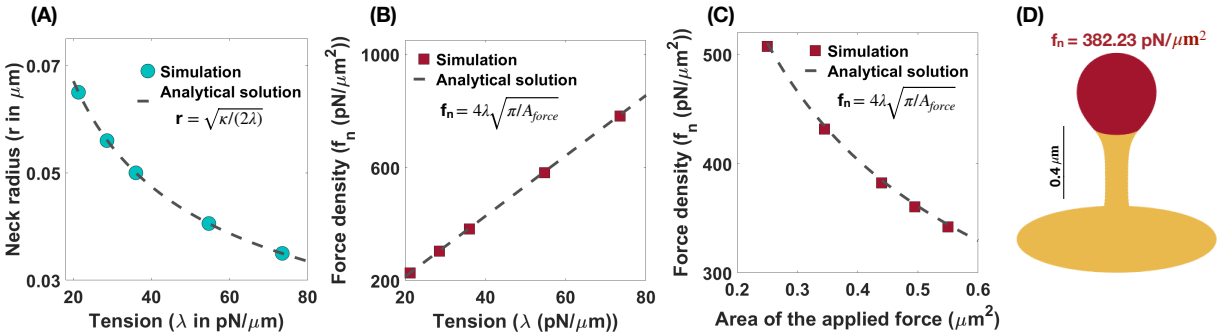

Figure 6.3: Formation of thin-shaped spines with localized normal force density along the spine head. (A) Neck radius of a thin-shaped spine as a function of tension (r = $\sqrt{\kappa/(2\lambda)}$) [343]. (B) Linear relationship between the magnitude of normal force density needed to form a thin-shaped spine and the tension. Here the area of the applied force is set at A_{force} = 0.44 μm^2. The red squares represent the results obtained from simulation and the dashed line is the derived analytical solution ($f_n = 4\lambda\sqrt{\pi/A_{\text{force}}}$, Eq. 6.6). (C) The magnitude of a normal force density needed to form a thin-shaped spine as a function of the area of the spine head. The tension is set at λ =36 pN/μm. The red squares represent the results obtained from our simulations and the dashed line is the derived analytical solution ($f_n = 4\lambda\sqrt{\pi/A_{\text{force}}}$), Eq. 6.6. (D) A thin-shaped spine with a total length L = 0.98 μm, neck radius r = 0.05 μm, and head volume V = 0.033 μm^3 is formed with f_n = 382.23 pN/μm^2 applied along the head of spine which is shown in red (λ =36 pN/μm and A_{force} = 0.44 μm^2).

6.3.3 Non-uniform force distributions can result in mushroom spines

We next asked if changes to the force distributions could result in mushroom-shaped spines. We hypothesized that one possible way is to have a heterogeneous force distribution along the spine head and the PSD area. To understand how non-uniform distributions of normal forces can characterize the morphology of mushroom spines, we performed simulations assuming that

the normal force applied along the PSD area is different from the normal force density applied along the rest of the spine head (Fig. 6.4A).

In the case of mushroom-shaped spines, we have multiple geometric parameters to consider – (a) head volume, (b) area fraction of the PSD, and (c) neck diameter determined by tension. For example, to form a mushroom-shaped spine with a total length L = 1.51 μm, head volume V = 0.25 μm^3, and area of PSD/ area of head ratio = 0.2 (see Table 6.1), normal force densities of f_n = 84.04 pN/μm^2 and $f_{n,PSD}$ = 334.88 pN/μm^2 are required along the spine head (red region) and the PSD area (gray region), respectively (Fig. 6.4A). The value of tension was set to $\lambda = 9$ pN/μm to obtain a neck radius of about r $\approx$ 0.1 μm (see Table 6.1 and Fig. D.4). The magnitude of these force densities is independent of the height of the spine (Fig. D.3C).

We observed that the morphology of the spine head changes with varying magnitude of tension; the spine head flattens for large tensions (Fig. 6.4B). This is consistent with previous studies that have investigated membrane shape at high tensions, e.g., the membrane remains almost flat during vesicle budding [135, 535], or in the case of a red blood cell, the biconcave cell flattens to a pancake shape [9, 449]. To further investigate how a change in the morphology of the spine head can affect the volume of the head, we plotted the volume of the head (V) as a function of tension (Fig. 6.4B). We found that the head volume is a non-monotonic function of tension; as tension increases, the volume of the spine head increases and then decreases (Fig. 6.4B).

This is because initially when increasing tension from low to intermediate values the head flattens and the volume of the head increases. However, for high tensions, the shrinkage of the head becomes dominant and as a result the volume decreases (Fig. 6.4B). Consistent with these observations, a larger normal force is required to bend a stiffer membrane and form a mushroom-shaped spine (Fig. 6.4C). For example, based on our calculation, when increasing tension from λ = 5 pN/μm to λ = 20 pN/μm, the normal force densities in the spine head and PSD area increase by almost 120 pN/μm^2 and 680 pN/μm^2, respectively (Fig. 6.4C).

To study how the ratio of PSD area to the total area of the spine head affects the magnitude of normal force densities, we performed simulations for a range of area of PSD/area of head ratios (Fig. D.5). Our results show that with increasing area of PSD/area of head ratio, a larger normal force density in the spine head and a smaller normal force in the PSD region are required (Fig. D.5A). Additionally, increasing the ratio of the PSD area to the total area of the head results in the flattening of the spine head with a larger volume (Fig. D.5B). Thus, mushroom-shaped spines can be formed from a multitude of mechanical pathways – heterogeneous forces in the spine head, balancing tension and force distributions, and using different area localizations of the forces.

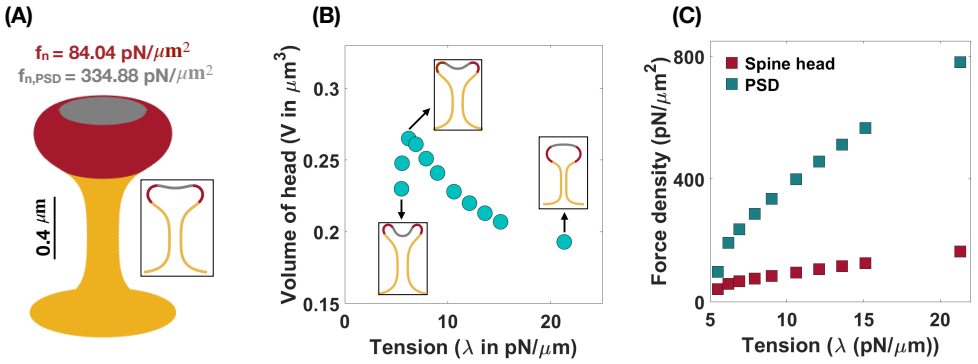

Figure 6.4: Formation of mushroom-shaped spines with localized normal forces along the spine head and PSD. (A) A mushroom-shaped spine with a total length L = 1.51 μm, neck radius r = 0.1 μm, head volume V = 0.25 μm^3, and area of PSD/area of head = 0.2 is formed with f_n = 84.04 pN/μm^2 applied along the head of spine (red domain) and $f_{n,PSD}$ = 334.88 pN/μm^2 applied along the PSD (gray domain) (λ =9 pN/μm). (B) The nonmonotonic behavior of the volume of a mushroom-shaped spine head when increasing tension. Three different shapes of mushroom-shaped spines are shown for low, intermediate, and high tensions. With increasing magnitude of tension, the mushroom-shaped spine head flattens. (C) The magnitude of normal force densities in the spine head (red squares) and in PSD (gray squares) increases with increasing tension.

6.3.4 Induced spontaneous deviatoric curvature by periodic F-actins structures and BAR domain proteins can generate characteristic dendritic spine necks

Recently, super-resolution microscopy methods have revealed the presence of ubiquitous actin ring structures along spine necks [90, 511]. It has been suggested that these ring-like structures and BAR-domain proteins can together support the tubular shape of dendritic spines [505, 536]. To understand how periodic F-actin structures and BAR domain proteins can regulate the tubular shape of spine necks, we implemented their net effect in our model by including spontaneous deviatoric curvature in the energy density of the system (Eq. 6.3) [176, 178, 181, 324, 526].

Consider a tubular membrane with radius r and a spontaneous deviatoric curvature D_m along the neck with total length l (Fig. 6.1A), the equilibrium radius in the presence of spontaneous deviatoric curvature is given by $r = \sqrt{\kappa/(2(\lambda + \kappa D_m^2))}$ (Eq. D.36). Since this radius depends on both the value of tension and the spontaneous deviatoric curvature (Fig. 6.5A), we define an effective tension $(\lambda + \kappa D_m^2)$. As a result, the relationship between neck radius, spontaneous deviatoric curvature, and tension in Fig. 6.5A collapses onto a single curve (Fig. D.6B) as a function of this effective tension. Simulations confirm that the radii of tubular necks obtained from numerical solutions collapse onto a single curve as a function of effective tension (Fig. 6.5B).

Similarly, the axial force required to maintain a tubular membrane with radius r and spontaneous deviatoric curvature D_m along the total length L, is given by $F_z = 2\pi(\sqrt{2\kappa(\lambda + \kappa D_m^2)} - \kappa D_m)$ (Eq. D.36). In Fig. 6.5C, we plotted the axial force as a function of tension and spontaneous deviatoric curvature. We found that the axial force has a local minimum along the red line (Fig. 6.5C) where $\lambda = \kappa D_m^2$ (Eq. D.37) and $F_{z,min} = 2\pi\kappa D_m$ (Eq. D.37). The 3D surface in Fig.

6.5C can be reduced to a single curve by defining the effective axial force as $F_z + 2\pi\kappa D_m$ and plotting it as a function of effective tension (Fig. D.6D). We also plotted the effective axial force obtained from numerical solutions as a function of effective tension (Fig. 6.5D). We observed that consistent with the analytical prediction, for different tensions, the effective axial forces collapse onto a single curve as a function of effective tension (Fig. 6.5D). These results suggest that effective tension ($\lambda + \kappa D_m^2$) regulates the radius of dendritic spine necks.

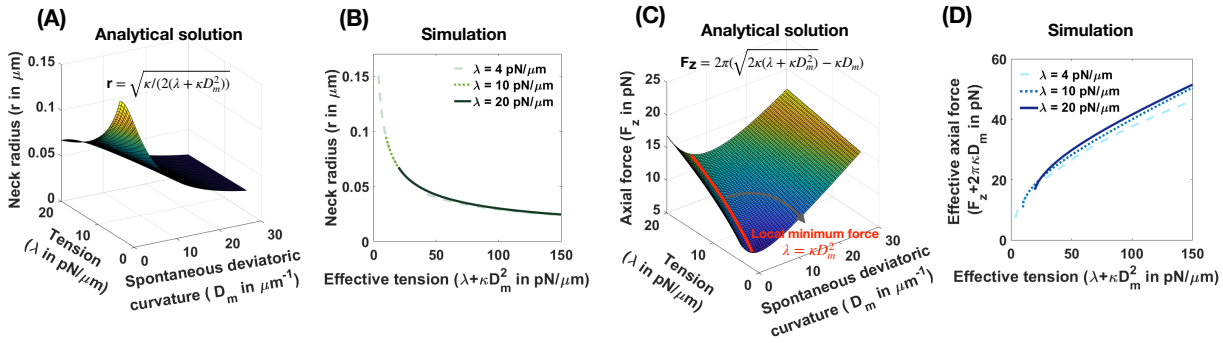

Figure 6.5: Effective tension including spontaneous deviatoric curvature regulates the neck radius and the magnitude of axial force in a tubular membrane. (A) Analytical solution for the neck radius of a tubular membrane as a function of spontaneous deviatoric curvature and tension ($r = \sqrt{\kappa/(2(\lambda + \kappa D_m^2))}$, Eq. D.36). (B) The neck radius obtained from numerical solutions as a function of effective tension ($\lambda + \kappa D_m^2$). Here, for fixed three different tensions, we varied the effective tension by changing the spontaneous deviatoric curvature between $0 < D_m < 30\ \mu m^{-1}$. The radii of the membrane necks collapse onto a single curve for different tensions. (C) Analytical solution for the magnitude of an axial force needed to maintain a tubular protrusion as a function of spontaneous deviatoric curvature and tension ($F_z = 2\pi(\sqrt{2\kappa(\lambda + \kappa D_m^2)} - \kappa D_m)$, Eq. D.36). The axial force needed to maintain a tubular protrusion has a local minimum along the red line where $\lambda = \kappa D_m^2$ (Eq. D.38). (D) The effective axial force ($F_z + 2\pi\kappa D_m$) obtained from numerical solutions as a function of effective tension ($\lambda + \kappa D_m^2$). Here, for fixed three different tensions, we varied the effective tension by changing the spontaneous deviatoric curvature between $0 < D_m < 30\ \mu m^{-1}$. Effective axial forces collapse onto a single curve for different tensions.

6.3.5 Cooperation of forces and induced spontaneous deviatoric curvature offers multiple pathways for spine shape maintenance

Thus far, we have focused on the role of forces (axial and normal) on spine head shape and the role of spontaneous deviatoric curvature representing periodic rings on the spine neck radius. Next, we asked if the cooperation of these two different mechanisms could further influence the spine geometries and the energy landscape associated with these features. In other words, we asked if the combination of spontaneous deviatoric curvature and applied forces could result in lower energy states for the same spine geometry. To answer this question, we sought to identify the parameters that give rise to thin spines with the same geometric parameters. We explain this approach with a specific example below.

As noted before, when only normal forces are used, a normal force density of $f_n = 382.23$ pN/μm^2 under a tension of $\lambda = 36$ pN/μm is required to form a thin spine with a neck radius of $r = 0.05$ μm and head volume of $V = 0.033$ μm^3 (Fig. 6.6A, left). We can also obtain a thin spine with the same dimensions, by using a prescribed spontaneous deviatoric curvature $D_m = 10$ μm^{-1} along the neck and an applied force density of $f_n = 143.33$ pN/μm^2 along the head for $\lambda = 10$ pN/μm (Fig. 6.6A, right). Thus, for the same shape parameters, in the presence of spontaneous deviatoric curvature, the value of force density required is roughly one-third of the force density required in the absence of spontaneous deviatoric curvature (Fig. 6.6A). Similarly, when a combination of axial force along the spine head and spontaneous deviatoric curvature along the neck is used, a thin spine with $r \sim 0.05$ μm and head volume $V \sim 0.033$ μm^3 can be formed with $F_z = 7.71$ pN and spontaneous deviatoric curvature $D_m = 10$ μm^{-1} when $\lambda = 10$ pN/μm (Fig. 6.6B). Thus, in both these cases (axial and normal forces) for the formation of thin spines, we note that access to spontaneous deviatoric curvature significantly reduces the forces required to form and maintain thin spines.

Not surprisingly, these same results hold for mushroom-shaped spines too. As we have

shown before, to form a mushroom spine with a neck radius of r = 0.1 μm and head volume of V $\sim$ 0.25 μm^3, normal force densities of f_n = 84.04 pN/μm^2 along the spine head and $f_{n,PSD}$ = 334.88 pN/μm^2 along the PSD are required under a tension of λ = 9 pN/μm (Fig. 6.6C, left). We can also form a mushroom spine with the same dimensions and lower tension (λ = 5.5 pN/μm) by prescribing a spontaneous deviatoric curvature D_m = 1.8 μm^{-1} along the spine neck and normal force densities of f_n = 57.14 pN/μm^2 and $f_{n,PSD}$ = 154 pN/μm^2 along the spine head and PSD, respectively (Fig. 6.6C, right).

In Figs. 6.6D-F, we plotted the magnitude of forces that are required to form thin and mushroom-shaped spines with or without spontaneous deviatoric curvature as a function of tension alone (with no spontaneous deviatoric curvature) or effective tension (with spontaneous deviatoric curvature). We observed that with increasing effective tension, the magnitude of the normal force density that is required to form a thin spine with spontaneous deviatoric curvature (red squares) is almost constant (Fig. 6.6D). However, the magnitude of the normal force density that is needed to form a thin spine without spontaneous deviatoric curvature (dashed line) increases linearly with increasing tension (Eq.6.6 and Fig. 6.6D). In the case of the formation of a thin spine with an axial force, we found that in the presence of spontaneous deviatoric curvature, the magnitude of axial force (blue squares) decreases slightly and then becomes constant with increasing effective tension (Fig. 6.6E). In contrast, without spontaneous deviatoric curvature, the magnitude of axial force (dashed line) increases with increasing tension (Fig. 6.6E). Similar to the thin-shaped spine, with spontaneous deviatoric curvature along the spine neck, the magnitude of normal force densities in the head (red square) and PSD (gray square) region that are required to form a mushroom spine is almost constant with increasing effective tension (Fig. 6.6F). However, without spontaneous deviatoric curvature, the magnitude of force densities in both regions increases with increasing tension (Fig. 6.6F).

To further compare thin and mushroom spines shown in Fig. 6.6, we computed the

components of energy (Eq. 6.1) and the total energy of the system for each shape (Tables D.3 & D.4 and Figs. 6.7C & D). Based on our results, by prescribing spontaneous deviatoric curvature D_m along the spine neck, the bending energy due to deviatoric curvature decreases (Tables. D.3 & D.4). This is because the deviatoric curvature D along the neck tends to D_m and minimizes the bending energy (Tables D.3 & D.4). Additionally, in the presence of spontaneous deviatoric curvature, in our simulation, we set the tension to lower values compared to the condition that $D_m = 0$. Therefore, the work that is done by tension and forces to bend the membrane reduces for the case that the spines obtained with a combination of force and spontaneous deviatoric curvature (Tables. D.3 & D.4). For example, to form a thin spine shown in Fig. 6.6, the work that is done by an axial force with a spontaneous deviatoric curvature (Fig. 6.6B) is almost one third of the work that is done by a normal force without spontaneous deviatoric curvature (Fig. 6.6A and Tables. D.3 & D.4).

In the bar plots of Figs. 6.7C &D, we compared the total energy of thin and mushroom spines formed with different mechanisms. We observed that in both thin and mushroom spines, the total energy of the system dramatically decreases when the spines form with a combination of forces and spontaneous deviatoric curvature (Figs. 6.7C &D). This result suggests that spontaneous deviatoric curvature can alter the energy landscape of thin and mushroom dendritic spines to a lower energy state.

6.4 Discussion

In this thesis, we present a simplified mechanical model for studying the role of different force distributions and energy contributions that are associated with the different spine shapes noted in the literature. Our results show that different spine shapes can be associated with different forces and spontaneous deviatoric curvature distributions, giving us insight into the mechanical

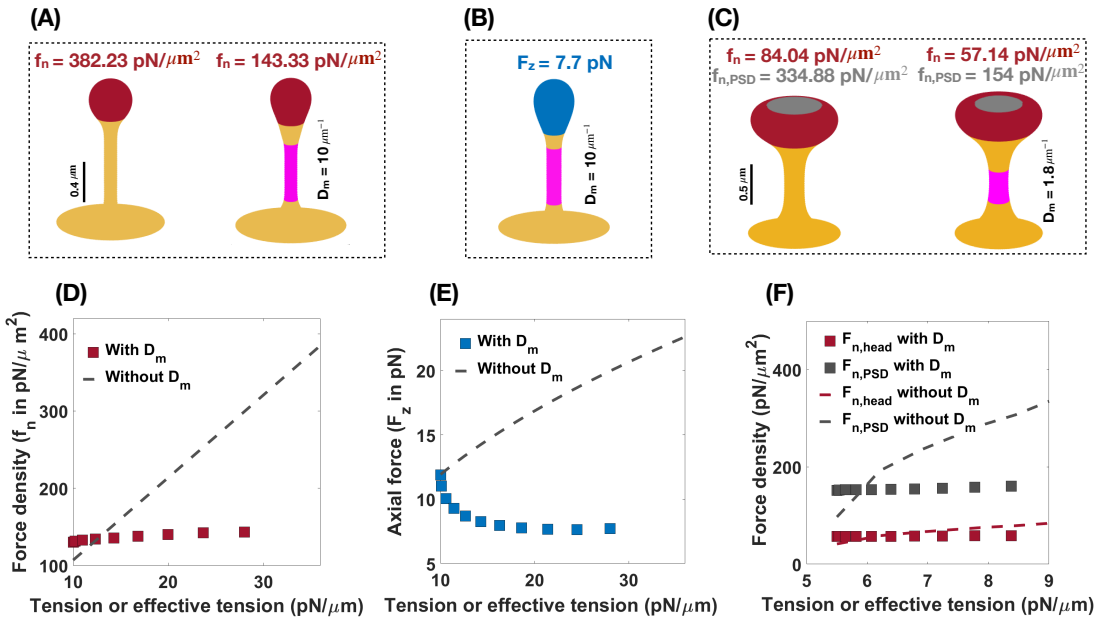

Figure 6.6: Formation of thin and mushroom shaped spines with a combination of forces and spontaneous deviatoric curvature. (A) Formation of a thin-shaped spine by applying a uniform normal force density along the spine head (left) versus applying a uniform normal force density along the head and spontaneous deviatoric curvature (purple region) along the spine neck (right) (λ =10 pN/μm). (B) Formation of a thin-shaped spine by applying an axial force along the spherical cap (blue region) and spontaneous deviatoric curvature along the spine neck (purple region), λ =10 pN/μm. All thin spines in panels A and B have a neck radius r $\sim$ 0.05 μm and head volume V $\sim$ 0.033 μm^3. (C) Formation of a mushroom-shaped spine by applying a non-uniform normal force density along the spine head (left) versus applying a non-uniform normal force density along the head and spontaneous deviatoric curvature along the spine neck (purple region), (right), λ =5.5 pN/μm. The formed mushroom spine with normal force densities f_n = 57.14 pN/μm^2 and $f_{n,PSD}$ = 154 pN/μm^2 and deviatoric curvature D_m = 1.8 μm^{-1} has a neck radius r $\sim$ 0.1 μm and head volume V $\sim$ 0.27 μm^3. (D) The magnitude of a normal force density that is required to form a thin-shaped spine with and without spontaneous deviatoric curvature as a function of effective tension and tension, respectively. (E) The magnitude of an axial force that is required to form a thin-shaped spine with and without spontaneous deviatoric curvature as a function of effective tension and tension, respectively. (F) The magnitude of normal force densities in the spine head and in PSD that is required to form a mushroom spine with and without spontaneous deviatoric curvature as a function of effective tension and tension, respectively.

design principles of spine formation and maintenance (Fig. 6.7).

We show that stubby spines can be formed for a wide range of tensions and low forces (Fig. 6.2). From a spine formation viewpoint, this makes sense, since during development the

stubby spines can be the initial protrusions that form out of the dendrites. Given the ubiquitous nature of stubby spines [475, 483, 489], our results suggest that the prevalence of stubby spines could be due to the mechanical ease which they can be formed. They may also represent a temporarily stable state adopted by shrinking spines during synapse removal. Filopodia have the same force-length and force-radius relationships as membrane tubules that can be formed with micropipettes [537], optical tweezers [538], or by kinesin motor proteins [539] (Fig. 6.2). Based on our results, dendritic filopodia can be formed with a relatively small axial force, which make them good candidates as initial protrusions for the formation of mature thin and mushroom spines. Thin and mushroom spines, which have defined head shapes, require more mechanical features – heterogeneous force distributions, normal or axial forces, and an induced spontaneous deviatoric curvature representing the periodic protein rings or other deviatoric curvature inducing mechanics along the neck.

In the case of thin spines, we find that the mechanical design principles that support the formation of a spherical head are (1) large normal force along the head (Fig. 6.3), (2) normal force along the head with a spontaneous deviatoric curvature along the neck (Fig. 6.6A), and (3) an axial force along the head with a spontaneous deviatoric curvature along the neck (Fig. 6.6B). Within these mechanisms, the presence of spontaneous deviatoric curvature significantly reduces the total energy of the spine (Fig. 6.7C). Similarly, for mushroom spines, in addition to non-uniform forces along the head and the PSD (Fig. 6.4), the spine can be formed with a combination of forces in the head and spontaneous deviatoric curvature along the neck (Fig. 6.6C) while the spontaneous deviatoric curvature results in a lower energy state (Fig. 6.7D).

These findings have implications for our understanding of how mechanical aspects of membrane dynamics such as bending, tension, membrane-protein interactions, and interactions of the membrane with the cytoskeleton play critical roles in spine geometry maintenance, particularly in structural plasticity. Many of the events associated with synaptic plasticity alter spine size

and shape through changes in F-actin dynamics and the dynamics of the actin related proteins [83, 505, 506]. The net impact of changes in actin remodeling would likely result in changes in force distribution. Another important and, as yet, under explored aspect of synaptic plasticity is the role of cortical membrane tension, including the effect of the membrane in-plane stresses and membrane-cytoskeleton interactions. We know that spines are sites of active vesicle trafficking events, such as endo- and exocytosis, and that these processes alter the membrane surface area and thereby alter the membrane tension [540, 541]. Here, we show that the effective membrane tension can play an important role in altering the energy required for the maintenance of different spine shapes. One of the main impacts of such effective tension is that because of the cooperative effects of spontaneous deviatoric curvature and the applied forces, the energy required to maintain certain spine shapes may be lower. Thus, we show that there are different mechanical pathways that are likely associated with the different spine shapes and that some mechanisms may be energetically more favorable than others.

Despite these insights, our model has certain limitations. We do not explicitly consider the remodeling of the actin network or the dynamics of the associated proteins, but use force as a lumped parameter. Additionally, the use of axisymmetric coordinates restricts our ability to obtain realistic spine shapes [542].

The impact of mechanical aspects of actin remodeling and membrane mechanics on structural plasticity is highly intriguing and we are only beginning to understand their effects on spine functionality. This complexity is immediately apparent in dendritic spines, which undergo dynamic changes, both mechanical and biochemical during structural plasticity spatiotemporal scales. Our minimal model provides insights into the possible mechanical aspects underlying the characteristic geometries associated with dendritic spines. This is an important step towards deciphering the intricate mechanochemistry of structural plasticity and dendritic spine development.

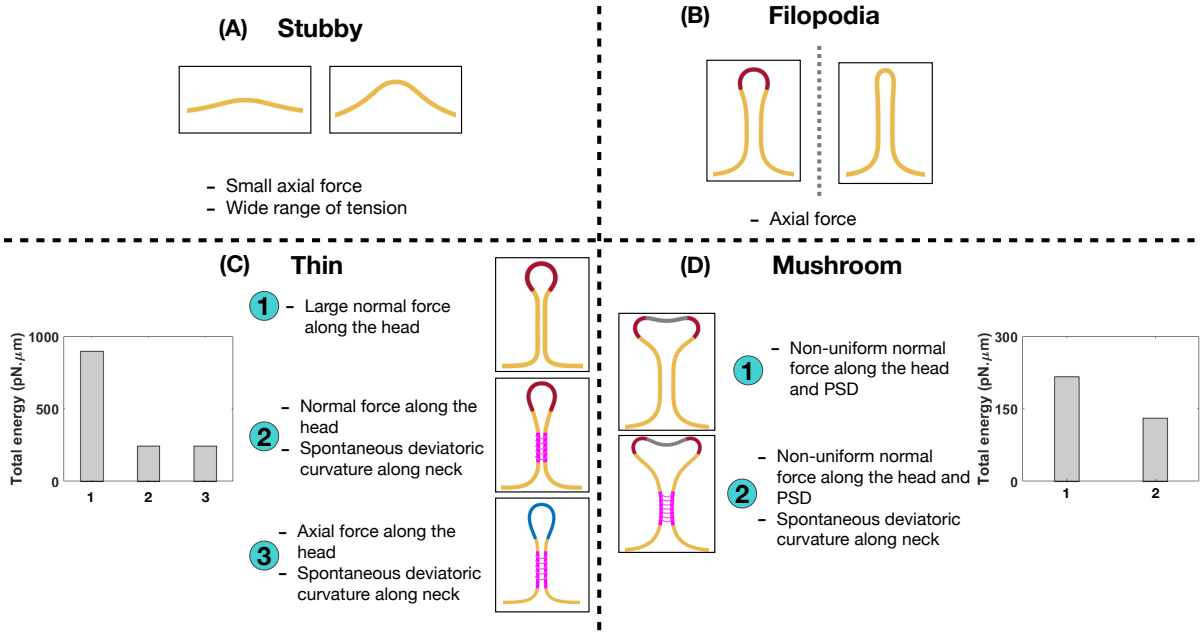

Figure 6.7: Characterizing different shapes of dendritic spines based on the mechanical model. (A) Stubby spines can be formed with an axial force and in a wide range of tensions. (B) An axial force is sufficient to form a long filopodial spine. (C) A thin-shaped spine can be formed with three different mechanisms; (1) a uniform normal force density along the spine head, (2) a uniform normal force density along the spine head and spontaneous deviatoric curvature along the neck, and (3) a uniform axial force density along the spine head and spontaneous deviatoric curvature along the neck. In the bar plot, the total energy of the system is shown for three different mechanisms. The total energy of the system for the second and third mechanisms with spontaneous deviatoric curvature is much less than the energy for the first mechanism with just a normal force. (D) A mushroom-shaped spine can be formed with two different mechanisms; (1) a non-uniform normal force density along the spine head and PSD region and (2) a non-uniform normal force density along the spine head and PSD region plus a spontaneous deviatoric curvature along the spine neck. The resulting mushroom spine with a combination of normal forces and spontaneous deviatoric curvature has lower energy compared to the spine that is formed with just normal forces (bar graph).

6.5 Acknowledgements

I would like to acknowledge my co-authors Miriam Bell, Prof. Shelley Halpain, and Prof. Padmini Rangamani.

Chapter 7

Summary and future work

Cell shape and function are intricately coupled; cells must maintain specific shapes to migrate, divide normally, form tissues and organs during development, and support their physiological functions. To dynamically alter the membrane curvature, cells harness diverse mechanisms of curvature generation from membrane-protein interactions to cytoskeletal forces. Each mechanism generates unique surface stresses on the membrane, and these surface stresses can be mapped onto the shape to understand the mechanical aspects of the membrane deformation. Currently, modern advances in high-resolution imaging technologies have provided a vast amount of information about morphological and the intracellular machinery underlying the cell membrane deformation. However, it remains difficult to experimentally image membrane deformations due to the small length and timescales.

In this dissertation, we develop theoretical to study the physics underlying membrane deformation by curvature-inducing proteins and forces exerted by the cytoskeleton. We propose (i) an approach to extract effective line tension at the protein interface based on the morphology and the composition of the membrane (Chapter 3), (ii) the local heterogeneity in the membrane properties drives the beading morphology of membrane nanotubes (chapter 4), (iii) a new molecu-

lar mechanism –a non-uniform force distribution coupled with membrane tension– to maintain the unique biconcave shape of RBCs (Chapter 5), and (iv) a minimal biophysical model of membrane-actin interactions to characterize the classic spine shapes. The following sections summarize the contributions of this dissertation and outlinethe future directions (Chapter 6).

7.1 Thesis summary

7.1.1 Membrane curvature generation by proteins

Cellular membranes take on an elaborate set of highly curved and bent shapes which are essential to diverse cellular functions. The interaction between cellular membrane and membrane proteins is one of the major sources of the curvature production in cells. In Chapter 3, we presented a framework for the calculation of axial and radial tractions for nonlinear deformations of the membrane in the presence of heterogeneities, solely based on the membrane geometry and material properties [6]. This allowed us to to extract effective line tension at the membrane-protein interface based on the morphology and the composition of membrane, while experimentally measuring line tension is still challenging [6]. Also, in Chapter 3, we used our membrane continuum model to show that protein phase separation on membrane surfaces generates considerable stresses that can drive the spontaneous assembly of membrane buds and tubules with physiologically relevant dimensions [7]. Our theoretical model predicted that tubule diameter should increase with increasing membrane rigidity and increasing rigidity ratio, trends confirmed by experiments (Chapter 3) [7]. In Chapter 4, we studied the role of membrane mechanics in governing the architecture of membrane nanotubes [5]. We showed that the formation of bead-like structures along the nanotubes can result from local heterogeneities in the membrane either due to protein aggregation or due to membrane composition [5].

7.1.2 Membrane curvature generation by cytoskeleton

The spectrin-actin network of the membrane skeleton plays an important role in controlling specialized cell membrane morphology. In the paradigmatic red blood cell (RBC), where actin filaments are present exclusively in the membrane skeleton, recent experiments reveal that nonmuscle myosin IIA (NMIIA) motor contractility maintains the RBC biconcave disk shape [82]. In Chapter 5, we have identified criteria for micron-scale distributions of NMIIA forces at the membrane required to maintain the biconcave disk shape of an RBC in the resting condition [9]. Supported by experimental measurements of RBC NMIIA distribution, we showed that a heterogeneous force distribution with a larger force density at the dimple is able to capture the experimentally observed biconcave morphology of an RBC with better accuracy compared to previous models that did not consider the heterogeneity in the force distribution (Chapter 5) [9]. In addition to playing a key role in RBC morphology, membrane-actin interactions are also thought to play an important role in governing the geometries of dendritic spines. In Chapter 6, we developed a mathematical model of actin-mediated forces, curvature-inducing actin or protein rings, and membrane dynamics that can regulate the shape and size of dendritic spines [10]. Using our model, we identified the possible force regimes that give rise to the classic spine shapes and investigate how the spine neck might be stabilized using periodic rings of actin or associated proteins [10]. We also used our model to predict that the cooperation between actin-mediated forces, cortical tension, and induced spontaneous deviatoric curvatures can change the energy landscape, providing various mechanical pathways to sustain different spine shapes (Chapter 6) [10, 543].

7.2 Future direction

Although the current membrane continuum models have provided insight into the molecular machinery of cell shape regulation, all of them have been developed based on simplifying assumptions that need to be revisited in the pursuit of closing the gap between experiment and theory. In order to achieve this goal, multidisciplinary efforts between physicists, mathematicians, engineers, and biologists are required to match different pieces of this cell biology puzzle. Here, we highlight some current challenges that we believe must be considered in the next generation of continuum models.

- Membrane deformation is a dynamic process, surrounding fluid flow, thermal fluctuation, and diffusion of proteins actively regulate the shape of the membrane at each instance [202, 307, 544–547]. Currently, the models for membranes at mechanical equilibrium are well-developed but the models for dynamic processes have not been as well-developed and the community must invest some effort in this aspect.

- In vivo, multiple mechanisms coupling membrane deformation and cytoskeletal remodeling are commonplace (Figure 7.1A). Therefore, the models should be extended to include dynamic effects and the rearrangement of the actin cytoskeleton underneath of the membrane.

- Membrane deformation and protein absorption/rearrangement are often considered as two separate processes with little to no impacts on each other. However, recent studies show that proteins can sense the membrane curvature (Figure 7.1B). Therefore, there is a feedback loop between the protein distribution and the membrane configuration. While some models have considered this feedback loop [189, 548–551], we still need more quantitative agreements between theory and experiment.

- Cell shape can control signal transduction at the plasma membrane, and on the other hands, intracellular signaling changes the membrane tension [552] (Figure 7.1C). This

coupling between the cell shape and the signaling network inside the cell should be further understood in terms of both quantitative experimental and theoretical biology.

- As discussed above, membrane deformation is a multiscale phenomena that results from the reorientation of lipids to large-scale change in the membrane curvature. This suggests the extension of available models toward multiscale models that could represent each biological process over multiple lengths scales [553, 554].

Despite these challenges, with increasingly quantitative measurement techniques available experimentally, ease of access to high throughput computing systems, and interdisciplinary training of the next generation of scientist leaders, the future of theoretical modeling of biological membranes and cellular membrane processes is brighter than ever.

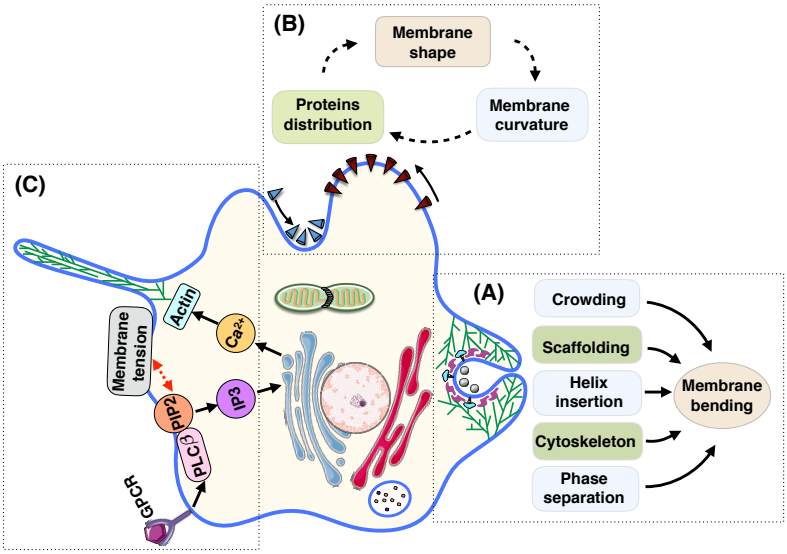

Figure 7.1: Perspective for the future of theoretical models for membrane curvature generating mechanisms. (A) Various mechanisms are involved in trafficking (B) The coupling between membrane shape, membrane curvature, and membrane proteins distribution. The convex proteins (indicated with red cones) aggregate and flow toward the hill where the membrane curvature is negative (assuming the normal vector to the surface is outward). On the other hand, the concave proteins (represented by blue cones) accumulate and move toward the valley where the membrane curvature is large and positive [189]. (C) The coupling between the formation of a filopodial protrusion and the intracellular signaling inside the cell.

Appendix A

Derivation of traction stresses

A.1 Table of notation

Table A.1: Notation used in the Chapter 3

Notation	Description	Units
E	Strain energy	$\mathrm{pN}\cdot\mathrm{nm}$
p	Pressure difference across the membrane	$\mathrm{pN}/\mathrm{nm}^2$
C	Spontaneous curvature	nm^{-1}
θ^α	Parameters describing the surface	
W	Local energy per unit area	pN/nm
$\mathbf{r}$	Position vector	
$\mathbf{n}$	Normal to the membrane surface	unit vector
$m\nu$	Tangent to the membrane surface in direction of increasing arc length	unit vector
$m\tau$	Rightward normal in direction of revolution	unit vector
$\mathbf{a}_\alpha$	Basis vectors describing the tangent plane	
λ	Membrane tension, $-(W+\gamma)$	pN/nm
H	Mean curvature of the membrane	nm^{-1}
K	Gaussian curvature of the membrane	nm^{-2}
D	Deviator curvature of the membrane	nm^{-2}
κ	Bending modulus	$\mathrm{pN}\cdot\mathrm{nm}$
κ_G	Gaussian modulus	$\mathrm{pN}\cdot\mathrm{nm}$
s	Arc length	nm
θ	Azimuthal angle	
ψ	Angle between $\mathbf{e}_r$ and $\mathbf{a}_s$	

Table A.2: Notation used in the Chapter 3

Notation	Description	Units
$\mathbf{e}_r(\theta)$	Radial basis vector	unit vector
$\mathbf{e}_\theta$	Azimuthal basis vector	unit vector
$\mathbf{k}$	Altitudinal basis vector	unit vector
$\mathbf{F}$	External force	pN
$\mathbf{f}$	Applied force per unit area	$\mathrm{pN}/\mathrm{nm}^2$
κ_τ	Transverse curvature	nm^{-1}
κ_ν	Tangential curvature	nm^{-1}
τ	Surface twist	nm^{-1}
$\tilde{\mathbf{f}}$	Traction (force per unit length)	pN/nm
$\tilde{f}_r$	Component of traction in radial direction	pN/nm
$\tilde{f}_z$	Component of traction in axial direction	pN/nm
$\tilde{f}_n$	Component of traction in normal direction	pN/nm
$\tilde{f}_\nu$	Component of traction in transverse direction	pN/nm
$\tilde{F}_z$	Calculated force in axial direction	pN
ξ	Energy per unit length	pN
M	Bending couple	$\mathrm{pN}\cdot\mathrm{nm}$
t	Arc length around curve of revolution	nm
a	Membrane area in mapped coordinate	nm^2
A	Membrane area in referenced frame	nm^2
γ	unit vector representing orientation of a protein coat	
μ	unit vector normal to γ and $\mathbf{n}$	
κ_{coat}	Bending modulus along protein coat	$\mathrm{pN}\cdot\mathrm{nm}$
D_0	Spontaneous membrane curvature deviator	nm^{-1}
κ_{mean}	Mean value of bending modulus	$\mathrm{pN}\cdot\mathrm{nm}$
κ_{error}	Error in bending modulus	$\mathrm{pN}\cdot\mathrm{nm}$
λ_{mean}	Mean value of membrane tension	pN/nm
λ_{error}	Error in membrane tension	pN/nm
V	Confined volume by membrane area	nm^3
s_{max}	Maximum arc length at the base	nm
R_0	Patch radius	nm
κ	Bending rigidity of bare membrane	$\mathrm{pN}\cdot\mathrm{nm}$
λ_0	Surface tension at boundary	pN/nm
L	Shape equation variable	nm^{-1}
x	Dimensionless radial distance	
y	Dimensionless height	
h	Dimensionless mean curvature	
c	Dimensionless spontaneous curvature	
l	Dimensionless L	

A.2 Model development

A.2.1 Assumptions

- Membrane curvature generated due to forces or protein-induced spontaneous curvature is much larger than the thickness of the bilayer. Based on this assumption, we model the lipid bilayer as a thin elastic shell with a bending energy given by the Helfrich-Canham energy, which is valid for radii of curvatures much larger than the thickness of the bilayer [133,351].

- We neglect the surrounding fluid flow or inertial dynamics and assume that the membrane is in mechanical equilibrium at all times [305]. This assumption is commonly used in the modeling of membrane curvature to keep the mathematics tractable [150].

- The membrane is incompressible because the energetic cost of stretching the membrane is high [352]. This constraint is implemented using a Lagrange multiplier.

- Finally, for simplicity in the numerical simulations, we assume that the membrane in the region of interest is rotationally symmetric (Fig. 3.2).

A.2.2 Equations of motion

At equilibrium, the integration of local energy density (W) over the total membrane surface area ω gives the strain energy of the system written as [180, 183, 266]

$$E = \int_{\omega} W(H,K,D;\theta^{\alpha})da, \tag{A.1}$$

where E is total strain energy, H is the mean curvature of the surface, K is the Gaussian curvature, D is the curvature deviator, and θ^{α} $\{\alpha = 1,2\}$ denotes the surface coordinate.

To impose the area incompresibility condition, we can rewrite the energy equation Eq. A.1 using a Lagrange multiplier

$$E = \int_{\omega} [JW(H,K,D;\theta^{\alpha}) + \lambda(\theta^{\alpha})(J-1)]dA, \tag{A.2}$$

where λ is a Lagrange multiplier and

$$J = \sqrt{a/A}, \tag{A.3}$$

is the local areal stretch due to mapping from a reference frame to the actual surface.

Minimization of the energy Eq. A.2 by usage of the variational approach gives the governing shape equation and the incompressibility condition in a heterogeneous membrane

$$\begin{aligned} p + \mathbf{f}\cdot\mathbf{n} = \Delta\frac{1}{2}W_H + (W_K)_{;\alpha\beta}\tilde{b}^{\alpha\beta} + W_H(2H^2 - K) + 2H(KW_K - W) - 2\lambda H \\ + \frac{1}{2}[W_D(\gamma^{\alpha}\gamma^{\beta} - \mu^{\alpha}\mu^{\beta})]_{;\beta\alpha} + \frac{1}{2}W_D(\gamma^{\alpha}\gamma^{\beta} - \mu^{\alpha}\mu^{\beta})b_{\alpha\xi}b^{\xi}_{\beta}, \end{aligned} \tag{A.4}$$

and

$$(\frac{\partial W}{\partial x^{\alpha}}_{|exp} + \lambda_{,\alpha} + W_D[b_{\alpha\beta}(\gamma^{\alpha}\gamma^{\beta})_{;\eta}])a^{\beta\alpha} = \mathbf{f}\cdot\mathbf{a}_s. \tag{A.5}$$

where $\Delta(\cdot)$ is the surface Laplacian, p is the pressure difference across the membrane, $\mathbf{f}$ is any externally applied force per unit area on the membrane, $\mathbf{n}$ is the normal vector to the surface, $\mathbf{a}_s$ is the tangent vector on surface, $a^{\alpha\beta}$ is the dual metric, $b_{\alpha\beta}$ are the coefficients of the second fundamental form, b^{α}_{β} are the mixed components of the curvature, $\tilde{b}^{\alpha\beta}$ is the co-factor of the curvature tensor, and $()_{|exp}$ denotes the explicit derivative with respect to coordinate θ^{α}. Also, γ^{α}

and μ^{α} are the projections of $m\gamma$ and $m\mu$ along the tangential vectors with

$$\begin{aligned} \gamma^{\alpha} &= m\gamma \cdot \mathbf{a}^{\alpha}, \\ \mu^{\alpha} &= m\mu \cdot \mathbf{a}^{\alpha} \end{aligned} \tag{A.6}$$

where $m\gamma$ is a unit vector representing the orientation of a protein coat tangential to the one-dimensional curve on the surface, and $m\mu$ is a unit vector defined by

$$m\mu = \mathbf{n} \times m\gamma \tag{A.7}$$

In what follows, we explore different commonly used forms of energy as follows

(i). Helfrich energy for isotropic spontaneous curvature

(ii). Helfrich energy for anisotropic spontaneous curvature

Helfrich energy for isotropic spontaneous curvature

For a lipid bilayer membrane, we use a modified version of the Helfrich energy to account for the spatial variation of spontaneous curvature [136, 137],

$$W = \kappa(\theta^{\alpha})(H - C(\theta^{\alpha}))^2 + \kappa_G(\theta^{\alpha})K, \tag{A.8}$$

C is the spontaneous curvature, and κ and κ_G are bending and Gaussian modulii respectively, which in general case of heterogeneous membrane can vary along thesurface coordinate. It should be mentioned that Eq. A.8 is different from the standard Helfrich energy by a factor of 2. We take this net effect into consideration by choosing the value of the bending modulus to be twice that of the standard value of bending modulus typically used for lipid bilayers [133].

Substituting the Helfrich energy function Eq. A.8, in Eqs. A.4 and A.5

$$\underbrace{\kappa\Delta\left[(H-C)\right]+2H\Delta\kappa_G-(\kappa_G)_{;\alpha\beta}+2\kappa(H-C)\left(2H^2-K\right)-2\kappa H\left(H-C\right)^2}_{\text{Elastic Effects}}$$

$$=\underbrace{p+2\lambda H}_{\substack{\text{Capillary}\\ \text{effects}}}+\underbrace{\mathbf{f}\cdot\mathbf{n}}_{\substack{\text{Force induced}\\ \text{variation}}}, \tag{A.9}$$

and

$$\underbrace{\lambda_{,\alpha}}_{\substack{\text{Gradient of}\\ \text{surface tension}}}=\underbrace{-\frac{\partial\kappa}{\partial\theta^\alpha}(H-C)^2}_{\substack{\text{bending modulus}\\ \text{-induced variation}}}+\underbrace{2\kappa(H-C)\frac{\partial C}{\partial\theta^\alpha}}_{\text{Protein-induced variation}}-\underbrace{\frac{\partial\kappa_G}{\partial\theta^\alpha}}_{\substack{\text{Gaussian modulus}\\ \text{-induced variation}}}-\underbrace{\mathbf{f}\cdot\mathbf{a}_\alpha}_{\substack{\text{Force induced}\\ \text{variation}}}. \tag{A.10}$$

Helfrich energy for an anisotropic curvature

In order to represent anisotropic curvature generated due to membrane-proteins interactions, we consider the local energy density function as [180, 266]

$$W=\kappa(\theta^\alpha)(H-C(\theta^\alpha))^2+\kappa(\theta^\alpha)(D-D_0)^2+\kappa_G(\theta^\alpha)K, \tag{A.11}$$

where D_0 is spontaneous membrane curvature deviator. Substituting this form of energy density Eq. A.11 in Eqs. A.9 and A.10 give

$$\underbrace{\kappa\Delta\left[(H-C)\right]+2H\Delta\kappa_G-(\kappa_G)_{;\alpha\beta}+2\kappa(H-C)\left(2H^2-K\right)-2\kappa H\left(H-C\right)^2}_{\text{Elastic Effects}}$$

$$+\underbrace{\left[\kappa(D-D_0)(\gamma^\alpha\gamma^\beta-\mu^\alpha\mu^\beta)\right]_{;\beta\alpha}+\kappa(D-D_0)(\gamma^\alpha\gamma^\beta-\mu^\alpha\mu^\beta)b_{\alpha\xi}b^\xi_\beta}_{\text{Deviotoric effects}}=\underbrace{p+2\lambda H}_{\text{Capillary effects}}+\underbrace{\mathbf{f}\cdot\mathbf{n}}_{\substack{\text{Force induced}\\ \text{variation}}}, \tag{A.12}$$

and

$$\underbrace{\lambda_{,\alpha}}_{\substack{\text{Gradient of}\\ \text{surface tension}}} = \underbrace{-\frac{\partial \kappa}{\partial \theta^{\alpha}}(H-C)^2}_{\substack{\text{bending modulus}\\ \text{-induced variation}}} + \underbrace{2\kappa(H-C)\frac{\partial C}{\partial \theta^{\alpha}}}_{\text{Protein-induced variation}}$$

$$- \underbrace{\frac{\partial \kappa_G}{\partial \theta^{\alpha}}}_{\substack{\text{Gaussian modulus}\\ \text{-induced variation}}} - \underbrace{\mathbf{f}\cdot\mathbf{a}_{\alpha}}_{\substack{\text{Force induced}\\ \text{variation}}} + \underbrace{2\kappa(D-D_0)[b_{\alpha\beta}(\gamma^{\alpha}\gamma^{\beta})_{;\eta}]}_{\text{Deviatoric effects}}.$$

A.2.3 Axisymmetric coordinates

Equations of motion for isotropic curvature

We parameterize a surface of revolution (Fig. 3.1B) by

$$\mathbf{r}(s,\theta) = r(s)\mathbf{e}_r(\theta) + z(s)\mathbf{k}. \tag{A.13}$$

We define ψ as the angle made by the tangent with respect to the horizontal. This gives $r'(s) = \cos(\psi)$, $z'(s) = \sin(\psi)$, which satisfies the identity $(r')^2 + (z')^2 = 1$. Using this, we define the normal to the surface as $\mathbf{n} = -\sin\psi\mathbf{e}_r(\theta) + \cos\psi\mathbf{k}$, the tangent to the surface in the direction of increasing arc length as $m\nu = \cos\psi\mathbf{e}_r(\theta) + \sin\psi\mathbf{k}$, and unit vector $m\tau = \mathbf{e}_{\theta}$ tangent to the boundary $\partial\omega$ in the direction of the surface of revolution.

This parameterization yields the following expressions for tangential (κ_ν) and transverse (κ_τ) curvatures, and twist (τ):

$$\kappa_\nu = \psi', \quad \kappa_\tau = r^{-1}\sin\psi, \quad \tau = 0. \tag{A.14}$$

The mean curvature (H) and Gaussian curvature (K) are obtained by summation and multiplication

of the tangential and transverse curvatures

$$H = \frac{1}{2}(\kappa_v + \kappa_\tau) = \frac{1}{2}(\psi^{'} + r^{-1}\sin\psi), \quad K = \kappa_\tau \kappa_v = \frac{\psi^{'}\sin\psi}{r}. \tag{A.15}$$

Defining $L = \frac{1}{2\kappa} r (W_H)'$, we write the system of first order differential equations governing the problem as [135],

$$\begin{aligned}
r' = \cos\psi, \quad z' = \sin\psi, \quad r\psi' = 2rH - \sin\psi, \\
rH' = L + rC' - \frac{r\kappa'}{\kappa}(H-C), \quad \lambda' = 2\kappa(H-C)C' - \kappa'(H-C)^2 - \kappa'_G K - \mathbf{f}\cdot\mathbf{a_s}, \\
\frac{L'}{r} = \frac{p}{k} + \frac{\mathbf{f}\cdot\mathbf{n}}{\kappa} + 2H\left[(H-C)^2 + \frac{\lambda}{\kappa}\right] - 2(H-C)\left[H^2 + \left(H - r^{-1}\sin\psi\right)^2\right] \\
- \frac{\kappa'}{\kappa}\frac{L}{r} - \frac{\kappa''_G}{\kappa}\frac{\sin\psi}{r} - \frac{\kappa'_G}{\kappa}\frac{\cos\psi}{r}(2H - \frac{\sin\psi}{r}).
\end{aligned} \tag{A.16}$$

The applied boundary conditions are

$$\begin{aligned}
r(0^+) = 0, \quad L(0^+) = 0, \quad \psi(0^+) = 0, \\
z(s_{max}) = 0, \quad \psi(s_{max}) = 0, \quad \lambda(s_{max}) = \lambda_0.
\end{aligned} \tag{A.17}$$

In asymmetric coordinates, the manifold area can be expressed in term of arc length

$$a(s) = 2\pi \int_0^s r(\xi) d\xi \quad \rightarrow \quad \frac{da}{ds} = 2\pi r. \tag{A.18}$$

Eq. A.18 allows us to convert Eq. A.16 to an area derivative and prescribe the total area of the membrane.

We non-dimensionalized the system of equations as

$$\begin{gathered}\zeta = \frac{a}{2\pi R_0^2}, \quad x = \frac{r}{R_0}, \quad y = \frac{y}{R_0}, \quad h = HR_0, \quad c = CR_0, \quad l = LR_0, \\ \lambda^* = \frac{\lambda R_0^2}{\kappa_0}, \quad p^* = \frac{pR_0^3}{\kappa_0}, \quad f^* = \frac{fR_0^3}{\kappa_0}, \quad \kappa^* = \frac{\kappa}{\kappa_0}, \quad \kappa_G^* = \frac{\kappa_G}{k0}, \quad K^* = KR_0^2,\end{gathered} \tag{A.19}$$

where R_0 is the radius of the initially circular membrane patch. Rewriting Eq. A.16 in terms of the dimensionless variables, we get [135]

$$\begin{gathered}x\dot{x} = \cos\psi, \quad x\dot{y} = \sin\psi \quad x^2\dot{\psi} = 2xh - \sin\psi, \quad x^2\dot{h} = l + x^2\dot{c} - x^2\frac{\dot{\kappa^*}}{\kappa^*}(h-c) \\ \dot{l} = \frac{p^*}{\kappa^*} + \frac{\mathbf{f}^* \cdot \mathbf{n}}{\kappa^*} + 2h\left[(h-c)^2 + \frac{\lambda^*}{\kappa^*}\right] - 2(h-c)\left[h^2 + \left(h - x^{-1}\sin\psi\right)^2\right] \\ -\frac{\dot{\kappa^*}}{\kappa^*}l - x\frac{\ddot{\kappa}_G^*}{\kappa^*}\sin\psi - \frac{\dot{\kappa}_G^*}{\kappa}\cos\psi(2h - \frac{\sin\psi}{x}), \\ \dot{\lambda^*} = 2\kappa^*(h-c) - \dot{\kappa^*}(h-c)^2\dot{c} - \dot{\kappa}_G^* K^* - \frac{\mathbf{f}^* \cdot \mathbf{a_s}}{x}.\end{gathered} \tag{A.20}$$

The spontaneous curvature field is modeled by a hyperbolic tangent functional as

$$C = \frac{1}{2}[\tanh(g(\zeta - a_0))], \tag{A.21}$$

where a_0 is the area of applied spontaneous curvature and $g = 20$ is a constant that ensures a sharp but smooth transition.

Force balance along the membrane for isotropic spontaneous curvature

***(i)* Constant bending and Gaussian moduli**

A general force balance for a surface ω, bounded by a curve $\partial\omega$, is (Fig. 3.2)

$$\int_\omega p\mathbf{n}da + \int_{\partial\omega} \tilde{\mathbf{f}}dt + \mathbf{F} = 0, \tag{A.22}$$

where $t = r(s)\theta$ is the length along the curve of revolution perimeter, p is the pressure difference across the membrane, $\tilde{\mathbf{f}}$ is the traction along the curve of revolution t and $\mathbf{F}$ is any externally applied force on the membrane. Along any circumferential curve on the membrane at constant z, the traction is given by [137]

$$\tilde{\mathbf{f}} = \tilde{f}_\nu m\nu + \tilde{f}_n \mathbf{n} + \tilde{f}_\tau m\tau, \tag{A.23}$$

where

$$\begin{aligned} \tilde{f}_n &= (\tau W_K)' - 1/2(W_H)_{,\nu} - (W_K)_{,\beta}\tilde{b}^{\alpha\beta}\nu_\alpha, \\ \tilde{f}_\nu &= W + \lambda - \kappa_\nu M, \\ \tilde{f}_\tau &= -\tau M, \end{aligned} \tag{A.24}$$

where $\tilde{f}_n$, $\tilde{f}_\nu$ and $\tilde{f}_\tau$ are force per unit length acting along the normal $\mathbf{n}$, tangent $m\nu$ to the surface, and transverse tangent $\mathbf{e}_\theta$ respectively. In Eq. A.24, M is the bending couple given by

$$M = \frac{1}{2}W_H + \kappa_\nu W_K. \tag{A.25}$$

Because $\tau = 0$ (no twist) in asymmetric coordinates, the normal and tangential tractions become

$$\tilde{f}_n = -\kappa(H' - C'), \tag{A.26a}$$

$$\tilde{f}_\nu = \kappa(H - C)(H - C - \psi') + \lambda. \tag{A.26b}$$

Projecting Eq. A.23 onto the orthogonal bases $\mathbf{e}_r$ and $\mathbf{k}$ gives axial and radial tractions [137],

$$\tilde{f}_r = \underbrace{\kappa(H'-C')\sin\psi}_{\substack{\text{Curvature gradient}\\ \text{contribution}}} + \underbrace{\kappa(H-C)(H-C-\psi')\cos\psi}_{\substack{\text{Curvature}\\ \text{contribution}}} + \underbrace{\lambda\cos\psi}_{\substack{\text{Tension}\\ \text{contribution}}}, \tag{A.27a}$$

$$\tilde{f}_z = \underbrace{-\kappa(H'-C')\cos\psi}_{\substack{\text{Curvature gradient}\\ \text{contribution}}} + \underbrace{\kappa(H-C)(H-C-\psi')\sin\psi}_{\substack{\text{Curvature}\\ \text{contribution}}} + \underbrace{\lambda\sin\psi}_{\substack{\text{Tension}\\ \text{contribution}}}. \tag{A.27b}$$

Because $\int_{\partial\omega} dt = 2\pi r$, the applied force in the axial direction can be evaluated by substituting Eqs. A.27a, and A.27b into Eq. A.22,

$$-\mathbf{F}_z = \underbrace{2\pi r\left(-\kappa(H'-C')\cos\psi\right) + \kappa(H-C)(H-C-\psi')\sin\psi + \lambda\sin\psi}_{\text{Force due to traction}} + \underbrace{2\pi\int_0^s pr(\xi)\cos\psi d\xi}_{\text{Force due to pressure}}. \tag{A.28}$$

This can be rewritten in terms of tractions as

$$-\mathbf{f}_z = \underbrace{\left(-\kappa(H'-C')\cos\psi\right) + \kappa(H-C)(H-C-\psi')\sin\psi + \lambda\sin\psi}_{\text{axial traction}} + \underbrace{\frac{\int_0^s pr(\xi)\cos\psi d\xi}{r}}_{\text{Traction due to pressure}}, \tag{A.29}$$

where $\mathbf{f}_z = \frac{\mathbf{F}_z}{2\pi r}$. The energy per unit length ξ, or "effective line tension," can be found by integrating Eq. A.27a along the perimeter boundary $\partial\omega$,

$$\xi = 2\pi r\Big[\underbrace{\kappa(H-C)(H-C-\psi')\cos\psi}_{\substack{\text{Curvature}\\ \text{contribution}}} + \underbrace{\lambda\cos\psi}_{\substack{\text{Tension}\\ \text{contribution}}} + \underbrace{\kappa(H'-C')\sin\psi}_{\substack{\text{Curvature gradient}\\ \text{contribution}}}\Big]. \tag{A.30}$$

***(ii)* Spatially heterogenous bending and Gaussian moduli**

For a membrane with a spatially heterogenous bending and Gaussian moduli, the normal and tangential tractions in Eqs. A.26a, A.26b become

$$\tilde{f}_n = -\kappa(H'-C') - \kappa'(H-C) - \frac{\sin\psi}{r}\kappa'_G, \tag{A.31a}$$

$$\tilde{f}_v = \kappa(H-C)(H-C-\psi') + \lambda. \tag{A.31b}$$

The radial and axial tractions in Eqs. A.27a and A.27b can be rewritten for the general case as

$$\begin{aligned}\tilde{f}_r = {} & \kappa(H'-C')\sin\psi + \kappa(H-C)(H-C-\psi')\cos\psi + \lambda\cos\psi \\ & + \underbrace{\kappa'(H-C)\sin\psi}_{\substack{\text{Variable bending}\\ \text{modulus}}} + \underbrace{\frac{\sin\psi^2}{r}\kappa'_G}_{\substack{\text{Variable Gaussian}\\ \text{modulus}}},\end{aligned} \tag{A.32a}$$

$$\begin{aligned}\tilde{f}_z = {} & -\kappa(H'-C')\cos\psi + \kappa(H-C)(H-C-\psi')\sin\psi + \lambda\sin\psi \\ & - \underbrace{\kappa'(H-C)\cos\psi}_{\substack{\text{Variable bending}\\ \text{modulus}}} - \underbrace{\frac{\sin\psi\cos\psi}{r}\kappa'_G}_{\substack{\text{Variable Gaussian}\\ \text{modulus}}}.\end{aligned} \tag{A.32b}$$

Similarly, the axial force and energy per unit lengths in Eqs. A.28, A.30 can be rewritten as

$$\begin{aligned}\mathbf{F}_z = {} & \Big[2\pi r(-\kappa(H'-C')\cos\psi + \kappa(H-C)(H-C-\psi')\sin\psi + \lambda\sin\psi \\ & -\kappa'(H-C)\cos\psi - \frac{\sin\psi\cos\psi}{r}\kappa'_G)\Big] \\ & + \underbrace{2\pi\int_0^s pr(\xi)\cos\psi d\xi}_{\text{Force due to pressure}},\end{aligned} \tag{A.33a}$$

$$\xi = 2\pi r\Big[\underbrace{\kappa(H-C)(H-C-\psi')\cos\psi}_{\substack{\text{Curvature}\\ \text{contribution}}} + \underbrace{\lambda\cos\psi}_{\substack{\text{Tension}\\ \text{contribution}}} + \underbrace{\kappa(H'-C')\sin\psi}_{\substack{\text{Curvature gradient}\\ \text{contribution}}} + \underbrace{\kappa'(H-C)\sin\psi}_{\substack{\text{Variable bending}\\ \text{contribution}}} + \underbrace{\frac{\sin\psi^2}{r}\kappa'_G}_{\substack{\text{Variable Gaussian}\\ \text{contribution}}}\Big]. \tag{A.34a}$$

Equation of motion for anisotropic spontaneous curvatures

By using the surface parametrization Eq. A.13, we are able to define the curvature deviator (D) as

$$D = \frac{1}{2}(\kappa_\tau - \kappa_\nu) = \frac{1}{2}(r^{-1}\sin\psi - \psi') = r^{-1}\sin\psi - H, \tag{A.35}$$

Here, we need to revise our defined L as $L = \frac{1}{2\kappa}r[(W_H)' - (W_D)']$, therefore for uniform bending and Gaussain modulii, the system of first order differential equations modify as [183],

$$\begin{aligned}
r' = \cos\psi, \quad z' = \sin\psi, \quad r\psi' &= 2rH - \sin\psi,\\
2rH' &= L + rC' - rD_0{}' + 2H\cos(\psi) - \frac{2\cos(\psi)\sin(\psi)}{r},\\
\lambda' &= 2\kappa(H-C)C' + 2\kappa(\frac{\sin(\psi)}{r} - H - D_0)D_0' - \mathbf{f}\cdot\mathbf{a_s},\\
\frac{L'}{r} &= \frac{p}{k} + \frac{\mathbf{f}\cdot\mathbf{n}}{\kappa} + 2H\Big[(H-C)^2 + \frac{\lambda}{\kappa} + (\frac{\sin(\psi)}{r} - H - D0)^2\\
&-2(\frac{\sin(\psi)}{r} - H - D_0)(\frac{\sin(\psi)}{r} - H)\Big] - 2(H-C)\left[H^2 + \left(H - r^{-1}\sin\psi\right)^2\right]\\
&-2\frac{\cos(\psi)}{r}\Big[\frac{H\cos(\psi)}{r} - \frac{\sin(\psi)\cos(\psi)}{r^2} - \frac{D_0'}{2} - \frac{C'}{2}\Big] + \frac{L\cos(\psi)}{r^2}.
\end{aligned} \tag{A.36}$$

Force balance along the membrane for anisotropic spontaneous curvatures

By considering the anisotropic spontaneous curvature contribution to the strain energy A.11, the traction components in Eq. A.24 and bending couple in Eq. A.25 are modified

$$\tilde{f_n} = (\tau W_K)' - 1/2(W_H)_{,\nu} - (W_K)_{,\beta}\tilde{b}^{\alpha\beta}\nu_\alpha + \frac{1}{2}(W_D)_{,\nu} - (W_D\gamma^\alpha\gamma^\beta)_{;\beta}\nu_\alpha - (W_D\gamma^\alpha\gamma^\beta\nu_\beta\tau_\alpha)',$$
$$\tilde{f_\nu} = W + \lambda - \kappa_\nu M,$$
$$\tilde{f_\tau} = -\tau M, \tag{A.37}$$

and

$$M = \frac{1}{2}W_H + \kappa_\nu W_K + W_D\gamma^\alpha\gamma^\beta\nu_\beta\nu_\alpha - \frac{1}{2}W_D. \tag{A.38}$$

In asymmetric coordinates, the normal and tangential tractions simplify as

$$\tilde{f_n} = -\kappa(H' - C' - D' + D_0') = -\kappa(2H' - \frac{\psi'\cos(\psi)}{r} + \frac{\sin(\psi)\cos(\psi)}{r^2} - C' + D_0'), \tag{A.39a}$$
$$\tilde{f_\nu} = \kappa(H-C)(H-C-\psi') + \lambda + \kappa(D-D_0)(D-D_0+\psi') \tag{A.39b}$$
$$= \kappa(H-C)(H-C-\psi') + \lambda + \kappa(\frac{\sin(\psi)}{r} - H - D_0)(\frac{\sin(\psi)}{r} - H - D_0 + \psi').$$

Using Eqs. A.37 to simplify the traction equations

$$\tilde{f_n} = -\kappa\frac{L}{r}, \tag{A.40a}$$
$$\tilde{f_\nu} = \kappa(H-C)(\frac{\sin(\psi)}{r} - H - C) + \lambda + \kappa(\frac{\sin(\psi)}{r} - H - D_0)(H - D_0). \tag{A.40b}$$

Axial force can then be written as

$$F_z = 2\pi r\Big(\kappa\frac{L}{r}\sin(\psi)+(\kappa(H-C)(\frac{\sin(\psi)}{r}-H-C)+\lambda+\kappa(\frac{\sin(\psi)}{r}-H-D_0)(H-D_0))\cos(\psi)\Big). \tag{A.41}$$

A.2.4 Asymptotic approximation for small radius

To ensure continuity at the poles, we use $L = H' = 0$ as a boundary condition in our simulations. However, this boundary condition reduces the expressions for tractions (Eqs. A.27b, A.27a) to zero at the pole. To avoid this discrepancy, we derive an asymptotic expression for tractions at small arc length. We proceed by assuming that the pole is at $x = 0$ and choose a rescaled variable given by

$$X = \frac{x}{\varepsilon}. \tag{A.42}$$

Here, ε is a small parameter, so that X is order of one. We can extend this to other small variables in Eq. A.20 near the pole to get

$$y = y_0 + Y\varepsilon, \quad \psi = P\varepsilon, \quad s = S\varepsilon, \tag{A.43}$$

where Y, P, S are the corresponding rescaled parameters and y_0 is membrane height at the pole.

In the simple case with no spontaneous curvature ($C = 0$), no external force $\mathbf{f} = 0$ and no pressure difference $p = 0$, we substitute Eqs. A.43 and A.42 into Eq. A.20 and use a Taylor

expansion to get

$$\dot{X} = 1 - \frac{(P\varepsilon)^2}{2}, \quad \dot{Y} = P\varepsilon - \frac{(P\varepsilon)^3}{3!}, \quad \dot{P} = 2h - \frac{P}{X} + \frac{\varepsilon^2}{3!}\frac{P^3}{X}, \quad X\dot{h} = l,$$
$$\dot{l} = \varepsilon^2 2Xh\left[\frac{\lambda^*}{k^*} - \left(h - \frac{P}{X} + \frac{P^3\varepsilon^2}{X3!}\right)^2\right],$$
$$\dot{\lambda^*} = 0. \tag{A.44}$$

We look for a solutions with form of

$$h = h^0 + \varepsilon h^1 + \mathrm{ord}(\varepsilon^2), \quad X = X^0 + \varepsilon X^1 + \mathrm{ord}(\varepsilon^2), \quad Y = Y^0 + \varepsilon Y^1 + \mathrm{ord}(\varepsilon^2),$$
$$l = l^0 + \varepsilon l^1 + \mathrm{ord}(\varepsilon^2), \quad P = P^0 + \varepsilon P^1 + \mathrm{ord}(\varepsilon^2), \quad \lambda^* = \lambda^{*0} + \varepsilon\lambda^{*1} + \mathrm{ord}(\varepsilon^2). \tag{A.45}$$

The leading order terms in Eq. A.45 are

$$\dot{X^0} = 1, \quad \dot{Y^0} = 0, \quad \dot{P^0} = 2h^0 - \frac{P^0}{X^0}, \quad \dot{h^0} = \frac{l^0}{X^0}, \quad \dot{l^0} = 0, \quad \dot{\lambda}^{*0} = 0. \tag{A.46}$$

Integrating the differential equations in Eq. A.46, we get

$$X^0 = S, \quad Y^{*0} = Y_0, \quad P^0 = S\left(H_0 + L_0\log(S) - \frac{L_0}{2}\right),$$
$$h^0 = L_0\log(S) + H_0, \quad l^0 = L_0, \quad \lambda^0 = \lambda_0, \tag{A.47}$$

where Y_0, H_0 and L_0, λ_0 are integration constants. We then look at order ε^1 terms in Eq. A.44

$$\dot{X^1} = 0, \quad \dot{Y^1} = P, \quad \dot{P^1} = 2h^1 + \frac{P^0X^1}{X^{0^2}}, \quad X^0\dot{h^1} + X^1\dot{h^0} = l^1, \quad \dot{l^1} = 0, \quad \dot{\lambda}^{*1} = 0. \tag{A.48}$$

The first order terms are thus given by

$$X^1 = X_1, \quad Y^1 = P_1 S + Y_1, \quad l^1 = L_1, \quad \lambda^{*1} = \lambda_1, \quad h^1 = L_1 \log(S) + \frac{X_1 L_0}{S} + H_1,$$
$$P^1 = 2S(L_1 \log(S) - L_1 + H_1) + X_1 L_0 \log(S)(\frac{3}{2} + \frac{\log(S)}{2} + \frac{H_0}{L_0}). \quad \text{(A.49)}$$

Combining the leading order and first order terms and substituting into Eq. A.45, our system of variables can be written as

$$X = S + \varepsilon X_1, \quad Y = Y_0 + \varepsilon(P_1 S + Y_1), \quad l = L_0 + \varepsilon L_1,$$
$$\lambda^* = \lambda_0 + \varepsilon\lambda_1, \quad P = S\left(H_0 + L_0 \log(S) - \frac{L_0}{2}\right)$$
$$+\varepsilon\Big(2S(L_1 \log(S) - L_1 + H_1) + X_1 L_0 \log(S)(\frac{3}{2} + \frac{\log(S)}{2} + \frac{H_0}{L_0})\Big),$$
$$h = H_0 + L_0 \log(S) + \varepsilon\Big(L_1 \log(S) + \frac{X_1 L_0}{S} + H_1\Big). \quad \text{(A.50)}$$

We are interested in the asymptotic expansion of mean curvature near the pole, which is given by

$$h = H_0 + L_0 \log(S) + \varepsilon\Big(L_1 \log(S) + \frac{X_1 L_0}{S} + H_1\Big). \quad \text{(A.51)}$$

This can be rewritten as

$$h = H_0 + L_0 \log(A + S - A) + \varepsilon H_1,$$
$$h = H_0 + L_0 \log(A) + L_0 \log(1 + \frac{S-A}{A}) + \varepsilon\Big(L_1 \log(S) + \frac{X_1 L_0}{S} + H_1\Big), \quad \text{(A.52)}$$

where A is a constant. If $\frac{S-A}{A}$ is small, we can perform a Taylor expansion around $S = A$ to get the leading order

$$
\begin{aligned}
h = H_0 + L_0 \log(A) + L_0 \left(\frac{S-A}{A} - \frac{1}{2} (\frac{S-A}{A})^2 \dots \right) \\
h \sim H_0 + L_0 \log(A) - L_0 + L_0 \left(\frac{S}{A} \right) \\
h \sim H_0 + L_0 \left(\log(A) - 1 + \frac{S}{A} \right) \\
h \sim H_0 + L_0 \log(A) - L_0 + L_0 \left(\frac{s}{A\varepsilon} \right) \\
h \sim C_1 + C_2 s, \qquad \text{(A.53)}
\end{aligned}
$$

where C_1 and C_2 are constants. This shows that the mean curvature can be approximated as a linear solution near the pole for $S \sim A$ or $s \sim A\varepsilon$. In our image analysis, inaccuracies near the pole begin at orders of magnitude of 10^{-2}. At this range, we can approximate a linear solution for mean curvature.

Similarly, we consider an asymptotic expansion for ψ near the pole at leading order

$$
P = S \left(H_0 + L_0 \log(S) - \frac{L_0}{2} \right), \qquad \text{(A.54)}
$$

which can be rewritten as

$$
\psi = s \left(H_0 + L_0 \log(s) - L_0 \varepsilon - \frac{L_0}{2} \right) \rightarrow \psi = s \left(D_1 + D_2 \log(s) \right), \qquad \text{(A.55)}
$$

where D_1 and D_2 are constants. We can now substitute the approximation for mean curvature and

ψ near the pole into Eq. A.27a and A.27b to get

$$\tilde{f}_r \sim -\kappa(C_1 + C_2 s - C)(C_1 + C_2 s - C - D_2 - D_1 - D_2 \log(s)) - \lambda, \tag{A.56a}$$

$$\tilde{f}_z \sim -\kappa(C_2 - C'). \tag{A.56b}$$

Using $\log(s) = \log(s + A - A) = \log(A) + \log(1 + \frac{s-A}{A})$ and expanding around $s \sim A$, Eq. A.56b can be simplified to

$$\tilde{f}_r \sim -\kappa(F_1 s^2 + F_2 s + F_3) - \lambda, \tag{A.57a}$$

$$\tilde{f}_z \sim -\kappa(C_2), \tag{A.57b}$$

where F_1, F_2 are constants. We can thus approximate radial traction as quadratic in arc length near the pole, while axial traction can be correspondingly approximated as constant. In this work, we choose to start the asymptotic solution at the local minimum of mean curvature near the pole, which is $\varepsilon \sim 0.1$.

A.3 Additional bud formation simulations

A.3.1 Axial and radial tractions in bud formation

The axial and radial tractions for the budding simulation, Fig. 3.3 of the main text, are shown in Fig A.1. The axial traction along the membrane is negligible in all the stages of bud formation (Fig. A.1A). The axial force due to traction Eq. A.28 depends on three different terms, curvature, curvature gradient and surface tension. The calculated axial force at the interface is zero because tension term cancels out the force due to curvature gradient and the force associated

with curvature is zero by itself (Fig. A.1B). This means that neck formation is purely regulated by radial stresses (Fig. A.1C). For small deformations, the radial traction is positive throughout, which shows that the membrane works to oppose the deformation. However, with the formation of U-shaped caps, radial traction changes sign and acts inward, representing the membrane's tendency to form small necks.

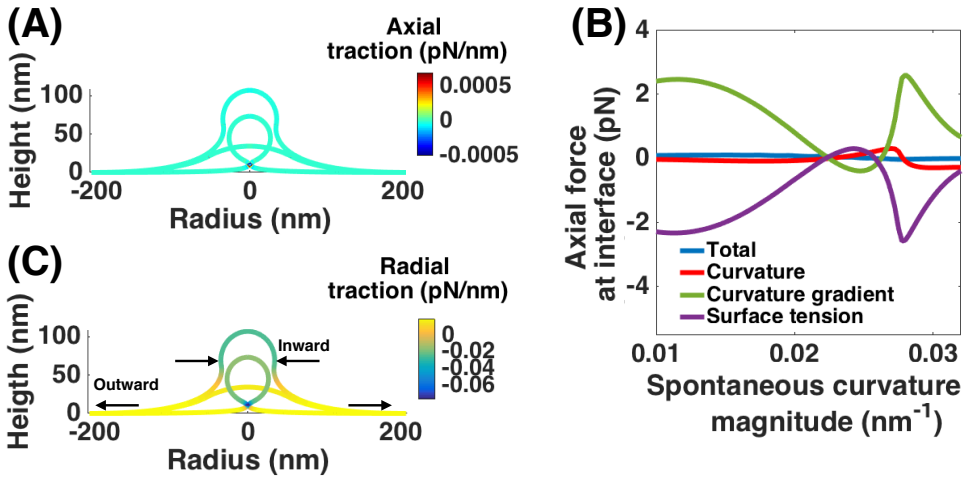

Figure A.1: Bud formation from a flat membrane for increasing spontaneous curvature and a constant area of spontaneous curvature field $A = 10,053\,\mathrm{nm}^2$. The spontaneous curvature magnitude increases from $C = 0$ to $C = -0.034\,\mathrm{nm}^{-1}$, the bending modulus is $\kappa = 320\,\mathrm{pN}\cdot\mathrm{nm}$ and surface tension at the edge is $\lambda_0 = 0.02\,\mathrm{pN/nm}$. Axial traction does not play any role in invagination. (A) Axial traction along the membrane is negligible for all shapes. (B) Axial force at the interface is almost zero. Terms due to tension and curvature gradient cancel each other and force due to curvature is automatically zero. (C) Radial traction distribution for three shapes. A large negative radial traction at the neck should favor membrane scission.

A.3.2 Bud formation in arc length

In Fig.3.3 we fixed the total area of the membrane and increased the magnitude of the spontaneous curvature and applied force respectively (Eqs. A.20). However, in active non-equilibrium processes such as endocytosis, the available membrane area can vary. One possible way to consider the impact of the membrane area adjustment is solving the equations in arc length (Eqs. A.16) instead of area. Here, we repeated the simulations of Figs. 3.3 for a fixed arc length of

membrane. In the case of the bud, we fixed the arc length coverage of the coat and increased the spontaneous curvature from 0 to C=-0.032 nm^{-1} (Fig. A.2A). The tractions and energy per unit length distribution along different shapes are shown in Fig. A.2B-D. Evidently, independent of whether the available area of the membrane is fixed or not, the energy per unit length at the interface is between 6 to -6 pN and changes sign from positive to negative with formation of a neck (Fig. A.2E).

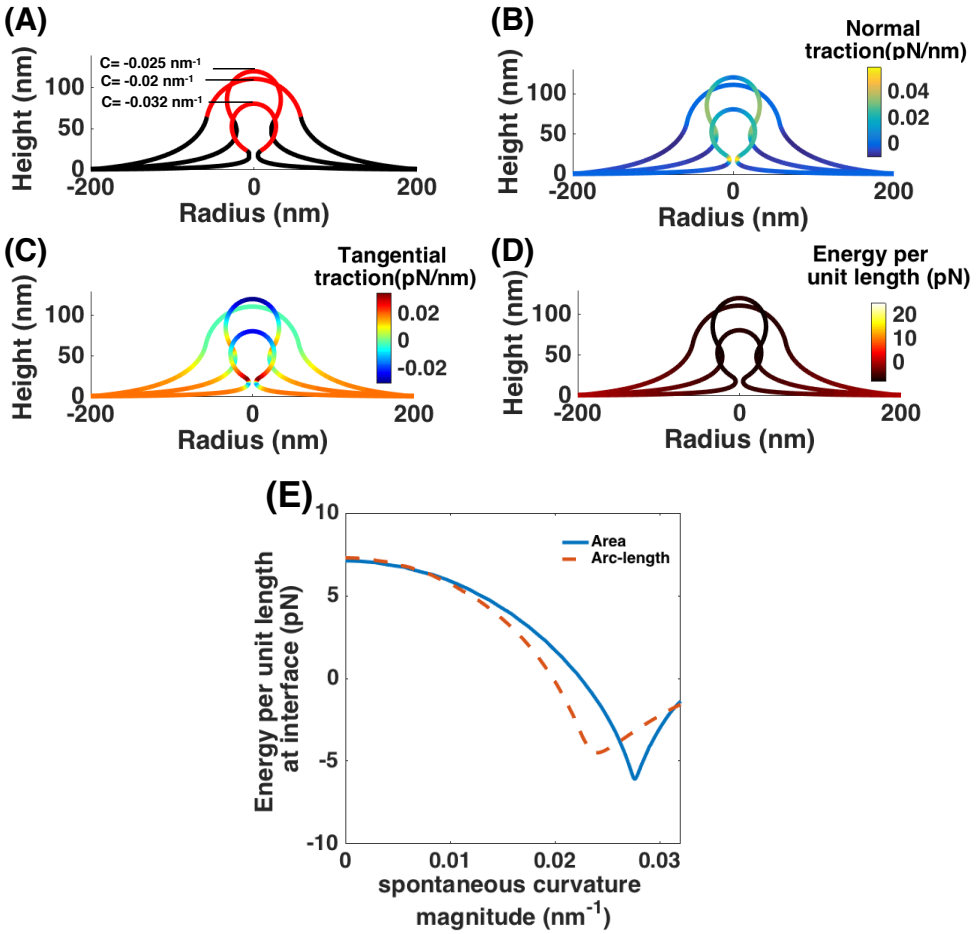

Figure A.2: Budding simulation with protein-induced spontaneous curvature for a fixed arc length instead of a fixed membrane area. (A) Three different membrane shapes with increasing spontaneous curvature. (B-D) Normal traction, tangential traction and energy per unit length distribution along the observed shapes in panel (A). (E) Energy per unit length at the edge of the protein coat. Blue solid line is for the fixed membrane area (Fig. 3.4) and the red dashed line represents the case with constant arc length.

A.3.3 Bud formation with a rigid protein coat

In Fig.3.3, we assumed the bending rigidity is homogeneous all along the membrane. However, various force microscopy measurements have shown that bending rigidity along the protein coat is much larger than the bare membrane [276]. To investigate the effect of spatial heterogeneity in the bending moduli on bud morphology and traction distributions, we repeated the simulation in Fig. 3.3, assuming that the bending rigidity along the spontaneous curvature field is 7.5 times larger than the bare membrane ($\kappa_{\text{coat}} = 7.5 \times \kappa = 2400$ pN/nm (Fig. A.3A)). Comparing these shapes to those in main text (Fig. 3.3), we see that in this case, a larger spontaneous curvature is required to form a narrow neck because the membrane is stiffer and harder to bend. Using Eqs. A.31a, A.31b and A.34a, the normal, tangential tractions and energy per unit length distributions are plotted along the shapes (Figs. A.3B, C and D). The positive normal traction distribution indicates the resistance of the membrane to bending. Similar to the case of a homogeneous membrane, the line tension can be divided into two sections. In the first section (small spontaneous curvature), tent shaped buds form and the line tension changes sign from positive to negative. Here, the average difference in the line tension magnitude between the two cases is less than 1 pN. However, in the second section (large spontaneous curvature), the line tension magnitude decreases with the formation of an Ω-shaped bud, and the average difference in the line tension magnitude is signifcantly larger (~ 4 pN) (Fig. A.3E).

A.3.4 Bud formation with cytoskeleton forces

We consider the effects of the cytoskeleton during endocytosis as previously described in [135]. In Fig. A.4, we apply actin-mediated forces on a U-shaped bud such that actin polymerizes in the form of a ring at the base of the endocytic pit with the network attached to the protein coat [135, 282]. Fig. A.4B-D show the tractions and energy per unit length distributions along the initial and final shapes as the membrane is pulled out. Fig. A.4E shows the match

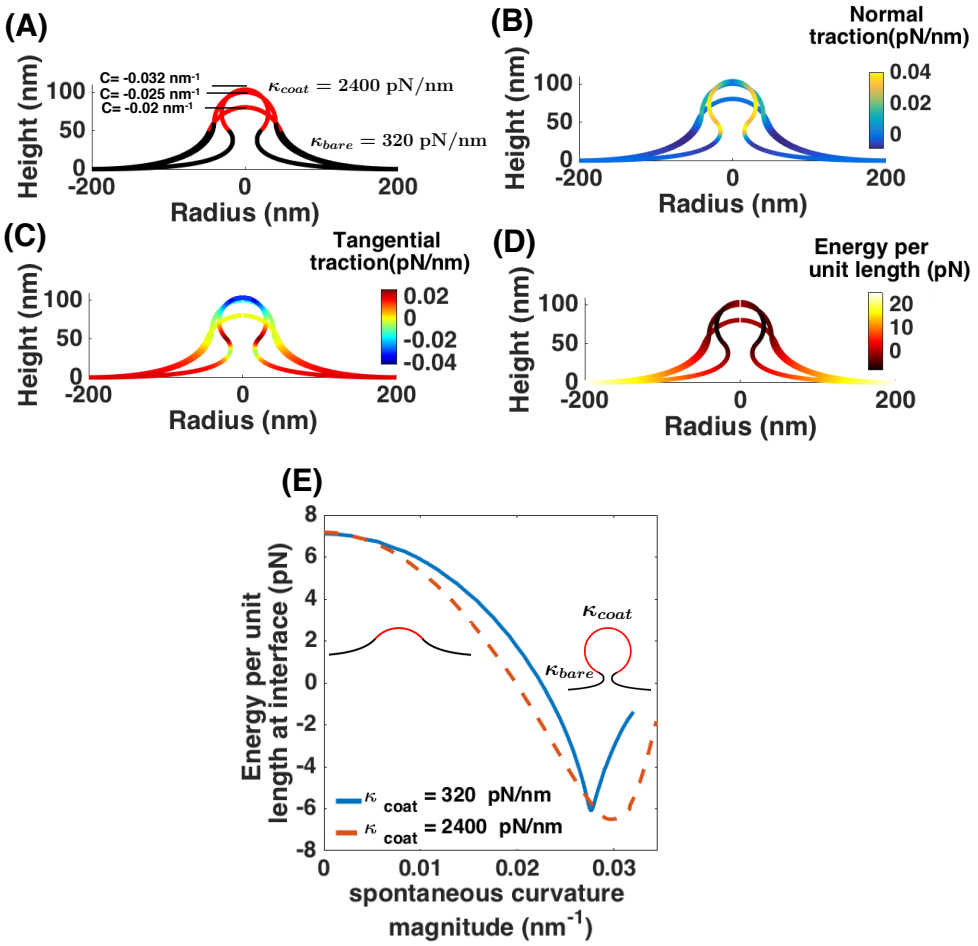

Figure A.3: Analysis of membrane budding due to protein-induced spontaneous curvature with a rigid coat. Simulations for Fig. 3.3 is repeated for $\kappa_{coat} = 2400$ pN/nm and $\kappa = 320$ pN/nm. (A) Membrane shapes for same three spontaneous curvature as Fig. 3.3 A. (B) Normal traction along the membrane for the shapes shown in (A). (C) Tangential traction distribution (D) Energy per unit length distribution for the chosen shapes. (E) Energy per unit length at the edge of the edge of the spontaneous curvature field as a function of spontaneous curvature for the homogeneous membrane in Fig. 3.3 (blue solid line) and a rigid protein coat (red dashed line). In large values of spontaneous curvature (Ω-shaped bud) the average difference between the line tension magnitudes is almost 4 pN.

obtained between the applied force and axial force calculated at the edge of the protein coat. Here, we note that calculating the axial force at the base predicts zero applied force – a consequence of the actin ring acting at the base that integrates to zero. To further emphasize this point, we repeated the simulation without this downward force at the base (Fig. A.5) and show that the

match between applied force and axial force can be obtained both at the base of the membrane and at the edge of the protein coat. Fig A.5B shows that the large tangential traction along the neck is limited to a smaller region (red) compared to Fig. A.4B, because without considering the actin ring force at the base, there is lesser axial stretch along the bud neck.

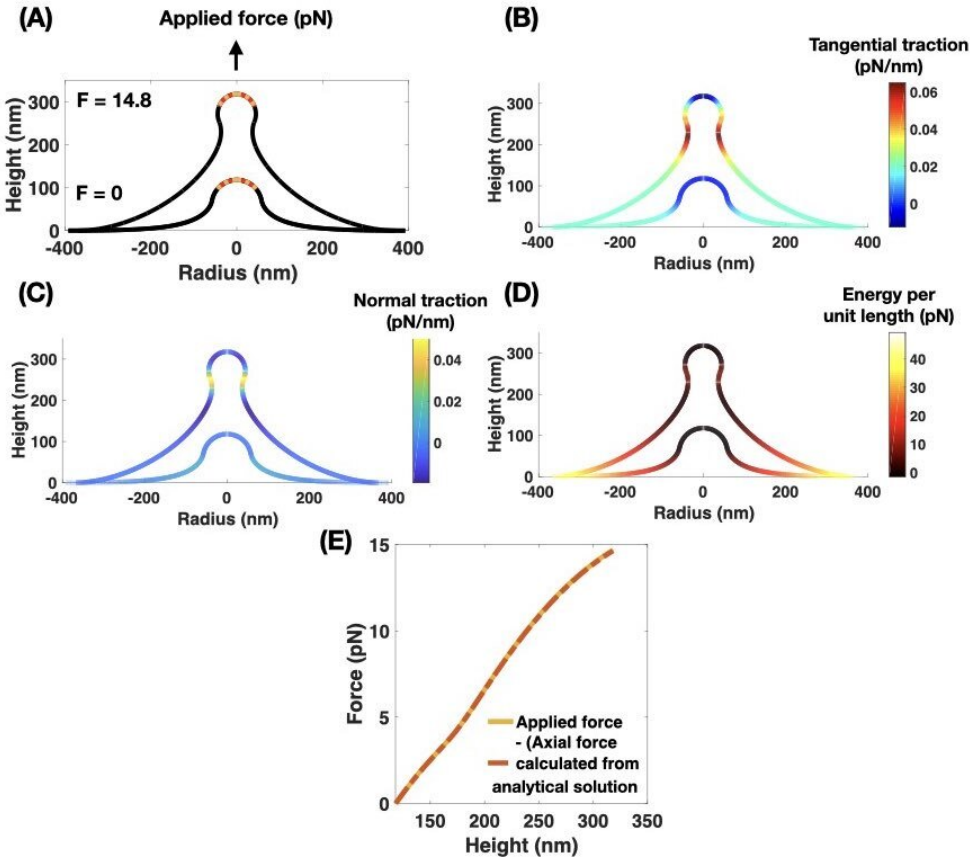

Figure A.4: Application of axial forces (brown) onto a U-shaped bud covered by a protein coat (red). Spontaneous curvature magnitude $C = -0.02\,\mathrm{nm}^{-1}$, area of spontaneous curvature field $\mathrm{A} = 17,593\,\mathrm{nm}^2$, bending modulus $\kappa = 320\,\mathrm{pN}\cdot\mathrm{nm}$ and surface tension at the edge $\lambda_0 = 0.02\,\mathrm{pN/nm}$. Here, axial forces are applied such that there is an upward force over the protein coat and a downward force acting as a ring at the base [135]. (A) Initial and final membrane shapes obtained. (B) Tangential traction distribution along the membrane shapes in (A). (C) Normal traction distribution along the membrane shapes in (A). (D) Energy per unit length along the membrane shapes in (A). (E) Force match obtained between applied force and negative of axial force calculated using Eq. A.28. Here, axial force is calculated at the edge of the protein coat. Axial force at the base is zero since the upward and downward forces balance each other out.

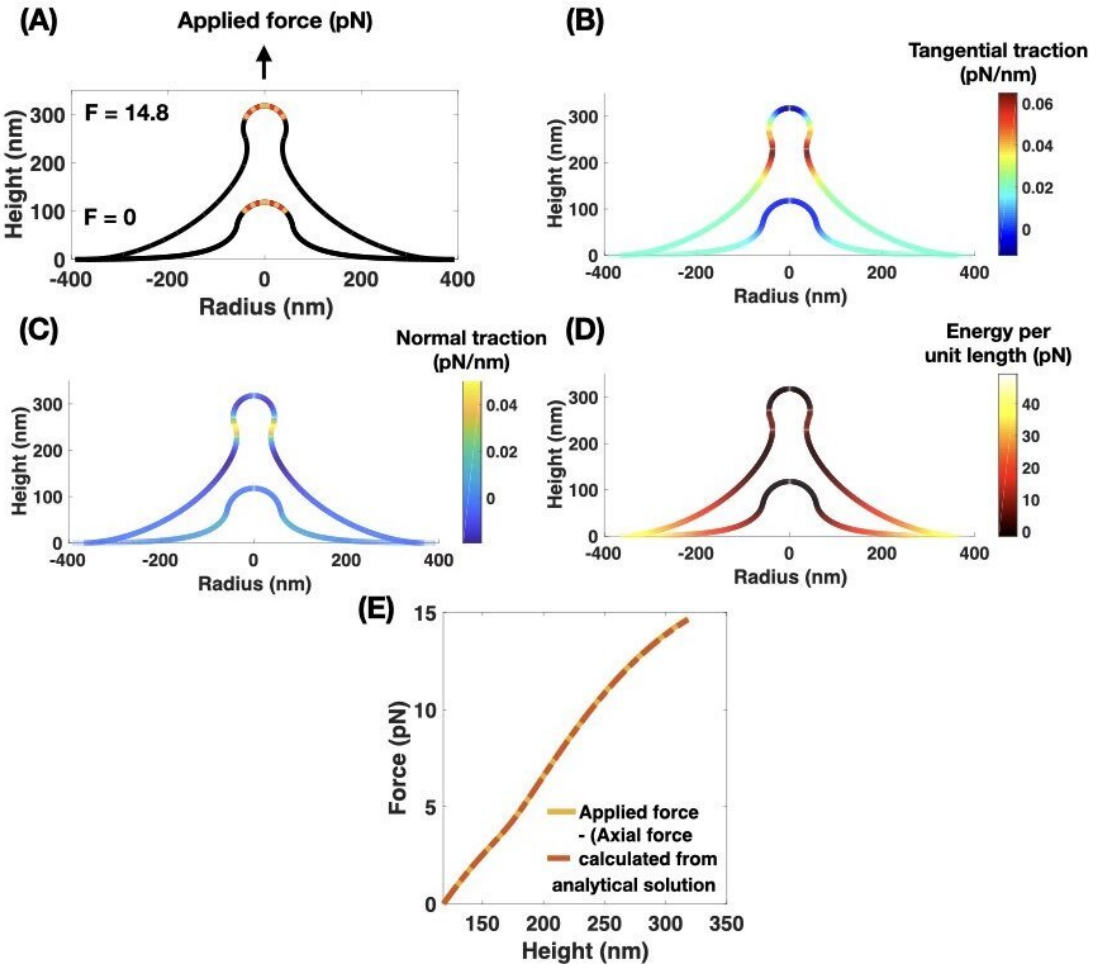

Figure A.5: Application of axial forces (brown) onto a U-shaped bud covered by a protein coat (red). Spontaneous curvature magnitude $C = -0.02\,\mathrm{nm}^{-1}$, area of spontaneous curvature field $\mathrm{A} = 17,593\,\mathrm{nm}^2$, bending modulus $\kappa = 320\,\mathrm{pN}\cdot\mathrm{nm}$ and surface tension at the edge $\lambda_0 = 0.02\,\mathrm{pN/nm}$. Here, axial forces are applied such that there is only an upward force over the protein coat. (A) Initial and final membrane shapes obtained. Force required is smaller than Fig. A.4. (B) Tangential traction distribution along the membrane shapes in (A). (C) Normal traction distribution along the membrane shapes in (A). (D) Energy per unit length along the membrane shapes in (A). (E) Force match obtained between applied force and negative of axial force calculated using Eq. A.28. Here, axial force is calculate at the base of the membrane. The same match can be obtained at the edge of the protein coat.

A.3.5 Bud formation with anisotropic spontaneous curvature

Proteins induce a highly anisotropic local spontaneous curvature [180, 266]. To model this effect, we used a modified energy functional (Eq. A.11) that includes deviatoric curvature effects.

This then can be written as the shape equation (Eq. A.12) and tangential variation equation. We solve this system of equations for a deviatoric curvature field applied over the cylindrical portion of a membrane tube (Fig. A.6, [282]). Fig A.6A shows neck formation in a membrane tube with increasing deviatoric curvature. The membrane invagination obtained resembles the PM shape seen during assembly of rvs proteins at the neck of a tube [282]. Fig. A.6D shows that the energy per unit length at both interfaces matches the trend seen in Fig. 6 leading up to neck formation. Fig. A.6E shows that the axial forces can be matched to applied forces. Axial forces decrease as a consequence of the membrane height being constrained.

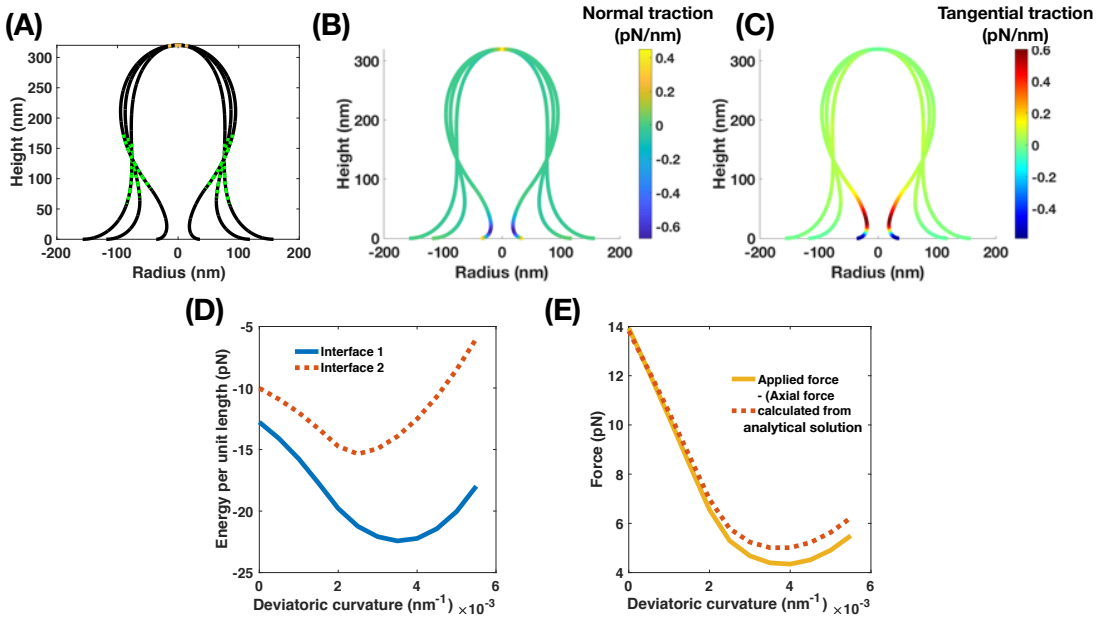

Figure A.6: Application of a deviatoric spontaneous curvature along the cylindrical portion of a membrane tube leads to neck formation [282]. (A) Membrane shapes at a spontaneous curvature $C = 0\,\mathrm{nm}^{-1}$, $C = -0.004\,\mathrm{nm}^{-1}$, $C = -0.01\,\mathrm{nm}^{-1}$ and deviatoric spontaneous curvature $D = 0\,\mathrm{nm}^{-1}$, $D = 0.004\,\mathrm{nm}^{-1}$, $D = 0.01\,\mathrm{nm}^{-1}$ respectively. (B) Normal traction distribution along the membrane shapes in (A). (C) Tangential traction distribution along the membrane shapes in (A). (D) Energy per unit length at both interfaces with increasing deviatoric curvature. The trend of energy per unit length resembles the trend leading up to neck formation in Fig 3.3. (E) Match between applied force and axial force calculated using Eq. A.41. Axial force relaxes with membrane neck formation.

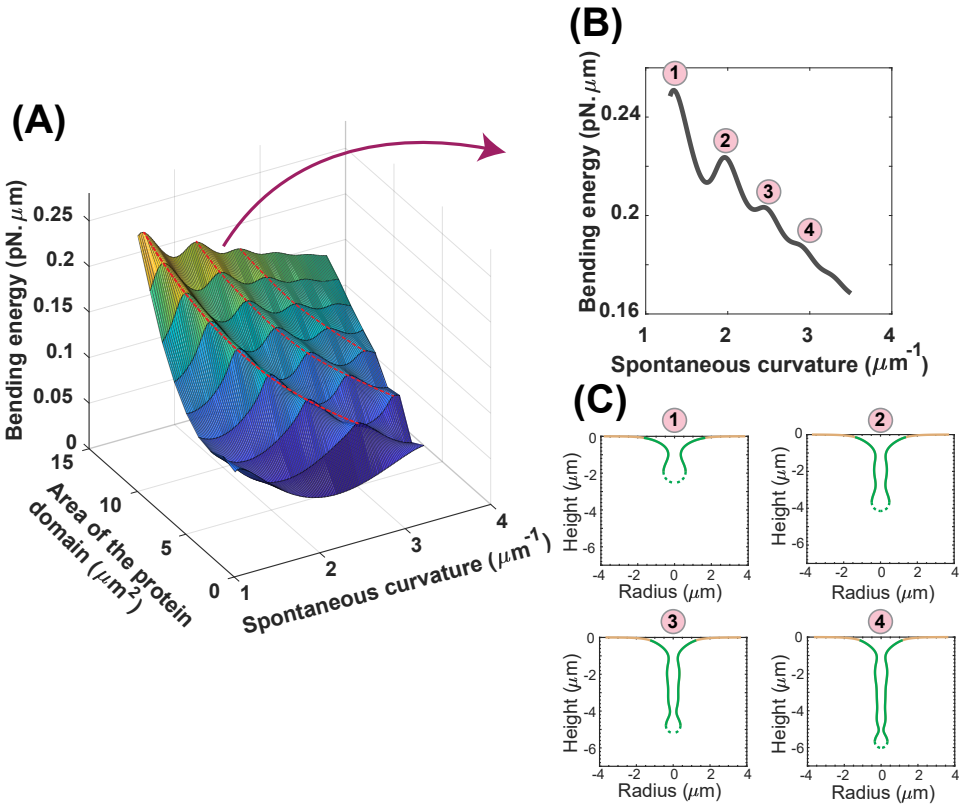

Figure A.7: Spontaneous curvature and the area of the protein domain regulate the morphology of the undulated tubules. (A) Bending energy of the protein domain as the function of the spontaneous curvature and area of the protein domain. For a small area of the protein domain, there is just a local maximum with increasing the magnitude of the spontaneous curvature. However, for the larger area of the protein domain, the bending energy has an oscillation behavior with multiple local maxima as a function the spontaneous curvature. With decreasing the area of the protein domain, the bending energy decreases and also local maximum shifts toward the larger values of the spontaneous curvature (red dotted lines). (B) The bending energy as the function of spontaneous curvature for $A_0 = 4\pi\mu$m . With increasing the magnitude of spontaneous curvature, there are multiple local maxima. Here, we labeled the four local maxima with numbers one to four. (C) The morphology of the membrane at the local maximum bending energy points in panel B.

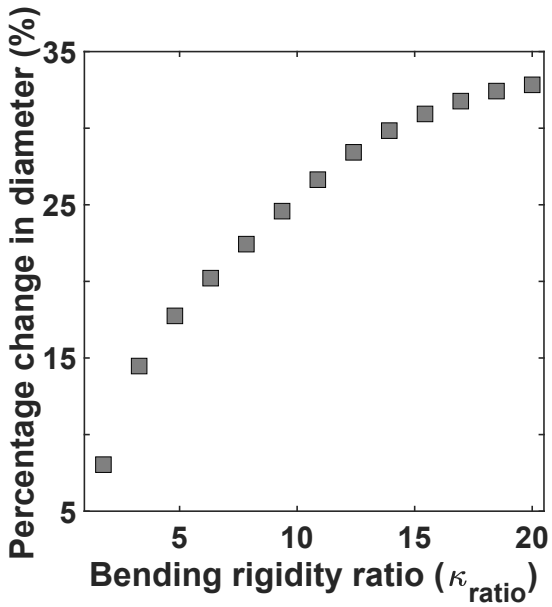

Figure A.8: The tubule diameter increases with increasing the bending rigidity of the protein domain compared to the bare membrane. We defined the percentage of change in the tubule diameter as $D - D_{\kappa_{\text{ratio}}=1}/D_{\kappa_{\text{ratio}}=1}$ and $\kappa_{\text{ratio}} = \kappa_{\text{protein}}/\kappa_{\text{membrane}}$. Here, we set C_0=3.5 μm^{-1}, $\lambda_0 = 4\pi\text{pN/nm}$, $A_0 = 4\pi\mu\text{m}^2$, and increased the bending rigidity ratio from κ_{ratio} 1 (uniform rigidity) to κ_{ratio}. Based on our results, with increasing the bending rigidity of the protein domain to κ_{ratio}= 20, the tubule diameter increases about 35% compared to the uniform bending rigidity.

Appendix B

Membrane thin-shell formulations

B.1 Table of notation

Table B.1: Notation used in the Chapter 4

Notation	Description	Units
E	Strain energy	$\mathrm{pN}\cdot\mathrm{nm}$
γ	Lagrange multiplier for incompressibility constraint	$\mathrm{pN}\cdot\mathrm{nm}^{-1}$
p	Pressure difference across the membrane	$\mathrm{pN}\cdot\mathrm{nm}^{-2}$
σ	Protein density	nm^{-2}
C	Spontaneous curvature	nm^{-1}
θ^{ξ}	The surface coordinatwe	
W	Local energy per unit area	$\mathrm{pN}\cdot\mathrm{nm}^{-1}$
$\mathbf{r}$	Position vector	
$\mathbf{n}$	Normal to the membrane surface	unit vector
$\mathbf{a}_{\xi}$	Basis vectors describing the tangent plane	
λ	Membrane tension, $-(W+\gamma)$	pN/nm
H	Mean curvature of the membrane	nm^{-1}
K	Gaussian curvature of the membrane	nm^{-2}
κ_{ν}	Tangential curvature	nm^{-1}
κ_{τ}	Transverse curvature	nm^{-1}

Table B.2: Notation used in the Chapter 4

Notation	Description	Units
κ	Bending modulus	$pN \cdot nm$
k_BT	Boltzman energy	$pN \cdot nm$
κ_G	Gaussian modulus	$pN \cdot nm$
s	Arclength	nm
θ	Azimuthal angle	
ψ	Angle between $\mathbf{e}_r$ and $\mathbf{a}_s$	
φ	Angle between normal vector to surface $\mathbf{n}$ and protein meridian	
α	Protein-Protein aggregation strength	$nm^3 \cdot pN$
β	Constant representing the excluded area	$nm^5 \cdot pN$
μ	Constant indicating lipid-protein moietic length scale	nm
R	Radial distance	nm
Z	Elevation from base plane	nm
$\mathbf{e}_r(\theta)$	Radial basis vector	unit vector
$\mathbf{e}_\theta$	Azimuthal basis vector	unit vector
$\mathbf{k}$	Altitudinal basis vector	unit vector
s_{max}	Maximum arclength	nm
λ_0	Surface tension at boundary	$pN \cdot nm^{-1}$
σ_0	Number of proteins per unit area	nm^{-2}
L_c	Length of cylinder	nm
R_c	Radius of cylinder	nm
r_b	Radius of bead	nm
L	Shape equation variable	nm^{-1}
$L_{separation}$	Distance between two beads	μm
L_{rigid}	Length of the rigid segment	μm
$L_{protein}$	Length of the coat protein	μm
κ_{lipid}	Bending modulus of the bare lipid bilayer	$pN \cdot nm$
$\kappa_{protein}$	Bending modulus of the rigid protein domain	$pN \cdot nm$
κ_{ratio}	Bending rigidity ratio $\kappa_{protein}/\kappa$	
$\kappa_{G,lipid}$	Gaussian modulus of the bare lipid bilayer	$pN \cdot nm$
$\kappa_{G,protein}$	Gaussian modulus of the protein domain	$pN \cdot nm$
$H_{analytical}$	Aanalytical mean curvature	nm^{-1}
$r_{b,analytical}$	Aanalytical radius of the bead	nm^{-1}
R_0	Radius of the cylinder	nm
l_k	Induced length scale by a rigid protein domain	nm
l_σ	Induced length scale by a protein-enriched domain	nm

B.2 Methods

B.2.1 Membrane mechanics

In this section, we present a brief derivation of the generalized equations of motion for biological membranes under the assumptions stated in the main text. We then restrict the equations to axisymmetric coordinates and solve them in a prescribed membrane domain. Details of all the derivations can be found in [150, 305, 353].

The local force balance in the absence of inertia for any material point on the membrane is given by

$$m\Gamma^{\xi}_{;\xi} + p\mathbf{n} = 0, \tag{B.1}$$

where $()_{;\xi}$ is the surface divergence, $m\Gamma^{\xi}$ is the stress vector, p is the pressure difference between the inside and outside of the volume bounded by the membrane, and $\mathbf{n}$ is the unit vector normal to the membrane. The surface divergence in Eq. (B.1) can be rewritten as [150]

$$m\Gamma^{\xi}_{;\xi} = (\sqrt{a})^{-1}(\sqrt{a}m\Gamma^{\xi})_{,\xi}, \tag{B.2}$$

where a is the determinant of the first fundamental form metric $a_{\xi\eta}$ and $()_{,}$ is the partial derivative with respect to the coordinate. The stress vector in Eq. (B.1) can be decomposed into normal and tangential components as

$$m\Gamma^{\xi} = mT^{\xi} + S^{\xi}\mathbf{n}. \tag{B.3}$$

For elastic surfaces for which the energy density per unit mass $F(a_{\xi\eta}, b_{\xi\eta})$ depends on the first and second fundamental forms, the normal and tangential components of the stress vector in Eq. (B.3) can be expressed as [150]

$$\mathbf{T}^{\xi} = T^{\xi\eta}\mathbf{a}_{\eta} \quad \text{with} \quad T^{\xi\eta} = \Gamma^{\xi\eta} + b^{\eta}_{\mu}M^{\mu\xi}, \quad \text{and} \quad S^{\xi} = -M^{\xi\eta}_{;\eta}, \tag{B.4}$$

where

$$\Gamma^{\xi\eta} = \rho\left(\frac{\partial F(\rho,H,K;x^{\xi})}{\partial a_{\xi\eta}} + \frac{\partial F(\rho,H,K;x^{\xi})}{\partial a_{\eta\xi}}\right), \quad M^{\xi\eta} = \frac{\rho}{2}\left(\frac{\partial F(\rho,H,K;x^{\xi})}{\partial b_{\xi\eta}} + \frac{\partial F(\rho,H,K;x^{\xi})}{\partial b_{\eta\xi}}\right). \tag{B.5}$$

Here, ρ is the surface mass density, and H and K are the mean and Gaussian curvatures given by

$$H = \frac{1}{2}a^{\xi\eta}b_{\xi\eta}, \quad K = \frac{1}{2}\varepsilon^{\xi\eta}\varepsilon^{\lambda\mu}b_{\xi\lambda}b_{\eta\mu}. \tag{B.6}$$

Here $(a^{\xi\eta}) = (a_{\xi\eta})$ is the dual metric and $\varepsilon^{\xi\eta}$ is the permutation tensor defined by $\varepsilon^{12} = -\varepsilon^{21} = 1/\sqrt{a}, \varepsilon^{11} = \varepsilon^{22} = 0$.

In the case of area incompressibility ($J = 1$), the general form of free energy density per unit mass can be rewritten as

$$F(\rho,H,K;x^{\xi}) = \tilde{F}(H,K;x^{\xi}) - \frac{\gamma(x^{\xi},t)}{\rho}, \tag{B.7}$$

where $\gamma(x^{\xi},t)$ is a Lagrange multiplier field required to impose invariance of ρ on the whole of

the surface (see [150] for full derivation). Substituting $W = \rho\tilde{F}$ into Eq. (B.7) we get

$$\Gamma^{\xi\eta} = (\lambda + W)a^{\xi\eta} - (2HW_H + 2\kappa W_K)a^{\xi\eta} + W_H\tilde{b}^{\xi\eta}, \tag{B.8}$$

$$M^{\xi\eta} = \frac{1}{2}W_H a^{\xi\eta} + W_K\tilde{b}^{\xi\eta}, \tag{B.9}$$

where $b^{\tilde{\xi}\eta}$ is the co-factor of the curvature tensor, and $\lambda = -(\gamma + W)$ can be interpreted as the membrane tension [6].

Combining Eqs. (B.9), (B.4), and (B.3) with Eq. (B.1) gives the equation of motion in normal and tangential directions as

$$\text{Normal:} \quad p = \Delta\frac{1}{2}W_H + (W_K)_{;\xi\eta}\tilde{b}^{\xi\eta} + W_H(2H^2 - K) + 2H(KW_K - W) - 2\lambda H, \tag{B.10}$$

and

$$\text{Tangential:} \quad N^{\eta\xi}_{;\xi} - S^{\xi}b^{\eta}_{\xi} = -(\gamma_{,\xi} + W_K k_{,\xi} + W_H H_{,\xi})a^{\eta\xi} = (\frac{\partial W}{\partial x^{\xi}}|_{\exp} + \lambda_{,\xi})a^{\eta\xi} = 0. \tag{B.11}$$

Here $\Delta(\cdot)$ is the surface Laplacian, and $()_{|\exp}$ denotes the explicit derivative respect to coordinate θ^{ξ}.

B.2.2 Helfrich energy and mechanical equilibrium

For the local energy density of a lipid bilayer membrane, we use an augmented version of the Helfrich energy accounting for the protein-protein interaction, the protein density gradient and the thermal entropic contributions given by [188, 189, 356, 364, 365]

$$W(H,K,\sigma;\theta^{\xi}) = \underbrace{\kappa(\theta^{\xi})\left[H - C(\sigma(\theta^{\xi}))\right]^2 + \kappa_G(\theta^{\xi})K}_{\text{Bending}} \quad \underbrace{-\alpha\sigma(\theta^{\xi})^2}_{\text{Protein aggregation}} \quad + \quad \underbrace{\beta(\nabla\sigma)^2}_{\substack{\text{Inhomogeneous} \\ \text{protein distribution}}} \\ \underbrace{+ k_B T\sigma(\log(\frac{\sigma}{\sigma_s}) - 1),}_{\substack{\text{Entropic contribution} \\ \text{due to thermal diffusion}}} \tag{B.12}$$

where W is the local energy density, C is the induced spontaneous curvature due to lipid-protein interactions, σ is the protein density, κ is the bending modulus, κ_G is the Gaussian modulus, α indicates the strength of the attractive energy between two neighboring proteins [189, 364], β is a positive constant that depends on the excluded area and the effective interaction area of the proteins [186, 357], ∇ is the gradient operator, k_B is the Boltzmann constant, and T is the temperature. Assuming that the system in the room temperature ($k_B T = 4.114$ pN$\cdot$nm), we note that in Eq. B.12, $\frac{k_B T}{\kappa}$ is small because the membrane bending rigidity is in the range of 20-40 $k_B T$ [367]. Additionally, in the dilute regime of low protein density $k_B T\sigma \ll 1$. Based on this analysis, we neglect the entropic term in the rest of our calculations.

In Eq. (B.12), protein density (σ) depends explicitly on the surface coordinates θ^{ξ} to allow for local heterogeneity. It should be noted that the bending term in Eq. (B.12) is different from the standard Helfrich energy by a factor of 2. We take this net effect into consideration by choosing the value of the bending modulus to be twice that of the standard value of bending modulus typically used for lipid bilayers [133].

For low protein densities (dilute regime), the induced-spontaneous curvature $C(\sigma)$ in Eq. (B.12) can be expressed in term of protein density as [202]

$$C(\sigma) = (\mu\varphi)\sigma, \tag{B.13}$$

where φ is the angle between cone-shaped proteins meridian and the normal vector to the surface ($\mathbf{n}$), and μ is a length-scale correction representing the lipid-protein specific interaction [555].

Substituting the modified version of Helfrich energy function (Eq. (B.12)) and Eq. (B.13) into the first functional normal variation of total energy (Eq. (B.10)) gives the so-called "shape equation," [152]

$$\underbrace{\Delta[\kappa(H-(\mu\varphi)\sigma)]-(\kappa_G)_{;\xi\eta}\tilde{b}^{\xi\eta}-2\kappa H\left(H-(\mu\varphi)\sigma\right)^2+2\kappa(H-(\mu\varphi)\sigma)\left(2H^2-K\right)}_{\text{Elastic effects}} + \underbrace{2H(\alpha\sigma^2)}_{\substack{\text{Protein}\\ \text{aggregation}}} - \underbrace{2H\beta(\nabla\sigma)^2)}_{\substack{\text{Inhomogeneous}\\ \text{protein distribution}}} = \underbrace{(p+2\lambda H)}_{\substack{\text{Capillary}\\ \text{effect}}}, \tag{B.14}$$

A consequence of the spatial variation of membrane properties and protein density is that λ is not homogeneous along the membrane [135, 137]. Substituting Eq. (B.12) into the balance of forces tangential to the membrane Eq. (B.11) gives the spatial variation of membrane tension,

$$\underbrace{\nabla\lambda}_{\substack{\text{Gradient of}\\ \text{membrane tension}}} = \underbrace{2[\kappa\mu\varphi(H-(\mu\varphi)\sigma)+\alpha]\frac{\partial\sigma}{\partial\theta^\xi}-\beta(\nabla\sigma)\frac{\partial(\nabla\sigma)}{\partial\theta^\xi}}_{\text{Protein density variation}} - \underbrace{\frac{\partial\kappa}{\partial\theta^\xi}(H-(\mu\varphi)\sigma)^2}_{\substack{\text{Bending modulus-}\\ \text{induced variation}}} - \underbrace{\frac{\partial\kappa_G}{\partial\theta^\xi}K}_{\substack{\text{Gaussian modulus-}\\ \text{induced variation}}}. \tag{B.15}$$

B.2.3 Governing equations in axisymmetric coordinates

We define a surface of revolution by

$$\mathbf{r}(s,\theta)=R(s)\mathbf{e}_r(\theta)+Z(s)\mathbf{k}, \tag{B.16}$$

where s is the arc length along the curve, R(s) is the radius from the axis of rotation, Z(s) is the height from the base plane and $(\mathbf{e}_r, \mathbf{e}_\theta, \mathbf{k})$ form the basis coordinate. Defining ψ as the angle made by the tangent with respect to the vertical gives

$$R'(s) = \cos(\psi), \quad Z'(s) = \sin(\psi), \tag{B.17}$$

satisfying the identity $(R')^2 + (Z')^2 = 1$, where $(')$ is the partial derivative with respect to the arc length. Using this, we can define the normal and tangent vectors to the surface as

$$\mathbf{n} = -\sin\psi\mathbf{e}_r(\theta) + \cos\psi\mathbf{k}, \quad \mathbf{a}_s = \cos\psi\mathbf{e}_r(\theta) + \sin\psi\mathbf{k}. \tag{B.18}$$

Using this parameterization, we can now write the tangential (κ_ν) and transverse (κ_τ) curvatures as

$$\kappa_\nu = \psi', \quad \kappa_\tau = \frac{\sin\psi}{R}. \tag{B.19}$$

The mean curvature (H) and Gaussian curvature (K) are obtained by summation and multiplication of the tangential and transverse curvatures

$$H = \frac{1}{2}(\kappa_\nu + \kappa_\tau) = \frac{1}{2}(\psi' + \frac{\sin\psi}{R}), \quad K = \kappa_\tau\kappa_\nu = \frac{\psi'\sin\psi}{R}. \tag{B.20}$$

Finally, we define $L = \frac{1}{2\kappa}R(W_H)'$ such that we obtain a system of first- order differential equations with six unknowns R, Z, ψ, H, L, and λ [36, 135, 152],

$$R' = \cos\psi, \quad Z' = \sin\psi, \quad R\psi' = 2RH - \sin\psi, \quad RH' = L + R\mu\varphi\sigma' - \frac{R\kappa'}{\kappa}(H - \mu\varphi\sigma),$$
$$\frac{L'}{R} = \frac{p}{k} + 2H\left[(H - (\mu\varphi)\sigma)^2 - \frac{\alpha\sigma^2}{\kappa} + \frac{\beta(\nabla\sigma)^2}{\kappa} + \frac{\lambda}{\kappa}\right]$$
$$-2(H - (\mu\varphi)\sigma)\left[H^2 + \left(H - \frac{\sin\psi}{R}\right)^2\right] - \frac{\kappa' L}{\kappa R} - \frac{\kappa_G'' \sin(\psi)}{\kappa R} - \frac{\kappa_G' \cos(\psi)}{\kappa R}(2H - \frac{\sin(\psi)}{R}),$$
$$\lambda' = 2\left[\kappa\mu\varphi(H - \mu\varphi\sigma) + \alpha\sigma - \beta\sigma''\right]\sigma' - \kappa'(H - (\mu\varphi)\sigma)^2 - \kappa_G' K. \tag{B.21}$$

In order to solve this system of equations (Eq. (B.21)), we need to provide six boundary conditions. We consider an axisymmetric cylindrical membrane with (1) fixed radius at both boundaries, (2) $\psi = \pi/2$ at both ends to ensure the edges remain vertical, (3) fixed height at one end and prescribed tension (λ_0) at the other end (see Fig. 4.1C). These boundary conditions can be summarized as follow,

$$R(0^+) = R_0, \quad \psi(0^+) = \frac{\pi}{2}, \quad z(0^+) = 0 \quad \lambda(0^+) = \lambda_0,$$
$$R(s_{\max}) = R_0, \quad \psi(s_{\max}) = \frac{\pi}{2}. \tag{B.22}$$

To non-dimensionalize the system of equations (Eq. (B.21)), we use two parameters, the radius of the initial cylindrical membrane (R_0), and lipid bilayer bending modulus (κ_0). Using these constants, we can define

$$t=\frac{s}{R_0},\quad y=\frac{Z}{R_0},\quad x=\frac{R}{R_0},\quad h=HR_0,\quad c=CR_0,\quad l=LR_0,\quad \tilde{\lambda}=\frac{\lambda R_0^2}{\kappa},\quad G=KR_0^2$$
$$\tilde{p}=\frac{pR_0^3}{\kappa_0},\quad \tilde{\kappa}_G=\frac{\kappa_G}{\kappa},\quad \tilde{\kappa}=\frac{\kappa}{\kappa_0},\quad \tilde{\alpha}=\frac{\alpha}{R_0^2\kappa_0},\quad \tilde{\beta}=\frac{\beta}{R_0^4\kappa_0},\quad \tilde{\mu}=\frac{\mu}{R_0},\quad \tilde{\sigma}=\frac{\sigma}{R_0^2}. \tag{B.23}$$

Rewriting Eq. (B.21) in terms of the dimensionless variables in Eq. (B.23), we get [135]

$$\begin{aligned}
\dot{x}=\cos\psi,\quad \dot{y}=\sin\psi,\quad x\dot{\psi}=2xh-\sin\psi,\quad x\dot{h}=l+x\tilde{\mu}\varphi\dot{\tilde{\sigma}}-x\frac{\dot{\tilde{\kappa}}}{\tilde{\kappa}}(h-\tilde{\mu}\varphi\tilde{\sigma}),\\
x^{-1}\dot{l}=\frac{\tilde{p}}{\tilde{\kappa}}+2h\left[(h-(\tilde{\mu}\varphi)\tilde{\sigma})^2-\frac{\tilde{\alpha}\tilde{\sigma}^2}{\tilde{\kappa}}+\frac{\tilde{\beta}(\nabla\tilde{\sigma})^2}{\tilde{\kappa}}+\frac{\tilde{\lambda}}{\tilde{\kappa}}\right]-2\left(h-(\tilde{\mu}\varphi)\tilde{\sigma}\right)\left[h^2+\left(h-\frac{\sin\psi}{x}\right)^2\right]\\
-\frac{\dot{\tilde{\kappa}}}{\tilde{\kappa}}x^{-1}l-x^{-1}\frac{\ddot{\tilde{\kappa}}_G}{\tilde{\kappa}}\sin(\psi)-x^{-1}\frac{\dot{\tilde{\kappa}}_G}{\tilde{\kappa}}\cos(\psi)(2h-\frac{\sin(\psi)}{x}),\\
\dot{\tilde{\lambda}}=2\Big[\tilde{\kappa}\tilde{\mu}\varphi\left(H-\tilde{\mu}\varphi\tilde{\sigma}\right)+\tilde{\alpha}\tilde{\sigma}-\tilde{\beta}\ddot{\tilde{\sigma}}]\dot{\sigma}-\dot{\tilde{\kappa}}(h-(\tilde{\mu}\varphi)\tilde{\sigma})^2-\dot{\tilde{\kappa}}_G G,
\end{aligned} \tag{B.24}$$

where $\dot{()}$ is the derivative respect to the non-dimensional variable t. The boundary conditions in Eq. (B.22) simplify to

$$\begin{aligned}
x(0^+)=1,\quad \psi(0^+)=\frac{\pi}{2},\quad y(0^+)=0,\quad \tilde{\lambda}(0^+)=\tilde{\lambda}_0\\
x(t_{\max})=1,\quad \psi(t_{\max})=\frac{\pi}{2},
\end{aligned} \tag{B.25}$$

where $t_{\max}=s_{\max}/R_0$ is the total dimensionless membrane length .

B.2.4 Analytical solutions (limit cases)

Ignoring the boundary effects and Gaussian curvature, for a nanotube with a length of L_c, radius R_c, uniform bending rigidity and no protein distribution ($\sigma = 0$), the free energy density (Eq. B.12) can be written

$$W_0 = \kappa H_0^2 = \kappa(\frac{1}{2R_c}^2), \tag{B.26}$$

where H_0 is the initial mean curvature that for a cylinder is proportional to the radius ($H_0 = \frac{1}{2R_c}$). Adding the proteins or having a heterogenous bending rigidity changes the energy of the system as

$$W = \kappa H^2 + \kappa(\mu\varphi\sigma)^2 - 2\kappa\mu\varphi\sigma - \alpha\sigma^2 + \beta(\nabla\sigma)^2, \tag{B.27}$$

where we assumed that neither topology nor boundary change and eliminated the Gaussian curvature term from the energy. Rearranging the terms in Eq. B.27, gives

$$W = \kappa H^2 - 2\kappa\mu\varphi\sigma + \sigma^2(\kappa(\mu\varphi)^2 - \alpha) + \beta(\nabla\sigma)^2. \tag{B.28}$$

Since $\varphi < 0$, the second term in Eq. (B.28) is positive. Also, for the set of parameters that we choose in this study, the third term in Eq. (B.28) is positive. Therefore, we can conclude that adding protein density or varying the bending rigidity increases the energy of the system ($W \geq W_0$). However, any system wants to have minimum energy. Thus, the mean curvature in Eq. (B.27) varies in order to decrease the energy of the system. Considering the limit case that

$W = W_0$, we find an analytical expression for the mean curvature as a function of the protein density and the bending rigidity as

$$H_{\text{analytical}} = \underbrace{\mu\varphi\sigma}_{\substack{\text{Spontaneous}\\ \text{curvature}}} \pm \sqrt{\underbrace{\frac{\frac{1}{(2R_c)^2}}{\kappa_{\text{ratio}}}}_{\substack{\text{Preexisting curvature}\\ \text{of the tube}}} + \underbrace{\frac{\frac{\alpha\sigma^2}{\kappa}}{\kappa_{\text{ratio}}}}_{\substack{\text{Aggregation}\\ \text{effects}}} - \underbrace{\frac{\frac{\beta(\nabla\sigma)^2}{\kappa}}{\kappa_{\text{ratio}}}}_{\substack{\text{Inhomogeneous}\\ \text{protein distribution}}}}, \tag{B.29}$$

where κ_{ratio} represents the ratio of the bending rigidity in the protein-enriched domain (κ_{rigid}) compared to the bending rigidity of the bare lipid membrane ($\kappa_{\text{ratio}} = \kappa_{\text{protein}}/\kappa$). In Eq. (B.29), the positive sign is only acceptable because the first term is negative ($\varphi < 0$), and therefore to have a positive curvature along the nanotube, the second term needs to be positive.

For small protein density ($\sigma \ll 1$), the higher order terms in Eq. B.29 can be ignored and the equation can be simplified by the Taylor expansion given by

$$H_{\text{analytical}} = \underbrace{\mu\varphi\sigma}_{\substack{\text{Spontaneous}\\ \text{curvature}}} + \frac{1}{\sqrt{\kappa_{\text{ratio}}}}\Big(\underbrace{\frac{1}{(2R_c)}}_{\substack{\text{Preexisting curvature}\\ \text{of the tube}}} + \frac{R_c}{\kappa}\big(\underbrace{\alpha\sigma^2}_{\substack{\text{Aggregation}\\ \text{effects}}} - \underbrace{\beta(\nabla\sigma)^2}_{\substack{\text{Inhomogeneous}\\ \text{protein distribution}}} \big)\Big), \tag{B.30}$$

Assuming that the nanotube remains as a cylinder after deformation ($H_{\text{analytical}} = \frac{1}{2r_{\text{b, analytical}}}$), where $r_{\text{b,analytical}}$ is the radius of the beaded nanotube, Eq. (B.29) simplifies as

$$2r_{\text{b,analytical}} = \left[\mu\varphi\sigma + \sqrt{\frac{\frac{1}{(2R_c)^2} + \frac{\alpha\sigma^2}{\kappa} - \frac{\beta(\nabla\sigma)^2}{\kappa}}{\kappa_{\text{ratio}}}}\right]^{-1}. \tag{B.31}$$

Similar to Eq. B.30, we can simplify Eq. 4.9 for small protein density given by

$$r_{b,analytical} = \sqrt{\kappa_{ratio}} R_c \left(1 - 2R_c \sqrt{\kappa_{ratio}} (\mu\varphi\sigma) - \frac{2R_c^2}{\kappa}(\alpha\sigma^2 - \beta(\nabla\sigma)^2)\right). \tag{B.32}$$

B.2.5 Numerical implementation

We solved the system of first-order differential equations (Eq. (B.24)) with boundary conditions Eq. (B.25) using the finite element software COMSOL MULTIPHYSICS ^{R} 5.3, using the "General Form PDE" module. Here, we summarize the steps and assumptions that we used for each simulation.

- All the simulations were performed for a fixed length of the membrane ($L_{membrane} = 20\,\mu$m).
- The membrane patch was initialized to be a perfect cylinder ($\psi = \pi/2$) with radius R_0= 200 nm.
- The membrane domain (0-s_{max}) was discretized equally with mesh size = 0.001.
- To have a sharp but smooth transition in heterogeneous properties, we used a hyperbolic tangent function given by

$$\chi = \frac{1}{2}[\tanh(g(t - s_0))], \tag{B.33}$$

where χ denoted the membrane property such as bending modulus (κ), Gaussian modulus (κ_G), or protein density (σ), g is the length of the transition regions between the protein-enriched domain and the bare membrane [357], and s_0 represents the domain of the protein aggregation.

B.3 Supplementary Figures

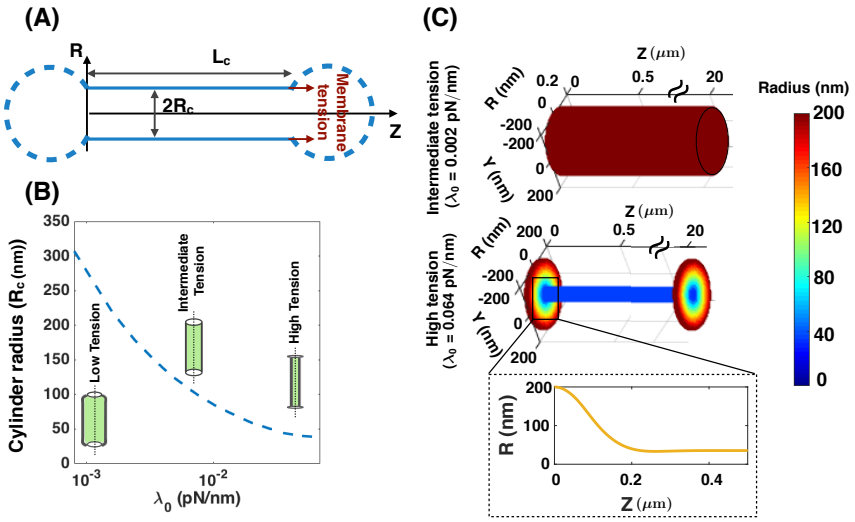

Figure B.1: Tension-mediated nanotube formation. (A) Schematic showing the simplest morphology for a nanotube, a cylinder with a radius R_c and length $L_c = 100R_c$ between two adjacent cells in the absence of both membrane cytoskeleton and osmotic pressure. (B) Tubular membrane becomes narrower by tuning the membrane tension at the boundary. Tube radius is plotted as a function of applied tension at the boundary (λ_0). With increasing edge tension, the cylinder radius (R_c) decreases. Based on the ratio of the length and radius, the observed shapes can be classified in three categories: (1) a wide cylinder ($L_c/R_c < 100$) at low tension, (2) a perfect cylinder ($L_c/R_c = 100$) at intermediate tension, and (3) a narrow cylinder similar to a nanotube ($L_c/R_c > 100$) at high tension. (C) Radius variation in a tubular membrane versus the narrow nanotube. A perfect cylinder stabilized at an intermediate tension ($\lambda_0 = \kappa_{\text{lipid}}/4R_c^2 = 0.002\,\text{pN/nm}$) has a uniform radius ($R_c = 200\,\text{nm}$). In contrast, the narrow nanotube at high tension ($\lambda_0 = 0.064\,\text{pN/nm}$), has large radii at the edges ($R_c = 200\,\text{nm}$) and a small radius along the connecting tubule ($R_c = 40\,\text{nm}$). The inset shows the smooth transition of the nanotube morphology at the edge boundary.

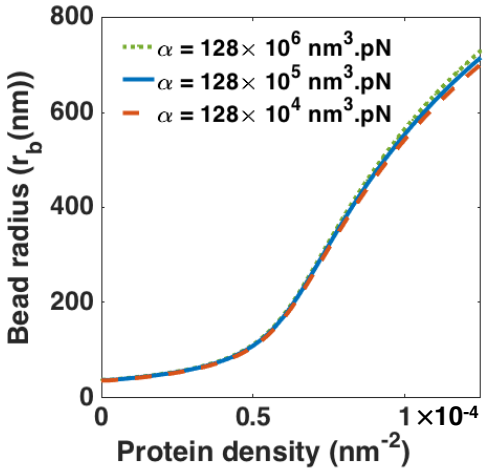

Figure B.2: Bead radius as a function of the protein density for three different values of protein aggregation strength (α). There is no significant change in the bead radius and morphology with varying α by two orders of magnitude.

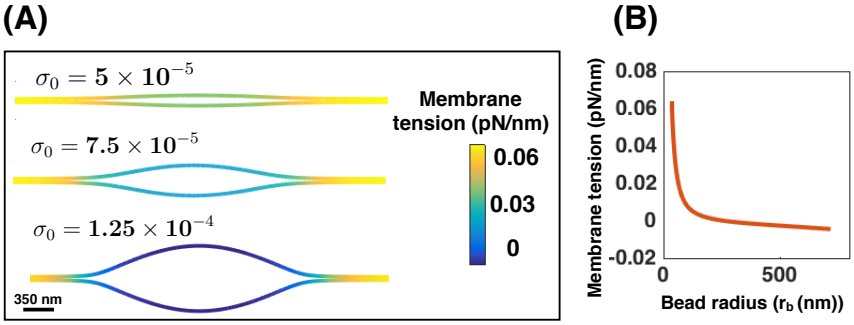

Figure B.3: Membrane tension distribution along nanotubes corresponding to local protein aggregation and shown in Fig. 4.3. (A) The region of the protein aggregation and bead-shaped deformations have a lower membrane tension compared to the rest of the membrane. (B) Reduction of the local membrane tension along the beading domain versus the bead radius. Here the negative membrane tension can be interpreted as a surface pressure.

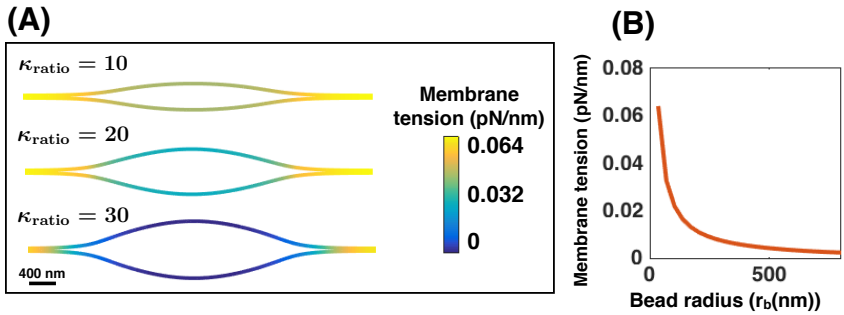

Figure B.4: Membrane tension distribution along nanotubes corresponding to local bending rigidity variation shown in Fig. 4.4. (A) The region of higher rigidity and bead-shaped deformations have a lower membrane tension compared to the rest of the membrane. (B) Reduction of the local membrane tension along the beading domain versus the bead radius.

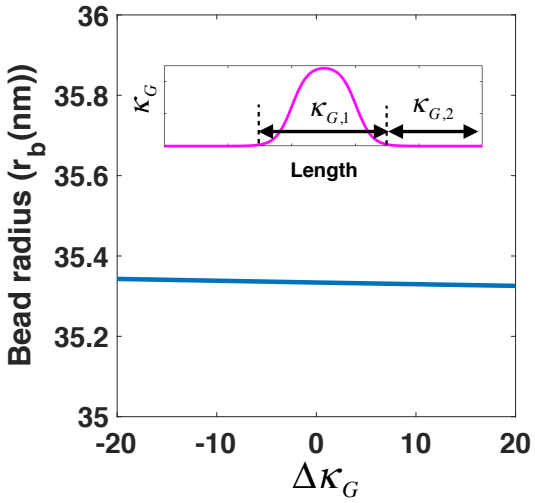

Figure B.5: Beads do not form with a localized Gaussian modulus variation. Here we applied a variable Gaussian modulus splay – prescribed as a hyperbolic tangent Eq. (B.33) – along a constant length of the membrane ($L_{Gaussian} = 8\,\mu$m) at the center of the nanotube, $\lambda_0 = 0.064\,$pN/nm. We define $\Delta\kappa_G = (\kappa_{G,1} - \kappa_{G,2})/\kappa_{lipid}$ varying between negative and positive values $[135, 260]$. There is a negligible membrane deformation with increasing the Gaussian moduli difference from $\Delta\kappa_G = -20$ to $\Delta\kappa_G = 20$ such that the bead radius is almost equal to the nanotube radius ($R_c = 35.334\,$nm) at $\Delta\kappa_G = 0$.

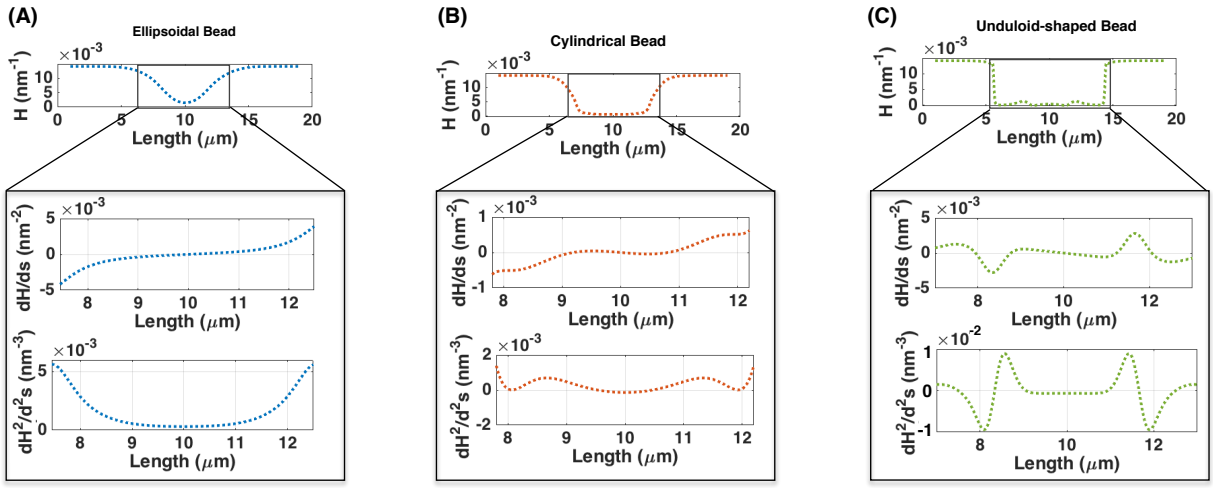

Figure B.6: Classification of three different beads based on the second derivative of the mean curvature (H'') along the protein-enriched domain.(A, upper) Mean curvature (H) along the ellipsoidal bead. (A, lower) H' changes sign from negative to positive along the ellipsoidal bead but H'' is always positive. (B, upper) H distribution along the cylindrical bead. (B, lower) Both H' and H'' are smaller compared to the ellipsoidal bead and their sign change along the bead. (C, upper) H distribution along the unduloid-shaped bead. (C, lower) The sign of both H' and H'' changes along the bead.

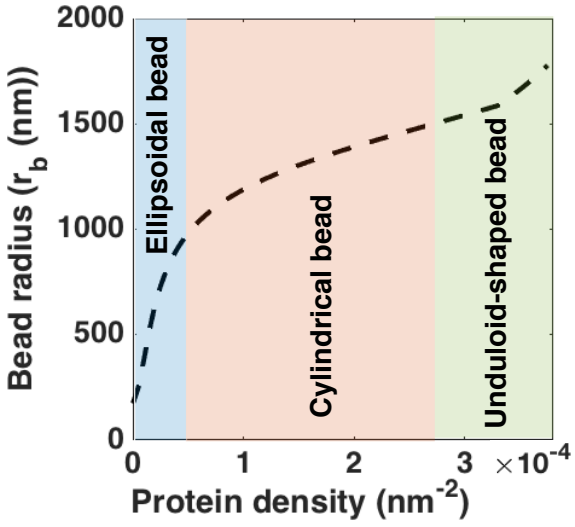

Figure B.7: Bead radius as a function of the protein density for a rigid protein-enriched domain ($\kappa_{ratio} = 5$). The three different observed bead morphologies in Fig. 4.6 are separated with the same colors. The slope of the bead radius versus the protein density in cylindrical and unduloid-shaped beads is smaller compared to the ellipsoidal bead.

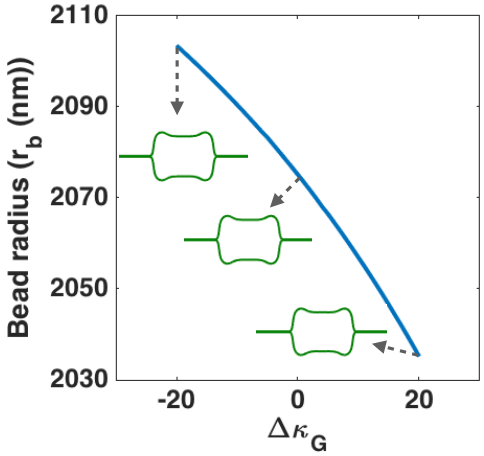

Figure B.8: Decrease in the radius of the undoid-shaped bead with increasing the Gaussian modulus $\Delta\kappa_G$ from negative to positive values, $\kappa_{\text{ratio}} = 11$ and $\sigma_0 = 1.85 \times 10^{-4}$ nm^{-2}. While the heterogeneity in the Gaussian modulus alters the radius of the bead, it does not affect the morphology of the bead, the undoloid-shape bead remains as a unduloid. Also, the change in the radius of the bead is small.

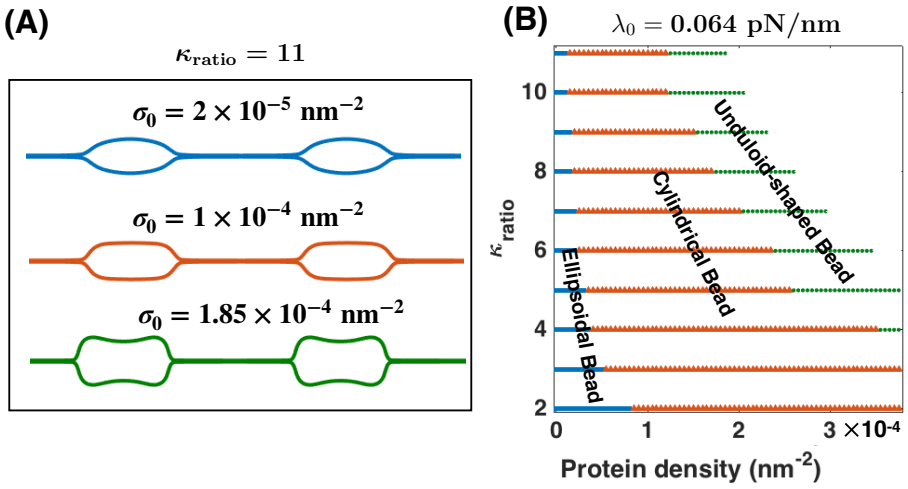

Figure B.9: Formation of two beads far away from each other with no interaction. (A) Three different shapes of two beads in the presence of two rigid domains of proteins with $\kappa_{\text{ratio}} = 11$, and $\lambda_0 = 0.064\,\text{pN/nm}$. Here, we set the protein density distribution the same as Fig. 4.7A. Similar to a single bead (Fig. 4.6A), as protein density increases, each bead shape transforms independently from an ellipsoidal bead to a cylindrical one and finally a unduloid-shaped bead. (B) The bending rigidity ratio versus the number of the proteins per unit area phase diagram for $\lambda_0 = 0.064\,\text{pN/nm}$. As expected, the phase diagram is exactly the same as Fig. 4.6A because the beads are far away from each other and therefore their shapes evolve completely independently of one another.

Appendix C

Derivation of RBC morphology myosin activity

C.1 Table of notation

Table C.1: Notation used in the Chapter 5

Notation	Description	Units
p	Pressure difference across the membrane	$\mathrm{pN}/\mathrm{nm}^2$
θ^α	The surface coordinate ($\alpha \in \{1,2\}$)	
W	Local energy per unit area	pN/nm
E	Total surface energy	pN·nm
E_b	Bending energy	pN·nm
E_f	Work done by forces	pN·nm
$\mathbf{r}$	Position vector	
$\mathbf{n}$	Normal unit vector to the membrane surface	unit vector
$m\tau$	Rightward normal in direction of revolution	unit vector
$\mathbf{a}_\xi$	Basis vectors describing the tangent plane	
λ	Membrane tension	pN/nm

Table C.2: Notation used in the Chapter 5

Notation	Description	Units
H	Mean curvature of the membrane	$1/\text{nm}$
K	Gaussian curvature of the membrane	$1/\text{nm}^2$
F	Normally applied force per unit area	$\text{pN}/\mu\text{m}^2$
κ	Bending modulus	$\text{pN} \cdot \text{nm}$
κ_G	Gaussian modulus	$\text{pN} \cdot \text{nm}$
s	Arclength	nm
θ	Azimuthal angle	
ψ	Angle between $\mathbf{e}_r$ and $\mathbf{a}_s$	
R	Radial distance	nm
Z	Elevation from base plane	nm
A	Membrane area	nm^2
s_{max}	Maximum arclength	nm
h_{max}	Maximum height at the rim	
h_{min}	Minimum height at the dimple	
L	The maximum cell diameter	
$\varepsilon_{\text{hmax}}$	Error in the maximum height	
$\varepsilon_{\text{hmin}}$	Error in the minimum height	
ε_{L}	Error in the length	
$\varepsilon_{\text{total}}$	Total error	
M	Shape equation variable	$1/\text{nm}$
R_0	Radius of the RBC cell	nm
$\text{F}_{\text{uniform}}$	Uniformly applied force	$\text{pN}/\mu\text{m}^2$
F_{dimple}	Local force at dimple region	$\text{pN}/\mu\text{m}^2$
F_{rim}	Local force at rim region	$\text{pN}/\mu\text{m}^2$
A_{dimple}	Membrane surface are in the dimple region	m^2
A_{rim}	Membrane surface are in the rim region	m^2
V_{dimple}	Occupied volume by the dimple region	m^3
V_{rim}	Occupied volume by the rim region	m^3
F_{ratio}	Ratio of the force at the dimple versus the rim region	

C.2 Model description

C.2.1 Assumptions

- We consider that the radii of the membrane curvatures are much larger than the thickness of the bilayer [409]. This allows us to treat the lipid bilayer as a thin elastic shell and model the bending energy of the membrane by the Helfrich–Canham energy, which depends only on the local curvatures of the surface and compositional heterogeneities [128, 133].

- Due to the high stretching modulus of lipid bilayers, we assume that the membrane is locally incompressible [352]. We use a Lagrange multiplier to implement this constraint [8, 150].

- We assume that the RBC is at mechanical equilibrium at all times, allowing us to neglect inertia [35, 423, 424]. This assumption is consistent with the experimentally observed shapes for the resting RBCs in both *vivo* and *vitro* [425, 426].

- We assume that the total surface area of the RBC membrane is constant and is 135 μm^2 [427, 428]. All our simulations are conducted using this constant area.

- For simplicity in the numerical simulations, we assume that the RBC is rotationally symmetric and also has a reflection symmetry with respect to the Z = 0 plane (see Fig. 5.1C) [128,165,427,429]. This assumption reduces the computational cost of the simulation to simply calculating the shape of the curve shown by red dotted line in Fig. 5.1C.

C.2.2 Membrane mechanics

In this section, we present a concise derivation of the governing mathematical shape equations for the RBC membrane at mechanical equilibrium. The complete derivation with details are given in [8, 136, 150, 152].

The total free energy of the lipid bilayer (E) including the bending energy of the membrane (E_b) and the work done by the applied forces by the membrane skeleton (E_f) is given by [5, 136, 183, 266]

$$E = E_b - E_f, \tag{C.1}$$

where

$$E_b = \int_\omega (W(H,K;\theta^\alpha) + \lambda(\theta^\alpha))da - pV, \quad \text{and} \tag{C.2a}$$

$$E_f = \int_\omega \mathbf{F}(\theta^\alpha).(\mathbf{r} - \mathbf{r}_0)da. \tag{C.2b}$$

Here ω is the total membrane surface area, W is the energy density, θ^α denotes the surface coordinate where $\alpha \in \{1,2\}$, H is the mean curvature of the surface, K is the Gaussian curvature, λ is the membrane tension field which is the Lagrange multiplier associated with the local area constraint, p is is the transmembrane pressure which is the Lagrange multiplier associated with the volume constraint, V is the enclosed volume, $\mathbf{F}$ is the force per unit area, $\mathbf{r}$ is the position vector in the current configuration, and $\mathbf{r}_0$ is the position vector in the reference frame.

Substituting Eq.s C.2a and C.2b into Eq. C.1 and using the variational approach to minimize the total energy gives us the so-called "shape equation" and the incompressibility

condition [136, 150]

$$\Delta\frac{1}{2}W_H + W_H(2H^2 - K) + 2H(KW_K - W) - 2\lambda H = p + \mathbf{F}\cdot\mathbf{n}, \tag{C.3a}$$

$$\lambda_{,\alpha} + \frac{\partial W}{\partial x^{\alpha}_{|\exp}} = -\mathbf{F}\cdot\mathbf{a}_s, \tag{C.3b}$$

where $\Delta(\cdot) = (\cdot)_{;\alpha\beta}a^{\alpha\beta}$ is the surface Laplacian where $(.)_{;\alpha}$ denotes the covariant derivative and $a^{\alpha beta}$ is the dual metric, $\mathbf{n}$ is the unit normal vector to the membrane surface, $\mathbf{a}_\alpha$ is the unit tangent vector in the α direction, and $(.)_{|\exp}$ represents the explicit derivative with respect to coordinate θ^α.

C.2.3 Helfrich-Canham energy

In this study, to model the bending energy of the RBC membrane, we used the classical Helfrich-Canham energy given by [5, 133, 409]

$$W(H, K; \theta^\alpha) = \kappa H(\theta^\alpha)^2 + \kappa_G K(\theta^\alpha), \tag{C.4}$$

where κ and κ_G are constants representing the bending and Gaussian moduli respectively.

Using Helfrich-Canham energy (Eq. C.4) simplifies the shape equation (Eq. C.3a) and the incompressibility condition (Eq. C.3b) as

$$\kappa\Delta H + 2\kappa H(H^2 - K) = p + 2\lambda H + \mathbf{F}\cdot\mathbf{n}, \tag{C.5a}$$

$$\lambda_{,\alpha} = -\mathbf{F}\cdot\mathbf{a}_\alpha, \tag{C.5b}$$

where $(.)_{,\alpha}$ is the partial derivative with respect to the coordinate θ^{α}.

C.2.4 Governing equations in axisymmetric coordinates

We assumed the RBC has a rotationally symmetric shape and define the surface of revolution (Fig. 5.1C) by

$$\mathbf{r}(s,\theta) = R(s)\mathbf{e}_r(\theta) + Z(s)\mathbf{k}, \tag{C.6}$$

where s is the arclength along the curve, R(s) is the radius from the axis of rotation, Z(s) is the height from the base plane, and $(\mathbf{e}_r, \mathbf{e}_\theta, \mathbf{k})$ form the basis coordinate. Defining ψ as the angle made by the tangent with respect to the vertical gives

$$R'(s) = \cos(\psi), \quad Z'(s) = \sin(\psi), \tag{C.7}$$

which satisfies the identity $(R')^2 + (Z')^2 = 1$, where $()'$ is the partial derivative with respect to the arclength. Using Eq. C.7, we can define the normal ($\mathbf{n}$) and tangent ($\mathbf{a}_s$) vectors to the surface as

$$\mathbf{n} = -\sin\psi\mathbf{e}_r(\theta) + \cos\psi\mathbf{k}, \quad \mathbf{a}_s = \cos\psi\mathbf{e}_r(\theta) + \sin\psi\mathbf{k}. \tag{C.8}$$

This parameterization allows us to write the tangential (κ_ν) and transverse (κ_τ) curvatures as

$$\kappa_\nu = \psi', \quad \kappa_\tau = \frac{\sin\psi}{R}. \tag{C.9}$$

The mean curvature (H) and Gaussian curvature (K) are obtained by summation and multiplication of the tangential and transverse curvatures

$$H = \frac{1}{2}(\kappa_v + \kappa_\tau) = \frac{1}{2}(\psi' + \frac{\sin\psi}{R}), \quad K = \kappa_\tau \kappa_v = \frac{\psi' \sin\psi}{R}. \tag{C.10}$$

Finally, we define $M = \frac{1}{2\kappa} R(W_H)'$ to reduce the governing equations (Eq. C.5a and Eq. C.5b) to a system of first- order differential equations with six unknowns R, Z, ψ, H, M, and λ [6, 135, 152],

$$\begin{aligned} R' = \cos\psi, \quad Z' = \sin\psi, \quad R\psi' = 2RH - \sin\psi, \quad RH' = M, \\ \frac{M'}{R} = \frac{p}{\kappa} + \frac{\mathbf{F}\cdot\mathbf{n}}{\kappa} + \frac{2H\lambda}{\kappa} - 2H\left(H - \frac{\sin\psi}{R}\right)^2 \\ \text{and } \lambda' = -\mathbf{F}\cdot\mathbf{a}_s. \end{aligned} \tag{C.11}$$

In order to solve the system of equations in Eq. C.11, we need to provide six boundary conditions. We consider an axisymmetric RBC with reflection symmetry with respect to the Z = 0 plane (see Fig. 5.1C). These assumptions can be applied as the following boundary conditions,

$$\begin{aligned} R(0^+) = 0, \quad \psi(0^+) = 0, \quad Z(s_{max}) = 0, \\ \psi(s_{max}) = \frac{-\pi}{2}, \quad M(s_{max}) = 0, \quad \text{and} \quad \lambda(s_{max}) = \lambda_0, \end{aligned} \tag{C.12}$$

where s_{max} is the maximum length of the computational domain and λ_0 is the prescribed membrane tension. One advantage of an asymmetric coordinate system is that the manifold area (A) and the

occupied volume (V) can be expressed in term of arclength,

$$A(s) = 2\pi \int_0^s R(\eta) d\eta, \tag{C.13a}$$

$$V(s) = 2\pi \int_0^s R(\eta) Z(\eta) \cos(\psi) d\eta, \tag{C.13b}$$

which allows us to conserve the total area of the RBC by changing the maximum length of the computational domain (s_{max}).

Considering the spherical shape of RBC with no applied force, we can calculate the reduced volume (v) as

$$v = V/V_{\text{sphere}} \tag{C.14}$$

where V_{sphere} is the volume of the sphere that we get from simulation when there is no applied force along membrane ($F = 0$).

C.2.5 Nondimensionalization

In order to perform the numerical computations, we nondimensionalized the system of equations (Eq. C.11) by using two positive constants, the radius of the RBC (R_0) and the lipid bilayer bending rigidity (κ_0). This allows us to define the dimensionless variables as

$$\begin{gathered} t = \frac{s}{R_0}, \quad r = \frac{R}{R_0}, \quad z = \frac{Z}{R_0}, \quad h = HR_0 \quad m = MR_0 \\ \tilde{\lambda} = \frac{\lambda R_0^2}{\kappa_0}, \quad \tilde{p} = \frac{pR_0^3}{\kappa_0} \quad \mathbf{f} = \frac{\mathbf{F}R_0^3}{\kappa_0}, \quad \tilde{\kappa} = \frac{\kappa}{\kappa_0}. \end{gathered} \tag{C.15}$$

Rewriting Eq. C.11 in terms of the dimensionless variables, we get [6]

$$\begin{aligned} \dot{r} = \cos\psi, \quad \dot{z} = \sin\psi, \quad r\dot{\psi} = 2rh - \sin\psi, \quad x\dot{h} = m, \\ \frac{\dot{m}}{r} = \frac{\tilde{p}}{\tilde{\kappa}} + \frac{\mathbf{f}\cdot\mathbf{n}}{\tilde{\kappa}} + \frac{2h\tilde{\lambda}}{\tilde{\kappa}} - 2h\left(h - \frac{\sin\psi}{r}\right)^2, \quad \dot{\tilde{\lambda}} = -\mathbf{f}\cdot\mathbf{a}_s, \end{aligned} \tag{C.16}$$

where $(\dot{})$ is the partial derivative with respect to t. With the defined dimensionless variables in Eq. C.15, the boundary conditions simplified as

$$\begin{aligned} r(0^+) = 0, \quad \psi(0^+) = 0, \quad z(\mathrm{t_{max}}) = 0 \\ \psi(\mathrm{t_{max}}) = \frac{-\pi}{2}, \quad m(\mathrm{t_{max}}) = 0, \quad \text{and} \quad \tilde{\lambda}(\mathrm{t_{max}}) = \tilde{\lambda}_0. \end{aligned} \tag{C.17}$$

C.2.6 Parametrization of RBC biconcave morphology and shape error estimation

There are several parametric models to describe the biconcave morphology of an RBC [433, 442, 444, 445]. Initially, Funaki proposed the Cassini oval model for the RBC biconcave morphology given by [442]

$$(R^2 + Z^2 + a^2) - 4a^2R^2 = c^4, \tag{C.18}$$

where a and c are constants with the condition that $a < c < \sqrt{2}a$. Yurkin modified the Cassini oval model to an implicit equation with four constants given by [444]

$$R^4 + 2C_4R^2Z^2 + Z^4 + C_1R^2 + C_2Z^2 + C_3 = 0, \tag{C.19}$$

where C_1, C_2, C_3, and C_4 are constants that depended on the RBC dimension ($C_1 = -14.85$, $C_2 = 40.40$, $C_3 = -6.65$, and $C_4 = -0.30$). Borovoi et al. introduced a function that represents the biconcave shape of an RBC in the spherical coordinate as [445]

$$R(\theta) = e\sin^q(\theta) + b, \tag{C.20}$$

where e, b, and q are constants that were determined by fitting the function to the standard shape of an RBC ($e = 3$ μm, $b = 0.75$ μm, and $q = 5$). The most realistic model for the biconcave shape of an RBC was proposed by Evans and Fung based on direct experimental measurements [433]

$$Z(R) = \pm 0.5\sqrt{1 - (\frac{2R}{L})}(D_1 + D_2(\frac{2R}{L})^2 - D_3(\frac{2R}{L})^4), \tag{C.21}$$

where D_1, D_2, and D_3 are the constants that were calculated by fitting the function to the average dimension of an experimentally observed RBC and statistical analysis ($D_1 = 0.81$ μm, $D_2 = 7.83$ μm, and $D_3 = -4.39$ μm). We plotted these different proposed parametric models together for the biconcave shape of an RBC for fixed h_{min}, h_{max}, and L (Fig. 5.2B). In this study, we used the given parametric function by Evans and Fung (Eq. C.21) as the reference geometry for the RBC experimental shape.

Typically, there is a mismatch between each RBC shape obtained from our mechanical model (Eq. C.16) and the RBC parametric shape (Eq. C.21). Considering the three characteristic

lengths (h_{min}, h_{max}, and L in Fig. 5.1C), we can define three errors that characterize the difference between each of these lengths in the simulated shapes and the reference experimental shape,

$$\begin{aligned} \varepsilon_{hmax} &= \frac{|h_{max,par} - h_{max,sim}|}{L_{par}} = \frac{|\Delta h_{max}|}{L_{par}} \\ \varepsilon_{hmin} &= \frac{|h_{min,par} - h_{min,sim}|}{L_{par}} = \frac{|\Delta h_{min}|}{L_{par}} \\ \varepsilon_{L} &= \frac{|L_{par} - L_{sim}|}{L_{par}} = \frac{|\Delta L|}{L_{par}}, \end{aligned} \tag{C.22}$$

where $(.)_{sim}$ is the calculated length from the simulated shape and $(.)_{par}$ is the measured length in the parametric RBC shape (Eq. C.21). The total error (ε_{total}) in the shape of the simulated RBC can be calculated by the root mean square (RMS) between each two mapped points of the simulated and parametric shapes

$$\varepsilon_{total} = \frac{\sqrt{\frac{1}{N}\left[\sum_{i=1}^{i=N}(Z_{i,sim} - Z_{i,par})^2 + (R_{i,sim} - R_{i,par})^2\right]}}{L_{par}}, \tag{C.23}$$

where N is the total number of nodes across the RBC shapes, i is the index node, $Z_{i,sim}$ and $Z_{i,par}$ are the height of the simulated and the RBC parametric (Eq. 3) shapes at index i, respectively. $R_{i,sim}$ is the radius of the simulated shape at index i, and $R_{i,par}$ is the radius of the RBC parametric shape (Eq. 3) at index i (see Fig. 5.2C). To trace the simulated shape and the parametric shape (Eq. 3), we mapped the points with the maximum height, minimum height, and maximum radius. Then, we discretized the domain equally between the points and calculated the errors.

C.2.7 Numerical implementation

We solved the system of first-order differential equations (Eq. C.16) with boundary conditions Eq. C.17 by the finite element software COMSOL MULTIPHYSICS ^{R} 5.3a, using the "General Form PDE" module. Here, we summarize the steps and assumptions that we used for each simulation.

- All the simulations were performed for fixed total arclength. However, in each simulation, the maximum arclength (s_{max}) varies to conserve the total area of the RBC membrane.
- The computational domain (t) was discretized equally with mesh size = 0.001.
- To have a sharp but smooth transition in the distribution of the force (**f**), we used a hyperbolic tangent function given by

$$\mathbf{f} = \frac{1}{2}[\tanh(g(t - s_{\text{dimple}}))], \tag{C.24}$$

  where g is a constant (here we set g=20) and s_{dimple} represents the length scale that the local force at the dimple is applied.
- The applied force in Figs. 5.4-5.5 and Fig. 5.7-5.8 was progressively increased such that each solution was used as an initial guess for the next step.

C.3 Supplementary figures

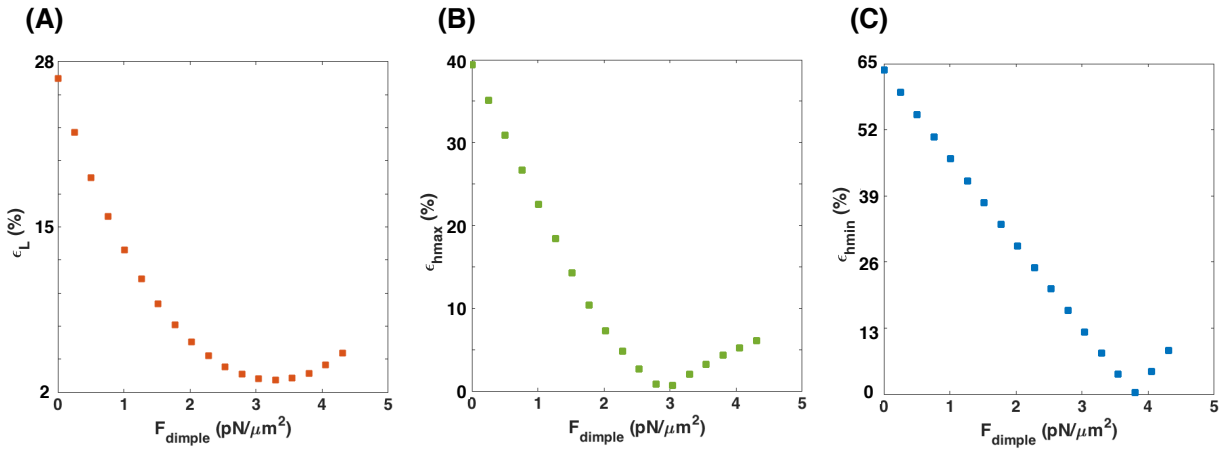

Figure C.1: The error in the characteristic lengths (Eq. C.22) is a nonlinear function of dimple force density (F_{dimple}). (A) Calculated error in the maximum length of the simulated RBC (ε_L) as a function of F_{dimple}. (B) Calculated error in the maximum height of the rim of the simulated RBC (ε_{hmax}) as a function of F_{dimple}. (C) Calculated error in the minimum height of the dimple of the simulated RBC (ε_{hmin}) as a function of F_{dimple}. In all three graphs, with increasing F_{dimple} from zero, initially the error decreases about an order of magnitude and attains a relative minimum. Any further increase in F_{dimple} toward the large dimple force density ($F_{dimple} > 4$ pN/μm^2) leads to a larger error in all characteristic lengths.

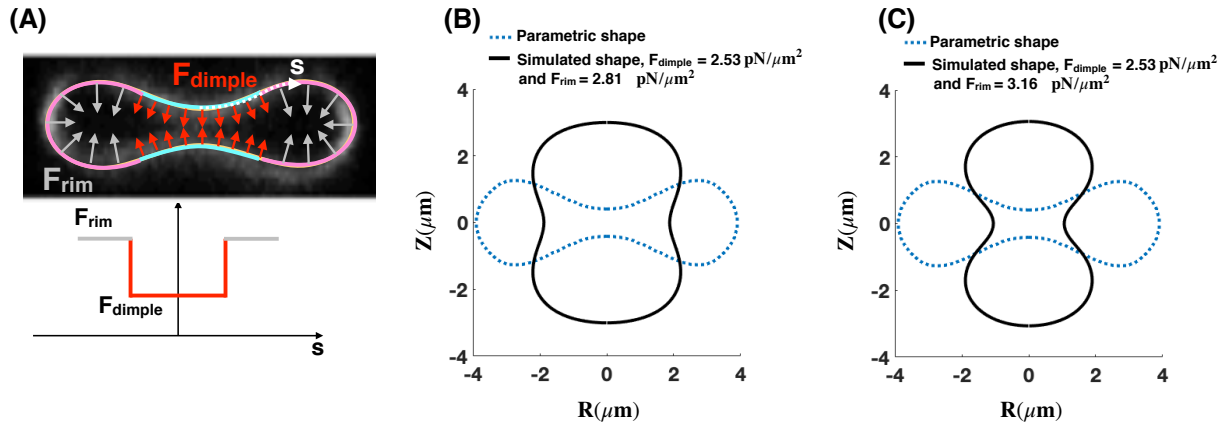

Figure C.2: Applying a large pulling force at the rim region causes a very large shape error. (A, upper) Schematic of a biconcave RBC with a small force per unit area (red arrows) at the dimple and a large force per unit area (gray arrows) at the rim section. (A, lower) The applied force along the membrane as a function of the arclength (Eq. C.24). (B) A comparison between the simulated shape of RBC with F_{dimple} = 2.53 pN/μm^2 and F_{rim} = 2.81 pN/μm^2 and the parametric shape of an RBC given by Eq. C.21. Having a larger force density along the rim region deviates the simulated shape from a biconcave to a peanut- shape geometry. Therefore, the calculated shape error becomes significantly large ($\varepsilon_{total} \sim 52\%$). (C) The parametric shape of an RBC (Eq. C.21) versus the shape that obtained from the simulation with F_{dimple} = 2.53 pN/μm^2 and F_{rim} = 3.16 pN/μm^2. As the rim force density increases, we found a much larger shape error in the simulated geometry ($\varepsilon_{total} \sim 91\%$).

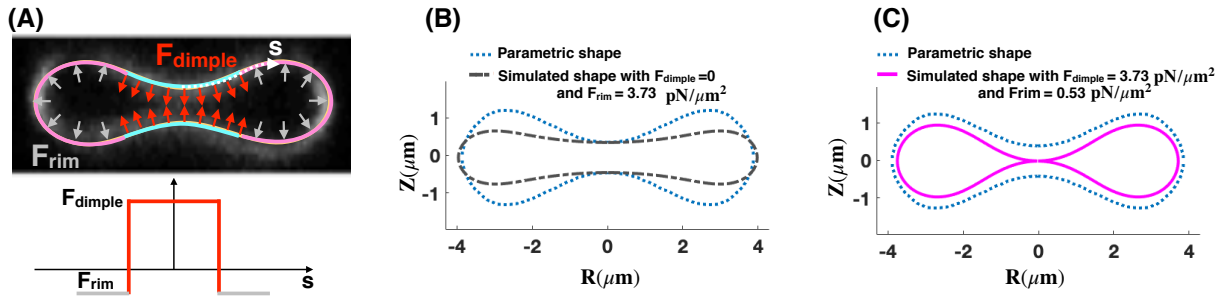

Figure C.3: Applying a pushing force at the rim region increases the total shape error (Eq. C.23). (A) (A, upper) Schematic of a biconcave RBC with an inward force per unit area (red arrows) at the dimple and an outward force per unit area (gray arrows) at the rim section. (A, lower) The applied force along the membrane as a function of the arclength (Eq. C.24). The simulated shape of RBC with only a pulling force at the dimple region (F_{rim} = 3.73 pN/μm^2). Here, the total shape error is $\varepsilon_{total} \sim 12.5\%$, which is larger than even the case with the uniform force per unit area (Fig. 3, center). (C) The simulated shape of RBC with both pulling and pushing forces at the dimple and rim regions respectively (F_{dimple} = 3.73 pN/μm^2 and F_{rim} = 0.53 pN/μm^2). Adding the small pushing force at the rim region compared to Fig. 5.4, increased the total shape error noticeably from $\varepsilon_{total} \sim 5.62\%$ to $\varepsilon_{total} \sim 9.71\%$.

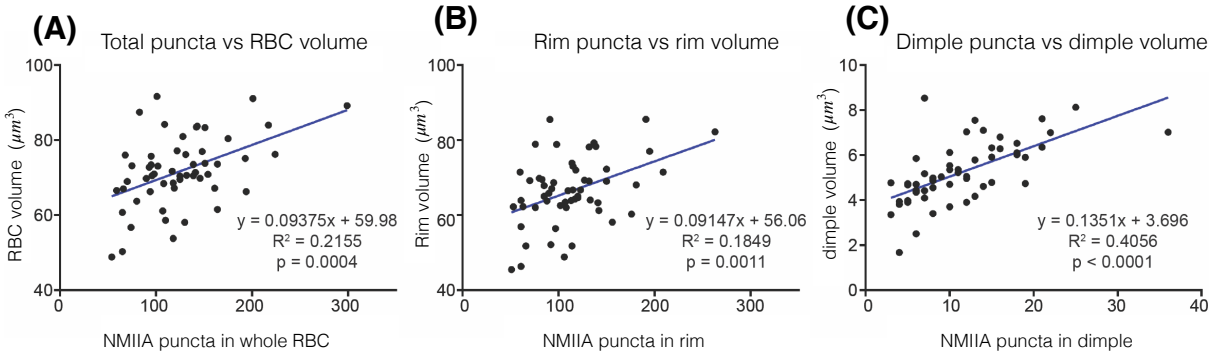

Figure C.4: The number of NMIIA puncta increases with region volume. (A-C) Scatterplots of NMIIA puncta in the whole RBC versus the whole RBC volume (A), NMIIA puncta in the rim versus the rim volume (B), and NMIIA puncta in the dimple versus the dimple volume (C). Blue lines represent linear best-fit lines. The equation for the best-fit line, the R^2 value, and the p-value for each linear regression are given next to the chart. In all three regions, the number of NMIIA puncta increases with increasing region volume. n = 55 RBCs from 3 individual donors (same RBCs as in Fig. 5.6).

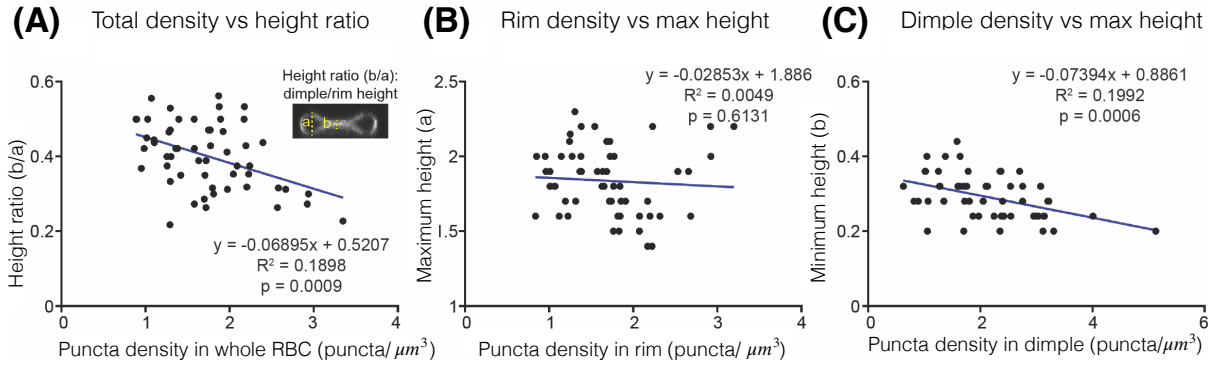

Figure C.5: RBCs with higher biconcavity have higher NMIIA density in the whole RBC and in the dimple. (A-C) Predictions about the relationship between NMIIA density and RBC shape based on the model. (A) Scatterplot of NMIIA puncta density in the whole RBC versus RBC biconcavity (height ratio) measured from the ratio of cell height at the dimple to maximum cell height at the rim from an XZ slice near the center of the cell (see inset). (B) Scatterplot of NMIIA puncta density in rim region versus maximum height at the rim (rim height (a) in (A)). (C) Scatterplot of NMIIA puncta density in dimple region versus minimum height at the dimple (dimple height (b) in (A)). (A-C) Blue lines represent linear best-fit lines. The equation for the best-fit line, the R^2 value, and the p-value for each linear regression are given next to the chart. Height ratio generally decreases (indicating increasing biconcavity) with increasing whole RBC puncta density (A), and minimum height at the dimple generally decreases with increasing dimple puncta density (C), though there is high variability in this trend between individual cells. Maximum height at the rim does not correlate with rim puncta density (B). n = 55 RBCs from 3 individual donors (same RBCs as in Fig. 5.6).

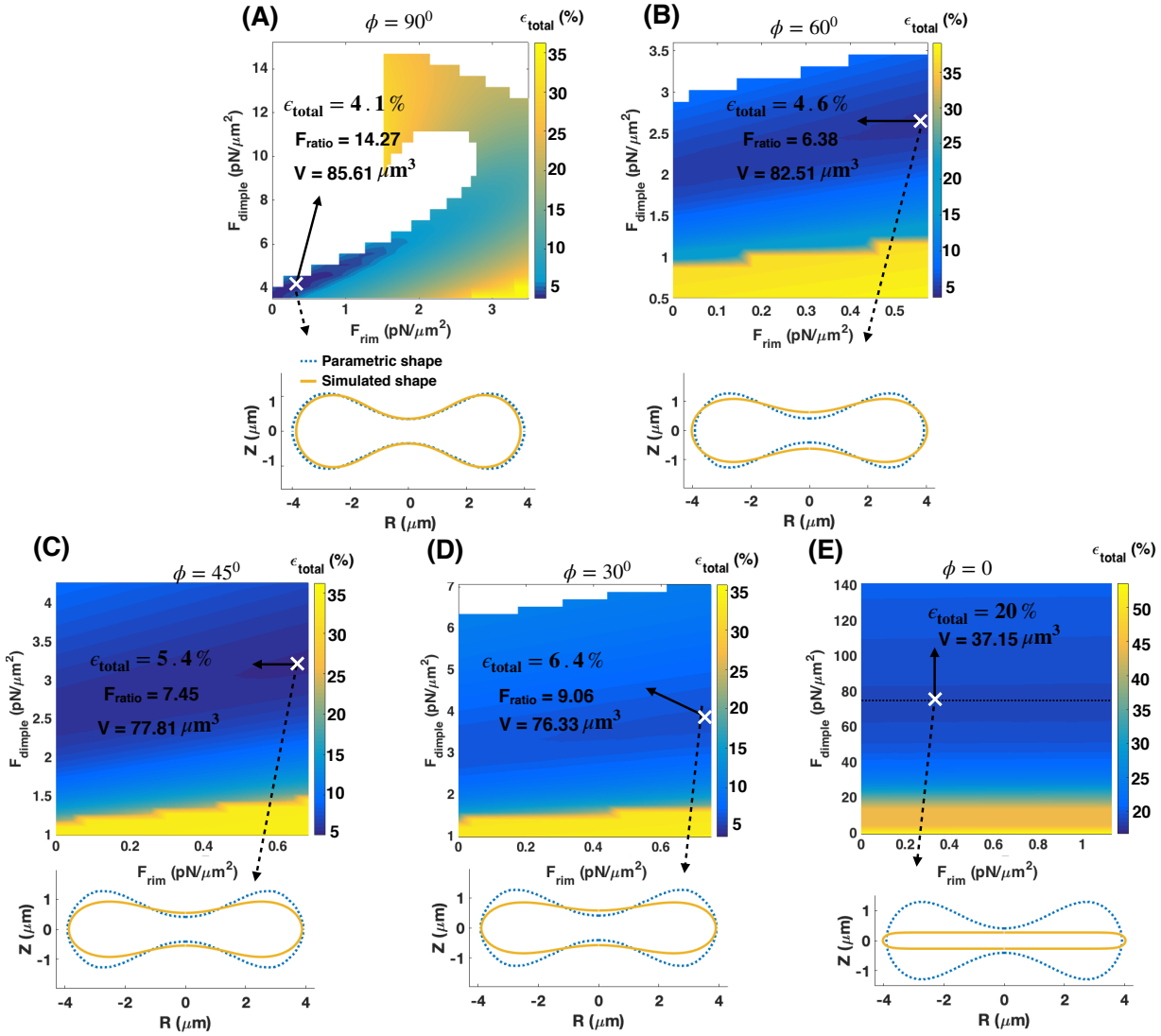

Figure C.6: For tensionless membrane (Tension =0), deviation of the applied forces from normal ($\phi = 90^0$) to the tangential orientation ($\phi = 0$) results in the formation of pancake-shaped geometries with large shape error. The Heat maps show the total error in the shape of the simulated RBCs for a range of force densities in the dimple and rim regions. (A) The applied forces are assumed to be normal ($\phi = 90^0$). (B) The applied forces make angle $\phi = 60^0$ with the tangent vector $\mathbf{a}_s$. (C) The applied forces make angle $\phi = 45^0$ with the tangent vector $\mathbf{a}_s$. (D) The applied forces make angle $\phi = 30^0$ with the tangent vector $\mathbf{a}_s$. (E) The applied forces are tangent to the membrane surface ($\phi = 0$).. In each heat map, the point with the minimum error is marked with '**X**'. Also, for each marked point, the volume of the simulated RBC (V) is calculated using Eq. C.13b and the shape (solid yellow line) is shown in comparison with the reference parametric given in Eq. C.21 (dotted blue line). In the case of tangential forces ($\phi = 0$), the shape error is independent of the magnitude of the rim force density (F_{rim}). Therefore, the shape error is minimum along a line

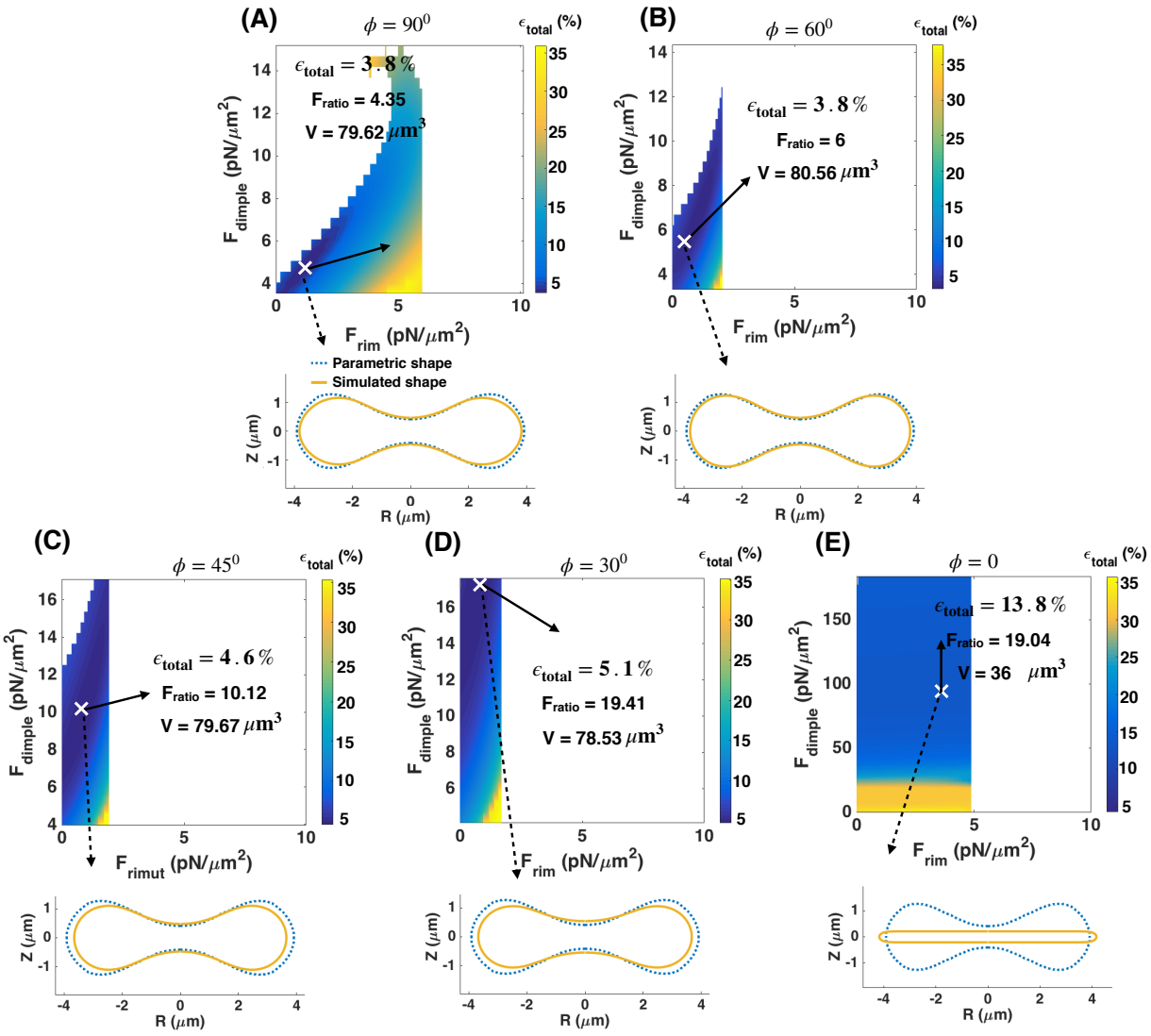

Figure C.7: For low membrane tension (Tension =10^{-4} pN/nm), deviation of the applied forces from normal ($\phi = 90^0$) to the tangential orientation ($\phi = 0$) results in the formation of pancake-shaped geometries with large shape error. The Heat maps show the total error in the shape of the simulated RBCs for a range of force densities in the dimple and rim regions. (A) The applied forces are assumed to be normal ($\phi = 90^0$). (B) The applied forces make angle $\phi = 60^0$ with the tangent vector $\mathbf{a}_s$. (C) The applied forces make angle $\phi = 45^0$ with the tangent vector $\mathbf{a}_s$. (D) The applied forces make angle $\phi = 30^0$ with the tangent vector $\mathbf{a}_s$. (E) The applied forces are tangent to the membrane surface ($\phi = 0$). In each heat map, the point with the minimum error is marked with '**X**'. Also, for each marked point, the volume of the simulated RBC (V) is calculated using Eq. C.13b and the shape (solid yellow line) is shown in comparison with the reference parametric given in Eq. C.21 (dotted blue line).

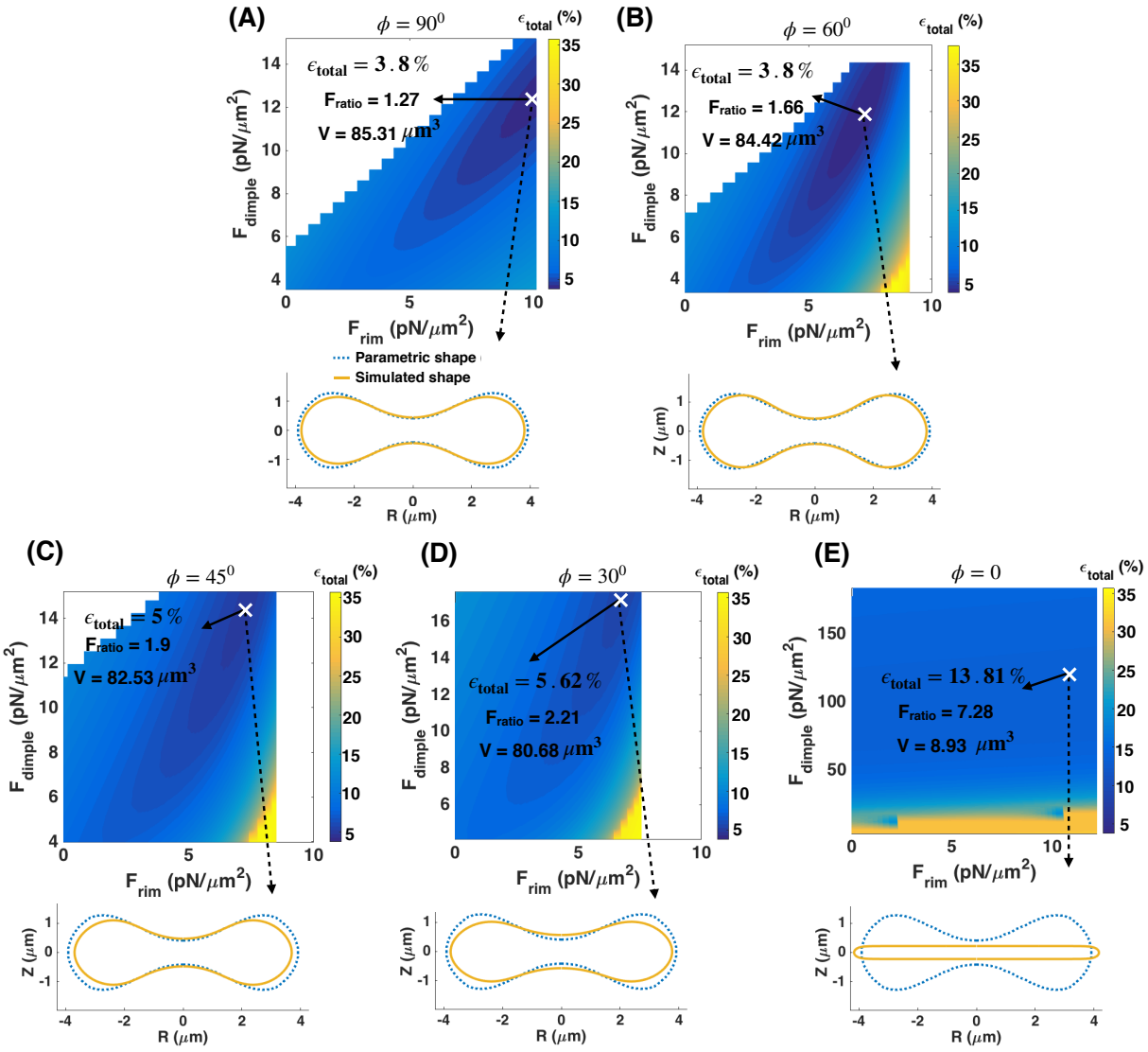

Figure C.8: For intermediate membrane tension (Tension $=10^{-3}$ pN/nm), deviation of the applied forces from normal ($\phi = 90^0$) to the tangential orientation ($\phi = 0$) results in the formation of pancake-shaped geometries with large shape error. The Heat maps show the total error in the shape of the simulated RBCs for a range of force densities in the dimple and rim regions. (A) The applied forces are assumed to be normal ($\phi = 90^0$). (B) The applied forces make angle $\phi = 60^0$ with the tangent vector $\mathbf{a}_s$. (C) The applied forces make angle $\phi = 45^0$ with the tangent vector $\mathbf{a}_s$. (D) The applied forces make angle $\phi = 30^0$ with the tangent vector $\mathbf{a}_s$. (E) The applied forces are tangent to the membrane surface ($\phi = 0$). In each heat map, the point with the minimum error is marked with '**X**'. Also, for each marked point, the volume of the simulated RBC (V) is calculated using Eq. C.13b and the shape (solid yellow line) is shown in comparison with the reference parametric given in Eq. C.21 (dotted blue line).

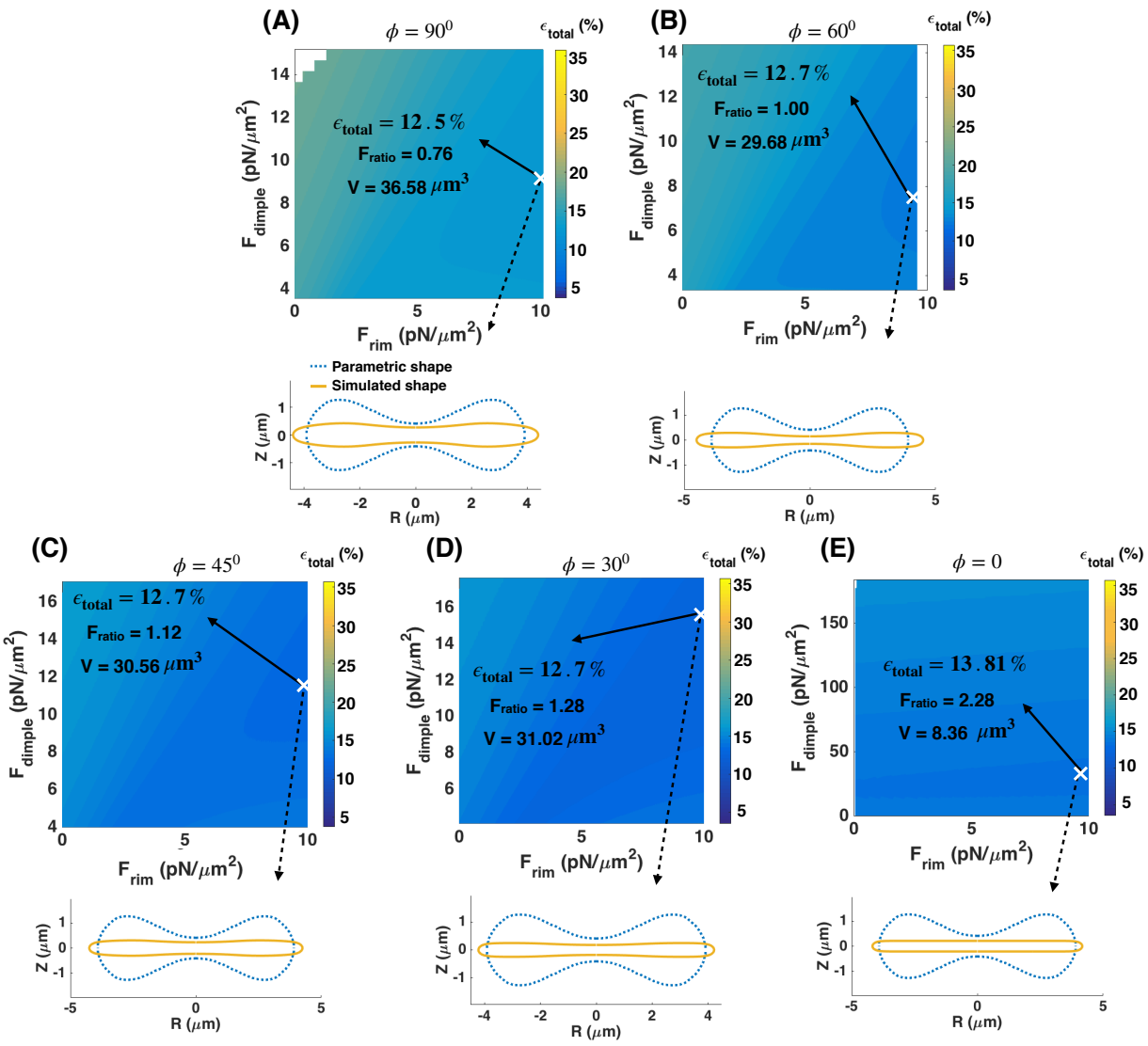

Figure C.9: For high membrane tension (Tension $=10^{-2}$ pN/nm), independent of the orientation of the force, the simulated shapes have pancake morphologies and the shape error is too large ($\varepsilon_{\text{total}} > 0.5\ \mu$m). The Heat maps show the total error in the shape of the simulated RBCs for a range of force densities in the dimple and rim regions. (A) The applied forces are assumed to be normal ($\phi = 90^0$). (B) The applied forces make angle $\phi = 60^0$ with the tangent vector $\mathbf{a}_s$. (C) The applied forces make angle $\phi = 45^0$ with the tangent vector $\mathbf{a}_s$. (D) The applied forces make angle $\phi = 30^0$ with the tangent vector $\mathbf{a}_s$. (E) The applied forces are tangent to the membrane surface ($\phi = 0$). In each heat map, the point with the minimum error is marked with '**X**'. Also, for each marked point, the volume of the simulated RBC (V) is calculated using Eq. C.13b and the shape (solid yellow line) is shown in comparison with the reference parametric given in Eq. C.21 (dotted blue line).

Appendix D

Governing equations of membrane actin interactions in spines

D.1 Table of notations

Table D.1: Notations used in the Chapter 6

Notation	Description	Units
E	Strain energy	pN $\cdot$ nm
p	Pressure difference across the membrane	pN$\cdot$nm^{-2}
θ^{α}	Surface parametrization	
σ	Local energy per unit area	pN $\cdot$nm^{-1}
$\mathbf{r}$	Position vector	
$\mathbf{n}$	Normal vector to the membrane surface	unit vector
λ	Tension, $-(W+\gamma)$	pN$\cdot$nm^{-1}
H	Mean curvature	nm^{-1}
K	Gaussian curvature	nm^{-2}
D	Curvature deviator	nm^{-1}
D_m	Spontaneous deviatoric curvature	nm^{-1}

Table D.2: Notations used in the Chapter 6

Notation	Description	Units
$\mathbf{a}_\alpha$	Basis vector describing the tangent plane	
$\mathbf{a}^\alpha$	Contravariant basis vector	
$a^{\alpha\beta}$	Dual metric	
κ	Bending modulus	$\mathrm{pN} \cdot \mathrm{nm}$
s	Arclength	nm
ψ	Angle between $\mathbf{e}_r$ and $\mathbf{a}_s$	
r	Radial distance	nm
z	Elevation from base plane	nm
$\mathbf{e}_r(\theta)$	Radial basis vector	unit vector
$\mathbf{e}_\theta$	Azimuthal basis vector	unit vector
$\mathbf{k}$	Altitudinal basis vector	unit vector
$\mathbf{f}$	Force density	$\mathrm{pN{\cdot}nm^{-2}}$
$\mathrm{f_z}$	Axial force density	$\mathrm{pN{\cdot}nm^{-2}}$
$\mathrm{f_n}$	Normal force density	$\mathrm{pN{\cdot}nm^{-2}}$
$\mathrm{F_z}$	Axial force	pN
κ_τ	Tangential curvature	$\mathrm{nm^{-1}}$
κ_ν	Transverse curvature	$\mathrm{nm^{-1}}$
A	Total area of membrane	$\mathrm{nm^2}$
A_{force}	Area of applied force	$\mathrm{nm^2}$
γ	unit vector representing orientation of a protein coat	
μ	unit vector normal to γ and $\mathbf{n}$	
V	Confined volume by membrane area	$\mathrm{nm^3}$
$A_{\max}$	Maximum area of membrane	$\mathrm{nm^2}$
λ_0	Surface tension at boundary	$\mathrm{pN{\cdot}nm^{-1}}$
L	Membrane height	nm
M	Shape equation variable	$\mathrm{nm^{-1}}$

D.2 Model development

D.2.1 Assumptions

- We treat the lipid bilayer as a continuous thin elastic shell assuming that the membrane thickness is negligible compared to the radii of membrane curvature [409]. This allows us to model the bending energy of the membrane using the modified version of the Helfrich–Canham energy including the effect of spatially varying deviatoric curvature to represent the induced anisotropic curvatures by periodic F-actin rings and other structures [5, 128, 133, 176, 178, 180].

- We assume that the membrane is locally inextensible since the stretching modulus of the lipid bilayer is an order of magnitude larger than the membrane bending modulus [352]. We implemented this constraint using a Lagrange multiplier which can be interpreted as the tension [150, 528]. We note that this membrane tension, in this study, is better interpreted as the effective contribution of the membrane in-plane stresses and membrane-cortex interactions [374].

- We assume that the time scales of mechanical forces are much faster than other events in dendritic spines allowing us to assume mechanical equilibrium and neglect inertia [150,509]. This assumption is reasonable because the time scale of the equilibration of the mechanical forces is much smaller than the time scale of actin polymerization in dendritic spines [530].

- We assume that the force exerted by the actin cytoskeleton can be represented as work done on the membrane and do not include the molecular details of the actin network [9, 135, 136, 509, 531]. Additionally, we assume that the periodic ring shaped structures of actin and related proteins such as βII spectrins, septics, and BAR-domain proteins can be represented using an anisotropic spontaneous curvature [176, 178, 180, 525].

- For ease of computation, we assume that the geometry of a dendritic spine is rotationally symmetric (see Fig. 6.1B) [509]. This assumption allows us to parametrize the whole surface by a single parameter which is the arclength.

D.2.2 Membrane mechanics

At equilibrium, the total energy of the system (E) including the elastic storage energy of the membrane (E_{elastic}) and the work done by the applied forces by the actin filament (W_{force}) is given by [5, 136, 183, 266]

$$E = E_{\text{elastic}} - W_{\text{force}}, \tag{D.1}$$

where

$$E_{\text{elastic}} = \int_{\omega} (\sigma(H, K, D; \theta^{\alpha}) + \lambda(\theta^{\alpha}))da - pV \quad \text{and} \tag{D.2a}$$

$$W_{\text{force}} = \int_{\omega} \mathbf{f}(\theta^{\alpha}) \cdot (\mathbf{r} - \mathbf{r}_0)da. \tag{D.2b}$$

Here ω is the total membrane surface area, σ is the energy density, θ^{α} denotes the surface coordinate where $\alpha \in \{1, 2\}$, H is the mean curvature of the surface, K is the Gaussian curvature, D is the curvature deviator, λ is the tension field which is the Lagrange multiplier associated with the local area constraint, p is the transmembrane pressure that is the Lagrange multiplier associated with the volume constraint, V is the enclosed volume, $\mathbf{f}$ is the applied force per unit area, $\mathbf{r}$ is the position vector in the current configuration, and $\mathbf{r}_0$ is the position vector in the reference frame. We can write the variation of the total free energy of the system as [136, 183]

$$\dot{E} = \dot{E}_{\text{elastic}} - \dot{W}_{\text{force}}, \tag{D.3}$$

where

$$\dot{E}_{\text{elastic}} = \int_{\omega} \dot{\sigma}\, da + \int_{\omega} (\sigma + \lambda)(\dot{J}/J)\, da - p\dot{V} \quad \text{and} \tag{D.4a}$$

$$\dot{W}_{\text{force}} = \int_{\omega} \mathbf{f}(\theta^{\alpha}) \cdot \mathbf{u}\, da, \tag{D.4b}$$

where $J = \sqrt{a/A}$ is the local areal stretch due to mapping from a reference frame (A) to the actual surface (a), and $\mathbf{u}$ is the virtual displacement of the surface given by

$$\mathbf{u}(\theta^{\alpha}) = \frac{\partial}{\partial \varepsilon} \mathbf{r}(\theta^{\alpha}, \varepsilon)|_{\varepsilon=0} = \dot{\mathbf{r}}. \tag{D.5}$$

Minimization of the energy in Eq. D.3 by usage of the variational approach gives the governing shape equation and the incompressibility condition in a heterogeneous membrane as

$$\begin{aligned} p + \mathbf{f} \cdot \mathbf{n} = \Delta(\frac{1}{2}\sigma_H) + (\sigma_K)_{;\alpha\beta}\tilde{b}^{\alpha\beta} + \sigma_H(2H^2 - K) + 2H(K\sigma_K - \sigma) - 2\lambda H \\ + \frac{1}{2}[\sigma_D(\gamma^{\alpha}\gamma^{\beta} - \mu^{\alpha}\mu^{\beta})]_{;\beta\alpha} + \frac{1}{2}\sigma_D(\gamma^{\alpha}\gamma^{\beta} - \mu^{\alpha}\mu^{\beta})b_{\alpha\eta}b^{\eta}_{\beta}, \end{aligned} \tag{D.6}$$

and

$$(\frac{\partial \sigma}{\partial \theta^{\alpha}_{|exp}} + \lambda_{,\alpha} + \sigma_D[b_{\alpha\beta}(\gamma^{\alpha}\gamma^{\beta})_{;\eta}])a^{\beta\alpha} = \mathbf{f}\cdot\mathbf{a}_s, \tag{D.7}$$

where $\Delta(\cdot)$ is the surface Laplacian, $\mathbf{n}$ is the normal vector to the surface, $\mathbf{a}_s$ is a tangent vector on the surface (we will define it in the next section for axisymmetric coordinates), $a^{\alpha\beta}$ is the dual metric, $b_{\alpha\beta}$ are the coefficients of the second fundamental form, b^{α}_{β} are the mixed components of the curvature, $\tilde{b}^{\alpha\beta}$ is the co-factor of the curvature tensor, $(.)_{;\alpha}$ is the covariant derivative, $(.)_{,\alpha}$ is the partial derivative, and $()_{|exp}$ denotes the explicit derivative with respect to coordinate θ^{α}. Also, γ^{α} and μ^{α} are the projections of and along the tangential vectors given by [183]

$$\begin{aligned} \gamma^{\alpha} &= \gamma\cdot\mathbf{a}^{\alpha} \\ \mu^{\alpha} &= \mu\cdot\mathbf{a}^{\alpha}, \end{aligned} \tag{D.8}$$

where $\mathbf{a}^{\alpha}$ is the contravariant basis vectors, is a unit vector representing the orientation of a one-dimensional curve on the surface which is tangential to the protein coat, and is a unit vector defined as

$$\mu = \mathbf{n}\times\gamma. \tag{D.9}$$

D.2.3 Helfrich energy including deviatoric curvature

We modeled the combined effects of BAR domain proteins and periodic F-actin by deviatoric curvature using the modified version of Helfrich energy that includes deviatoric curvature $D(\theta^{\alpha})$ [5, 128, 133, 176, 178, 180, 324] given as

$$\sigma(H,K,D;\theta^{\alpha}) = \kappa H^2 + \kappa(D - D_m(\theta^{\alpha}))^2, \tag{D.10}$$

where κ is the bending modulus and D_m is the spontaneous (intrinsic) deviatoric curvature [6,183]. Substituting this form of energy density (Eq. D.10) in Eqs. D.6 and D.7 gives

$$\begin{aligned} \underbrace{-\kappa\Big[2H(D-D_m)^2 - \Big((D-D_m)(\gamma^{\alpha}\gamma^{\beta} - \mu^{\alpha}\mu^{\beta})\Big)_{;\beta\alpha} - (D-D_m)(\gamma^{\alpha}\gamma^{\beta} - \mu^{\alpha}\mu^{\beta})b_{\alpha\eta}b^{\eta}_{\beta}\Big]}_{\text{Induced anistropic curvature effects}} \\ \underbrace{+\kappa\Delta H + 2\kappa H(H^2 - K)}_{\text{Elastic effects}} = \underbrace{p + 2\lambda H}_{\text{Capillary effects}} + \underbrace{\mathbf{f}\cdot\mathbf{n}}_{\text{Force due to actin}}, \end{aligned} \tag{D.11}$$

and

$$\underbrace{\lambda_{,\alpha}}_{\substack{\text{Tension}\\ \text{variation}}} = \underbrace{2\kappa(D-D_m)\frac{\partial D_m}{\partial \theta^{\alpha}} + 2\kappa(D-D_m)b_{\alpha\beta}(\gamma^{\alpha}\gamma^{\beta})_{;\eta}}_{\text{Anisotropic curvature induced variation}} - \underbrace{\mathbf{f}\cdot\mathbf{a_s}}_{\substack{\text{Force-induced}\\ \text{variation}}}. \tag{D.12}$$

It should be mentioned that in the modified version of Helfrich energy (Eq. D.10), we assumed that the induced isotropic spontaneous curvature (C) by BAR domain proteins or periodic F-actin is negligible and we ignored the effect of the spontaneous curvature ($C = 0$).

D.2.4 Governing equations in axisymmetric coordinates

Axisymmetric coordinates

We parameterize a surface of revolution with respect to the z axis (Fig. 1B) in the coordinate basis $(\mathbf{e}_r, \mathbf{e}_\theta, \mathbf{k})$ by

$$\mathbf{r}(s,\theta) = r(s)\mathbf{e}_r(\theta) + z(s)\mathbf{k}, \tag{D.13}$$

where s is the arclength along the curve, $r(s)$ is the radial distance from the axis of rotation, and $z(s)$ is the elevation from the reference plane. Since $(dr/ds)^2 + (dz/ds)^2 = 1$, we can define ψ (the angle made by the tangent with respect to the horizontal) such that the normal and tangent vectors are given by

$$\mathbf{n} = -\sin\psi\mathbf{e}_r(\theta) + \cos\psi\mathbf{k} \quad \text{and} \quad \mathbf{a}_s = \cos\psi\mathbf{e}_r(\theta) + \sin\psi\mathbf{k}. \tag{D.14}$$

Following this we have

$$r'(s) = \cos(\psi), \tag{D.15a}$$

$$z'(s) = \sin(\psi), \tag{D.15b}$$

where $(.)' = \frac{d(.)}{ds}$. We can now write the tangential (κ_ν) and transverse (κ_τ) principal curvatures as

$$\kappa_\nu = \psi', \quad \kappa_\tau = r^{-1}\sin\psi, \tag{D.16}$$

and the mean curvature (H), Gaussian curvature (K), and the curvature deviator (D) as

$$\begin{aligned} H &= \frac{1}{2}(\kappa_\nu + \kappa_\tau) = \frac{1}{2}(\psi' + r^{-1}\sin\psi), \\ K &= \kappa_\tau\kappa_\nu = \frac{\psi'\sin\psi}{r}, \\ D &= \frac{1}{2}(\kappa_\tau - \kappa_\nu) = \frac{1}{2}(r^{-1}\sin\psi - \psi') = r^{-1}\sin\psi - H. \end{aligned} \tag{D.17}$$

Equilibrium equations

In order to simplify the governing shape and incompressibility equations, we define M as

$$M = \frac{1}{2\kappa} r[(\sigma_H)' - (\sigma_D)'], \tag{D.18}$$

which allows us to simplify the shape equation (Eq. D.11) and the inextensibility condition (Eq. D.12) as a system of first order differential equations given by

$$\begin{aligned}
r' = \cos\psi, \quad z' = \sin\psi, \quad r\psi' = 2rH - \sin\psi, \\
2rH' = M - rD_m' + 2H\cos(\psi) - \frac{2\cos(\psi)\sin(\psi)}{r}, \\
\frac{M'}{r} = \frac{p}{\kappa} + \frac{\mathbf{f}\cdot\mathbf{n}}{\kappa} + 2H\Big[H^2 + \frac{\lambda}{\kappa} + (\frac{\sin(\psi)}{r} - H - D_m)^2 - 2(\frac{\sin(\psi)}{r} - H - D_m)(\frac{\sin(\psi)}{r} - H)\Big] \\
-2H\left[H^2 + \left(H - r^{-1}\sin\psi\right)^2\right] - 2\frac{\cos(\psi)}{r}\Big[\frac{H\cos(\psi)}{r} - \frac{\sin(\psi)\cos(\psi)}{r^2} - \frac{D_m'}{2} - \frac{M}{2r}\Big], \\
\lambda' = -2\kappa(\frac{\sin(\psi)}{r} - H - D_m)D_m' - \mathbf{f}\cdot\mathbf{a_s}.
\end{aligned} \tag{D.19}$$

In axisymmetric coordinates, the total area of the manifold (A) can be expressed in term of arclength as

$$A(s) = 2\pi\int_0^s r(t)dt \quad \rightarrow \quad \frac{dA}{ds} = 2\pi r. \tag{D.20}$$

This allows us to write the governing differential equations (Eq. D.19) in terms of the derivative of area instead of arclength.

In order to solve the coupled partial differential equations in Eq. D.19, we impose six boundary conditions as follow:

$$\begin{aligned} r(0^+) = 0, \quad M(0^+) = 0, \quad \psi(0^+) = 0, \\ z(A_{\max}) = 0, \quad \psi(A_{\max}) = 0, \quad \lambda(A_{\max}) = \lambda_0, \end{aligned} \tag{D.21}$$

where λ_0 is the tension at the far field boundary.

Numerical implementation

In order to solve the system of differential equations along with the boundary conditions, we used 'bvp4c,' a boundary value problem solver in MATLAB. In all simulations, we fixed the total area of the membrane as $A = 8\pi\mu\text{m}^2$ and set the transmembrane pressure to be zero ($p = 0$) to focus mainly on the mechanism of membrane-actin interactions in dendritic spine formation. The mesh points on the domain were chosen such that starting from $A = 0^+$, the mesh size is very small and then increases moving toward the far field boundary $A = A_{\max}$. To have a sharp but smooth transition at the boundaries of the applied forces, we prescribed the forces using a hyperbolic tangent function given as

$$f = \frac{f_0}{2}[\tanh(g(A - A_{\text{force}}))], \tag{D.22}$$

where g is a constant and A_{force} represents the area of the applied forces by actin filaments. Additionally, to get the tubular protrusions from a flat membrane, we prescribed the height of the protrusion as an extra boundary condition ($z(0^+) = z_p$) and calculated the magnitude of the applied force as an unknown parameter.

D.2.5 Analytical solutions

Analytical estimation for filopodia-shaped spines with an axial force

Let us consider a long tubular filopodium with radius r and height L has been pulled from a flat membrane with a axial force F_z (Fig. D.1A). Assuming that $L \gg r$, in the absence of spontaneous deviatoric curvature ($D_m = 0$) and pressure ($p = 0$), the total free energy of the system (Eq. D.1) can be written as

$$E_{\text{filopodium}} = \int_{\omega} (\kappa H^2 + \kappa D^2 + \lambda) da - F_z L. \tag{D.23}$$

For a tubular membrane (ignoring the spherical cap), $H = D = \frac{1}{2r}$, $\int da = 2\pi rL$, and thus the total energy can be simplified as

$$E_{\text{filopodium}} = (\frac{\kappa}{2r^2} + \lambda) 2\pi r L - F_z L. \tag{D.24}$$

Now, we can find the equilibrium radius of the tube (r) and the corresponding force (F_z) by taking $\partial E_{\text{filopodium}}/\partial r = 0$ and $\partial E_{\text{filopodium}}/\partial L = 0$ and solving for the radius and force as [272, 343, 556]

$$r = \sqrt{\frac{\kappa}{2\lambda}} \quad \text{and} \quad F_z = 2\pi\sqrt{2\lambda\kappa}. \tag{D.25}$$

Based on the Eq. D.25, the diameter of the filopodium and the magnitude of the applied forces depend on the tension and the bending rigidity. For example, for a fixed bending rigidity, a large force is required to bend a stiff membrane (large tension) and form a narrow filopodium.

Interestingly, in contrast to the stubby spine (Fig.6.2C), the magnitude of force to form a tubular filopodium is independent of the length of protrusion. In Eq. D.25, we can also find the tension based on the radius of the tubule and rewrite the axial force as

$$\mathrm{F_z} = \frac{2\pi\kappa}{\mathrm{r}}, \tag{D.26}$$

which indicates that to form a narrower filopodium, a larger axial force is required.

Analytical estimation for thin-shaped spines with a uniform normal force density

Let us consider an idealized geometry of a thin-shaped spine as a sphere with radius R that is connected to a cylinder with radius r and height l (Fig. D.1B). Considering the case that a uniform normal force density, $\mathrm{f_n}$, is applied all along the sphere and ignoring the interface between the sphere and the cylinder, we can write the total energy of the system as $E_{\text{thin}} = E_{\text{sphere}} + E_{\text{cylinder}}$. For the sphere, we know that $H = 1/\mathrm{R}$, $D = 0$, and the total surface area is $A_{\text{sphere}} = 4\pi\mathrm{R}^2$. Considering the axial displacement from a flat membrane, we can write the free energy of the spherical part of the thin-shaped spine as (assuming $p = 0$ and $D_m = 0$)

$$E_{\text{sphere}} = (\frac{\kappa}{\mathrm{R}^2} + \lambda)4\pi\mathrm{R}^2 - \int -\mathrm{f_n}\cos(\phi)\big(\mathrm{L} + \mathrm{R} - \mathrm{R}\cos(\phi)\big)da, \tag{D.27}$$

where da is the area element which can be written as $\int da = \int_0^{\pi} 2\pi\mathrm{R}^2\sin(\phi)d\phi$. Eq. D.27 gives

$$E_{\text{sphere}} = (\frac{\kappa}{\mathrm{R}^2} + \lambda)4\pi R^2 - \frac{4\pi}{3}\mathrm{R}^3\mathrm{f_n}. \tag{D.28}$$

For the cylindrical part of the thin-shaped spine, based on the previous section for the filopodia, we know that $H = D = 1/2\mathrm{r}$ and $\mathrm{r} = \sqrt{\kappa/2\lambda}$. Substituting these terms in the energy, we get

$$E_{\text{cylinder}} = 2\pi\sqrt{2\lambda\kappa}l. \tag{D.29}$$

Using Eqs. D.28 and D.29, we can write the total energy of the system as

$$E_{\text{thin}} = (\frac{\kappa}{\mathrm{R}^2} + \lambda)4\pi\mathrm{R}^2 - \frac{4\pi}{3}\mathrm{R}^3\mathrm{f_n} + 2\pi\sqrt{2\lambda\kappa}l. \tag{D.30}$$

Taking $\partial E_{\text{thin}}/\partial \mathrm{R} = 0$, we obtain

$$\mathrm{f_n} = \frac{2\lambda}{\mathrm{R}}. \tag{D.31}$$

In our simulation, we are prescribing the area of the applied normal force ($\mathrm{A_{force}}$) based on the area of the spine head ($\mathrm{A_{spine\text{-}head}}$). Assuming that the spine head has a spherical shape in the area of the applied force, we can find the radius of the sphere based on the area of spine head as

$$\mathrm{A_{force}} = \mathrm{A_{spine\text{-}head}} = \mathrm{A_{sphere}} = 4\pi\mathrm{R}^2 \rightarrow \mathrm{R} = \sqrt{\frac{\mathrm{A_{spine\text{-}head}}}{4\pi}}. \tag{D.32}$$

Substituting Eq. D.32 into Eq. D.31, we have

$$f_n = 4\lambda\sqrt{\frac{\pi}{A_{\text{spine-head}}}}. \tag{D.33}$$

Based on Eq. D.33, if we know the area of the spine head and the tension, we can estimate the required normal force to form a thin-shaped spine. For example, according to Eq. D.33, a smaller normal force density is required to form a thin-shaped spine with a larger head. Similar to the formation of a filopodium (Eq. D.25), the magnitude of the normal force in Eq. D.33 is also independent of the length of the spine.

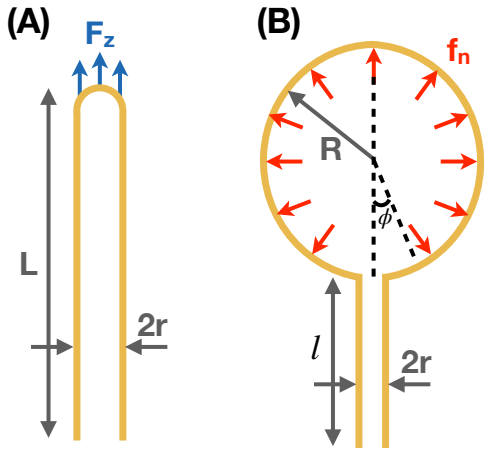

Figure D.1: (A) Schematic of a long filopodium with radius r and height L formed with an axial force F_z applied along the prescribed area shown in blue. (B) An idealized geometry of a thin shaped spine. A sphere with radius R is connected to a cylinder with radius r and height l. A uniform normal force density f_n is applied all along the sphere ($A_{\text{force}} = A_{\text{sphere}} = A_{\text{spine-head}}$).

Additionally, since the spine neck has a tubular shape, we can relate the tension to the radius of spine neck (Eq. D.25) and rewrite the normal force as

$$f_n = \frac{\kappa}{r^2}\sqrt{\frac{\pi}{A_{\text{spine-head}}}}, \tag{D.34}$$

where r is the radius of the spine neck (Fig. D.1B). Comparison of Eq. D.26 and Eq. D.34 shows that the required axial force to form a tubular filopodium is proportional to $1/\mathrm{r}$ while the normal force to form a thin-shaped spine is proportional to $1/\mathrm{r}^2$. This suggests that decreasing the neck diameter of a thin-shaped spines is harder and needs a larger magnitude of a force compared to the filopodial-shaped spines.

Spontaneous deviatoric curvature and the radius of the spines neck

Let us consider a tubular membrane with radius r and height L that has been pulled from a flat membrane with an axial force $\mathrm{F_z}$ and a spontaneous deviatoric curvature D_m along the neck region (Fig. D.2A). Ignoring the spherical cap, the total free energy of the system (Eq. D.1) can be written as

$$E_{\mathrm{tube}} = \Big(\frac{\kappa}{4\mathrm{r}^2} + \lambda + \kappa(\frac{1}{2\mathrm{r}} - D_m)^2\Big)2\pi\mathrm{rL} - \mathrm{F_z}l. \tag{D.35}$$

To find the equilibrium radius of the tube (r) and the corresponding force ($\mathrm{F_z}$), we take $\partial E_{\mathrm{tube}}/\partial \mathrm{r} = 0$ and $\partial E_{\mathrm{tube}}/\partial l = 0$ and solve for the radius and force as

$$\mathrm{r} = \sqrt{\frac{\kappa}{2(\lambda + \kappa D_m^2)}} \quad \text{and} \quad \mathrm{F_z} = 2\pi\Big(\sqrt{2\kappa(\lambda + \kappa D_m^2)} - \kappa D_m\Big), \tag{D.36}$$

which reduces to Eq. D.25 for zero spontaneous deviatoric curvature ($D_m = 0$). Based on Eq. D.36, we can see that the radius of a tubule decreases with increasing magnitude of spontaneous deviatoric curvature (Fig. 6.5A). This is consistent with the previous study by Walani et al. where they showed that a tubular membrane gets narrower with increasing strength of spontaneous deviatoric curvature [183]. In Fig. 6.5C, we plotted the magnitude of the axial force as a function

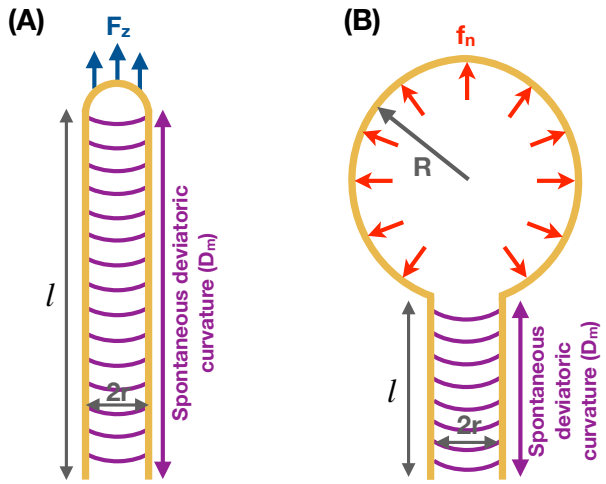

Figure D.2: Schematic of (A) a tubular membrane with an axial force (F_z) and spontaneous deviatoric curvature (D_m) along the neck with length l and (B) an idealized geometry of a thin-shaped spine with normal force density (f_n) along the head and spontaneous deviatoric curvature (D_m) along the neck.

of tension and spontaneous deviatoric curvature. As can be seen, axial force has a local minimum shown by the red dashed line. By taking $\partial F_z/\partial D = 0$, we can find the relationship between the tension and spontaneous deviatoric curvature along the red line (Fig. 6.5C) is

$$\lambda = \kappa D_m^2, \tag{D.37}$$

and the magnitude of local minimum force is given by

$$F_{z,\min} = 2\pi\kappa D_m, \tag{D.38}$$

which linearly depends on D_m. In addition, we can use the radius-tension relationship in Eq. D.36 to revise the normal force equation for the formation of thin-shaped spines (Eq. D.34) to include the effect of spontaneous deviatoric curvature and get

$$\mathrm{F_n} = 2\kappa(\frac{1}{2\mathrm{r}^2} - D_m^2)\sqrt{4\pi \mathrm{A_{spine\text{-}head}}}, \tag{D.39}$$

which indicates that by adding the effect of spontaneous deviatoric curvature, the magnitude of normal force needed to stabilize a thin-shaped spine decreases. Theoretically, if $D_m = \frac{1}{\sqrt{2}\mathrm{r_{neck}}}$, a thin-shaped spine can have a stable geometry without any actin-mediated forces.

D.3 Supplementary figures

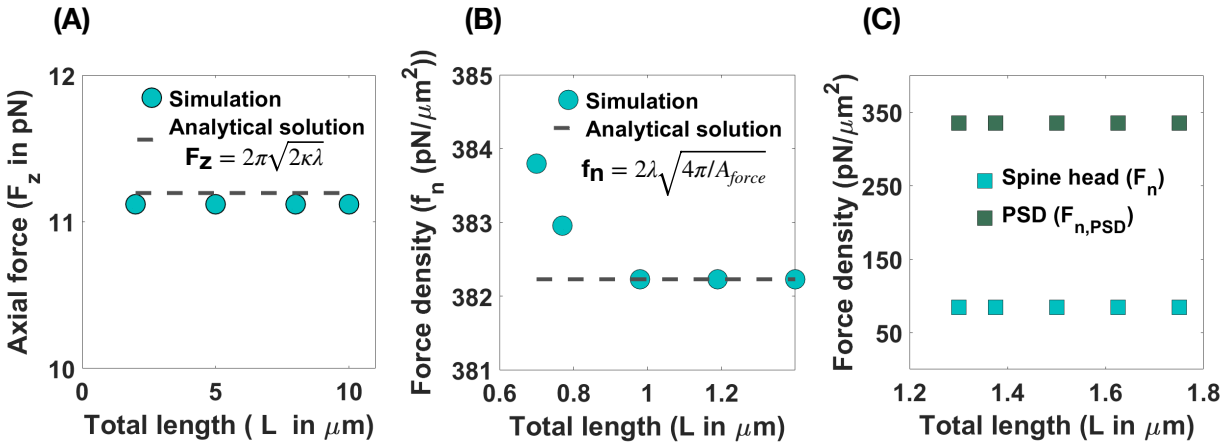

Figure D.3: The magnitude of axial and normal force densities that are required to form (A) filopodia, (B) thin, and (C) mushroom-shaped spines are independent of the length of the spines.

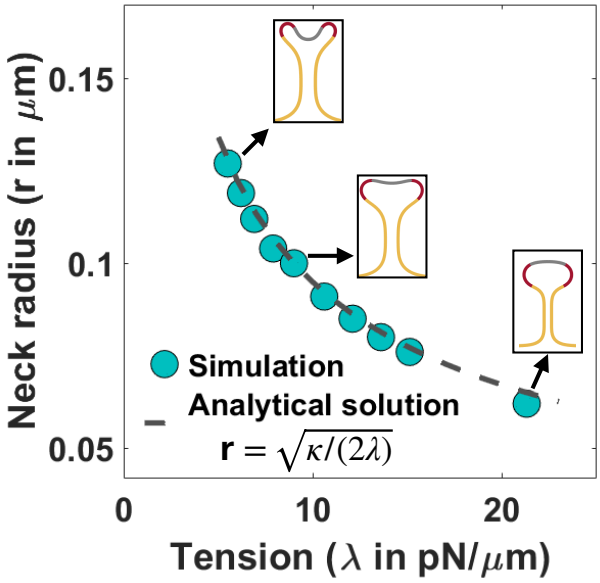

Figure D.4: (A) Neck radius of a mushroom-shaped spine as a function of tension for area of PSD/area of head = 0.2 ($r = \sqrt{\kappa/(2\lambda)}$) [343]. Three different shapes of mushroom-shaped spines are shown for low, intermediate, and high tension. With increasing magnitude of tension, the mushroom-shaped spine flattens.

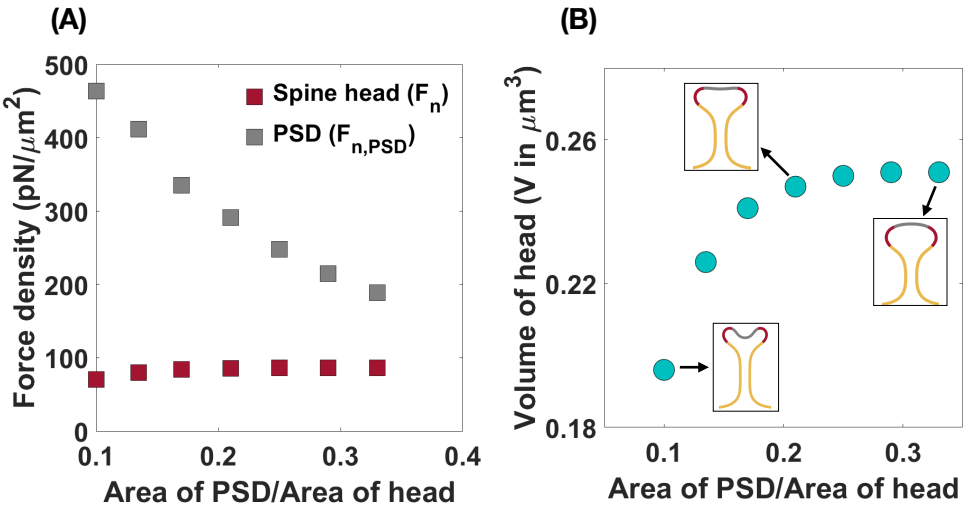

Figure D.5: The area of PSD with respect to the area of the spine head characterizes the normal force densities that are required to form a mushroom spine. (A) While the magnitude of normal force density in the spine head (red squares) slightly increases with increasing ratio of PSD area to head area, the magnitude of normal force density in the PSD (gray squares) decreases with increasing ratio of PSD area to head area. (B) A larger mushroom-shaped spine (larger head volume) with a flatten head forms with increasing ratio of PSD area to head area.

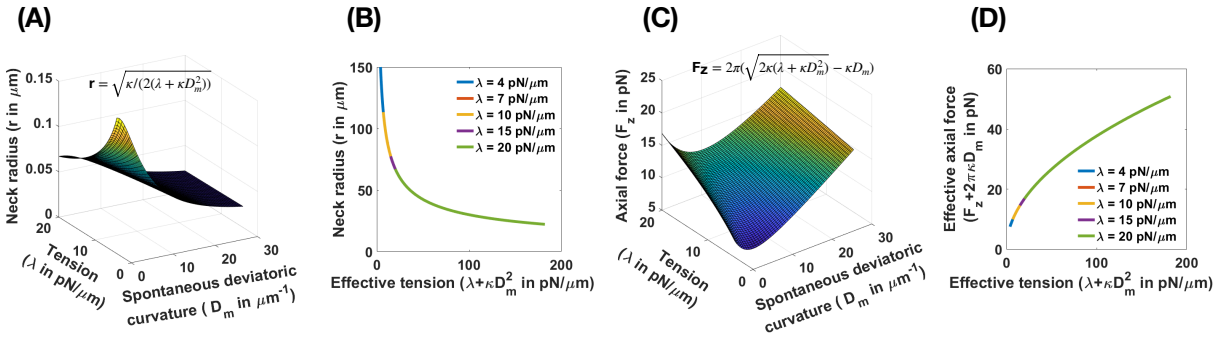

Figure D.6: (A) Analytical solution for the neck radius of a tubular membrane as functions of spontaneous deviatoric curvature and tension ($r = \sqrt{\kappa/(2(\lambda + \kappa D_m^2))}$, Eq. D.36). (B) The neck radius in panel A collapses onto a single curve as a function of effective tension. (C) Analytical solution for the magnitude of an axial force needed to maintain a tubular protrusion as functions of spontaneous deviatoric curvature and tension ($F_z = 2\pi(\sqrt{2\kappa(\lambda + \kappa D_m^2)} - \kappa D_m)$, Eq. D.36). (D) The effective axial force in panel C collapses onto a single curve as a function of effective tension.

Table D.3: Energy components and total energy for three different mechanisms of thin spine formation

	Bending energy (pN.μm) $\int \kappa H^2 da$	Bending energy due to deviatoric curvature (pN.μm) $\int \kappa (D - D_m)^2 da$	Work done by force (pN.μm) $\int \mathbf{f} \cdot (\mathbf{r} - \mathbf{r}_0) da$	Work done by tension (pN.μm) $\int \lambda da$	Total energy (pN.μm)
Uniform normal force density along head	6.2	6.2	-27.64	904.8	899.5
Uniform normal force density along head and spontaneous deviatoric curvature along neck	5.8	1.75	-16.35	254.34	245.5
Uniform axial force density along head and spontaneous deviatoric curvature along neck	5.28	1	-9.1	247.1	244.3

Table D.4: Energy components and total energy for three different mechanisms of mushroom spine formation

	Bending energy (pN.μm) $\int \kappa H^2 da$	Bending energy due to deviatoric curvature (pN.μm) $\int \kappa (D - D_m)^2 da$	Work done by force (pN.μm) $\int \mathbf{f} \cdot (\mathbf{r} - \mathbf{r}_0) da$	Work done by tension (pN.μm) $\int \lambda da$	Total energy (pN.μm)
Non-uniform normal force density along head	4.92	4.92	-18.65	226.2	217.4
Non-uniform normal force density along head and spontaneous deviatoric curvature along neck	513	4.29	-17.43	139.2	131

Bibliography

[1] K. M. Harris, F. E. Jensen, and B. Tsao, "Three-dimensional structure of dendritic spines and synapses in rat hippocampus (ca1) at postnatal day 15 and adult ages: implications for the maturation of synaptic physiology and long-term potentiation [published erratum appears in j neurosci 1992 aug; 12 (8): following table of contents]," *Journal of Neuroscience*, vol. 12, no. 7, pp. 2685–2705, 1992.

[2] A. Rodriguez, D. B. Ehlenberger, D. L. Dickstein, P. R. Hof, and S. L. Wearne, "Automated three-dimensional detection and shape classification of dendritic spines from fluorescence microscopy images," *PloS one*, vol. 3, no. 4, p. e1997, 2008.

[3] R. Kanjhan, P. G. Noakes, and M. C. Bellingham, "Emerging roles of filopodia and dendritic spines in motoneuron plasticity during development and disease," *Neural plasticity*, vol. 2016, 2016.

[4] J. Spacek and K. M. Harris, "Three-dimensional organization of smooth endoplasmic reticulum in hippocampal ca1 dendrites and dendritic spines of the immature and mature rat," *Journal of Neuroscience*, vol. 17, no. 1, pp. 190–203, 1997.

[5] H. Alimohamadi and P. Rangamani, "Modeling membrane curvature generation due to membrane–protein interactions," *Biomolecules*, vol. 8, no. 4, p. 120, 2018.

[6] H. Alimohamadi, R. Vasan, J. Hassinger, J. Stachowiak, and P. Rangamani, "The role of traction in membrane curvature generation," *Biophysical Journal*, vol. 114, no. 3, p. 600a, 2018.

[7] F. Yuan, H. Alimohamadi, B. Bakka, A. N. Trementozzi, K. J. Day, N. L. Fawzi, P. Rangamani, and J. C. Stachowiak, "Membrane bending by protein phase separation," *Proceedings of the National Academy of Sciences*, vol. 118, no. 11, 2021.

[8] H. Alimohamadi, B. Ovryn, and P. Rangamani, "Modeling membrane nanotube morphology: the role of heterogeneity in composition and material properties," *Scientific reports*, vol. 10, no. 1, pp. 1–15, 2020.

[9] H. Alimohamadi, A. S. Smith, R. B. Nowak, V. M. Fowler, and P. Rangamani, "Non-uniform distribution of myosin-mediated forces governs red blood cell membrane curvature through tension modulation," *PLOS Computational Biology*, vol. 16, no. 5, p. e1007890, 2020.

[10] H. Alimohamadi, M. Bell, S. Halpain, and P. Rangamani, "Mechanical principles governing the shapes of dendritic spines," *bioRxiv*, 2020.

[11] S. Mukherjee and F. R. Maxfield, "Role of membrane organization and membrane domains in endocytic lipid trafficking," *Traffic*, vol. 1, no. 3, pp. 203–211, 2000.

[12] J. Gruenberg, "The endocytic pathway: a mosaic of domains," *Nat. Rev. Mol. Cell Biol.*, vol. 2, no. 10, p. 721, 2001.

[13] B. Westermann, "Mitochondrial fusion and fission in cell life and death," *Nat. Rev. Mol. Cell Biol.*, vol. 11, no. 12, p. 872, 2010.

[14] A. M. Van der Bliek, Q. Shen, and S. Kawajiri, "Mechanisms of mitochondrial fission and fusion," *Cold Spring Harb Perspect Biol.*, vol. 5, no. 6, p. a011072, 2013.

[15] A. Grafmuller, J. Shillcock, and R. Lipowsky, "The fusion of membranes and vesicles: pathway and energy barriers from dissipative particle dynamics," *Biophys. J.*, vol. 96, no. 7, pp. 2658–2675, 2009.

[16] R. Jahn and D. Fasshauer, "Molecular machines governing exocytosis of synaptic vesicles," *Nature*, vol. 490, no. 7419, p. 201, 2012.

[17] G. C. Reilly and A. J. Engler, "Intrinsic extracellular matrix properties regulate stem cell differentiation," *J.Biomech.*, vol. 43, no. 1, pp. 55–62, 2010.

[18] B. S. Cowling, A. Toussaint, J. Muller, and J. Laporte, "Defective membrane remodeling in neuromuscular diseases: insights from animal models," *PLoS Genet.*, vol. 8, no. 4, p. e1002595, 2012.

[19] M. A. De Matteis and A. Luini, "Mendelian disorders of membrane trafficking," *N.Engl.J.Med.*, vol. 365, no. 10, pp. 927–938, 2011.

[20] K. E. Ward, J. P. Ropa, E. Adu-Gyamfi, and R. V. Stahelin, "C2 domain membrane penetration by group iva cytosolic phospholipase a2 induces membrane curvature changes," *J. Lipid Res.*, pp. jlr–M030718, 2012.

[21] C. A. Hewson, S. Patel, L. Calzetta, H. Campwala, S. Havard, E. Luscombe, P. A. Clarke, P. T. Peachell, M. G. Matera, M. Cazzola, *et al.*, "Preclinical evaluation of an inhibitor of cytosolic phospholipase a2α for the treatment of asthma," *J. Pharmacol. Exp. Ther*, vol. 340, no. 3, pp. 656–665, 2012.

[22] N. Tai, K. Kuwabara, M. Kobayashi, K. Yamada, T. Ono, K. Seno, Y. Gahara, J. Ishizaki, and Y. Hori, "Cytosolic phospholipase a2 alpha inhibitor, pyrroxyphene, displays anti-arthritic and anti-bone destructive action in a murine arthritis model," *Inflamm. Res.*, vol. 59, no. 1, pp. 53–62, 2010.

[23] K. Kishimoto, R.-C. Li, J. Zhang, J. A. Klaus, K. K. Kibler, S. Dore, R. C. Koehler, and A. Sapirstein, "Cytosolic phospholipase a 2 alpha amplifies early cyclooxygenase-2 expression, oxidative stress and map kinase phosphorylation after cerebral ischemia in mice," *J. Neuroinflammation*, vol. 7, no. 1, p. 42, 2010.

[24] R. Kerkela, M. Boucher, R. Zaka, E. Gao, D. Harris, J. Piuhola, J. Song, R. Serpi, K. C. Woulfe, J. Y. Cheung, *et al.*, "Cytosolic phospholipase a2α protects against ischemia/reperfusion injury in the heart," *Clin. Transl. Sci.*, vol. 4, no. 4, pp. 236–242, 2011.

[25] S. Sundarraj, S. Kannan, R. Thangam, and P. Gunasekaran, "Effects of the inhibition of cytosolic phospholipase a2α in non-small cell lung cancer cells," *J. Cancer Res. Clin. Oncol.*, vol. 138, no. 5, pp. 827–835, 2012.

[26] H. T. McMahon and J. L. Gallop, "Membrane curvature and mechanisms of dynamic cell membrane remodelling," *Nature*, vol. 438, no. 7068, pp. 590–596, 2005.

[27] I. K. Jarsch, F. Daste, and J. L. Gallop, "Membrane curvature in cell biology: An integration of molecular mechanisms," *J.Cell.Biol.*, vol. 214, no. 4, pp. 375–387, 2016.

[28] R. Hochmuth and R. Waugh, "Erythrocyte membrane elasticity and viscosity," *Annu. Rev. Physiol.*, vol. 49, no. 1, pp. 209–219, 1987.

[29] P. A. Giardini, D. A. Fletcher, and J. A. Theriot, "Compression forces generated by actin comet tails on lipid vesicles," *Proceedings of the National Academy of Sciences*, vol. 100, no. 11, pp. 6493–6498, 2003.

[30] A. E. Carlsson, "Membrane bending by actin polymerization," *Current opinion in cell biology*, vol. 50, pp. 1–7, 2018.

[31] M. Kaksonen, C. P. Toret, and D. G. Drubin, "Harnessing actin dynamics for clathrin-mediated endocytosis," *Nature reviews. Molecular cell biology*, vol. 7, no. 6, p. 404, 2006.

[32] J. Zimmerberg and M. M. Kozlov, "How proteins produce cellular membrane curvature," *Nature reviews Molecular cell biology*, vol. 7, no. 1, pp. 9–19, 2006.

[33] D. Argudo, N. P. Bethel, F. V. Marcoline, and M. Grabe, "Continuum descriptions of membranes and their interaction with proteins: Towards chemically accurate models," *Biochimica et Biophysica Acta (BBA)-Biomembranes*, vol. 1858, no. 7, pp. 1619–1634, 2016.

[34] M. M. Kozlov, F. Campelo, N. Liska, L. V. Chernomordik, S. J. Marrink, and H. T. McMahon, "Mechanisms shaping cell membranes," *Current opinion in cell biology*, vol. 29, pp. 53–60, 2014.

[35] J. Jenkins, "Static equilibrium configurations of a model red blood cell," *Journal of mathematical biology*, vol. 4, no. 2, pp. 149–169, 1977.

[36] H. Alimohamadi, R. Vasan, J. Hassinger, J. Stachowiak, and P. Rangamani, "The role of traction in membrane curvature generation," *Biophys. J.*, vol. 114, no. 3, p. 600a, 2018.

[37] J. Guven, "Membrane geometry with auxiliary variables and quadratic constraints," *Journal of Physics A: Mathematical and General*, vol. 37, no. 28, p. L313, 2004.

[38] M. Aridor, S. I. Bannykh, T. Rowe, and W. E. Balch, "Sequential coupling between copii and copi vesicle coats in endoplasmic reticulum to golgi transport.," *J. Cell Biol.*, vol. 131, no. 4, pp. 875–893, 1995.

[39] K. M. Davies, C. Anselmi, I. Wittig, J. D. Faraldo-Gomez, and W. Kuhlbrandt, "Structure of the yeast f1fo-atp synthase dimer and its role in shaping the mitochondrial cristae," *Proc Natl Acad Sci*, vol. 109, no. 34, pp. 13602–13607, 2012.

[40] E. M. Landau and J. P. Rosenbusch, "Lipidic cubic phases: a novel concept for the crystallization of membrane proteins," *Proc Natl Acad Sci*, vol. 93, no. 25, pp. 14532–14535, 1996.

[41] N. W. Schmidt, A. Mishra, J. Wang, W. F. DeGrado, and G. C. Wong, "Influenza virus a m2 protein generates negative gaussian membrane curvature necessary for budding and scission," *J. Am. Chem. Soc.*, vol. 135, no. 37, pp. 13710–13719, 2013.

[42] J. L. Gallop, C. C. Jao, H. M. Kent, P. J. G. Butler, P. R. Evans, R. Langen, and H. T. McMahon, "Mechanism of endophilin n-bar domain-mediated membrane curvature," *EMBO J.*, vol. 25, no. 12, pp. 2898–2910, 2006.

[43] T. J. Pucadyil and S. L. Schmid, "Conserved functions of membrane active gtpases in coated vesicle formation," *Science*, vol. 325, no. 5945, pp. 1217–1220, 2009.

[44] M. C. Lee, L. Orci, S. Hamamoto, E. Futai, M. Ravazzola, and R. Schekman, "Sar1p n-terminal helix initiates membrane curvature and completes the fission of a copii vesicle," *Cell*, vol. 122, no. 4, pp. 605–617, 2005.

[45] F. Campelo, H. T. McMahon, and M. M. Kozlov, "The hydrophobic insertion mechanism of membrane curvature generation by proteins," *Biophysical journal*, vol. 95, no. 5, pp. 2325–2339, 2008.

[46] L. Karotki, J. T. Huiskonen, C. J. Stefan, N. E. Ziółkowska, R. Roth, M. A. Surma, N. J. Krogan, S. D. Emr, J. Heuser, K. Grünewald, *et al.*, "Eisosome proteins assemble into a membrane scaffold," *J Cell Biol*, vol. 195, no. 5, pp. 889–902, 2011.

[47] O. Daumke, A. Roux, and V. Haucke, "Bar domain scaffolds in dynamin-mediated membrane fission," *Cell*, vol. 156, no. 5, pp. 882–892, 2014.

[48] J. C. Stachowiak, E. M. Schmid, C. J. Ryan, H. S. Ann, D. Y. Sasaki, M. B. Sherman, P. L. Geissler, D. A. Fletcher, and C. C. Hayden, "Membrane bending by protein–protein crowding," *Nature cell biology*, vol. 14, no. 9, pp. 944–949, 2012.

[49] D. J. Busch, J. R. Houser, C. C. Hayden, M. B. Sherman, E. M. Lafer, and J. C. Stachowiak, "Intrinsically disordered proteins drive membrane curvature," *Nature communications*, vol. 6, p. 7875, 2015.

[50] R. MacKinnon, "Potassium channels," *FEBS letters*, vol. 555, no. 1, pp. 62–65, 2003.

[51] N. Unwin, "Refined structure of the nicotinic acetylcholine receptor at 4 å resolution," *J. Mol. Biol.*, vol. 346, no. 4, pp. 967–989, 2005.

[52] B. D. Silverman, "Hydrophobicity of transmembrane proteins: spatially profiling the distribution," *Protein Sci.*, vol. 12, no. 3, pp. 586–599, 2003.

[53] T. Auth and G. Gompper, "Budding and vesiculation induced by conical membrane inclusions," *Phys. Rev. E*, vol. 80, no. 3, p. 031901, 2009.

[54] H. T. McMahon and E. Boucrot, "Membrane curvature at a glance," *J Cell Sci*, vol. 128, no. 6, pp. 1065–1070, 2015.

[55] T. Chou, K. S. Kim, and G. Oster, "Statistical thermodynamics of membrane bending-mediated protein–protein attractions," *Biophys. J.*, vol. 80, no. 3, pp. 1075–1087, 2001.

[56] B. J. Peter, H. M. Kent, I. G. Mills, Y. Vallis, P. J. G. Butler, P. R. Evans, and H. T. McMahon, "Bar domains as sensors of membrane curvature: the amphiphysin bar structure," *Science*, vol. 303, no. 5657, pp. 495–499, 2004.

[57] J. L. Gallop and H. T. McMahon, "Bar domains and membrane curvature: bringing your curves to the bar," in *Biochemical Society Symposia*, vol. 72, p. 223, London; Portland on behalf of The Biochemical Society; 1999, 2005.

[58] G. Ren, P. Vajjhala, J. S. Lee, B. Winsor, and A. L. Munn, "The bar domain proteins: molding membranes in fission, fusion, and phagy," *Microbiol. Mol. Biol. Rev.*, vol. 70, no. 1, pp. 37–120, 2006.

[59] V. K. Bhatia, K. L. Madsen, P.-Y. Bolinger, A. Kunding, P. Hedegaard, U. Gether, and D. Stamou, "Amphipathic motifs in bar domains are essential for membrane curvature sensing," *EMBO J.*, vol. 28, no. 21, pp. 3303–3314, 2009.

[60] S. J. Scales, M. Gomez, and T. E. Kreis, "Coat proteins regulating membrane traffic," in *Int. Rev. Cytol.*, vol. 195, pp. 67–144, Elsevier, 1999.

[61] H. T. McMahon and E. Boucrot, "Molecular mechanism and physiological functions of clathrin-mediated endocytosis," *Nature reviews. Molecular cell biology*, vol. 12, no. 8, p. 517, 2011.

[62] J. S. Bonifacino and J. Lippincott-Schwartz, "Coat proteins: shaping membrane transport," *Nat. Rev. Mol. Cell Biol.*, vol. 4, no. 5, p. 409, 2003.

[63] J. Agudo-Canalejo and R. Lipowsky, "Domes and cones: Adhesion-induced fission of membranes by escrt proteins," *PLOS Comput. Biol.*, vol. 14, no. 8, p. e1006422, 2018.

[64] M. Murrell, P. W. Oakes, M. Lenz, and M. L. Gardel, "Forcing cells into shape: the mechanics of actomyosin contractility," *Nature reviews Molecular cell biology*, vol. 16, no. 8, pp. 486–498, 2015.

[65] E. Paluch, C. Sykes, J. Prost, and M. Bornens, "Dynamic modes of the cortical actomyosin gel during cell locomotion and division," *Trends in cell biology*, vol. 16, no. 1, pp. 5–10, 2006.

[66] G. Salbreux, G. Charras, and E. Paluch, "Actin cortex mechanics and cellular morphogenesis," *Trends in cell biology*, vol. 22, no. 10, pp. 536–545, 2012.

[67] M. Vicente-Manzanares, X. Ma, R. S. Adelstein, and A. R. Horwitz, "Non-muscle myosin ii takes centre stage in cell adhesion and migration," *Nature reviews Molecular cell biology*, vol. 10, no. 11, pp. 778–790, 2009.

[68] S. M. Heissler and D. J. Manstein, "Nonmuscle myosin-2: mix and match," *Cellular and Molecular Life Sciences*, vol. 70, no. 1, pp. 1–21, 2013.

[69] M. A. Conti and R. S. Adelstein, "Nonmuscle myosin ii moves in new directions," *Journal of cell science*, vol. 121, no. 1, pp. 11–18, 2008.

[70] P. Agarwal and R. Zaidel-Bar, "Principles of actomyosin regulation in vivo," *Trends in cell biology*, vol. 29, no. 2, pp. 150–163, 2019.

[71] N. Gorfinkiel and G. B. Blanchard, "Dynamics of actomyosin contractile activity during epithelial morphogenesis," *Current opinion in cell biology*, vol. 23, no. 5, pp. 531–539, 2011.

[72] K. E. Kasza and J. A. Zallen, "Dynamics and regulation of contractile actin–myosin networks in morphogenesis," *Current opinion in cell biology*, vol. 23, no. 1, pp. 30–38, 2011.

[73] T. Lecuit, P.-F. Lenne, and E. Munro, "Force generation, transmission, and integration during cell and tissue morphogenesis," *Annual review of cell and developmental biology*, vol. 27, no. 1, pp. 157–184, 2011.

[74] K. M. Yamada and M. Sixt, "Mechanisms of 3d cell migration," *Nature Reviews Molecular Cell Biology*, vol. 20, no. 12, pp. 738–752, 2019.

[75] S. M. Lyons, E. Alizadeh, J. Mannheimer, K. Schuamberg, J. Castle, B. Schroder, P. Turk, D. Thamm, and A. Prasad, "Changes in cell shape are correlated with metastatic potential in murine and human osteosarcomas," *Biology open*, vol. 5, no. 3, pp. 289–299, 2016.

[76] S. Suresh, J. Spatz, J. P. Mills, A. Micoulet, M. Dao, C. Lim, M. Beil, and T. Seufferlein, "Connections between single-cell biomechanics and human disease states: gastrointestinal cancer and malaria," *Acta biomaterialia*, vol. 1, no. 1, pp. 15–30, 2005.

[77] A. Pecci, X. Ma, A. Savoia, and R. S. Adelstein, "Myh9: Structure, functions and role of non-muscle myosin iia in human disease," *Gene*, vol. 664, pp. 152–167, 2018.

[78] H. Elliott, R. S. Fischer, K. A. Myers, R. A. Desai, L. Gao, C. S. Chen, R. S. Adelstein, C. M. Waterman, and G. Danuser, "Myosin ii controls cellular branching morphogenesis and migration in three dimensions by minimizing cell-surface curvature," *Nature cell biology*, vol. 17, no. 2, pp. 137–147, 2015.

[79] N. Mohandas and E. Evans, "Mechanical properties of the red cell membrane in relation to molecular structure and genetic defects," *Annual review of biophysics and biomolecular structure*, vol. 23, no. 1, pp. 787–818, 1994.

[80] N. Mohandas and P. G. Gallagher, "Red cell membrane: past, present, and future," *Blood*, vol. 112, no. 10, pp. 3939–3948, 2008.

[81] V. M. Fowler, "The human erythrocyte plasma membrane: A rosetta stone for decoding membrane–cytoskeleton structure," *Current topics in membranes*, vol. 72, pp. 39–88, 2013.

[82] A. S. Smith, R. B. Nowak, S. Zhou, M. Giannetto, D. S. Gokhin, J. Papoin, I. C. Ghiran, L. Blanc, J. Wan, and V. M. Fowler, "Myosin iia interacts with the spectrin-actin membrane skeleton to control red blood cell membrane curvature and deformability," *Proceedings of the National Academy of Sciences*, vol. 115, no. 19, pp. E4377–E4385, 2018.

[83] P. Hotulainen and C. C. Hoogenraad, "Actin in dendritic spines: connecting dynamics to function," *The Journal of cell biology*, vol. 189, no. 4, pp. 619–629, 2010.

[84] F. Korobova and T. Svitkina, "Molecular architecture of synaptic actin cytoskeleton in hippocampal neurons reveals a mechanism of dendritic spine morphogenesis," *Molecular biology of the cell*, vol. 21, no. 1, pp. 165–176, 2010.

[85] S. Nanguneri, R. Pramod, N. Efimova, D. Das, M. Jose, T. Svitkina, and D. Nair, "Characterization of nanoscale organization of f-actin in morphologically distinct dendritic spines in vitro using supervised learning," *eNeuro*, vol. 6, no. 4, 2019.

[86] S. Halpain, "Actin and the agile spine: how and why do dendritic spines dance?," *Trends in neurosciences*, vol. 23, no. 4, pp. 141–146, 2000.

[87] A. Rao and A. M. Craig, "Signaling between the actin cytoskeleton and the postsynaptic density of dendritic spines," *Hippocampus*, vol. 10, no. 5, pp. 527–541, 2000.

[88] T. Tada and M. Sheng, "Molecular mechanisms of dendritic spine morphogenesis," *Current opinion in neurobiology*, vol. 16, no. 1, pp. 95–101, 2006.

[89] P. Hotulainen, O. Llano, S. Smirnov, K. Tanhuanpää, J. Faix, C. Rivera, and P. Lappalainen, "Defining mechanisms of actin polymerization and depolymerization during dendritic spine morphogenesis," *The Journal of cell biology*, vol. 185, no. 2, pp. 323–339, 2009.

[90] J. Bär, O. Kobler, B. Van Bommel, and M. Mikhaylova, "Periodic f-actin structures shape the neck of dendritic spines," *Scientific reports*, vol. 6, p. 37136, 2016.

[91] á. Racz and R. Weinberg, "Spatial organization of cofilin in dendritic spines," *Neuroscience*, vol. 138, no. 2, pp. 447–456, 2006.

[92] B. Rácz and R. J. Weinberg, "Microdomains in forebrain spines: an ultrastructural perspective," *Molecular neurobiology*, vol. 47, no. 1, pp. 77–89, 2013.

[93] W.-H. Lin and D. J. Webb, "Actin and actin-binding proteins: masters of dendritic spine formation, morphology, and function," *The open neuroscience journal*, vol. 3, p. 54, 2009.

[94] L. A. Helgeson and B. J. Nolen, "Mechanism of synergistic activation of arp2/3 complex by cortactin and n-wasp," *Elife*, vol. 2, p. e00884, 2013.

[95] N. Efimova, F. Korobova, M. C. Stankewich, A. H. Moberly, D. B. Stolz, J. Wang, A. Kashina, M. Ma, and T. Svitkina, "βiii spectrin is necessary for formation of the constricted neck of dendritic spines and regulation of synaptic activity in neurons," *Journal of Neuroscience*, vol. 37, no. 27, pp. 6442–6459, 2017.

[96] M. A. Mikati, E. E. Grintsevich, and E. Reisler, "Drebrin-induced stabilization of actin filaments," *Journal of Biological Chemistry*, vol. 288, no. 27, pp. 19926–19938, 2013.

[97] A. Chazeau and G. Giannone, "Organization and dynamics of the actin cytoskeleton during dendritic spine morphological remodeling," *Cellular and molecular life sciences*, vol. 73, no. 16, pp. 3053–3073, 2016.

[98] M. Kneussel and W. Wagner, "Myosin motors at neuronal synapses: drivers of membrane transport and actin dynamics," *Nature Reviews Neuroscience*, vol. 14, no. 4, pp. 233–247, 2013.

[99] Y. Shi, "A glimpse of structural biology through x-ray crystallography," *Cell*, vol. 159, no. 5, pp. 995–1014, 2014.

[100] C.-Y. Hsia, M. J. Richards, and S. Daniel, "A review of traditional and emerging methods to characterize lipid–protein interactions in biological membranes," *Anal. Methods*, vol. 7, no. 17, pp. 7076–7094, 2015.

[101] E. Betzig, G. H. Patterson, R. Sougrat, O. W. Lindwasser, S. Olenych, J. S. Bonifacino, M. W. Davidson, J. Lippincott-Schwartz, and H. F. Hess, "Imaging intracellular fluorescent proteins at nanometer resolution," *Science*, vol. 313, no. 5793, pp. 1642–1645, 2006.

[102] L. Gao, L. Shao, C. D. Higgins, J. S. Poulton, M. Peifer, M. W. Davidson, X. Wu, B. Goldstein, and E. Betzig, "Noninvasive imaging beyond the diffraction limit of 3d dynamics in thickly fluorescent specimens," *Cell*, vol. 151, no. 6, pp. 1370–1385, 2012.

[103] J. J. Bozzola and L. D. Russell, *Electron microscopy: principles and techniques for biologists*. Jones & Bartlett Learning, 1999.

[104] D. J. Stephens and V. J. Allan, "Light microscopy techniques for live cell imaging," *Science*, vol. 300, no. 5616, pp. 82–86, 2003.

[105] A. H. De Vries, A. E. Mark, and S. J. Marrink, "Molecular dynamics simulation of the spontaneous formation of a small dppc vesicle in water in atomistic detail," *J. Am. Chem. Soc.*, vol. 126, no. 14, pp. 4488–4489, 2004.

[106] F. V. Marcoline, N. Bethel, C. J. Guerriero, J. L. Brodsky, and M. Grabe, "Membrane protein properties revealed through data-rich electrostatics calculations," *Structure*, vol. 23, no. 8, pp. 1526–1537, 2015.

[107] J. L. MacCallum, W. D. Bennett, and D. P. Tieleman, "Partitioning of amino acid side chains into lipid bilayers: results from computer simulations and comparison to experiment," *J. Gen. Physiol.*, vol. 129, no. 5, pp. 371–377, 2007.

[108] Q. Du, C. Liu, and X. Wang, "Simulating the deformation of vesicle membranes under elastic bending energy in three dimensions," *J. Comput. Phys.*, vol. 212, no. 2, pp. 757–777, 2006.

[109] M. Muller, K. Katsov, and M. Schick, "Biological and synthetic membranes: What can be learned from a coarse-grained description?," *Phys. Rep.*, vol. 434, no. 5-6, pp. 113–176, 2006.

[110] W. Noid, J.-W. Chu, G. S. Ayton, V. Krishna, S. Izvekov, G. A. Voth, A. Das, and H. C. Andersen, "The multiscale coarse-graining method. i. a rigorous bridge between atomistic and coarse-grained models," *J. Chem. Phys.*, vol. 128, no. 24, p. 244114, 2008.

[111] H. Alimohamadi, B. Ovryn, and P. Rangamani, "Protein-mediated beads-on-a-string structure formation along membrane nanotubes in live cells," *Biophys. J.*, vol. 114, no. 3, p. 392a, 2018.

[112] D. Cuvelier, I. Derenyi, P. Bassereau, and P. Nassoy, "Coalescence of membrane tethers: experiments, theory, and applications," *Biophys. J.*, vol. 88, no. 4, pp. 2714–2726, 2005.

[113] R. Vasan, J. Hassinger, H. Alimohamadi, D. Drubin, and P. Rangamani, "Energetics and stability of neck formation in yeast and mammalian endocytosis," *Biophys. J.*, vol. 114, no. 3, p. 281a, 2018.

[114] G. Cevc and D. Marsh, *Phospholipid bilayers: physical principles and models*. Wiley, 1987.

[115] W. Stillwell, *An introduction to biological membranes: from bilayers to rafts*. Newnes, 2013.

[116] M. M. Terzi and M. Deserno, "Lipid membranes: From self-assembly to elasticity," in *The Role of Mechanics in the Study of Lipid Bilayers*, pp. 105–166, Springer, 2018.

[117] G. Guidotti, "The composition of biological membranes," *J. Intern. Med.*, vol. 129, no. 2, pp. 194–201, 1972.

[118] P. L. Yeagle, *The structure of biological membranes*. CRC press, 2011.

[119] H. Watson, "Biological membranes," *Essays Biochem.*, vol. 59, pp. 43–69, 2015.

[120] G. E. Schulz and R. H. Schirmer, *Principles of protein structure*. Springer Science and Business Media, 2013.

[121] P. Albersheim and A. J. Anderson-Prouty, "Carbohydrates, proteins, cell surfaces, and the biochemistry of pathogenesis," *Annu. Rev. Plant Biol.*, vol. 26, no. 1, pp. 31–52, 1975.

[122] M. K. Jain, R. C. Wagner, *et al.*, "Introduction to biological membranes," tech. rep., Wiley New York, 1988.

[123] S. J. Singer and G. L. Nicolson, "The fluid mosaic model of the structure of cell membranes," *Science*, vol. 175, no. 4023, pp. 720–731, 1972.

[124] J. E. Darnell, H. F. Lodish, D. Baltimore, *et al.*, *Molecular cell biology*, vol. 2. Scientific American Books New York, 1990.

[125] B. A. Seaton and M. F. Roberts, "Peripheral membrane proteins," in *Biological Membranes*, pp. 355–403, Springer, 1996.

[126] S. Singer, "The molecular organization of membranes," *Annu. Rev. Biochem.*, vol. 43, no. 1, pp. 805–833, 1974.

[127] N. Ramakrishnan, P. S. Kumar, and R. Radhakrishnan, "Mesoscale computational studies of membrane bilayer remodeling by curvature-inducing proteins," *Phys. Rep.*, vol. 543, no. 1, pp. 1–60, 2014.

[128] P. B. Canham, "The minimum energy of bending as a possible explanation of the biconcave shape of the human red blood cell," *Journal of theoretical biology*, vol. 26, no. 1, pp. 61IN777–76IN881, 1970.

[129] S. Safran, *Statistical thermodynamics of surfaces, interfaces, and membranes*. CRC Press, 2018.

[130] D. J. Tobias, K. Tu, and M. L. Klein, "Atomic-scale molecular dynamics simulations of lipid membranes," *Curr. Opin. Colloid Interface Sci.*, vol. 2, no. 1, pp. 15–26, 1997.

[131] D. P. Tieleman, S.-J. Marrink, and H. J. Berendsen, "A computer perspective of membranes: molecular dynamics studies of lipid bilayer systems," *Biochimica et Biophysica Acta (BBA)-Reviews on Biomembranes*, vol. 1331, no. 3, pp. 235–270, 1997.

[132] E. Lindahl and M. S. Sansom, "Membrane proteins: molecular dynamics simulations," *Curr. Opin. Struct. Biol.*, vol. 18, no. 4, pp. 425–431, 2008.

[133] W. Helfrich, "Elastic properties of lipid bilayers: theory and possible experiments," *Zeitschrift für Naturforschung C*, vol. 28, no. 11-12, pp. 693–703, 1973.

[134] R. A. Sauer, "On the computational modeling of lipid bilayers using thin-shell theory," in *The Role of Mechanics in the Study of Lipid Bilayers*, pp. 221–286, Springer, 2018.

[135] J. E. Hassinger, G. Oster, D. G. Drubin, and P. Rangamani, "Design principles for robust vesiculation in clathrin-mediated endocytosis," *Proceedings of the National Academy of Sciences*, vol. 114, no. 7, pp. E1118–E1127, 2017.

[136] N. Walani, J. Torres, and A. Agrawal, "Endocytic proteins drive vesicle growth via instability in high membrane tension environment," *Proceedings of the National Academy of Sciences*, vol. 112, no. 12, pp. E1423–E1432, 2015.

[137] A. Agrawal and D. J. Steigmann, "Boundary-value problems in the theory of lipid membranes," *Continuum Mechanics and Thermodynamics*, vol. 21, no. 1, pp. 57–82, 2009.

[138] A. Laadhari, P. Saramito, and C. Misbah, "An adaptive finite element method for the modeling of the equilibrium of red blood cells," *Int. J. Numer. Methods Fluids*, vol. 80, no. 7, pp. 397–428, 2016.

[139] R. A. Sauer, T. X. Duong, K. K. Mandadapu, and D. J. Steigmann, "A stabilized finite element formulation for liquid shells and its application to lipid bilayers," *J. Comput. Phys.*, vol. 330, pp. 436–466, 2017.

[140] T. X. Duong, F. Roohbakhshan, and R. A. Sauer, "A new rotation-free isogeometric thin shell formulation and a corresponding continuity constraint for patch boundaries," *Comput Methods Appl Mech Eng*, vol. 316, pp. 43–83, 2017.

[141] N. Ramakrishnan, P. S. Kumar, and J. H. Ipsen, "Monte carlo simulations of fluid vesicles with in-plane orientational ordering," *Phys. Rev. E*, vol. 81, no. 4, p. 041922, 2010.

[142] X. Guan, M. Ma, Z. Gan, Z. Xu, and B. Li, "Hybrid monte carlo and continuum modeling of electrolytes with concentration-induced dielectric variations," *Phys. Rev. E*, vol. 94, no. 5, p. 053312, 2016.

[143] K. Sreeja, J. H. Ipsen, and P. S. Kumar, "Monte carlo simulations of fluid vesicles," *J. Phys. Condens. Matter*, vol. 27, no. 27, p. 273104, 2015.

[144] C. Lau, W. E. Brownell, and A. A. Spector, "Internal forces, tension and energy density in tethered cellular membranes," *J Biomech*, vol. 45, no. 7, pp. 1328–1331, 2012.

[145] R. Gu, X. Wang, and M. Gunzburger, "Simulating vesicle–substrate adhesion using two phase field functions," *J. Comput. Phys.*, vol. 275, pp. 626–641, 2014.

[146] T. Banham, B. Li, and Y. Zhao, "Pattern formation by phase-field relaxation of bending energy with fixed surface area and volume," *Phys. Rev. E*, vol. 90, no. 3, p. 033308, 2014.

[147] Q. Du and X. Wang, "Convergence of numerical approximations to a phase field bending elasticity model of membrane deformations," 2006.

[148] J. Zhang, S. Das, and Q. Du, "A phase field model for vesicle–substrate adhesion," *J. Comput. Phys.*, vol. 228, no. 20, pp. 7837–7849, 2009.

[149] A. Arkhipov, Y. Yin, and K. Schulten, "Four-scale description of membrane sculpting by bar domains," *Biophysical journal*, vol. 95, no. 6, pp. 2806–2821, 2008.

[150] D. Steigmann, "Fluid films with curvature elasticity," *Archive for Rational Mechanics and Analysis*, vol. 150, no. 2, pp. 127–152, 1999.

[151] T. Kishimoto, Y. Sun, C. Buser, J. Liu, A. Michelot, and D. G. Drubin, "Determinants of endocytic membrane geometry, stability, and scission," *Proceedings of the National Academy of Sciences*, vol. 108, no. 44, pp. E979–E988, 2011.

[152] A. Agrawal and D. J. Steigmann, "Modeling protein-mediated morphology in biomembranes," *Biomechanics and modeling in mechanobiology*, vol. 8, no. 5, pp. 371–379, 2009.

[153] R. Lipowsky, "Spontaneous tubulation of membranes and vesicles reveals membrane tension generated by spontaneous curvature," *Faraday discussions*, vol. 161, pp. 305–331, 2013.

[154] P. Sens and M. S. Turner, "Theoretical model for the formation of caveolae and similar membrane invaginations," *Biophys. J.*, vol. 86, no. 4, pp. 2049–2057, 2004.

[155] B. Różycki, E. Boura, J. H. Hurley, and G. Hummer, "Membrane-elasticity model of coatless vesicle budding induced by escrt complexes," *PLoS Comput Biol*, vol. 8, no. 10, p. e1002736, 2012.

[156] J. Hu, Y. Shibata, C. Voss, T. Shemesh, Z. Li, M. Coughlin, M. M. Kozlov, T. A. Rapoport, and W. A. Prinz, "Membrane proteins of the endoplasmic reticulum induce high-curvature tubules," *Science*, vol. 319, no. 5867, pp. 1247–1250, 2008.

[157] J. Liu, Y. Sun, D. G. Drubin, and G. F. Oster, "The mechanochemistry of endocytosis," *PLoS Biol*, vol. 7, no. 9, p. e1000204, 2009.

[158] J. Liu, M. Kaksonen, D. G. Drubin, and G. Oster, "Endocytic vesicle scission by lipid phase boundary forces," *Proceedings of the National Academy of Sciences*, vol. 103, no. 27, pp. 10277–10282, 2006.

[159] M. E. A. Faris, D. Lacoste, J. Pécréaux, J.-F. Joanny, J. Prost, and P. Bassereau, "Membrane tension lowering induced by protein activity," *Phys. Rev. Lett.*, vol. 102, no. 3, p. 038102, 2009.

[160] J.-B. Manneville, P. Bassereau, S. Ramaswamy, and J. Prost, "Active membrane fluctuations studied by micropipet aspiration," *Phys. Rev. Lett.*, vol. 64, no. 2, p. 021908, 2001.

[161] Z. Shi, Z. T. Graber, T. Baumgart, H. A. Stone, and A. E. Cohen, "Cell membranes resist flow," *bioRxiv*, p. 290643, 2018.

[162] M. P. Sheetz and S. Singer, "Biological membranes as bilayer couples. a molecular mechanism of drug-erythrocyte interactions," *Proceedings of the National Academy of Sciences*, vol. 71, no. 11, pp. 4457–4461, 1974.

[163] L. Miao, U. Seifert, M. Wortis, and H.-G. Dobereiner, "Budding transitions of fluid-bilayer vesicles: the effect of area-difference elasticity," *Phys. Rev. E*, vol. 49, no. 6, p. 5389, 1994.

[164] S. Svetina, M. Brumen, and B. Zeks, "Lipid bilayer elasticity and the bilayer couple interpretation of red-cell shape transformations and lysis," *Stud Biophys*, vol. 110, no. 1-3, pp. 177–184, 1985.

[165] S. Svetina and B. Žekš, "Membrane bending energy and shape determination of phospholipid vesicles and red blood cells," *European biophysics journal*, vol. 17, no. 2, pp. 101–111, 1989.

[166] H.-G. Dobereiner, E. Evans, M. Kraus, U. Seifert, and M. Wortis, "Mapping vesicle shapes into the phase diagram: A comparison of experiment and theory," *Phys. Rev. E*, vol. 55, no. 4, p. 4458, 1997.

[167] B. Bozic, S. Svetina, B. Zeks, and R. Waugh, "Role of lamellar membrane structure in tether formation from bilayer vesicles," *Biophys. J.*, vol. 61, no. 4, pp. 963–973, 1992.

[168] R. E. Waugh, "Elastic energy of curvature-driven bump formation on red blood cell membrane," *Biophys. J.*, vol. 70, no. 2, pp. 1027–1035, 1996.

[169] R. Mukhopadhyay, H. G. Lim, and M. Wortis, "Echinocyte shapes: bending, stretching, and shear determine spicule shape and spacing," *Biophysical Journal*, vol. 82, no. 4, pp. 1756–1772, 2002.

[170] G. L. Hw, M. Wortis, and R. Mukhopadhyay, "Stomatocyte–discocyte–echinocyte sequence of the human red blood cell: Evidence for the bilayer–couple hypothesis from membrane mechanics," *Proc Natl Acad Sci*, vol. 99, no. 26, pp. 16766–16769, 2002.

[171] S. Svetina, D. Kuzman, R. E. Waugh, P. Ziherl, and B. Zeks, "The cooperative role of membrane skeleton and bilayer in the mechanical behaviour of red blood cells," *Bioelectrochemistry*, vol. 62, no. 2, pp. 107–113, 2004.

[172] Y. Schweitzer and M. M. Kozlov, "Membrane-mediated interaction between strongly anisotropic protein scaffolds," *PLOS Comput. Biol.*, vol. 11, no. 2, p. e1004054, 2015.

[173] M. Simunovic, C. Prevost, A. Callan-Jones, and P. Bassereau, "Physical basis of some membrane shaping mechanisms," *Phil. Trans. R. Soc. A*, vol. 374, no. 2072, p. 20160034, 2016.

[174] A. Frost, R. Perera, A. Roux, K. Spasov, O. Destaing, E. H. Egelman, P. De Camilli, and V. M. Unger, "Structural basis of membrane invagination by f-bar domains," *Cell*, vol. 132, no. 5, pp. 807–817, 2008.

[175] A. Shimada, H. Niwa, K. Tsujita, S. Suetsugu, K. Nitta, K. Hanawa-Suetsugu, R. Akasaka, Y. Nishino, M. Toyama, L. Chen, *et al.*, "Curved efc/f-bar-domain dimers are joined end to end into a filament for membrane invagination in endocytosis," *Cell*, vol. 129, no. 4, pp. 761–772, 2007.

[176] V. Kralj-Iglič, S. Svetina, and B. Žekž, "Shapes of bilayer vesicles with membrane embedded molecules," *European biophysics journal*, vol. 24, no. 5, pp. 311–321, 1996.

[177] J. Fournier, "Nontopological saddle-splay and curvature instabilities from anisotropic membrane inclusions," *Phys. Rev. Lett.*, vol. 76, no. 23, p. 4436, 1996.

[178] V. Kralj-Iglič, V. Heinrich, S. Svetina, and B. Žekš, "Free energy of closed membrane with anisotropic inclusions," *The European Physical Journal B-Condensed Matter and Complex Systems*, vol. 10, no. 1, pp. 5–8, 1999.

[179] V. Kralj-Iglic, M. Remskar, G. Vidmar, M. Fosnaric, and A. Iglic, "Deviatoric elasticity as a possible physical mechanism explaining collapse of inorganic micro and nanotubes," *Phys. Lett. A*, vol. 296, no. 2-3, pp. 151–155, 2002.

[180] A. Iglič, H. Hägerstrand, P. Veranič, A. Plemenitaš, and V. Kralj-Iglič, "Curvature-induced accumulation of anisotropic membrane components and raft formation in cylindrical membrane protrusions," *Journal of Theoretical Biology*, vol. 240, no. 3, pp. 368–373, 2006.

[181] D. Kabaso, N. Bobrovska, W. Góźdź, N. Gov, V. Kralj-Iglič, P. Veranič, and A. Iglič, "On the role of membrane anisotropy and bar proteins in the stability of tubular membrane structures," *Journal of biomechanics*, vol. 45, no. 2, pp. 231–238, 2012.

[182] D. Kabaso, E. Gongadze, P. Elter, U. Van Rienen, J. Gimsa, V. Kralj-Iglic, and A. Iglic, "Attachment of rod-like (bar) proteins and membrane shape," *Mini-Rev. Med. Chem.*, vol. 11, no. 4, pp. 272–282, 2011.

[183] N. Walani, J. Torres, and A. Agrawal, "Anisotropic spontaneous curvatures in lipid membranes," *Physical Review E*, vol. 89, no. 6, p. 062715, 2014.

[184] B. J. Reynwar, G. Illya, V. A. Harmandaris, M. M. Müller, K. Kremer, and M. Deserno, "Aggregation and vesiculation of membrane proteins by curvature-mediated interactions," *Nature*, vol. 447, no. 7143, p. 461, 2007.

[185] R. W. Tourdot, N. Ramakrishnan, and R. Radhakrishnan, "Defining the free-energy landscape of curvature-inducing proteins on membrane bilayers," *Phys. Rev. E*, vol. 90, no. 2, p. 022717, 2014.

[186] Z. Shi and T. Baumgart, "Dynamics and instabilities of lipid bilayer membrane shapes," *Advances in colloid and interface science*, vol. 208, pp. 76–88, 2014.

[187] A. V. Shnyrova, V. A. Frolov, and J. Zimmerberg, "Domain-driven morphogenesis of cellular membranes," *Curr. Biol.*, vol. 19, no. 17, pp. R772–R780, 2009.

[188] A. Veksler and N. S. Gov, "Phase transitions of the coupled membrane-cytoskeleton modify cellular shape," *Biophys. J.*, vol. 93, no. 11, pp. 3798–3810, 2007.

[189] N. Gov, "Guided by curvature: shaping cells by coupling curved membrane proteins and cytoskeletal forces," *Phil. Trans. R. Soc. B*, vol. 373, no. 1747, p. 20170115, 2018.

[190] T. Gil, J. H. Ipsen, O. G. Mouritsen, M. C. Sabra, M. M. Sperotto, and M. J. Zuckermann, "Theoretical analysis of protein organization in lipid membranes," *Biochim. Biophys. Acta*, vol. 1376, no. 3, pp. 245–266, 1998.

[191] S. Givli, H. Giang, and K. Bhattacharya, "Stability of multicomponent biological membranes," *SIAM J Appl Math*, vol. 72, no. 2, pp. 489–511, 2012.

[192] S. Katz and S. Givli, "Curvature-induced spatial ordering of composition in lipid membranes," *Comput Math Methods Med*, vol. 2017, 2017.

[193] D. Kabaso, R. Shlomovitz, K. Schloen, T. Stradal, and N. S. Gov, "Theoretical model for cellular shapes driven by protrusive and adhesive forces," *PLoS computational biology*, vol. 7, no. 5, p. e1001127, 2011.

[194] R. Shlomovitz and N. Gov, "Exciting cytoskeleton-membrane waves," *Phys. Rev. E*, vol. 78, no. 4, p. 041911, 2008.

[195] G. Orly, M. Naoz, and N. Gov, "Physical model for the geometry of actin-based cellular protrusions," *Biophysical journal*, vol. 107, no. 3, pp. 576–587, 2014.

[196] D. Kabaso, E. Gongadze, J. Jorgacevski, M. Kreft, U. Rienen, R. Zorec, and A. Iglic, "Exploring the binding dynamics of bar proteins," *Cell. Mol. Biol. Lett.*, vol. 16, no. 3, p. 398, 2011.

[197] T. R. Weikl, "Membrane-mediated cooperativity of proteins," *Annu. Rev. Phys. Chem.*, vol. 69, pp. 521–539, 2018.

[198] R. Phillips, T. Ursell, P. Wiggins, and P. Sens, "Emerging roles for lipids in shaping membrane-protein function," *Nature*, vol. 459, no. 7245, p. 379, 2009.

[199] T. R. Weikl, M. Asfaw, H. Krobath, B. Rozycki, and R. Lipowsky, "Adhesion of membranes via receptor–ligand complexes: Domain formation, binding cooperativity, and active processes," *Soft Matter*, vol. 5, no. 17, pp. 3213–3224, 2009.

[200] B. Daum, A. Auerswald, T. Gruber, G. Hause, J. Balbach, W. Kuhlbrandt, and A. Meister, "Supramolecular organization of the human n-bar domain in shaping the sarcolemma membrane," *J. Struct. Biol.*, vol. 194, no. 3, pp. 375–382, 2016.

[201] H. Noguchi, "Membrane tubule formation by banana-shaped proteins with or without transient network structure," *Sci. Rep.*, vol. 6, p. 20935, 2016.

[202] A. Agrawal and D. J. Steigmann, "A model for surface diffusion of trans-membrane proteins on lipid bilayers," *Zeitschrift für Angewandte Mathematik und Physik (ZAMP)*, vol. 62, no. 3, pp. 549–563, 2011.

[203] T. Kirchhausen, "Bending membranes," *Nature cell biology*, vol. 14, no. 9, p. 906, 2012.

[204] G. Guigas and M. Weiss, "Effects of protein crowding on membrane systems," *Biochim. Biophys. Acta*, vol. 1858, no. 10, pp. 2441–2450, 2016.

[205] J. C. Stachowiak, F. M. Brodsky, and E. A. Miller, "A cost-benefit analysis of the physical mechanisms of membrane curvature," *Nature cell biology*, vol. 15, no. 9, pp. 1019–1027, 2013.

[206] J. Derganc and A. Čopič, "Membrane bending by protein crowding is affected by protein lateral confinement," *Biochimica et Biophysica Acta (BBA)-Biomembranes*, vol. 1858, no. 6, pp. 1152–1159, 2016.

[207] M. Linden, P. Sens, and R. Phillips, "Entropic tension in crowded membranes," *PLOS Comput. Biol.*, vol. 8, no. 3, p. e1002431, 2012.

[208] G. J. Van Wylen and R. E. Sonntag, "Fundamentals of classical thermodynamics," tech. rep., 1965.

[209] S. Luding, "Global equation of state of two-dimensional hard sphere systems," *Phys. Rev. E*, vol. 63, no. 4, p. 042201, 2001.

[210] N. F. Carnahan and K. E. Starling, "Equation of state for nonattracting rigid spheres," *J. Chem. Phys.*, vol. 51, no. 2, pp. 635–636, 1969.

[211] W. T. Snead, C. C. Hayden, A. K. Gadok, C. Zhao, E. M. Lafer, P. Rangamani, and J. C. Stachowiak, "Membrane fission by protein crowding," *Proceedings of the National Academy of Sciences*, vol. 114, no. 16, pp. E3258–E3267, 2017.

[212] J. C. Stachowiak, C. C. Hayden, and D. Y. Sasaki, "Steric confinement of proteins on lipid membranes can drive curvature and tubulation," *Proc Natl Acad Sci*, vol. 107, no. 17, pp. 7781–7786, 2010.

[213] Z. Chen, E. Atefi, and T. Baumgart, "Membrane shape instability induced by protein crowding," *Biophys. J.*, vol. 111, no. 9, pp. 1823–1826, 2016.

[214] A. Callan-Jones and P. Bassereau, "Curvature-driven membrane lipid and protein distribution," *CURR OPIN SOLID ST M*, vol. 17, no. 4, pp. 143–150, 2013.

[215] W. Snead, W. Zeno, G. Kago, R. Perkins, J. B. Richter, E. Lafer, and J. Stachowiak, "Bar scaffolds drive membrane fission by crowding disordered domains," *bioRxiv*, p. 276147, 2018.

[216] R. E. Dalbey, "Leader peptidase," *Mol. Microbiol.*, vol. 5, no. 12, pp. 2855–2860, 1991.

[217] H. R. Kaback, S. Frillingos, H. Jung, K. Jung, G. G. Prive, M. Ujwal, C. Weitzman, J. Wu, and K. Zen, "The lactose permease meets frankenstein.," *J. Exp. Biol.*, vol. 196, no. 1, pp. 183–195, 1994.

[218] J. A. Killian, "Hydrophobic mismatch between proteins and lipids in membranes," *Biochim. Biophys. Acta*, vol. 1376, no. 3, pp. 401–416, 1998.

[219] R. L. Thurmond, A. R. Niemi, G. Lindblom, A. Wieslander, and L. Rilfors, "Membrane thickness and molecular ordering in acholeplasma laidlawii strain a studied by 2h nmr spectroscopy," *Biochemistry*, vol. 33, no. 45, pp. 13178–13188, 1994.

[220] D. Duque, X.-j. Li, K. Katsov, and M. Schick, "Molecular theory of hydrophobic mismatch between lipids and peptides," *J. Chem. Phys.*, vol. 116, no. 23, pp. 10478–10484, 2002.

[221] D. R. Fattal and A. Ben-Shaul, "Mean-field calculations of chain packing and conformational statistics in lipid bilayers: comparison with experiments and molecular dynamics studies.," *Biophys. J.*, vol. 67, no. 3, p. 985, 1994.

[222] D. Argudo, N. P. Bethel, F. V. Marcoline, C. W. Wolgemuth, and M. Grabe, "New continuum approaches for determining protein-induced membrane deformations," *Biophysical journal*, vol. 112, no. 10, pp. 2159–2172, 2017.

[223] O. Mouritsen and M. Bloom, "Mattress model of lipid-protein interactions in membranes," *Biophys. J.*, vol. 46, no. 2, pp. 141–153, 1984.

[224] E. A. Guggenheim, *Mixtures: the theory of the equilibrium properties of some simple classes of mixtures, solutions and alloys*. Clarendon Press, 1952.

[225] O. S. Andersen and R. E. Koeppe, "Bilayer thickness and membrane protein function: an energetic perspective," *Annu. Rev. Biophys. Biomol. Struct.*, vol. 36, pp. 107–130, 2007.

[226] S. Marcelja, "Lipid-mediated protein interaction in membranes," *Biochim. Biophys. Acta*, vol. 455, no. 1, pp. 1–7, 1976.

[227] J. C. Owicki and H. M. McConnell, "Theory of protein-lipid and protein-protein interactions in bilayer membranes," *Proc Natl Acad Sci*, vol. 76, no. 10, pp. 4750–4754, 1979.

[228] B. A. Lewis and D. M. Engelman, "Lipid bilayer thickness varies linearly with acyl chain length in fluid phosphatidylcholine vesicles," *J. Mol. Biol.*, vol. 166, no. 2, pp. 211–217, 1983.

[229] N. J. Ryba and D. Marsh, "Protein rotational diffusion and lipid/protein interactions in recombinants of bovine rhodopsin with saturated diacylphosphatidylcholines of different chain lengths studied by conventional and saturation-transfer electron spin resonance," *Biochemistry*, vol. 31, no. 33, pp. 7511–7518, 1992.

[230] J. Vonck, "A three-dimensional difference map of the n intermediate in the bacteriorhodopsin photocycle: part of the f helix tilts in the m to n transition," *Biochemistry*, vol. 35, no. 18, pp. 5870–5878, 1996.

[231] J. Fournier and P. Galatola, "Tubular vesicles and effective fourth-order membrane elastic theories," *EPL (Europhysics Letters)*, vol. 39, no. 2, p. 225, 1997.

[232] M. Deserno, "Fluid lipid membranes: From differential geometry to curvature stresses," *Chemistry and physics of lipids*, vol. 185, pp. 11–45, 2015.

[233] D. P. Siegel, "Fourth-order curvature energy model for the stability of bicontinuous inverted cubic phases in amphiphile- water systems," *Langmuir*, vol. 26, no. 11, pp. 8673–8683, 2010.

[234] G. Brannigan and F. L. Brown, "Contributions of gaussian curvature and nonconstant lipid volume to protein deformation of lipid bilayers," *Biophys. J.*, vol. 92, no. 3, pp. 864–876, 2007.

[235] K. Kim, J. Neu, and G. Oster, "Effect of protein shape on multibody interactions between membrane inclusions," *Phys. Rev. E*, vol. 61, no. 4, p. 4281, 2000.

[236] N. R. Latorraca, K. M. Callenberg, J. P. Boyle, and M. Grabe, "Continuum approaches to understanding ion and peptide interactions with the membrane," *J. Membr. Biol.*, vol. 247, no. 5, pp. 395–408, 2014.

[237] J. N. Israelachvili, *Intermolecular and surface forces*. Academic press, 2011.

[238] Y. Zhou, B. Lu, and A. A. Gorfe, "Continuum electromechanical modeling of protein-membrane interactions," *Phys. Rev. E*, vol. 82, no. 4, p. 041923, 2010.

[239] D. Steigmann and A. Agrawal, "Electromechanics of polarized lipid bilayers," *Math. Mech. Complex Syst.*, vol. 4, no. 1, pp. 31–54, 2016.

[240] A. Roux, D. Cuvelier, P. Nassoy, J. Prost, P. Bassereau, and B. Goud, "Role of curvature and phase transition in lipid sorting and fission of membrane tubules," *The EMBO journal*, vol. 24, no. 8, pp. 1537–1545, 2005.

[241] S. Aimon, A. Callan-Jones, A. Berthaud, M. Pinot, G. E. Toombes, and P. Bassereau, "Membrane shape modulates transmembrane protein distribution," *Developmental cell*, vol. 28, no. 2, pp. 212–218, 2014.

[242] P. K. Mattila and P. Lappalainen, "Filopodia: molecular architecture and cellular functions," *Nature reviews Molecular cell biology*, vol. 9, no. 6, pp. 446–454, 2008.

[243] T. Baumgart, S. T. Hess, and W. W. Webb, "Imaging coexisting fluid domains in biomembrane models coupling curvature and line tension," *Nature*, vol. 425, no. 6960, pp. 821–824, 2003.

[244] W. Römer, L. Berland, V. Chambon, K. Gaus, B. Windschiegl, D. Tenza, M. R. Aly, V. Fraisier, J.-C. Florent, D. Perrais, *et al.*, "Shiga toxin induces tubular membrane invaginations for its uptake into cells," *Nature*, vol. 450, no. 7170, p. 670, 2007.

[245] M. G. Ford, I. G. Mills, B. J. Peter, Y. Vallis, G. J. Praefcke, P. R. Evans, and H. T. McMahon, "Curvature of clathrin-coated pits driven by epsin," *Nature*, vol. 419, no. 6905, p. 361, 2002.

[246] R. Lipowsky, "Bending of membranes by anchored polymers," *EPL (Europhysics Letters)*, vol. 30, no. 4, p. 197, 1995.

[247] R. Capovilla and J. Guven, "Stresses in lipid membranes," *Journal of Physics A: Mathematical and General*, vol. 35, no. 30, p. 6233, 2002.

[248] J.-B. Fournier, "On the stress and torque tensors in fluid membranes," *Soft Matter*, vol. 3, no. 7, pp. 883–888, 2007.

[249] K. Farsad and P. De Camilli, "Mechanisms of membrane deformation," *Current opinion in cell biology*, vol. 15, no. 4, pp. 372–381, 2003.

[250] G. A. Holzapfel, R. Eberlein, P. Wriggers, and H. W. Weizsäcker, "Large strain analysis of soft biological membranes: Formulation and finite element analysis," *Computer methods in applied mechanics and engineering*, vol. 132, no. 1-2, pp. 45–61, 1996.

[251] D. Einstein, P. Reinhall, M. Nicosia, R. Cochran, and K. Kunzelman, "Dynamic finite element implementation of nonlinear, anisotropic hyperelastic biological membranes," *Computer Methods in Biomechanics & Biomedical Engineering*, vol. 6, no. 1, pp. 33–44, 2003.

[252] D. Lingwood and K. Simons, "Lipid rafts as a membrane-organizing principle," *science*, vol. 327, no. 5961, pp. 46–50, 2010.

[253] M. R. Mofrad and R. D. Kamm, "Cellular mechanotransduction," 2010.

[254] R. Phillips, J. Kondev, J. Theriot, and H. Garcia, *Physical biology of the cell*. Garland Science, 2012.

[255] Y.-c. Fung, *Biomechanics: mechanical properties of living tissues*. Springer Science & Business Media, 2013.

[256] I. Todhunter, *A History of the Theory of Elasticity and of the Strength of Materials: Galilei to Saint-Venant, 1639-1850.-v. 2. pt. 1-2. Saint-Venant to Lord Kelvin*, vol. 1. University Press, 1886.

[257] R. M. Hochmuth, "Micropipette aspiration of living cells," *J. Biomech.*, vol. 33, pp. 15–22, Jan. 2000.

[258] L. M. Lee and A. P. Liu, "The application of micropipette aspiration in molecular mechanics of single cells," *J. Nanotechnol. Eng. Med.*, vol. 5, pp. 0408011–0408016, Nov. 2014.

[259] H. J. Lee, E. L. Peterson, R. Phillips, W. S. Klug, and P. A. Wiggins, "Membrane shape as a reporter for applied forces," *Proceedings of the National Academy of Sciences*, vol. 105, no. 49, pp. 19253–19257, 2008.

[260] T. Baumgart, S. Das, W. W. Webb, and J. T. Jenkins, "Membrane elasticity in giant vesicles with fluid phase coexistence," *Biophysical journal*, vol. 89, no. 2, pp. 1067–1080, 2005.

[261] L. Karotki, J. T. Huiskonen, C. J. Stefanand, N. E. Ziółkowska, R. Roth, M. A. Surma, N. J. Krogan, S. D. Emr, J. Heuser, K. Grünewald, and T. C. Walther, "Eisosome proteins assemble into a membrane scaffold.," *J. Cell Biol.*, vol. 195, no. 5, pp. 889–902, 2011.

[262] C. Buser and D. G. Drubin, "Ultrastructural imaging of endocytic sites in saccharomyces cerevisiae by transmission electron microscopy and immunolabeling," *Microscopy and Microanalysis*, vol. 19, no. 02, pp. 381–392, 2013.

[263] R. Lipowsky, "Spontaneous tubulation of membranes and vesicles reveals membrane tension generated by spontaneous curvature," *Faraday Discuss.*, vol. 161, pp. 305–331, 2013.

[264] H. Zhao, A. Michelot, E. Koskela, V. Tkach, D. Stamou, D. Drubin, and P. Lappalainen, "Membrane-Sculpting BAR Domains Generate Stable Lipid Microdomains," *Cell Rep*, vol. 4, pp. 1213–1223, 2013.

[265] P. Bassereau, B. Sorre, and A. Lévy, "Bending lipid membranes: Experiments after w. helfrich's model," *Advances in colloid and interface science*, vol. 208, pp. 47–57, 2014.

[266] M. Lokar, D. Kabaso, N. Resnik, K. Sepčić, V. Kralj-Iglič, P. Veranič, R. Zorec, and A. Iglič, "The role of cholesterol-sphingomyelin membrane nanodomains in the stability of intercellular membrane nanotubes," *International journal of nanomedicine*, vol. 7, p. 1891, 2012.

[267] R. Capovilla and J. Guven, "Geometry of lipid vesicle adhesion," *Physical Review E*, vol. 66, no. 4, p. 041604, 2002.

[268] R. Capovilla and J. Guven, "Stress and geometry of lipid vesicles," *Journal of Physics: Condensed Matter*, vol. 16, no. 22, p. S2187, 2004.

[269] U. Seifert, "Configurations of fluid membranes and vesicles," *Advances in physics*, vol. 46, no. 1, pp. 13–137, 1997.

[270] J. Buehrle, S. Herminghaus, and F. Mugele, "Impact of line tension on the equilibrium shape of liquid droplets on patterned substrates," *Langmuir*, vol. 18, no. 25, pp. 9771–9777, 2002.

[271] Z. A. McDargh, P. Vázquez-Montejo, J. Guven, and M. Deserno, "Constriction by dynamin: Elasticity versus adhesion," *Biophysical journal*, vol. 111, no. 11, pp. 2470–2480, 2016.

[272] T. R. Powers, G. Huber, and R. E. Goldstein, "Fluid-membrane tethers: minimal surfaces and elastic boundary layers," *Physical Review E*, vol. 65, no. 4, p. 041901, 2002.

[273] D. L. Richmond, E. M. Schmid, S. Martens, J. C. Stachowiak, N. Liska, and D. A. Fletcher, "Forming giant vesicles with controlled membrane composition, asymmetry, and contents," *Proceedings of the National Academy of Sciences*, vol. 108, no. 23, pp. 9431–9436, 2011.

[274] N. Dan and S. Safran, "Effect of lipid characteristics on the structure of transmembrane proteins," *Biophysical Journal*, vol. 75, no. 3, pp. 1410–1414, 1998.

[275] R. Lipowsky, "Budding of membranes induced by intramembrane domains," *Journal de Physique II*, vol. 2, no. 10, pp. 1825–1840, 1992.

[276] A. J. Jin, K. Prasad, P. D. Smith, E. M. Lafer, and R. Nossal, "Measuring the elasticity of clathrin-coated vesicles via atomic force microscopy," *Biophysical journal*, vol. 90, no. 9, pp. 3333–3344, 2006.

[277] A. Tian, C. Johnson, W. Wang, and T. Baumgart, "Line tension at fluid membrane domain boundaries measured by micropipette aspiration," *Physical review letters*, vol. 98, no. 20, p. 208102, 2007.

[278] P. I. Kuzmin, S. A. Akimov, Y. A. Chizmadzhev, J. Zimmerberg, and F. S. Cohen, "Line tension and interaction energies of membrane rafts calculated from lipid splay and tilt," *Biophysical journal*, vol. 88, no. 2, pp. 1120–1133, 2005.

[279] S. Semrau and T. Schmidt, "Membrane heterogeneity–from lipid domains to curvature effects," *Soft Matter*, vol. 5, no. 17, pp. 3174–3186, 2009.

[280] D. G. Robinson, F. Brandizzi, C. Hawes, and A. Nakano, "Vesicles versus tubes: Is endoplasmic reticulum-golgi transport in plants fundamentally different from other eukaryotes?," *Plant Physiology*, vol. 168, no. 2, pp. 393–406, 2015.

[281] A. Mozdy, J. McCaffery, and J. Shaw, "Dnm1p gtpase-mediated mitochondrial fission is a multi-step process requiring the novel integral membrane component fis1p," *The Journal of cell biology*, vol. 151, no. 2, pp. 367–380, 2000.

[282] A. Picco, M. Mund, J. Ries, F. Nédélec, and M. Kaksonen, "Visualizing the functional architecture of the endocytic machinery," *Elife*, vol. 4, p. e04535, 2015.

[283] A. Varma, M. Morbidelli, and H. Wu, *Parametric sensitivity in chemical systems*. Cambridge University Press, 2005.

[284] S. Wäldchen, J. Lehmann, T. Klein, S. Van De Linde, and M. Sauer, "Light-induced cell damage in live-cell super-resolution microscopy," *Scientific reports*, vol. 5, p. 15348, 2015.

[285] A. M. Sydor, K. J. Czymmek, E. M. Puchner, and V. Mennella, "Super-resolution microscopy: from single molecules to supramolecular assemblies," *Trends in cell biology*, vol. 25, no. 12, pp. 730–748, 2015.

[286] V. Lučić, A. Rigort, and W. Baumeister, "Cryo-electron tomography: the challenge of doing structural biology in situ," *J Cell Biol*, vol. 202, no. 3, pp. 407–419, 2013.

[287] C. P. Brangwynne, P. Tompa, and R. V. Pappu, "Polymer physics of intracellular phase transitions," *Nature Physics*, vol. 11, no. 11, pp. 899–904, 2015.

[288] E. Kreyszig, "Differential geometry," in *Differential Geometry*, University of Toronto Press, 2019.

[289] H. Naito, M. Okuda, and O.-Y. Zhong-Can, "New solutions to the helfrich variation problem for the shapes of lipid bilayer vesicles: beyond delaunay's surfaces," *Physical review letters*, vol. 74, no. 21, p. 4345, 1995.

[290] R. Bar-Ziv and E. Moses, "Instability and" pearling" states produced in tubular membranes by competition of curvature and tension," *Physical review letters*, vol. 73, no. 10, p. 1392, 1994.

[291] J. Sanborn, K. Oglecka, R. S. Kraut, and A. N. Parikh, "Transient pearling and vesiculation of membrane tubes under osmotic gradients," *Faraday discussions*, vol. 161, pp. 167–176, 2013.

[292] I. Tsafrir, D. Sagi, T. Arzi, M.-A. Guedeau-Boudeville, V. Frette, D. Kandel, and J. Stavans, "Pearling instabilities of membrane tubes with anchored polymers," *Physical review letters*, vol. 86, no. 6, p. 1138, 2001.

[293] K. A. Burke, A. M. Janke, C. L. Rhine, and N. L. Fawzi, "Residue-by-residue view of in vitro fus granules that bind the c-terminal domain of rna polymerase ii," *Molecular cell*, vol. 60, no. 2, pp. 231–241, 2015.

[294] E. A. DiMarzio and F. L. McCrackin, "One-dimensional model of polymer adsorption," *The Journal of Chemical Physics*, vol. 43, no. 2, pp. 539–547, 1965.

[295] C. H. V. Indrani and R. Lipowsky, "Membranes with anchored polymers at the adsorption transition," *EPL (Europhysics Letters)*, vol. 36, no. 7, p. 491, 1996.

[296] Y. W. Kim and W. Sung, "Membrane curvature induced by polymer adsorption," *Physical Review E*, vol. 63, no. 4, p. 041910, 2001.

[297] W. Wiese, W. Harbich, and W. Helfrich, "Budding of lipid bilayer vesicles and flat membranes," *Journal of physics: Condensed matter*, vol. 4, no. 7, p. 1647, 1992.

[298] H. Lee and R. W. Pastor, "Coarse-grained model for pegylated lipids: effect of pegylation on the size and shape of self-assembled structures," *The Journal of Physical Chemistry B*, vol. 115, no. 24, pp. 7830–7837, 2011.

[299] L. Mesarec, W. Gozdz, S. Iglivc, Veronika Kralj, and A. Iglivc, "Closed membrane shapes with attached bar domains subject to external force of actin filaments," *Colloids and Surfaces B: Biointerfaces*, vol. 141, pp. 132–140, 2016.

[300] J. D. Nickels, S. Chatterjee, C. B. Stanley, S. Qian, X. Cheng, D. A. Myles, R. F. Standaert, J. G. Elkins, and J. Katsaras, "The in vivo structure of biological membranes and evidence for lipid domains," *PLoS biology*, vol. 15, no. 5, p. e2002214, 2017.

[301] G. W. Brodland, J. H. Veldhuis, S. Kim, M. Perrone, D. Mashburn, and M. S. Hutson, "Cellfit: a cellular force-inference toolkit using curvilinear cell boundaries," *PloS one*, vol. 9, no. 6, p. e99116, 2014.

[302] J. H. Veldhuis, D. Mashburn, M. S. Hutson, and G. W. Brodland, "Practical aspects of the cellular force inference toolkit (cellfit)," in *Methods in cell biology*, vol. 125, pp. 331–351, Elsevier, 2015.

[303] A. Frost, V. M. Unger, and P. De Camilli, "The bar domain superfamily: membrane-molding macromolecules," *Cell*, vol. 137, no. 2, pp. 191–196, 2009.

[304] P. N. Dannhauser and E. J. Ungewickell, "Reconstitution of clathrin-coated bud and vesicle formation with minimal components," *Nature Cell Biology*, vol. 14, no. 6, pp. 634–639, 2012.

[305] D. Steigmann, E. Baesu, R. E. Rudd, J. Belak, and M. McElfresh, "On the variational theory of cell-membrane equilibria," *Interfaces and Free Boundaries*, vol. 5, no. 4, pp. 357–366, 2003.

[306] P. M. Naghdi, "The theory of shells and plates," in *Linear Theories of Elasticity and Thermoelasticity*, pp. 425–640, Springer, 1973.

[307] C. Monzel and K. Sengupta, "Measuring shape fluctuations in biological membranes," *Journal of Physics D: Applied Physics*, vol. 49, no. 24, p. 243002, 2016.

[308] J. Steinkühler, B. Różycki, C. Alvey, R. Lipowsky, T. R. Weikl, R. Dimova, and D. E. Discher, "Membrane fluctuations and acidosis regulate cooperative binding of "marker of self" cd47 with macrophage checkpoint receptor sirpα," *J Cell Sci*, pp. jcs–216770, 2018.

[309] R. Shlomovitz, N. S. Gov, and A. Roux, "Membrane-mediated interactions and the dynamics of dynamin oligomers on membrane tubes," *New J. Phys.*, vol. 13, p. 065008, June 2011.

[310] A. Rustom, R. Saffrich, I. Markovic, P. Walther, and H.-H. Gerdes, "Nanotubular highways for intercellular organelle transport," *Science*, vol. 303, no. 5660, pp. 1007–1010, 2004.

[311] D. M. Davis and S. Sowinski, "Membrane nanotubes: dynamic long-distance connections between animal cells," *Nat. Rev. Mol. Cell. Biol.*, vol. 9, no. 6, p. 431, 2008.

[312] H.-H. Gerdes and R. N. Carvalho, "Intercellular transfer mediated by tunneling nanotubes," *Curr. Opin. Cell. Biol*, vol. 20, no. 4, pp. 470–475, 2008.

[313] B. Onfelt, S. Nedvetzki, K. Yanagi, and D. M. Davis, "Cutting edge: Membrane nanotubes connect immune cells," *J. Immunol*, vol. 173, no. 3, pp. 1511–1513, 2004.

[314] S. Sowinski, C. Jolly, O. Berninghausen, M. A. Purbhoo, A. Chauveau, K. Kohler, S. Oddos, P. Eissmann, F. M. Brodsky, C. Hopkins, *et al.*, "Membrane nanotubes physically connect t cells over long distances presenting a novel route for hiv-1 transmission," *Nat. Cell. Biol*, vol. 10, no. 2, p. 211, 2008.

[315] T. Bhatia, J. Agudo-Canalejo, R. Dimova, and R. Lipowsky, "Membrane nanotubes increase the robustness of giant vesicles," *ACS Nano*, vol. 12, no. 5, pp. 4478–4485, 2018.

[316] R. W. Davenport, P. Dou, V. Rehder, and S. Kater, "A sensory role for neuronal growth cone filopodia," *Nature*, vol. 361, no. 6414, p. 721, 1993.

[317] S. L. Gupton and F. B. Gertler, "Filopodia: the fingers that do the walking," *Sci. Signal.*, vol. 2007, no. 400, p. re5, 2007.

[318] N. S. Parkar, B. S. Akpa, L. C. Nitsche, L. E. Wedgewood, A. T. Place, M. S. Sverdlov, O. Chaga, and R. D. Minshall, "Vesicle formation and endocytosis: function, machinery, mechanisms, and modeling," *Antioxid. Redox Signal.*, vol. 11, no. 6, pp. 1301–1312, 2009.

[319] L. Caneparo, P. Pantazis, W. Dempsey, and S. E. Fraser, "Intercellular bridges in vertebrate gastrulation," *PLoS One*, vol. 6, no. 5, p. e20230, 2011.

[320] X. Wang, N. V. Bukoreshtliev, and H.-H. Gerdes, "Developing neurons form transient nanotubes facilitating electrical coupling and calcium signaling with distant astrocytes," *PloS One*, vol. 7, no. 10, p. e47429, 2012.

[321] D. L. Tanelian and V. S. Markin, "Biophysical and functional consequences of receptor-mediated nerve fiber transformation," *Biophys. J.*, vol. 72, no. 3, pp. 1092–1108, 1997.

[322] E. Lou, "Intercellular conduits in tumors: The new social network," *Trends in cancer*, vol. 2, no. 1, pp. 3–5, 2016.

[323] Y. Liu, J. Agudo-Canalejo, A. Grafmuller, R. Dimova, and R. Lipowsky, "Patterns of flexible nanotubes formed by liquid-ordered and liquid-disordered membranes," *ACS Nano*, vol. 10, no. 1, pp. 463–474, 2015.

[324] A. Iglivc, B. Babnik, U. Gimsa, and V. Kralj-Iglivc, "On the role of membrane anisotropy in the beading transition of undulated tubular membrane structures," *J. Phys. A*, vol. 38, no. 40, p. 8527, 2005.

[325] A. H. Bahrami and G. Hummer, "Formation and stability of lipid membrane nanotubes," *ACS nano*, 2017.

[326] L. Marzo, K. Gousset, and C. Zurzolo, "Multifaceted roles of tunneling nanotubes in intercellular communication," *Fron. Physiol*, vol. 3, 2012.

[327] Z. Yan, S. Li, Z. Luo, Y. Xu, and T. Yue, "Membrane nanotube pearling restricted by confined polymers," *Soft matter*, 2018.

[328] H. Jiang, B. P. English, R. B. Hazan, P. Wu, and B. Ovryn, "Tracking surface glycans on live cancer cells with single-molecule sensitivity," *Angew. Chem.*, vol. 54, no. 6, pp. 1765–1769, 2015.

[329] K. Schara, V. Jansa, V. Sustar, D. Dolinar, J. I. Pavlic, M. Lokar, V. Kralj-Iglic, P. Veranic, and A. Iglic, "Mechanisms for the formation of membranous nanostructures in cell-to-cell communication," *Cell. Mol. Biol. Lett.*, vol. 14, no. 4, p. 636, 2009.

[330] P. Veranivc, M. Lokar, G. J. Schutz, J. Weghuber, S. Wieser, H. Hagerstrand, V. Kralj-Iglivc, and A. Iglivc, "Different types of cell-to-cell connections mediated by nanotubular structures," *Biophys. J.*, vol. 95, no. 9, pp. 4416–4425, 2008.

[331] J. A. F. Plateau, *Statique experimentale et theorique des liquides soumis aux seules forces moleculaires*, vol. 2. Gauthier-Villars, 1873.

[332] L. Rayleigh, "On the instability of jets," *P. LOND. MATH. SOC.*, vol. 1, no. 1, pp. 4–13, 1878.

[333] S. Tomotika, "On the instability of a cylindrical thread of a viscous liquid surrounded by another viscous fluid," *Proc. R. Soc. Lond. A*, vol. 150, no. 870, pp. 322–337, 1935.

[334] R. Bar-Ziv, E. Moses, and P. Nelson, "Dynamic excitations in membranes induced by optical tweezers," *Biophys. J.*, vol. 75, no. 1, pp. 294–320, 1998.

[335] K. P. Sinha, S. Gadkari, and R. M. Thaokar, "Electric field induced pearling instability in cylindrical vesicles," *Soft Matter*, vol. 9, no. 30, pp. 7274–7293, 2013.

[336] C. Menager, M. Meyer, V. Cabuil, A. Cebers, J.-C. Bacri, and R. Perzynski, "Magnetic phospholipid tubes connected to magnetoliposomes: pearling instability induced by a magnetic field," *Eur. Phys. J. E*, vol. 7, no. 4, pp. 325–337, 2002.

[337] M. Yanagisawa, M. Imai, and T. Taniguchi, "Shape deformation of ternary vesicles coupled with phase separation," *Phys. Rev. Lett.*, vol. 100, no. 14, p. 148102, 2008.

[338] V. Narsimhan, A. P. Spann, and E. S. Shaqfeh, "Pearling, wrinkling, and buckling of vesicles in elongational flows," *J. Fluid Mech.*, vol. 777, pp. 1–26, 2015.

[339] U. Jelerčič and N. S. Gov, "Pearling instability of membrane tubes driven by curved proteins and actin polymerization," *Phys. Biol.*, vol. 12, no. 6, p. 066022, 2015.

[340] S. Chaieb and S. Rica, "Spontaneous curvature-induced pearling instability," *Phys. Rev. E.*, vol. 58, no. 6, p. 7733, 1998.

[341] V. Kralj-Iglič, H. Hägerstrand, P. Veranič, K. Jezernik, B. Babnik, D. R. Gauger, and A. Iglič, "Amphiphile-induced tubular budding of the bilayer membrane," *Eur. Biophys. J.*, vol. 34, no. 8, pp. 1066–1070, 2005.

[342] L. Mesarec, W. Gozdz, S. Kralj, M. Fosnaric, S. Penic, V. Kralj-Iglic, and A. Iglic, "On the role of external force of actin filaments in the formation of tubular protrusions of closed membrane shapes with anisotropic membrane components," *Eur. Biophys. J.*, vol. 46, no. 8, pp. 705–718, 2017.

[343] I. Derényi, F. Jülicher, and J. Prost, "Formation and interaction of membrane tubes," *Physical review letters*, vol. 88, no. 23, p. 238101, 2002.

[344] M. Fosnaric, S. Penic, A. Iglic, V. Kralj-Iglic, M. Drab, and N. Gov, "Theoretical study of vesicle shapes driven by coupling curved proteins and active cytoskeletal forces," *arXiv preprint arXiv:1812.01460*, 2018.

[345] R. R. Molina, S. Liese, H. Alimohamadi, P. Rangamani, and A. Carlson, "Diffuso-kinetic membrane budding dynamics," *Soft matter*, vol. 16, no. 48, pp. 10889–10899, 2020.

[346] M. D. Kolba, W. Dudka, M. Zareba-Koziol, A. Kominek, P. Ronchi, L. Turos, J. Wlodarczyk, Y. Schwab, D. Cysewski, K. Srpan, *et al.*, "Tunneling nanotubes contribute to the stroma-mediated imatinib resistance of leukemic cells," *bioRxiv*, p. 425041, 2018.

[347] A. Marki, E. Gutierrez, Z. Mikulski, A. Groisman, and K. Ley, "Microfluidics-based side view flow chamber reveals tether-to-sling transition in rolling neutrophils," *Sci. Rep.*, vol. 6, p. 28870, 2016.

[348] K. Gousset, E. Schiff, C. Langevin, Z. Marijanovic, A. Caputo, D. T. Browman, N. Chenouard, F. De Chaumont, A. Martino, J. Enninga, *et al.*, "Prions hijack tunnelling nanotubes for intercellular spread," *Nat. Cell Biol.y*, vol. 11, no. 3, p. 328, 2009.

[349] T. Belay, C. I. Kim, and P. Schiavone, "Bud formation of lipid membranes in response to the surface diffusion of transmembrane proteins and line tension," *Math. Mech. Solids.*, p. 1081286516657684, 2016.

[350] B. Alberts, *Molecular biology of the cell*. Garland science, 2017.

[351] S. E. Miller, S. Mathiasen, N. A. Bright, F. Pierre, B. T. Kelly, N. Kladt, A. Schauss, C. J. Merrifield, D. Stamou, S. Höning, *et al.*, "Calm regulates clathrin-coated vesicle size and maturation by directly sensing and driving membrane curvature," *Developmental cell*, vol. 33, no. 2, pp. 163–175, 2015.

[352] W. Rawicz, K. Olbrich, T. McIntosh, D. Needham, and E. Evans, "Effect of chain length and unsaturation on elasticity of lipid bilayers," *Biophysical journal*, vol. 79, no. 1, pp. 328–339, 2000.

[353] D. J. Steigmann, "Mechanics and physics of lipid bilayers," in *The Role of Mechanics in the Study of Lipid Bilayers*, pp. 1–61, Springer, 2018.

[354] A. Callan-Jones, M. Durand, and J.-B. Fournier, "Hydrodynamics of bilayer membranes with diffusing transmembrane proteins," *Soft matter*, vol. 12, no. 6, pp. 1791–1800, 2016.

[355] P. Wiggins and R. Phillips, "Membrane-protein interactions in mechanosensitive channels," *Biophys. J.*, vol. 88, no. 2, pp. 880–902, 2005.

[356] S. Leibler and D. Andelman, "Ordered and curved meso-structures in membranes and amphiphilic films," *Journal de physique*, vol. 48, no. 11, pp. 2013–2018, 1987.

[357] J. W. Cahn and J. E. Hilliard, "Free energy of a nonuniform system. i. interfacial free energy," *The Journal of chemical physics*, vol. 28, no. 2, pp. 258–267, 1958.

[358] M. Mercker, M. Ptashnyk, J. Kühnle, D. Hartmann, M. Weiss, and W. Jäger, "A multiscale approach to curvature modulated sorting in biological membranes," *Journal of theoretical biology*, vol. 301, pp. 67–82, 2012.

[359] E. L. Elson, E. Fried, J. E. Dolbow, and G. M. Genin, "Phase separation in biological membranes: integration of theory and experiment," *Annual review of biophysics*, vol. 39, pp. 207–226, 2010.

[360] M. Mercker, A. Marciniak-Czochra, T. Richter, and D. Hartmann, "Modeling and computing of deformation dynamics of inhomogeneous biological surfaces," *SIAM Journal on Applied Mathematics*, vol. 73, no. 5, pp. 1768–1792, 2013.

[361] M. Karlsson, M. Davidson, R. Karlsson, A. Karlsson, J. Bergenholtz, Z. Konkoli, A. Jesorka, T. Lobovkina, J. Hurtig, M. Voinova, *et al.*, "Biomimetic nanoscale reactors and networks," *Annu. Rev. Phys. Chem.*, vol. 55, pp. 613–649, 2004.

[362] B. Bauer, M. Davidson, and O. Orwar, "Direct reconstitution of plasma membrane lipids and proteins in nanotube- vesicle networks," *Langmuir*, vol. 22, no. 22, pp. 9329–9332, 2006.

[363] D. Kabaso, N. Bobrovska, W. Gozdz, E. Gongadze, V. Kralj-Iglic, R. Zorec, and A. Iglic, "The transport along membrane nanotubes driven by the spontaneous curvature of membrane components," *Bioelectrochemistry*, vol. 87, pp. 204–210, 2012.

[364] H. Hagerstrand, L. Mrowczynska, U. Salzer, R. Prohaska, K. A. Michelsen, V. Kralj-Iglic, and A. Iglic, "Curvature-dependent lateral distribution of raft markers in the human erythrocyte membrane," *Mol. Membr. Biol.*, vol. 23, no. 3, pp. 277–288, 2006.

[365] D. Andelman, T. Kawakatsu, and K. Kawasaki, "Equilibrium shape of two-component unilamellar membranes and vesicles," *EPL (Europhysics Letters)*, vol. 19, no. 1, p. 57, 1992.

[366] K. De Haas, C. Blom, D. Van den Ende, M. H. Duits, and J. Mellema, "Deformation of giant lipid bilayer vesicles in shear flow," *Physical Review E*, vol. 56, no. 6, p. 7132, 1997.

[367] R. Dimova, "Recent developments in the field of bending rigidity measurements on membranes," *Advances in colloid and interface science*, vol. 208, pp. 225–234, 2014.

[368] J. Dai, M. P. Sheetz, X. Wan, and C. E. Morris, "Membrane tension in swelling and shrinking molluscan neurons," *Journal of Neuroscience*, vol. 18, no. 17, pp. 6681–6692, 1998.

[369] A. J. Laude and I. A. Prior, "Plasma membrane microdomains: organization, function and trafficking," *Mol. Membr. Biol.*, vol. 21, no. 3, pp. 193–205, 2004.

[370] S. Dmitrieff and F. Nédélec, "Membrane mechanics of endocytosis in cells with turgor," *PLoS computational biology*, vol. 11, no. 10, p. e1004538, 2015.

[371] S. Ramadurai, A. Holt, V. Krasnikov, G. van den Bogaart, J. A. Killian, and B. Poolman, "Lateral diffusion of membrane proteins," *J. Am. Chem. Soc.*, vol. 131, no. 35, pp. 12650–12656, 2009.

[372] M. E. Kurczy, L. J. Mellander, N. Najafinobar, and A.-S. Cans, "Composition based strategies for controlling radii in lipid nanotubes," *Plos One*, vol. 9, no. 1, p. e81293, 2014.

[373] D. Brown and E. London, "Functions of lipid rafts in biological membranes," *Annu. Rev. Cell Dev. Biol.*, vol. 14, no. 1, pp. 111–136, 1998.

[374] A. Diz-Muñoz, D. A. Fletcher, and O. D. Weiner, "Use the force: membrane tension as an organizer of cell shape and motility," *Trends in cell biology*, vol. 23, no. 2, pp. 47–53, 2013.

[375] A. Rouvinski, S. Karniely, M. Kounin, S. Moussa, M. D. Goldberg, G. Warburg, R. Lyakhovetsky, D. Papy-Garcia, J. Kutzsche, C. Korth, *et al.*, "Live imaging of prions reveals nascent prpsc in cell-surface, raft-associated amyloid strings and webs," *J Cell Biol*, vol. 204, no. 3, pp. 423–441, 2014.

[376] R. Shlomovitz and N. Gov, "Membrane-mediated interactions drive the condensation and coalescence of ftsz rings," *Phys. Biol.*, vol. 6, no. 4, p. 046017, 2009.

[377] G. Golani, N. Ariotti, R. G. Parton, and M. M. Kozlov, "Membrane curvature and tension control the formation and collapse of caveolar superstructures," *Dev. Cell*, 2019.

[378] J. Adam, N. Basnet, and N. Mizuno, "Structural insights into the cooperative remodeling of membranes by amphiphysin/bin1," *Sci. Rep.*, vol. 5, p. 15452, 2015.

[379] M. Daniel, J. Řezníčková, M. Handl, A. Iglič, and V. Kralj-Iglič, "Clustering and separation of hydrophobic nanoparticles in lipid bilayer explained by membrane mechanics," *Sci. Rep.*, vol. 8, 2018.

[380] M. R. Rasch, E. Rossinyol, J. L. Hueso, B. W. Goodfellow, J. Arbiol, and B. A. Korgel, "Hydrophobic gold nanoparticle self-assembly with phosphatidylcholine lipid: membrane-loaded and janus vesicles," *Nano letters*, vol. 10, no. 9, pp. 3733–3739, 2010.

[381] P. Angelikopoulos, L. Sarkisov, Z. Cournia, and P. Gkeka, "Self-assembly of anionic, ligand-coated nanoparticles in lipid membranes," *Nanoscale*, vol. 9, no. 3, pp. 1040–1048, 2017.

[382] Y. Li, R. Lipowsky, and R. Dimova, "Membrane nanotubes induced by aqueous phase separation and stabilized by spontaneous curvature," *Proceedings of the National Academy of Sciences*, vol. 108, no. 12, pp. 4731–4736, 2011.

[383] M. Goulian, "Inclusions in membranes," *Current Opinion in Colloid & Interface Science*, vol. 3, no. 1, pp. 358–361, 1996.

[384] K. Bohinc, V. Kralj-Iglič, and S. May, "Interaction between two cylindrical inclusions in a symmetric lipid bilayer," *The Journal of chemical physics*, vol. 119, no. 14, pp. 7435–7444, 2003.

[385] B. J. Reynwar and M. Deserno, "Membrane-mediated interactions between circular particles in the strongly curved regime," *Soft Matter*, vol. 7, no. 18, pp. 8567–8575, 2011.

[386] C. Yolcu and M. Deserno, "Membrane-mediated interactions between rigid inclusions: an effective field theory," *Physical Review E*, vol. 86, no. 3, p. 031906, 2012.

[387] C. Nielsen and O. S. Andersen, "Inclusion-induced bilayer deformations: effects of monolayer equilibrium curvature," *Biophysical Journal*, vol. 79, no. 5, pp. 2583–2604, 2000.

[388] J. H. Ipsen, T. Gil, O. G. Mouritsen, M. C. Sabra, M. M. Sperotto, and M. J. Zuckermann, "Theoretical analysis of protein organizationin lipid membranes," *BBA General Subjects*, vol. 1376, pp. 245–266, 1998.

[389] M. Simunovic and G. A. Voth, "Membrane tension controls the assembly of curvature-generating proteins," *Nature communications*, vol. 6, 2015.

[390] A.-F. Bitbol, P. G. Dommersnes, and J.-B. Fournier, "Fluctuations of the casimir-like force between two membrane inclusions," *Physical Review E*, vol. 81, no. 5, p. 050903, 2010.

[391] E. Atilgan and B. Ovryn, "Nucleation and growth of integrin adhesions," *Biophys. J.*, vol. 96, no. 9, pp. 3555–3572, 2009.

[392] T. R. Weikl, J. Hu, G.-K. Xu, and R. Lipowsky, "Binding equilibrium and kinetics of membrane-anchored receptors and ligands in cell adhesion: Insights from computational model systems and theory," *Cell. Adhes. Migr*, vol. 10, no. 5, pp. 576–589, 2016.

[393] G. K. Atkin-Smith and I. K. Poon, "Disassembly of the dying: mechanisms and functions," *Trends in cell biology*, vol. 27, no. 2, pp. 151–162, 2017.

[394] R. R. Daga and F. Chang, "Dynamic positioning of the fission yeast cell division plane," *Proc. Natl. Acad. Sci.*, vol. 102, no. 23, pp. 8228–8232, 2005.

[395] F. R. Maxfield, "Plasma membrane microdomains," *Curr. Opin. Cell. Biol.*, vol. 14, no. 4, pp. 483–487, 2002.

[396] E. Delage, D. C. Cervantes, E. Penard, C. Schmitt, S. Syan, A. Disanza, G. Scita, and C. Zurzolo, "Differential identity of filopodia and tunneling nanotubes revealed by the opposite functions of actin regulatory complexes," *Sci. Rep.*, vol. 6, p. 39632, 2016.

[397] M. Diez-Silva, M. Dao, J. Han, C.-T. Lim, and S. Suresh, "Shape and biomechanical characteristics of human red blood cells in health and disease," *MRS bulletin*, vol. 35, no. 5, pp. 382–388, 2010.

[398] F. Bronner, *Cell shape: determinants, regulation, and regulatory role*. Elsevier, 2012.

[399] S. Chien, "Red cell deformability and its relevance to blood flow," *Annual review of physiology*, vol. 49, no. 1, pp. 177–192, 1987.

[400] L. Da Costa, J. Galimand, O. Fenneteau, and N. Mohandas, "Hereditary spherocytosis, elliptocytosis, and other red cell membrane disorders," *Blood reviews*, vol. 27, no. 4, pp. 167–178, 2013.

[401] G. J. Kato, M. H. Steinberg, and M. T. Gladwin, "Intravascular hemolysis and the pathophysiology of sickle cell disease," *The Journal of clinical investigation*, vol. 127, no. 3, pp. 750–760, 2017.

[402] B. M. Cooke, N. Mohandas, and R. L. Coppel, "The malaria-infected red blood cell: structural and functional changes," 2001.

[403] E. S. Zuccala and J. Baum, "Cytoskeletal and membrane remodelling during malaria parasite invasion of the human erythrocyte," *British journal of haematology*, vol. 154, no. 6, pp. 680–689, 2011.

[404] W. Gratzer, "The red cell membrane and its cytoskeleton," *Biochemical Journal*, vol. 198, no. 1, pp. 1–8, 1981.

[405] R. B. Nowak, H. Alimohamadi, K. Pestonjamasp, P. Rangamani, and V. M. Fowler, "Nanoscale organization of actin filaments in the red blood cell membrane skeleton," *bioRxiv*, 2021.

[406] D. S. Gokhin and V. M. Fowler, "Feisty filaments: actin dynamics in the red blood cell membrane skeleton," *Current opinion in hematology*, vol. 23, no. 3, p. 206, 2016.

[407] D. E. Discher, "New insights into erythrocyte membrane organization and microelasticity," *Current opinion in hematology*, vol. 7, no. 2, pp. 117–122, 2000.

[408] H. Deuling and W. Helfrich, "The curvature elasticity of fluid membranes: a catalogue of vesicle shapes," *Journal de Physique*, vol. 37, no. 11, pp. 1335–1345, 1976.

[409] H. Deuling and W. Helfrich, "Red blood cell shapes as explained on the basis of curvature elasticity," *Biophysical journal*, vol. 16, no. 8, pp. 861–868, 1976.

[410] A. Iglič, V. Kralj-Iglič, and H. Hägerstrand, "Amphiphile induced echinocyte-spheroechinocyte transformation of red blood cell shape," *European Biophysics Journal*, vol. 27, no. 4, pp. 335–339, 1998.

[411] V. Markin, "Lateral organization of membranes and cell shapes," *Biophysical journal*, vol. 36, no. 1, pp. 1–19, 1981.

[412] S. Leibler, "Curvature instability in membranes," *Journal de Physique*, vol. 47, no. 3, pp. 507–516, 1986.

[413] A. Iglič, M. Fošnarič, H. Hägerstrand, and V. Kralj-Iglič, "Coupling between vesicle shape and the non-homogeneous lateral distribution of membrane constituents in golgi bodies," *FEBS letters*, vol. 574, no. 1-3, pp. 9–12, 2004.

[414] M. Tachikawa and A. Mochizuki, "Golgi apparatus self-organizes into the characteristic shape via postmitotic reassembly dynamics," *Proceedings of the National Academy of Sciences*, vol. 114, no. 20, pp. 5177–5182, 2017.

[415] M. Fošnarič, S. Penič, A. Iglič, V. Kralj-Iglič, M. Drab, and N. S. Gov, "Theoretical study of vesicle shapes driven by coupling curved proteins and active cytoskeletal forces," *Soft Matter*, vol. 15, no. 26, pp. 5319–5330, 2019.

[416] Z. Peng, X. Li, I. V. Pivkin, M. Dao, G. E. Karniadakis, and S. Suresh, "Lipid bilayer and cytoskeletal interactions in a red blood cell," *Proceedings of the National Academy of Sciences*, vol. 110, no. 33, pp. 13356–13361, 2013.

[417] Y. Park, C. A. Best, T. Auth, N. S. Gov, S. A. Safran, G. Popescu, S. Suresh, and M. S. Feld, "Metabolic remodeling of the human red blood cell membrane," *Proceedings of the National Academy of Sciences*, vol. 107, no. 4, pp. 1289–1294, 2010.

[418] J. Li, G. Lykotrafitis, M. Dao, and S. Suresh, "Cytoskeletal dynamics of human erythrocyte," *Proceedings of the National Academy of Sciences*, vol. 104, no. 12, pp. 4937–4942, 2007.

[419] A. Iglič, "A possible mechanism determining the stability of spiculated red blood cells," *Journal of biomechanics*, vol. 30, no. 1, pp. 35–40, 1997.

[420] V. M. Fowler, J. Q. Davis, and V. Bennett, "Human erythrocyte myosin: identification and purification.," *The Journal of cell biology*, vol. 100, no. 1, pp. 47–55, 1985.

[421] A. J. Wong, D. P. Kiehart, and T. D. Pollard, "Myosin from human erythrocytes.," *Journal of Biological Chemistry*, vol. 260, no. 1, pp. 46–49, 1985.

[422] M. Higashihara, D. J. Hartshorne, R. Craig, and M. Ikebe, "Correlation of enzymic properties and conformation of bovine erythrocyte myosin," *Biochemistry*, vol. 28, no. 4, pp. 1642–1649, 1989.

[423] J. T. Jenkins, "The equations of mechanical equilibrium of a model membrane," *SIAM Journal on Applied Mathematics*, vol. 32, no. 4, pp. 755–764, 1977.

[424] B. K. Pai and H. D. Weymann, "Equilibrium shapes of red blood cells in osmotic swelling," *Journal of biomechanics*, vol. 13, no. 2, pp. 105–112, 1980.

[425] G. Lim HW, M. Wortis, and R. Mukhopadhyay, "Red blood cell shapes and shape transformations: newtonian mechanics of a composite membrane: sections 2.1–2.4," *Soft Matter: Lipid Bilayers and Red Blood Cells*, vol. 4, pp. 83–139, 2008.

[426] N. Mohandas and J. Chasis, "Red blood cell deformability, membrane material properties and shape: regulation by transmembrane, skeletal and cytosolic proteins and lipids.," in *Seminars in hematology*, vol. 30, pp. 171–192, 1993.

[427] Y. Fung and P. Tong, "Theory of the sphering of red blood cells," *Biophysical journal*, vol. 8, no. 2, pp. 175–198, 1968.

[428] H. Park, S. Lee, M. Ji, K. Kim, Y. Son, S. Jang, and Y. Park, "Measuring cell surface area and deformability of individual human red blood cells over blood storage using quantitative phase imaging," *Scientific reports*, vol. 6, p. 34257, 2016.

[429] J. C. Luke, "A method for the calculation of vesicle shapes," *SIAM Journal on Applied Mathematics*, vol. 42, no. 2, pp. 333–345, 1982.

[430] R. P. Rand and A. Burton, "Mechanical properties of the red cell membrane: I. membrane stiffness and intracellular pressure," *Biophysical journal*, vol. 4, no. 2, pp. 115–135, 1964.

[431] P. Canham and A. C. Burton, "Distribution of size and shape in populations of normal human red cells," *Circulation research*, vol. 22, no. 3, pp. 405–422, 1968.

[432] S. Chien, S. Usami, R. J. Dellenback, and C. A. Bryant, "Comparative hemorheology—hematological implications of species differences in blood viscosity," *Biorheology*, vol. 8, no. 1, pp. 35–57, 1971.

[433] E. Evans and Y.-C. Fung, "Improved measurements of the erythrocyte geometry," *Microvascular research*, vol. 4, no. 4, pp. 335–347, 1972.

[434] Y. Fung, W. C. Tsang, and P. Patitucci, "High-resolution data on the geometry of red blood cells," *Biorheology*, vol. 18, no. 3-6, pp. 369–385, 1981.

[435] G. V. Richieri, S. P. Akeson, and H. C. Mel, "Measurement of biophysical properties of red blood cells by resistance pulse spectroscopy: volume, shape, surface area, and deformability," *Journal of biochemical and biophysical methods*, vol. 11, no. 2-3, pp. 117–131, 1985.

[436] O. Linderkamp, E. Friederichs, and H. J. Meiselman, "Mechanical and geometrical properties of density-separated neonatal and adult erythrocytes," *Pediatric research*, vol. 34, no. 5, pp. 688–693, 1993.

[437] K. G. Engström and H. J. Meiselman, "Optical and mathematical corrections of micropipette measurements of red blood cell geometry during anisotonic perifusion," *Cytometry: The Journal of the International Society for Analytical Cytology*, vol. 17, no. 4, pp. 279–286, 1994.

[438] D. Tycko, M. Metz, E. Epstein, and A. Grinbaum, "Flow-cytometric light scattering measurement of red blood cell volume and hemoglobin concentration," *Applied optics*, vol. 24, no. 9, pp. 1355–1365, 1985.

[439] P. Tarasov, M. Yurkin, P. Avrorov, K. Semyanov, A. Hoekstra, and V. Maltsev, "Optics of erythrocytes," in *Optics of Biological Particles*, pp. 243–259, Springer, 2007.

[440] Ö. Ergül, A. Arslan-Ergül, and L. Gürel, "Computational study of scattering from healthy and diseased red blood cells," *Journal of biomedical optics*, vol. 15, no. 4, p. 045004, 2010.

[441] M. Das, B. Das, A. Das, I. Chatterjee, and D. Majumder, "Computational analysis of ultrastructural images of red blood cells," *Journal of Oncology Translational Research*, vol. 1, no. 1, p. 103, 2015.

[442] H. FUNAKI, "Contributions on the shapes of red blood corpuscles," *The Japanese journal of physiology*, vol. 5, pp. 81–92, 1955.

[443] P. W. Kuchel and E. D. Fackerell, "Parametric-equation representation of biconcave erythrocytes," *Bulletin of mathematical biology*, vol. 61, no. 2, pp. 209–220, 1999.

[444] M. A. Yurkin *et al.*, *Discrete dipole simulations of light scattering by blood cells*. Universiteit van Amsterdam [Host], 2007.

[445] A. G. Borovoi, E. I. Naats, and U. G. Oppel, "Scattering of light by a red blood cell," *Journal of biomedical optics*, vol. 3, no. 3, pp. 364–373, 1998.

[446] L. Bi and P. Yang, "Modeling of light scattering by biconcave and deformed red blood cells with the invariant imbedding t-matrix method," *Journal of biomedical optics*, vol. 18, no. 5, p. 055001, 2013.

[447] M. A. Yurkin, K. A. Semyanov, P. A. Tarasov, A. V. Chernyshev, A. G. Hoekstra, and V. P. Maltsev, "Experimental and theoretical study of light scattering by individual mature red blood cells by use of scanning flow cytometry and a discrete dipole approximation," *Applied Optics*, vol. 44, no. 25, pp. 5249–5256, 2005.

[448] J. Lyu, P. G. Chen, G. Boedec, M. Leonetti, and M. Jaeger, "Hybrid continuum–coarse-grained modeling of erythrocytes," *Comptes Rendus Mécanique*, vol. 346, no. 6, pp. 439–448, 2018.

[449] E. A. Evans, *Mechanics and thermodynamics of biomembranes*. CRC press, 2018.

[450] A. H. Lewis and J. Grandl, "Mechanical sensitivity of piezo1 ion channels can be tuned by cellular membrane tension," *Elife*, vol. 4, p. e12088, 2015.

[451] J. Evans, W. Gratzer, N. Mohandas, K. Parker, and J. Sleep, "Fluctuations of the red blood cell membrane: relation to mechanical properties and lack of atp dependence," *Biophysical journal*, vol. 94, no. 10, pp. 4134–4144, 2008.

[452] J. Huff, "The airyscan detector from zeiss: confocal imaging with improved signal-to-noise ratio and super-resolution," *Nature methods*, vol. 12, no. 12, pp. i–ii, 2015.

[453] G. Popescu, T. Ikeda, K. Goda, C. A. Best-Popescu, M. Laposata, S. Manley, R. R. Dasari, K. Badizadegan, and M. S. Feld, "Optical measurement of cell membrane tension," *Physical review letters*, vol. 97, no. 21, p. 218101, 2006.

[454] J. Molloy, J. Burns, J. Kendrick-Jones, R. Tregear, and D. White, "Movement and force produced by a single myosin head," *Nature*, vol. 378, no. 6553, pp. 209–212, 1995.

[455] D. Hodgkin and J. J. Lister, "Xxvi. notice of some miscroscopic observations of the blood and animal tissues," *The Philosophical Magazine*, vol. 2, no. 8, pp. 130–138, 1827.

[456] N. Gov and S. Safran, "Red blood cell membrane fluctuations and shape controlled by atp-induced cytoskeletal defects," *Biophysical journal*, vol. 88, no. 3, pp. 1859–1874, 2005.

[457] L. Mesarec, W. Góźdź, A. Iglič, V. Kralj-Iglič, E. Virga, and S. Kralj, "Normal red blood cells' shape stabilized by membrane's in-plane ordering," *Scientific reports*, vol. 9, no. 1, pp. 1–11, 2019.

[458] A. Colom, E. Derivery, S. Soleimanpour, C. Tomba, M. Dal Molin, N. Sakai, M. González-Gaitán, S. Matile, and A. Roux, "A fluorescent membrane tension probe," *Nature chemistry*, vol. 10, no. 11, p. 1118, 2018.

[459] G. Lan and S. X. Sun, "Dynamics of myosin-driven skeletal muscle contraction: I. steady-state force generation," *Biophysical Journal*, vol. 88, no. 6, pp. 4107–4117, 2005.

[460] F. Jähnig, "What is the surface tension of a lipid bilayer membrane?," *Biophysical journal*, vol. 71, no. 3, p. 1348, 1996.

[461] M. Sheetz, "Membrane skeletal dynamics: role in modulation of red cell deformability, mobility of transmembrane proteins, and shape.," in *Seminars in hematology*, vol. 20, pp. 175–188, 1983.

[462] M. F. Norstrom, P. A. Smithback, and R. S. Rock, "Unconventional processive mechanics of non-muscle myosin iib," *Journal of Biological Chemistry*, vol. 285, no. 34, pp. 26326–26334, 2010.

[463] N. Hundt, W. Steffen, S. Pathan-Chhatbar, M. H. Taft, and D. J. Manstein, "Load-dependent modulation of non-muscle myosin-2a function by tropomyosin 4.2," *Scientific reports*, vol. 6, no. 1, pp. 1–12, 2016.

[464] J. F. Hoffman, "Biconcave shape of human red-blood-cell ghosts relies on density differences between the rim and dimple of the ghost's plasma membrane," *Proceedings of the National Academy of Sciences*, vol. 113, no. 51, pp. 14847–14851, 2016.

[465] S. Svetina, T. Š. Kebe, and B. Božič, "A model of piezo1-based regulation of red blood cell volume," *Biophysical journal*, vol. 116, no. 1, pp. 151–164, 2019.

[466] B. Kaoui, G. Biros, and C. Misbah, "Why do red blood cells have asymmetric shapes even in a symmetric flow?," *Physical review letters*, vol. 103, no. 18, p. 188101, 2009.

[467] S. Svetina, G. Kokot, T. Š. Kebe, B. Žekš, and R. E. Waugh, "A novel strain energy relationship for red blood cell membrane skeleton based on spectrin stiffness and its application to micropipette deformation," *Biomechanics and modeling in mechanobiology*, vol. 15, no. 3, pp. 745–758, 2016.

[468] A. Iglic, S. Svetina, and B. Zeks, "Depletion of membrane skeleton in red blood cell vesicles," *Biophysical journal*, vol. 69, no. 1, pp. 274–279, 1995.

[469] E. J. Spangler, C. W. Harvey, J. D. Revalee, P. S. Kumar, and M. Laradji, "Computer simulation of cytoskeleton-induced blebbing in lipid membranes," *Physical Review E*, vol. 84, no. 5, p. 051906, 2011.

[470] H. Hägerstrand, V. Kralj-Iglič, M. Bobrowska-Hägerstrand, and A. Iglič, "Membrane skeleton detachment in spherical and cylindrical microexovesicles," *Bulletin of mathematical biology*, vol. 61, no. 6, pp. 1019–1030, 1999.

[471] A. Goujon, A. Colom, K. Strakova, V. Mercier, D. Mahecic, S. Manley, N. Sakai, A. Roux, and S. Matile, "Mechanosensitive fluorescent probes to image membrane tension in mitochondria, endoplasmic reticulum, and lysosomes," *Journal of the American Chemical Society*, vol. 141, no. 8, pp. 3380–3384, 2019.

[472] J. Nishiyama, "Plasticity of dendritic spines: Molecular function and dysfunction in neurodevelopmental disorders," *Psychiatry and Clinical Neurosciences*, 2019.

[473] Y. Nakahata and R. Yasuda, "Plasticity of spine structure: local signaling, translation and cytoskeletal reorganization," *Frontiers in synaptic neuroscience*, vol. 10, p. 29, 2018.

[474] M. Bosch and Y. Hayashi, "Structural plasticity of dendritic spines," *Current opinion in neurobiology*, vol. 22, no. 3, pp. 383–388, 2012.

[475] E. G. Gray, "Electron microscopy of synaptic contacts on dendrite spines of the cerebral cortex," *Nature*, vol. 183, no. 4675, pp. 1592–1593, 1959.

[476] G. M. Shepherd, "The dendritic spine: a multifunctional integrative unit," *Journal of neurophysiology*, vol. 75, no. 6, pp. 2197–2210, 1996.

[477] K. M. Harris and S. Kater, "Dendritic spines: cellular specializations imparting both stability and flexibility to synaptic function," *Annual review of neuroscience*, vol. 17, no. 1, pp. 341–371, 1994.

[478] J. I. Arellano, R. Benavides-Piccione, J. DeFelipe, and R. Yuste, "Ultrastructure of dendritic spines: correlation between synaptic and spine morphologies," *Frontiers in neuroscience*, vol. 1, p. 10, 2007.

[479] M. Patterson and R. Yasuda, "Signalling pathways underlying structural plasticity of dendritic spines," *British journal of pharmacology*, vol. 163, no. 8, pp. 1626–1638, 2011.

[480] F. Engert and T. Bonhoeffer, "Dendritic spine changes associated with hippocampal long-term synaptic plasticity," *Nature*, vol. 399, no. 6731, p. 66, 1999.

[481] M. F. Bear and R. C. Malenka, "Synaptic plasticity: Ltp and ltd," *Current opinion in neurobiology*, vol. 4, no. 3, pp. 389–399, 1994.

[482] K. M. Harris, J. C. Fiala, and L. Ostroff, "Structural changes at dendritic spine synapses during long-term potentiation," *Philosophical Transactions of the Royal Society of London. Series B: Biological Sciences*, vol. 358, no. 1432, pp. 745–748, 2003.

[483] K. M. Harris, "Structure, development, and plasticity of dendritic spines," *Current opinion in neurobiology*, vol. 9, no. 3, pp. 343–348, 1999.

[484] L. E. Ostroff, J. C. Fiala, B. Allwardt, and K. M. Harris, "Polyribosomes redistribute from dendritic shafts into spines with enlarged synapses during ltp in developing rat hippocampal slices," *Neuron*, vol. 35, no. 3, pp. 535–545, 2002.

[485] L. J. Petrak, K. M. Harris, and S. A. Kirov, "Synaptogenesis on mature hippocampal dendrites occurs via filopodia and immature spines during blocked synaptic transmission," *Journal of Comparative Neurology*, vol. 484, no. 2, pp. 183–190, 2005.

[486] E. Fifkova, "A possible mechanism of morphometric changes in dendritic spines induced by stimulation," *Cellular and molecular neurobiology*, vol. 5, no. 1-2, pp. 47–63, 1985.

[487] B. Calabrese, M. S. Wilson, and S. Halpain, "Development and regulation of dendritic spine synapses," *Physiology*, vol. 21, no. 1, pp. 38–47, 2006.

[488] A. Peters and I. R. Kaiserman-Abramof, "The small pyramidal neuron of the rat cerebral cortex. the perikaryon, dendrites and spines," *American Journal of Anatomy*, vol. 127, no. 4, pp. 321–355, 1970.

[489] J. C. Fiala, M. Feinberg, V. Popov, and K. M. Harris, "Synaptogenesis via dendritic filopodia in developing hippocampal area ca1," *Journal of Neuroscience*, vol. 18, no. 21, pp. 8900–8911, 1998.

[490] A. J. Holtmaat, J. T. Trachtenberg, L. Wilbrecht, G. M. Shepherd, X. Zhang, G. W. Knott, and K. Svoboda, "Transient and persistent dendritic spines in the neocortex in vivo," *Neuron*, vol. 45, no. 2, pp. 279–291, 2005.

[491] Y. Zuo, A. Lin, P. Chang, and W.-B. Gan, "Development of long-term dendritic spine stability in diverse regions of cerebral cortex," *Neuron*, vol. 46, no. 2, pp. 181–189, 2005.

[492] H. Kasai, M. Matsuzaki, J. Noguchi, N. Yasumatsu, and H. Nakahara, "Structure–stability–function relationships of dendritic spines," *Trends in neurosciences*, vol. 26, no. 7, pp. 360–368, 2003.

[493] J. Bourne and K. M. Harris, "Do thin spines learn to be mushroom spines that remember?," *Current opinion in neurobiology*, vol. 17, no. 3, pp. 381–386, 2007.

[494] K. P. Berry and E. Nedivi, "Spine dynamics: are they all the same?," *Neuron*, vol. 96, no. 1, pp. 43–55, 2017.

[495] J. Grutzendler, N. Kasthuri, and W.-B. Gan, "Long-term dendritic spine stability in the adult cortex," *Nature*, vol. 420, no. 6917, pp. 812–816, 2002.

[496] J. T. Trachtenberg, B. E. Chen, G. W. Knott, G. Feng, J. R. Sanes, E. Welker, and K. Svoboda, "Long-term in vivo imaging of experience-dependent synaptic plasticity in adult cortex," *Nature*, vol. 420, no. 6917, pp. 788–794, 2002.

[497] M. Matsuzaki, G. C. Ellis-Davies, T. Nemoto, Y. Miyashita, M. Iino, and H. Kasai, "Dendritic spine geometry is critical for ampa receptor expression in hippocampal ca1 pyramidal neurons," *Nature neuroscience*, vol. 4, no. 11, p. 1086, 2001.

[498] O. Ganeshina, R. Berry, R. Petralia, D. Nicholson, and Y. Geinisman, "Synapses with a segmented, completely partitioned postsynaptic density express more ampa receptors than other axospinous synaptic junctions," *Neuroscience*, vol. 125, no. 3, pp. 615–623, 2004.

[499] M. C. Ashby, S. R. Maier, A. Nishimune, and J. M. Henley, "Lateral diffusion drives constitutive exchange of ampa receptors at dendritic spines and is regulated by spine morphology," *Journal of Neuroscience*, vol. 26, no. 26, pp. 7046–7055, 2006.

[500] R. Yuste and T. Bonhoeffer, "Genesis of dendritic spines: insights from ultrastructural and imaging studies," *Nature Reviews Neuroscience*, vol. 5, no. 1, p. 24, 2004.

[501] M. E. Dailey and S. J. Smith, "The dynamics of dendritic structure in developing hippocampal slices," *Journal of neuroscience*, vol. 16, no. 9, pp. 2983–2994, 1996.

[502] M. Miller and A. Peters, "Maturation of rat visual cortex. ii. a combined golgi-electron microscope study of pyramidal neurons," *Journal of Comparative Neurology*, vol. 203, no. 4, pp. 555–573, 1981.

[503] N. E. Ziv and S. J. Smith, "Evidence for a role of dendritic filopodia in synaptogenesis and spine formation," *Neuron*, vol. 17, no. 1, pp. 91–102, 1996.

[504] A. J. Koleske, "Molecular mechanisms of dendrite stability," *Nature Reviews Neuroscience*, vol. 14, no. 8, pp. 536–550, 2013.

[505] E. Bertling and P. Hotulainen, "New waves in dendritic spine actin cytoskeleton: From branches and bundles to rings, from actin binding proteins to post-translational modifications," *Molecular and Cellular Neuroscience*, vol. 84, pp. 77–84, 2017.

[506] D. Landis and T. S. Reese, "Cytoplasmic organization in cerebellar dendritic spines.," *The Journal of cell biology*, vol. 97, no. 4, pp. 1169–1178, 1983.

[507] C. S. Peskin, G. M. Odell, and G. F. Oster, "Cellular motions and thermal fluctuations: the brownian ratchet," *Biophysical journal*, vol. 65, no. 1, pp. 316–324, 1993.

[508] A. Mogilner and G. Oster, "Cell motility driven by actin polymerization," *Biophysical journal*, vol. 71, no. 6, pp. 3030–3045, 1996.

[509] C. Miermans, R. Kusters, C. Hoogenraad, and C. Storm, "Biophysical model of the role of actin remodeling on dendritic spine morphology," *PloS one*, vol. 12, no. 2, p. e0170113, 2017.

[510] N. A. Frost, H. Shroff, H. Kong, E. Betzig, and T. A. Blanpied, "Single-molecule discrimination of discrete perisynaptic and distributed sites of actin filament assembly within dendritic spines," *Neuron*, vol. 67, no. 1, pp. 86–99, 2010.

[511] M. Bucher, T. Fanutza, and M. Mikhaylova, "Cytoskeletal makeup of the synapse: Shaft versus spine," *Cytoskeleton*, vol. 77, no. 3-4, pp. 55–64, 2020.

[512] N. Honkura, M. Matsuzaki, J. Noguchi, G. C. Ellis-Davies, and H. Kasai, "The subspine organization of actin fibers regulates the structure and plasticity of dendritic spines," *Neuron*, vol. 57, no. 5, pp. 719–729, 2008.

[513] A. R. Huehn, J. P. Bibeau, A. C. Schramm, W. Cao, M. Enrique, and C. V. Sindelar, "Structures of cofilin-induced structural changes reveal local and asymmetric perturbations of actin filaments," *Proceedings of the National Academy of Sciences*, 2020.

[514] P. J. Goldschmidt-Clermont, L. M. Machesky, S. K. Doberstein, and T. D. Pollard, "Mechanism of the interaction of human platelet profilin with actin.," *The Journal of cell biology*, vol. 113, no. 5, pp. 1081–1089, 1991.

[515] K.-I. Okamoto, R. Narayanan, S. H. Lee, K. Murata, and Y. Hayashi, "The role of camkii as an f-actin-bundling protein crucial for maintenance of dendritic spine structure," *Proceedings of the National Academy of Sciences*, vol. 104, no. 15, pp. 6418–6423, 2007.

[516] J. Borovac, M. Bosch, and K. Okamoto, "Regulation of actin dynamics during structural plasticity of dendritic spines: Signaling messengers and actin-binding proteins," *Molecular and Cellular Neuroscience*, 2018.

[517] S. Khan, Y. Zou, A. Amjad, A. Gardezi, C. L. Smith, C. Winters, and T. S. Reese, "Sequestration of camkii in dendritic spines in silico," *Journal of computational neuroscience*, vol. 31, no. 3, pp. 581–594, 2011.

[518] B. Calabrese and S. Halpain, "Essential role for the pkc target marcks in maintaining dendritic spine morphology," *Neuron*, vol. 48, no. 1, pp. 77–90, 2005.

[519] I. Hlushchenko, M. Koskinen, and P. Hotulainen, "Dendritic spine actin dynamics in neuronal maturation and synaptic plasticity," *Cytoskeleton*, vol. 73, no. 9, pp. 435–441, 2016.

[520] J. Saarikangas, N. Kourdougli, Y. Senju, G. Chazal, M. Segerstråle, R. Minkeviciene, J. Kuurne, P. K. Mattila, L. Garrett, S. M. Hölter, *et al.*, "Mim-induced membrane bending promotes dendritic spine initiation," *Developmental cell*, vol. 33, no. 6, pp. 644–659, 2015.

[521] B. R. Carlson, K. E. Lloyd, A. Kruszewski, I.-H. Kim, R. M. Rodriguiz, C. Heindel, M. Faytell, S. M. Dudek, W. C. Wetsel, and S. H. Soderling, "Wrp/srgap3 facilitates the initiation of spine development by an inverse f-bar domain, and its loss impairs long-term memory," *Journal of Neuroscience*, vol. 31, no. 7, pp. 2447–2460, 2011.

[522] M. M. Kessels and B. Qualmann, "Different functional modes of bar domain proteins in formation and plasticity of mammalian postsynapses," *J Cell Sci*, vol. 128, no. 17, pp. 3177–3185, 2015.

[523] Y. Wakita, T. Kakimoto, H. Katoh, and M. Negishi, "The f-bar protein rapostlin regulates dendritic spine formation in hippocampal neurons," *Journal of Biological Chemistry*, vol. 286, no. 37, pp. 32672–32683, 2011.

[524] V. Kralj-Iglič, A. Iglič, H. Hägerstrand, and P. Peterlin, "Stable tubular microexovesicles of the erythrocyte membrane induced by dimeric amphiphiles," *Physical Review E*, vol. 61, no. 4, p. 4230, 2000.

[525] A. Iglič, B. Babnik, K. Bohinc, M. Fošnarič, H. Hägerstrand, and V. Kralj-Iglič, "On the role of anisotropy of membrane constituents in formation of a membrane neck during budding of a multicomponent membrane," *Journal of biomechanics*, vol. 40, no. 3, pp. 579–585, 2007.

[526] A. Iglič, V. Kralj-Iglič, and J. Majhenc, "Cylindrical shapes of closed lipid bilayer structures correspond to an extreme area difference between the two monolayers of the bilayer," *Journal of biomechanics*, vol. 32, no. 12, pp. 1343–1347, 1999.

[527] M. Bonilla-Quintana, F. Wörgötter, C. Tetzlaff, and M. Fauth, "Modeling the shape of synaptic spines by their actin dynamics," *bioRxiv*, p. 817932, 2019.

[528] H. Alimohamadi, B. Ovryn, and P. Rangamani, "Modeling membrane nanotube morphology: the role of heterogeneity in composition and material properties," *Scientific Reports*, vol. 10, no. 1, pp. 1–15, 2020.

[529] E. T. Barfod, A. L. Moore, B. G. Van de Graaf, and S. D. Lidofsky, "Myosin light chain kinase and src control membrane dynamics in volume recovery from cell swelling," *Molecular biology of the cell*, vol. 22, no. 5, pp. 634–650, 2011.

[530] J. Weichsel and P. L. Geissler, "The more the tubular: Dynamic bundling of actin filaments for membrane tube formation," *PLoS computational biology*, vol. 12, no. 7, p. e1004982, 2016.

[531] E. Atilgan, D. Wirtz, and S. X. Sun, "Mechanics and dynamics of actin-driven thin membrane protrusions," *Biophysical journal*, vol. 90, no. 1, pp. 65–76, 2006.

[532] B. Pontes, Y. Ayala, A. C. C. Fonseca, L. F. Romão, R. F. Amaral, L. T. Salgado, F. R. Lima, M. Farina, N. B. Viana, V. Moura-Neto, *et al.*, "Membrane elastic properties and cell function," *PLoS One*, vol. 8, no. 7, p. e67708, 2013.

[533] M. Bonilla-Quintana, F. Wörgötter, C. Tetzlaff, and M. Fauth, "Modeling the shape of synaptic spines by their actin dynamics," *Frontiers in Synaptic Neuroscience*, vol. 12, p. 9, 2020.

[534] G. G. Borisy and T. M. Svitkina, "Actin machinery: pushing the envelope," *Current opinion in cell biology*, vol. 12, no. 1, pp. 104–112, 2000.

[535] M. Saleem, S. Morlot, A. Hohendahl, J. Manzi, M. Lenz, and A. Roux, "A balance between membrane elasticity and polymerization energy sets the shape of spherical clathrin coats," *Nature communications*, vol. 6, no. 1, pp. 1–10, 2015.

[536] S. Ebrahimi and S. Okabe, "Structural dynamics of dendritic spines: molecular composition, geometry and functional regulation," *Biochimica et Biophysica Acta (BBA)-Biomembranes*, vol. 1838, no. 10, pp. 2391–2398, 2014.

[537] E. Evans, H. Bowman, A. Leung, D. Needham, and D. Tirrell, "Biomembrane templates for nanoscale conduits and networks," *Science*, vol. 273, no. 5277, pp. 933–935, 1996.

[538] D. Raucher and M. P. Sheetz, "Characteristics of a membrane reservoir buffering membrane tension," *Biophysical journal*, vol. 77, no. 4, pp. 1992–2002, 1999.

[539] A. Roux, G. Cappello, J. Cartaud, J. Prost, B. Goud, and P. Bassereau, "A minimal system allowing tubulation with molecular motors pulling on giant liposomes," *Proceedings of the National Academy of Sciences*, vol. 99, no. 8, pp. 5394–5399, 2002.

[540] T. A. Blanpied, D. B. Scott, and M. D. Ehlers, "Dynamics and regulation of clathrin coats at specialized endocytic zones of dendrites and spines," *Neuron*, vol. 36, no. 3, pp. 435–449, 2002.

[541] G. L. Collingridge, J. T. Isaac, and Y. T. Wang, "Receptor trafficking and synaptic plasticity," *Nature Reviews Neuroscience*, vol. 5, no. 12, pp. 952–962, 2004.

[542] C. T. Lee, J. G. Laughlin, N. A. de La Beaumelle, R. E. Amaro, J. A. McCammon, R. Ramamoorthi, M. Holst, and P. Rangamani, "3d mesh processing using gamer 2 to enable reaction-diffusion simulations in realistic cellular geometries," *PLoS computational biology*, vol. 16, no. 4, p. e1007756, 2020.

[543] H. Alimohamadi, M. Bell, S. Halpain, and P. Rangamani, "Biophysical modeling of membrane-actin interactions governing the morphology of dendritic spines," *Bulletin of the American Physical Society*, 2021.

[544] D. J. Steigmann, *The Role of Mechanics in the Study of Lipid Bilayers*, vol. 577. Springer, 2017.

[545] R. Shlomovitz, N. Gov, and A. Roux, "Membrane-mediated interactions and the dynamics of dynamin oligomers on membrane tubes," *New Journal of Physics*, vol. 13, no. 6, p. 065008, 2011.

[546] Z. Peng, R. J. Asaro, and Q. Zhu, "Multiscale simulation of erythrocyte membranes," *Physical Review E*, vol. 81, no. 3, p. 031904, 2010.

[547] H. Noguchi and G. Gompper, "Fluid vesicles with viscous membranes in shear flow," *Phys. Rev. Lett.*, vol. 93, no. 25, p. 258102, 2004.

[548] C. Prévost, H. Zhao, J. Manzi, E. Lemichez, P. Lappalainen, A. Callan-Jones, and P. Bassereau, "Irsp53 senses negative membrane curvature and phase separates along membrane tubules," *Nature communications*, vol. 6, 2015.

[549] R. Wedlich-Soldner and T. Betz, "Self-organization: the fundament of cell biology," 2018.

[550] S. Ramaswamy, J. Toner, and J. Prost, "Nonequilibrium fluctuations, traveling waves, and instabilities in active membranes," *Phys. Rev. Lett.*, vol. 84, no. 15, p. 3494, 2000.

[551] K. L. Madsen, V. Bhatia, U. Gether, and D. Stamou, "Bar domains, amphipathic helices and membrane-anchored proteins use the same mechanism to sense membrane curvature," *FEBS letters*, vol. 584, no. 9, pp. 1848–1855, 2010.

[552] D. Raucher, T. Stauffer, W. Chen, K. Shen, S. Guo, J. D. York, M. P. Sheetz, and T. Meyer, "Phosphatidylinositol 4,5-bisphosphate functions as a second messenger that regulates cytoskeleton-plasma membrane adhesion," *Cell*, vol. 100, pp. 221–228, Jan. 2000.

[553] M. Chabanon, J. C. Stachowiak, and P. Rangamani, "Systems biology of cellular membranes: a convergence with biophysics," *Wiley Interdisciplinary Reviews: Systems Biology and Medicine*, vol. 9, no. 5, 2017.

[554] G. S. Ayton, J. L. McWhirter, and G. A. Voth, "A second generation mesoscopic lipid bilayer model: Connections to field-theory descriptions of membranes and nonlocal hydrodynamics," *J. Chem. Phys.*, vol. 124, no. 6, p. 064906, 2006.

[555] M. Chabanon and P. Rangamani, "Gaussian curvature directs the distribution of spontaneous curvature on bilayer membrane necks," *Soft matter*, vol. 14, no. 12, pp. 2281–2294, 2018.

[556] F. Hochmuth, J.-Y. Shao, J. Dai, and M. P. Sheetz, "Deformation and flow of membrane into tethers extracted from neuronal growth cones," *Biophysical journal*, vol. 70, no. 1, pp. 358–369, 1996.